The Dissertation Committee for Erik Johnson Archibald

certifies that this is the approved version of the following dissertation:

Fire & Explosion Hazards due to Thermal Runaway Propagation in Lithium-Ion Battery Systems

Committee:

Ofodike Ezekoye, Supervisor

Atila Novoselac

Eric Williamson

Kevin Marr

Fire & Explosion Hazards due to Thermal Runaway Propagation in Lithium-Ion Battery Systems

by

Erik Johnson Archibald

Dissertation

Presented to the Faculty of the Graduate School of

The University of Texas at Austin

in Partial Fulfillment

of the Requirements

for the Degree of

Doctor of Philosophy

The University of Texas at Austin

May 2021

Dedicated to:

Alyssa, Taft, Joel, Kent & Evan - May you love learning throughout your life

Acknowledgments

I would like to thank Dr. Ofodike Ezekoye for his mentorship and guidance. Thanks for believing in me and my potential as a researcher and for giving me the support I need to learn and grow. Thanks for trusting me do important work, lead teams and perform large fire and explosion experiments.

I would like to thank all of the UTFRG students that helped me design, build and run experiments. Ilisha D'Souza helped keep me organized in my first experiments and run SEM analysis on battery samples. Eduardo Aguirre used his talents to fabricate experimental setups and the fire/explosion experiment hood. Robyn Richmond was very eager to learn and led data acquisition on my large cell, module and rack experiments. I am grateful to Jaime Estrada for his help in creating the thermocouples and instrumenting modules to collect hundreds of channels of data on module thermal runaway. Thanks to Noah Graff for working hard to build the rack system used on the rack experiments. Finally, I am grateful to Sam Matthews who has been my right-hand man in the planning, development, fabrication and execution of single-cell, module, rack and explosion experiments. Sam is a talented engineer who is not afraid to get his hands dirty and take on any challenge.

I would like to acknowledge my fellow graduate students at UTFRG, Serhat Bilyaz,

Jan Cabrera, Tyler Buffington, Savannah Wessies, Robert Kennedy, Austin Baird, Dan Wanegar and Ben Trettel. Thanks for all the things I've learned from you and for all your help in my research. Your companionship and support has made my research experience enjoyable and worthwhile.

I would like to thank my parents Jim and Margaret for always being supportive and encouraging to learn and explore. Everyday I am blessed that they nurtured me to love learning from an early age. I will be forever grateful for my mother who was fully supportive of her son joining the volunteer fire company as a junior firefighter at age 16. I am thankful for my father who taught me essential engineering skills such as Ohm's law and how to solder at a young age. I still solder at an elementary school level and I am grateful that most of the assembly of the circuit board I designed was performed in China. Finally, I would like to thank my wife, Emily for her love, support, optimism and patience. She has supported me in my education from the very beginning and somehow always thought this was a good idea even when I did not. Her patience and loving care for our 5 beautiful children has made my doctoral studies possible.

Erik Johnson Archibald

The University of Texas at Austin

May 2021

Fire & Explosion Hazards due to Thermal Runaway Propagation in Lithium-Ion Battery Systems

Publication No. _____

Erik Johnson Archibald, Ph.D.
The University of Texas at Austin, 2021

Supervisor: Ofodike Ezekoye

Lithium-ion battery technologies are increasingly used in electric vehicles as well for electrical energy storage at residences, businesses and utilities. In a failure event, these cells may produce large quantities of gas that pose fire, explosion and toxicity hazards to building occupants and firefighters. To understand the hazard, it is important to understand how single cells fail and how that failure propagates to other cells. Once the quantity and composition of the gas released by a single cell is understood and the failure process to surrounding cells is understood then models can be applied to quantify the explosion or fire hazard of the system.

A series of experiments is conducted using single cell and linear 1D arrays of lithium-ion pouch cells to understand the thermal runaway process for a single cell and compare it to how thermal runaway propagates through an array of cells. Due to the difference in heating between single cells and cells failing in an array, there are differences in failure characteristics. Single cells vent gases faster and more violently than those failed in an array. This causes damaged cells to look very different. An idealized process for thermal runaway propagation in an array of cells is presented.

Many systems have complex geometry in which heat transfer via conduction, convection and radiation may cause thermal runaway propagation in 3 dimensions. Experiments are conducted with individual prismatic lithium-ion cells and modules comprising 14 cells to study the more complex runaway propagation behavior of commercially available energy storage modules. The quantity and species of gases released by a single cell is measured. The propagation of thermal runaway through the 14 cells in a module is observed for both a module in open air and modules in a rack. The impact on the temperature and heat flux within the rack and throughout the room is measured. A computational fluid dynamics model is developed and used to predict temperatures, heat fluxes and gas concentrations in the compartment.

Gas sensing, ignition and control systems are developed to perform explosion experiments with lithium-ion cells. Explosion experiments are performed at lab scale, intermediate scale and full-size closet scale. Full scale experiments are conducted in a closet which reveal that a single 94 Ah cell provides both the fuel and ignition to cause a partial volume deflagration which breaks the closet door.

Once gas release and propagation behavior are understood, a series of models can be used to estimate explosion consequences. Simple models are described to predict

possible flammable gas mixing prior to an explosion. Battery vent gas compositions are used with models to calculate flammability limits, laminar flame speed, maximum adiabatic pressure and other properties. Gas mixture properties and compartment geometry is used in a 0D deflagration code to predict pressures and impulses. Single degree of freedom calculations are used to predict possible consequences from the calculated pressures and impulses. Models are validated against experimental literature and demonstrated in case studies. Flammability properties are calculated and summarized for a database of gas composition data. Gas properties are used to determine minimum amounts of energy storage required to cause an explosion.

...

Contents

List of Tables

List of Figures

Chapter 1

Introduction

1.1 Overview and Motivation

Lithium-ion batteries are used in a wide range of applications. Lithium-ion cells are found in consumer electronics such as watches, phones, laptops and drones. Larger portable lithium-ion battery systems are found in electric vehicles which can range from single-user scooters to trucks, trains and aircraft. Large fixed location lithium-ion systems are used in energy storage at residential, commercial, industrial and grid level installations. Unfortunately, lithium-ion batteries can fail in thermal runaway, causing the generation of heat and release of flammable gases. These flammable gases pose serious fire and explosion hazards. When the volume of flammable gas is significant compared to the volume of the compartment, there is a potential for enough flammable gas to accumulate to cause an explosion.

1.2 Notable Incidents involving Lithium-Ion Systems

Firefighters around the world are responding to an increasing number of incidents involving lithium-ion battery technologies. A review of recent incidents shows a few of the ways in which the hazard is manifest.

1.2.1 Fire Incidents

In 2017, a containerized lithium-ion battery energy storage system (ESS) burned at a utility plant near Brussels, Belgium. This system was equipped with fire detection and suppression equipment which failed to extinguish the fire [16]. Figure 1.1 shows the unit on fire shortly before fire department arrival.

Figure 1.1: Engie ESS Fire at the time of fire department arrival. [3]

In the course of less than two years, South Korea experienced 23 fire incidents involving energy storage systems. For example, in 2018 a cement plant in Jecheon, North Chungcheong Province incurred over $3 million in damage due to an ESS fire. [17]. An investigation into these fires found that some of the causes included insufficient shock protection, environmental effects, faulty installation and poor systems integration [18, 19]. The fire incidents in South Korea have led to serious concerns about the safety of lithium-ion energy storage systems.

1.2.2 Explosion Incidents

In 2017 the top container on a double-stacked container train car in Houston, Texas exploded. The container was carrying drums of used consumer lithium-ion batteries to a recycling facility. The explosion was forceful enough to break windows on buildings 500 feet away. It also threw a man across a room inside a house about 500 feet away from the train. [20, 21].

Figure 1.2: Top container on double-stacked train car was completed destroyed in explosion caused by thermal runaway of lithium-ion batteries packed in drums being being sent to recycling facility (Yi-Chin Lee, Houston Chronicle) [4]

In April 2019, a 2 MW ESS system in Surprise, AZ exploded resulting in eight injured firefighters. [22, 23]. The explosion threw one firefighter 73 feet and another firefighter 30 feet, causing serious trauma in addition to chemical burns and chemical inhalation exposure [5]. This incident comes after a 2012 fire involving the same electric utility [24].

Figure 1.3: ESS Building After Explosion showing green door which was blown off of the building [5]

In March 2020 a fire occurred in the battery room on the fifth floor of a Griffith University office building in Australia [25]. Soon after firefighters opened the battery room door, an explosion occurred which threw a firefighter about 10 feet. The firefighter was thrown just a few feet away from a ledge. If he had gone over the edge, he would have fallen several stories and been severely injured or killed. On the ground and across the street, onlookers saw a large fireball at the time of the explosion [6].

Figure 1.4: Fifth floor battery room explosion at Griffith University caused fireball visible to onlookers at street level [6]

In July 2019, the battery in a Hyundai Kona electric car went into thermal runaway and caused an explosion in a garage in Montreal, Quebec, Canada [7]. The explosion blew a hole in the garage roof and launched the garage door across the street.

Figure 1.5: Garage after Hyundai Kona thermal runaway caused explosion which threw garage door across the street and damaged roof (Mathiue Wagner - Radio Canada) [7]

These incidents highlight the breadth of the fire and explosion hazards due to battery thermal runaway. Thermal runaway has caused both large and small fires and explosions in places ranging from homes to large utility installations.

1.3 Lithium-Ion Battery Operation

Lithium-ion batteries are made of several components. The primary components are the anode, cathode, separator and electrolyte. Graphite and other carbon-based materials are used as the anode for most lithium-ion batteries. The anode is connected to the negative electrode using most often a copper foil current collector. Various formulations are used for the cathode active material. Common cathode composi-

tions are lithium cobalt oxide (LCO), nickel manganese cobalt (NMC), lithum nickel cobalt aluminum oxide (NCA) and lithium iron phosphate (LFP). The cathode is connected to the positive terminal typically with an aluminum foil current collector. The electrolyte consists of a lithium salt dissolved in an organic solvent. Typical lithium salts include $LiPF_6, LiBF_4$ and $LiClO_4$. Organic solvents are often mixtures of ethylene carbonate (EC), dimethyl carbonate (DMC) and diethyl carbonate (DEC). In between the cathode and anode, a thin separator prevents the two from coming in contact while still allowing the passage of lithium-ions from one side to the other. The separator is often made of polyethylene or polypropylene.

As a battery is charged, lithium-ions are passed from the cathode (positive terminal) to the anode (negative terminal). As the battery is discharged the ions move in the opposite direction going from the anode to the cathode.

There are a number of form factors for packaging of cells. Many smaller cells are packaged into cylindrical metal cans. These cans are equipped with terminals on either end. At one end, a terminal is constructed to act as a pressure relief that will vent and relieve pressure if the pressure inside the cell becomes excessive. Pouch cells are packaged inside soft pouches that protect the cell. Pouch material can consist of an aluminum foil which is coated in plastic such as polyethylene or polypropylene. Prismatic cells are encased in hard metal cans that are non-cylindrical. Unlike cylindrical cells, prismatic cells generally have both terminals and a separate vent on the top of the cell. Figure 1.6 shows the various form factors and sizes. This work uses all of the cells pictured in Figure 1.6 with the exception of the small 18650 cylindrical cell.

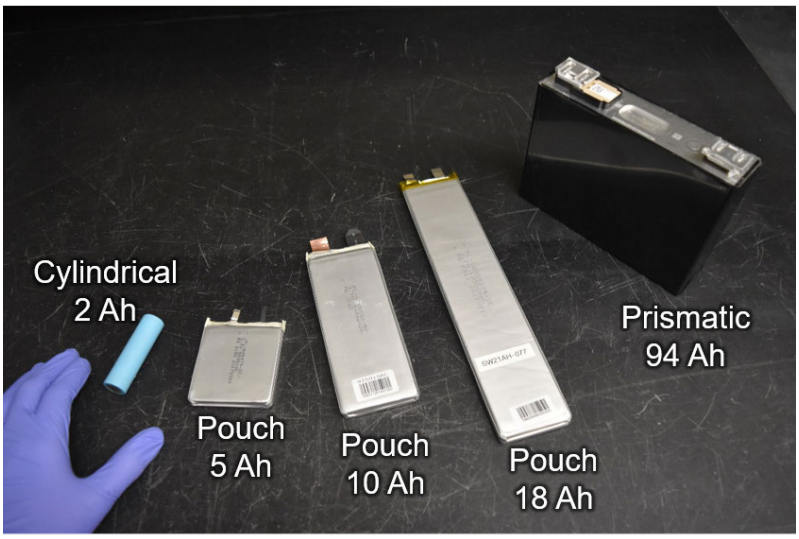

Figure 1.6: Various lithium-ion cell form factors and sizes.

Battery systems often include more than one cell. Multiple cells may be packaged together into a unit called a module. Modules may be constructed using cylindrical, pouch or prismatic cells. In an ESS multiple modules may be put together on a rack. The rack may also include additional equipment such as battery management system electronics. An ESS facility may consist of many racks. In electric vehicles multiple modules may be assembled together to create a battery pack. Figure 1.7 shows two modules used in this project.

1.4 Purpose and Objectives

Due to the evolving technology, there is limited understanding of the nature of fire and explosion hazards associated with lithium-ion battery systems. This is especially true for large systems and explosions. There are few experiments in the literature

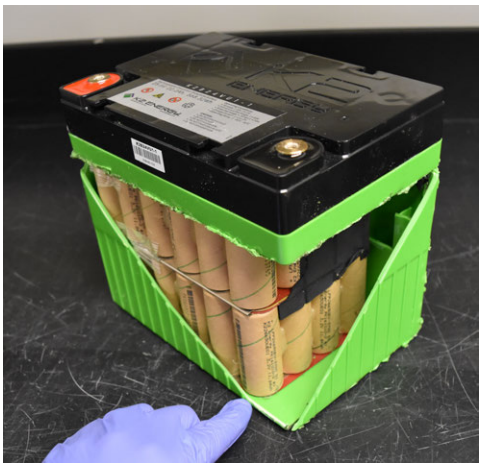

(a) A module consisting of 48 LFP cylindrical cells

(b) A rack-mount capable module consisting of 14 prismatic cells

Figure 1.7: Lithium-ion battery modules

involving intermediate and large systems and even less experiments characterizing the explosion potential. Although extensive work has been done on the explosion hazards of dusts and gasses, very little has been done to understand how battery systems can cause explosions. The purpose of this work is to improve understanding of how thermal runaway propagates through cells and modules and to apply that understanding to understand both fire and explosion hazards caused by lithium-ion battery systems. There are a number of key objectives:

1. Characterize the thermal runaway propagation behavior of pouch cells in a 1D linear array of cells.

2. Characterize the thermal runaway propagation process and effects for a commercially available ESS module in a compartment.

3. Conduct explosion experiments to observe the processes involved in an explosion of battery vent gas.

4. Develop models to estimate possible explosion hazard consequences for different scenarios.

1.5 Chapter Outline

This dissertation consists of five main content chapters, a conclusion chapter and appendices of supplemental material. In Chapter 2 experiments are used to understand thermal runaway in a single cell and how thermal runaway propagates in a 1D array of cells in direct thermal contact. However, real systems are often more complex than simple 1D arrays of cells and can cause fire and thermal consequences in the entire room. In Chapter 3 commercially available ESS modules are put into thermal runaway in a compartment to understand runaway propagation in an actual system and its effects on the room.

Chapters 4 and 5 investigate the explosion hazards associated with lithium-ion battery thermal runaway. Chapter 4 describes the development and execution of lithium-ion battery vent gas explosion experiments. Chapter 5 describes a number of models that can be used to understand whether an explosion can occur in a given scenario and what it's consequences may be. Chapter 6 demonstrates case studies and applications of the explosion hazard models. Chapter 7 provides conclusions. Appendix B describes experiments done with LFP cells.

Chapter 2

Thermal Runaway in Single Cells and 1D Arrays

Much of this chapter was written for and presented at the 1st International Symposium on Lithium Battery Fire Safety (ISLBFS) held on July 18–20 in 2019 in Hefei, China. This work was subsequently published in the Journal of Fire Technology [26]. This work was authored by Erik Archibald, Robert Kennedy, Dr. Judith Jeevarajan, Dr. Kevin Marr and Dr. Ofodike Ezekoye. All of the single cell experiments and the first few array experiments were performed and analyzed by Erik Archibald. Robert built the pressure vessel and data collection system and ran the remainder of the array experiments. Dr. Marr and Dr. Ezekoye assisted with direction and editing. Dr. Jeevarajan assisted with editing and review.

2.1 Introduction

Although the quantity of gas released by a single cell battery in a large space may not pose any explosion risk, propagation of thermal runaway from one cell to others can release enough gas to create serious explosion hazards. Thermal runaway propagation from cell to cell occurs as heat is transferred from a cell in thermal runaway to nearby cells that may not have been previously defective or damaged. Understanding the rate of propagation is useful to characterize the rate at which the system as a whole is releasing flammable gases.

Various experimental and modeling studies have been conducted to investigate thermal runaway propagation in multi-cell cylindrical cell arrays. Studies on runaway propagation in 18650 cylindrical cell arrays have shown that increased distance or insulation between cells[27, 28, 29, 30, 31] and phase change material inhibit cell-to-cell propagation [28]. Experiments on 18650 cell arrays have also shown that cells electrically connected in series are less likely to propagate compared to cells connected in parallel[29], and branched tabbing can reduce the chances of propagation for cells in parallel [30]. Other experiments have shown that a higher state of charge (SOC) and initiation near the center of a battery pack leads to faster propagation rates in 18650 arrays[32]. Experiments comparing different arrangements of 18650's found that cells arranged in a triangular array propagated runaway more slowly than those in parallelogram or square arrays [33]. Although cells with lower states of charge can reduce the severity of runaway, rapid discharging of surrounding cells while others are going into runaway has been found to increase the rate of propagation[33]. Huang et al. conducted experiments exposing large cylindrical 50 Ah LTO cells to flame and observed that runaway propagation can cause cells to explode[34]. Said et al.

performed experiments measuring the heat released by each cell in an 18650 array and found that an air environment significantly increased the rate of propagation when compared to nitrogen[35].

Fewer experiments on pouch cell thermal runaway propagation are documented in published literature. These experiments have shown that unlike 18650 arrays, changing cell electrical connections does not prevent propagation[29]. This is because pouch cells have strong heat conduction from cell to cell due to being in full contact and clamped together. Heat dissipation and increased thermal resistance between pouch cells are shown to be effective at preventing propagation in pouch cell arrays[36, 37]. Feng et al. conducted a pouch cell propagation experiment using pouch cells in an aluminum battery pack and developed a model to predict TR propagation. They show that a 1 mm thick insulating layer between cells can prevent propagation[36]. Li et al. developed a 3D model to predict runaway propagation as well and validate it against pouch cell array experiments. They show that an aluminum heatsink placed between cells can also stop runaway propagation[38]. Our work on pouch cell arrays [39] builds on these studies and will be described in section 2.3. Since this work was completed, Kennedy has gone on to explore gas generation associated with lithium cobalt oxide pouch arrays in detail[40].

2.2 5 Ah Pouch Single Cell Experiments

2.2.0.1 Purpose and Introduction

To understand the behavior of large systems comprised of tens, hundreds or thousands of cells, it is important to first understand the thermal runaway failure process

for a single cell. In these experiments the failure process of single 5 Ah pouch cells is observed. During thermal runaway, observations are made of appearance, temperature, cell voltage and stress on a load cell.

2.2.0.2 Experimental Setup

A series of experiments were performed using single lithium-ion pouch cells. These experiments were conducted using 3.7 V, 5 Ah lithium-ion pouch cells (Model PL-896474-2C) from AA Portable Power Corp [41]. The cells have dimensions of 75.5 mm x 64.5 mm x 9.0mm and a mass of 90.2 grams. A photo of the cell and a partially disassembled cell for mass composition measurement is shown in 2.1. The mass composition of the cell was determined by discharging cell, evaporating the electrolyte in a vacuum vessel and then dissembling the cell and measuring the mass of each component. The cell composition is given in Table 2.1.

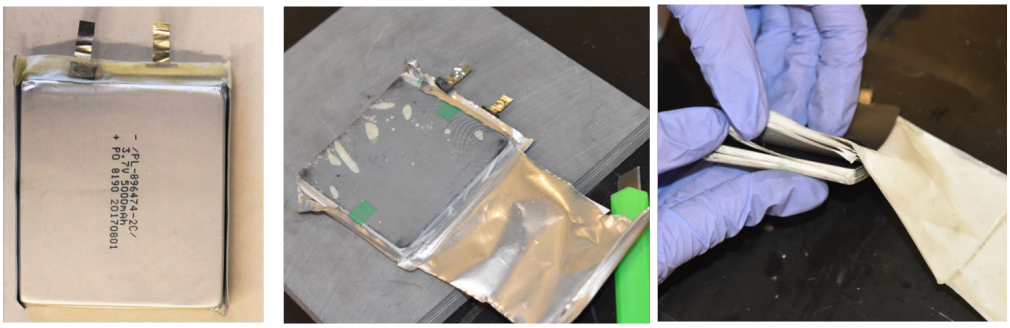

Figure 2.1: Photos showing the cell during various stages of disassembly to measure the mass composition of the cell.

The clamping, insulation and heating setup for these experiments is shown in Figure 2.2. In these tests, cells were heated slowly using custom fabricated aluminum block heaters. The block heater consists of two 6.35 mm diameter 300W cartridge heaters approximately 51 mm apart inserted into a 88.9 mm x 76.2 mm x 12.7 mm aluminum

Component	Composition	Mass Percentage
Cathode and Current Collector	Lithium Cobalt Oxide, Aluminum	49.1%
Anode and Current Collector	Graphite, Copper	33.0%
Electrolyte	LiPF6, EC, DEC, DMC	9.7%
Separator	Polypropylene	5.1%
Pouch	Aluminum, Nylon, Polypropylene	3.1%

Table 2.1: 5 Ah Pouch Cell Battery Components

block. A single cell is inserted between two block heaters and a constant ramp heating profile at an approximate rate of 5 °C/min was applied using a programmable temperature controller. This heating rate was selected because it is used in an industry test standard (UL 9540A) for thermal runaway tests [42].The aluminum block heaters are surrounded with rigid calcium silicate insulation (Johns Manville Super Firetemp X). The entire apparatus is clamped together using four bolts which run through the aluminum blocks. The bolts are tightened such that before the experiment they apply a pressure of approximately 100 kPa to the cell. On one side of the experimental setup an additional aluminum block is placed to secure a load cell which is used to measure the clamping force being exerted on the battery. The load cell is positioned here to measure the clamping force without being damaged by the heat of thermal runaway. The exposed sides of the setup (not bordered by calcium silicate insulation) are wrapped in ceramic fiber insulation. Temperatures at several locations on the cell surface and between the aluminum blocks and insulation were measured using 36 gauge K type thermocouples.

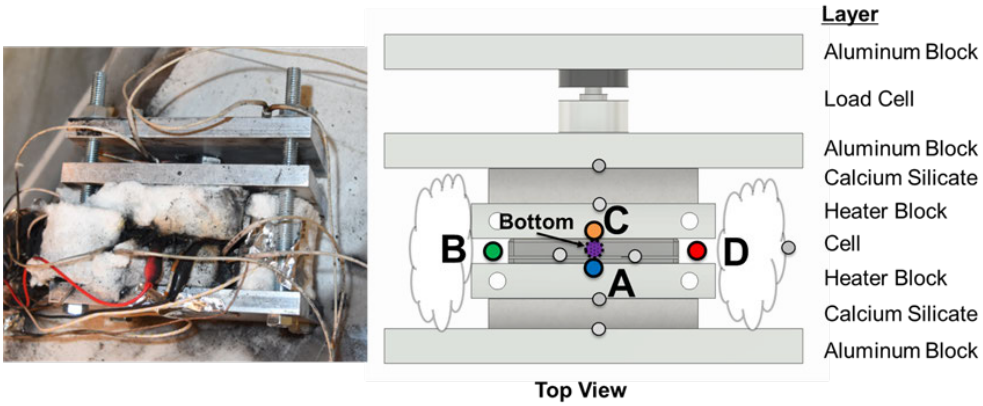

Figure 2.2: After-experiment photo and diagram of single cell test setup. Aluminum blocks are clamped with bolts and insulation surrounds cell and heater blocks. A, B,C,D is used to designate sides of test setup and corresponding thermocouple locations. Thermocouple locations are shown with filled in circles. The cell tabs are pointed upwards. White circles in heater blocks indicate locations of cylindrical cartridge heaters.

Prior to the experiment the batteries were cycled twice using a 5A discharge rate to verify that their actual capacity is within 5 % of their rated capacity. Before each experiment batteries were fully charged using a 1A constant current charge until 4.2V and a constant voltage charge at 4.2V until the current was less than 250 mA.

Three experiments were run using this procedure. The first two were conducted in ambient air underneath a vent hood. The third experiment was conducted in a nitrogen environment inside a pressure vessel.

2.2.0.3 Results

Cell voltage and interface surface temperature were measured and recorded throughout the tests. In addition to these measurements, force data from the load cell for all three experiments was also recorded. Load cell force values are divided by cell area

to calculate the clamping pressure on the cell. For testing in the pressure vessel, the chamber gas pressure and temperature were recorded to estimate gas release rates and volume. Temperatures and clamping stress from the load cell for the test in the pressure vessel were similar to the hood experiments and results are considered together. Figure 2.3 shows plots of heater temperature, load cell clamping stress, and pressure vessel gas pressure for the three experiments. The test results show good reproducibility. For convenience in comparing experiments, in Figure 2.3 and Figure 2.4 the origin of the time axis is offset so that t=0 references the time at which (dT/dt) for any thermocouple exceeds 100 °C/sec. In all three tests, the time of this rapid temperature increase occurred when the cell / heater interface temperature was between 185 °C and 196 °C. Results for Test 3 include the gas pressure time history in the pressure vessel.

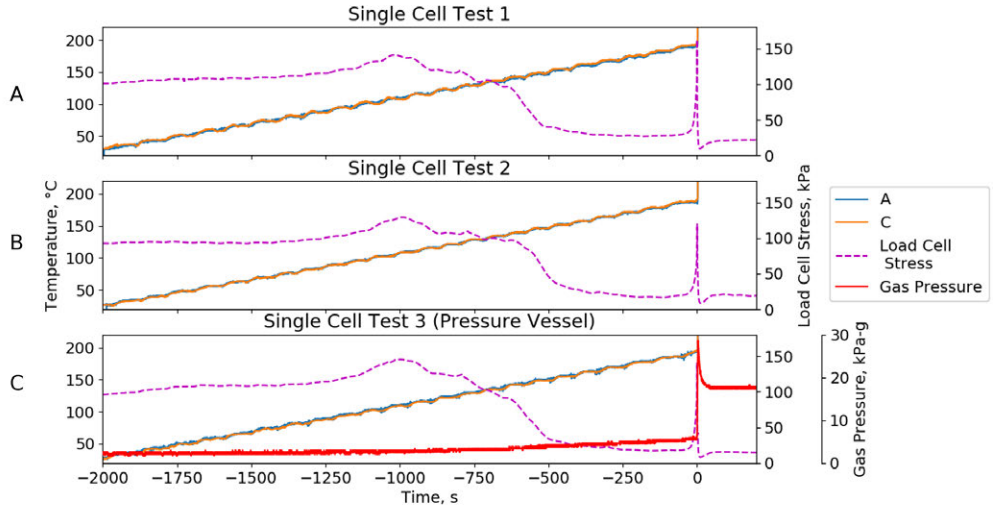

Figure 2.3: Temperature, load cell clamping stress and vessel gas pressure data shown for three single cell experiments from the beginning of cell heating until after runaway completion. Load cell clamping stress indicates cell pressure buildup and venting approximately 1000 seconds before runaway.

The load cell data provide additional insight into the events leading up to thermal runaway. As previously noted, the load cell force measures the mechanical force compressing the batteries. The initial stress measured by the load cell is due to the clamping force applied by tightening the bolts on the apparatus. Initially, this stress is largely resisted by the internal stresses in the battery solid materials. As the cell is heated, gas is generated from electrolyte evaporation and chemical decomposition of the active materials and electrolyte. The gas generation process increases the pressure inside the cell, which in turn increases the measured clamping stress. Since the clamping stress is resisted by internal stresses in the porous matrix (solids, liquid, and gas) within the cell, the clamping stress measured by the load cell is not an exact measure of cell internal gas pressure.

As the cell is steadily heated at 5°C/min, the load cell clamping stress remains fairly constant for about 10 minutes. The clamping stress gradually begins to increase at approximately -1400 sec when the cell is at about 75°C. This increase in stress aligns with the beginning of SEI layer decomposition which ARC testing shows begins at 70°C [43, 44]. The increase in pressure accelerates until the load cell pressure reaches a peak at -1000 sec when the cell is at 110°C. The increasing rate of pressure rise from -1400 sec to -1000 sec could be due to the reaction of intercalated lithium with the organic solvents which releases hydrocarbons. These reactions typically occur at 100°C[43]. At -1000 sec the pressure begins to fall because the pouch swells or containment fails and the confined gases begin to vent. These vented gases are not immediately visible to the naked eye but can be seen when the venting process is viewed through a thermal infrared camera. Initially, this incipient venting process does not release enough gas to cause a noticeable rise in gas pressure in the pressure

vessel. As time goes on, the rate of gas venting increases and venting becomes visible. Before the time the cell experiences rapid heating and intense venting at t=0 s, the vessel chamber pressure and temperature are used to infer that about 15 % of the total gas has already been released. Looking at temperature data, an early warning of thermal runaway is seen at -100 seconds where temperatures measured on the cell surface begin to exceed those on the heater surface. At -20 seconds, the load cell stress begins to increase at an increasing rate. This is indicative of higher pressures inside the cell as gas is produced at an increasing rate. At t=0 the first rapid temperature rise is recorded and the heater-cell temperature is between 185°C and 196°C. At this time, the load cell pressure drops suddenly due to rapid gas venting as a larger area of the cell pouch has burst. At this time the cell rapidly vents gas, electrolyte as shown in 2.5.

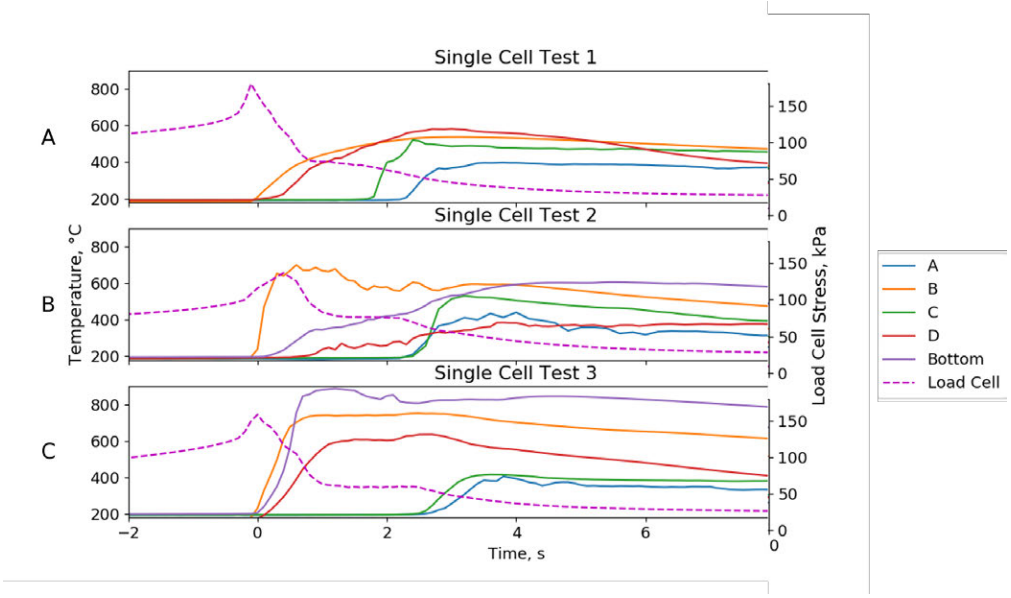

Figure 2.4: Temperature and load cell pressure data shown for three single cell experiments from 2 seconds before runaway until 10 seconds after.

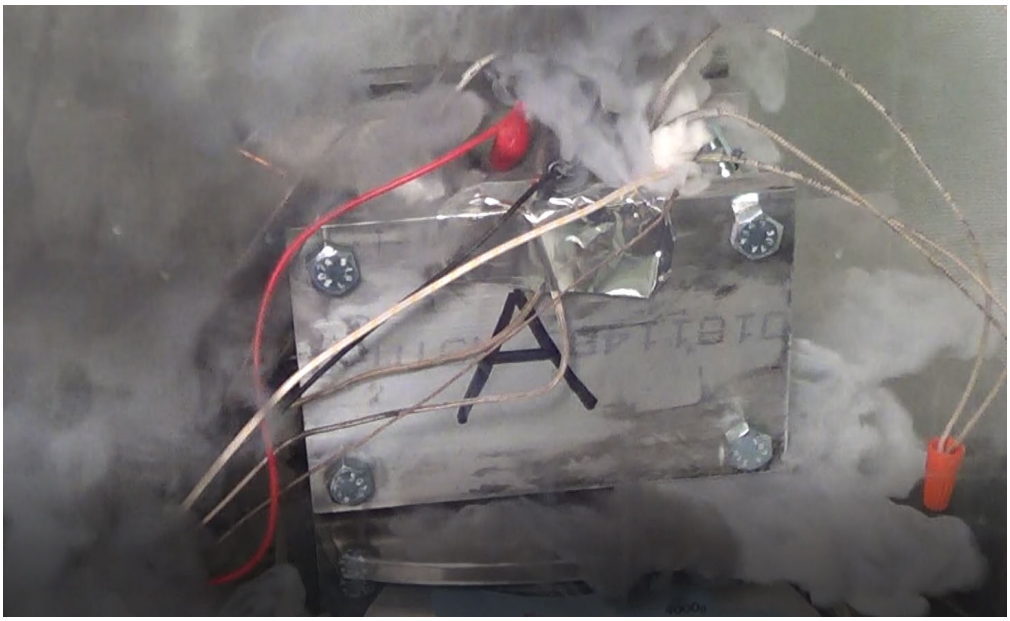

Figure 2.5: Cell during intense venting at approximately t=2 s

Figure 2.4 shows data from the same experiments as Figure 2.3, but focuses on temperatures and load cell pressures just before and during thermal runaway for the three experiments. For these experiments the A and C thermocouples are located on the interfaces between the cell and the heaters while the B and D thermocouples are located on the sides of the battery as shown in Figure 2.2. In this plot, runaway is first observed as thermocouples on the B and D sides of the cell rapidly increase in temperature. Although uniform heating was applied to both A and C sides of the cell, the rapid temperature increase associated with thermal runaway did not always occur simultaneously on the A and C sides or the B and D sides of the cell. This suggests that thermal runaway did not initiate at the center of the cell. This contrasts with the expectation that for a cell heated symmetrically on both sides, the thermal runaway chemical reactions should occur first at the center of the cell. This asymmetry will be seen again during battery teardowns.

In the Figure 2.4 Test 3 subplot, the bottom thermocouple rises very rapidly to 900°C. This very sudden increase in the thermocouple temperature to high temperatures is associated with a hot gas jet emerging from the side of the battery close to the thermocouple location. For each test the time between the first temperature rise which is seen on the B side, to the time of the temperature rise on the D side is between 200 and 900 ms. The time from the first temperature rise until temperature rise on the A and C sides is between 1.8 and 2.8 seconds. In total it takes on average 4 seconds to travel through the thickness (A to C side) of the battery. Using the dimensions of the battery, the speed at which the temperature disturbance propagates in the plane of the battery (from B to D side) is significantly faster than the disturbance speed in the through-thickness direction. Using array propagation data, it will be shown that these differences can be explained with a relatively simple convection-diffusion-reaction equation theory.

2.2.0.4 Post Experiment Teardown

After each experiment, all cells were dissected to observe the damage caused by runaway. For the single cells put through uniform 5°C/min heating, teardown results looked similar. Figure 2.10 shows two layers from the Test 2 teardown that are representative of what single cell experiment layers looked like. In Figure 2.10a a layer with light damage is shown. Areas with light damage like this were seen in layers closest to the A side and C side of the cell. On the left is the remains of the copper foil and the anode. On the right is a thin layer of brittle material where the cathode would have been. Scanning Electron Microscopy (SEM) and Energy

Dispersive X-Ray (EDX) Analysis was performed in-house by an undergraduate research assistant. Using SEM and EDX, it was seen that this layer contains a large amount of carbon. This carbon may have come from any of several sources. These sources include electrolyte reaction products, separator products, the anode which is graphite, and the cathode which contains a large percentage of conductive carbon. The aluminum current collector for the cathode does not remain intact.

Figure 2.10 shows a heavily damaged layer from the teardown of Test 2. This layer shows a single location where it appears a localized, high heating rate event began and then propagated outward. This location is marked by an area of severe damage where a jet appears to have exited the battery. This location was generally close to halfway between the A and C sides of the battery and towards the center of the battery but never exactly in the center. This randomness in initiation location is likely due to inherent variability in cell construction. In the area of the battery not showing heavy damage, radial striations show the path of hot gases exiting the cell in a less violent manner. For this test the first high temperature and the highest temperature was measured on the B side, which is the side that the jet exits.

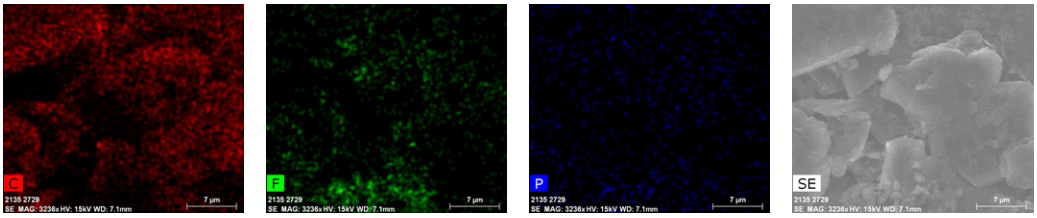

(a) Carbon (b) Fluorine (c) Phosphorous (d) SEM

Figure 2.6: New Anode EDX and SEM Images

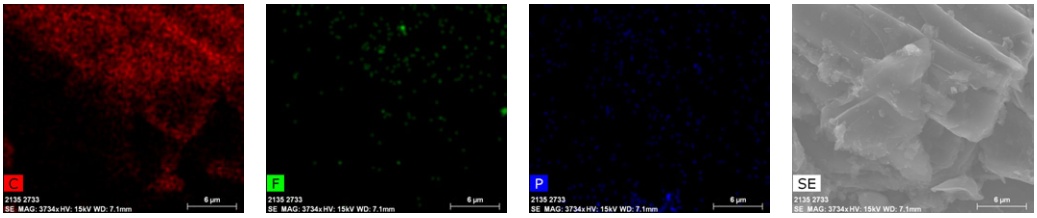

(a) Carbon (b) Fluorine (c) Phosphorous (d) SEM

Figure 2.7: Burned Anode EDX and SEM Images

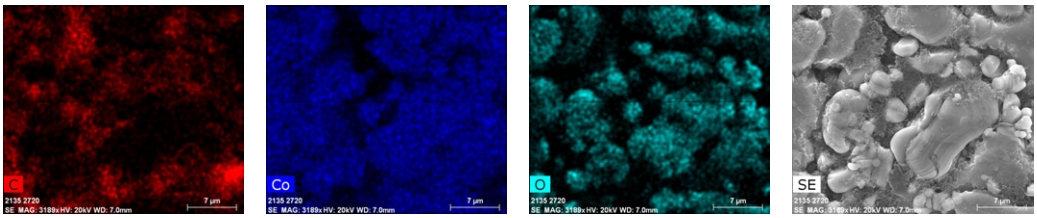

(a) Carbon (b) Cobalt (c) Oxygen (d) SEM

Figure 2.8: New Cathode EDX and SEM Images

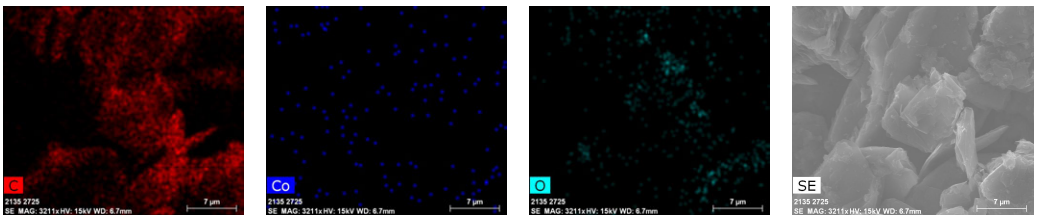

(a) Carbon (b) Cobalt (c) Oxygen (d) SEM

Figure 2.9: Burned Cathode EDX and SEM Images

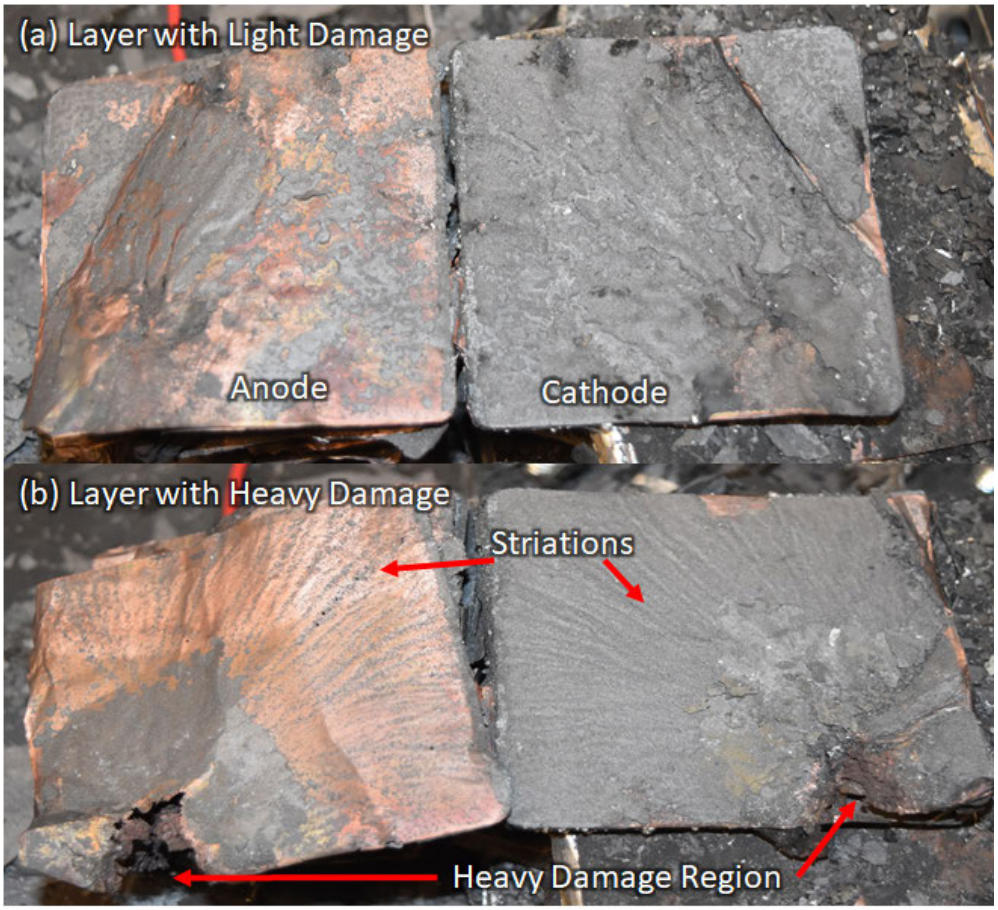

Figure 2.10: Layers from Single cell test 2 teardown.

Figure 2.11 shows a view of the B-side of the battery where the jet exited. From this angle it is apparent that the battery is thinner in the jet region, where more material was ejected than along the rest of the edge of the battery. Aluminum beads appear on the sides of the battery where hot gases escaped fast enough to push the melted aluminum, but slow enough to deposit it as it exited. In the jet region aluminum beads are not present due to the violent ejection of the jet.

Figure 2.11: Single cell test 2 jet region.

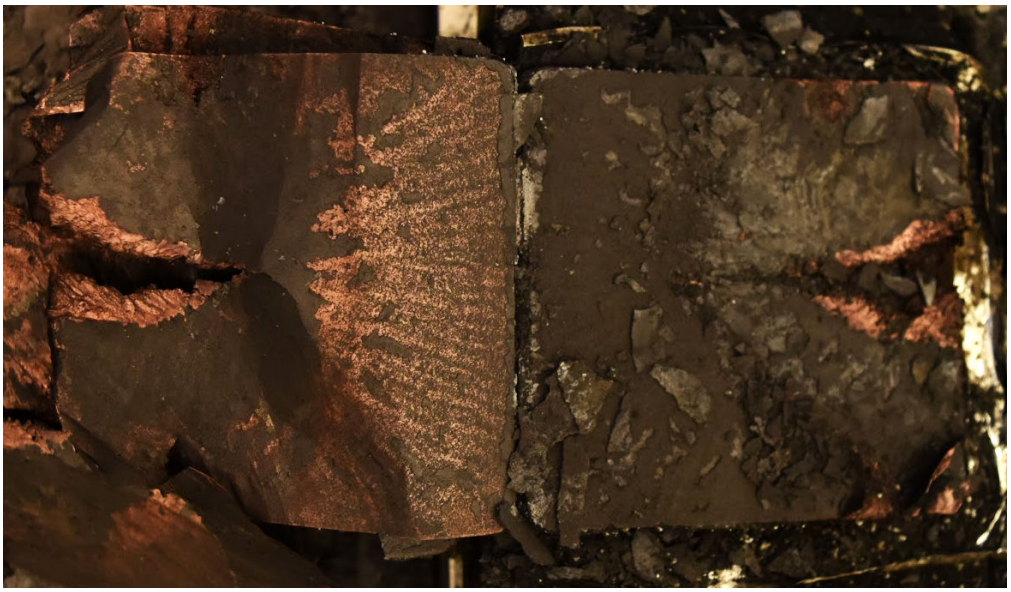

Figure 2.12: Single cell test 3 teardown.

Figure 2.12 shows the teardown for Test 3. As discussed previously, the Test 3 Bottom thermocouple recorded the highest temperature seen in this series of tests. This is because that thermocouple was located near the jet exit location on the bottom of the cell. In both photos we can observe that there was a single location that caused heavy damage and ejected not only decomposition products and electrolyte but also cathode and anode material as well as the copper and aluminum current collectors.

2.3 Study on Linear Array Propagation Process

To better understand the cell-to-cell propagation characteristics of multi-cell battery modules in larger battery systems, propagation tests were conducted by testing linear arrays of 5 Ah and 10 Ah cells. In these experiments the cells have direct contact with each other on the large faces of the cells, they do not have any electrical connections between cells.

2.3.0.1 Experimental Setup

The 5 Ah cells are the same as those previously used in the single cell experiments. The 10 Ah cells are lithium-cobalt oxide cathode cells with dimensions of 150 mm x 58 mm x 10.4 mm and a mass of 208.9 grams. The test fixture used in the array experiments is like the fixture used in the single cell experiments. Like the single cell setup, the array setup uses aluminum blocks to clamp the apparatus together and employs a load cell on one end to measure the clamping force exerted on the cells. In any given experiment, either five or ten cells were placed in a linear array. Insulation was placed in between the outermost cells and aluminum blocks. No insulation or

spacing was placed in between cells.

In the array experiments, a localized heating system was used rather than the block heaters used for single pouch cells in 2.2. In field failures caused by internal cell shorts, thermal runaway begins at a single cell where heating is localized. Because the heating is localized, the total amount of energy required to initiate thermal runaway may not be large. Typically, the energy generated by a localized failure does not significantly heat neighboring cells until thermal runaway of the initial cell occurs. For the slow heating rates used in the single cell experiments, a large amount of energy was required to initiate thermal runaway, which can preheat neighboring cells prior to thermal runaway occurring. Preheating neighboring cells would likely result in the preheated cells failing sooner compared to non-heated cells. To minimize this preheating effect on neighboring cells, a 15.9 mm diameter copper cylinder with a 150 W cartridge heater is used to heat a small localized area at the center of the cell at a high rate. The heater is turned on at full power and then turned off manually when a sharp rise (approximately 100°C/sec) in heater-cell interface temperature is observed. A maximum heating rate of approximately 100°C/min was measured at the heater and initiating cell interface before its temperature levels off between 400°C and 500°C until thermal runaway occurs.

The array tests were conducted in a nitrogen environment within a pressure vessel designed for battery testing. The pressure vessel remains sealed throughout the duration of the test to maintain a constant volume. The volume of the vessel is 55 L when empty and 54.4 L when a typical experiment setup is placed inside, not including the volume of the batteries. Figure 2.13 shows diagrams of the five-cell

array configurations for both the 10 Ah and 5 Ah cells. Thermocouples are placed along the centerline of the array at each interface between adjacent cells, the heater and initiating cell, and the last cell and insulation. Thermocouples are also placed in void spaces just above the setup and at the top and bottom of the pressure vessel. Vessel gauge pressure is measured using a pressure transducer mounted on the wall of the vessel. Figure 2.14 shows the 10-cell, 10 Ah array mounted in the vessel.

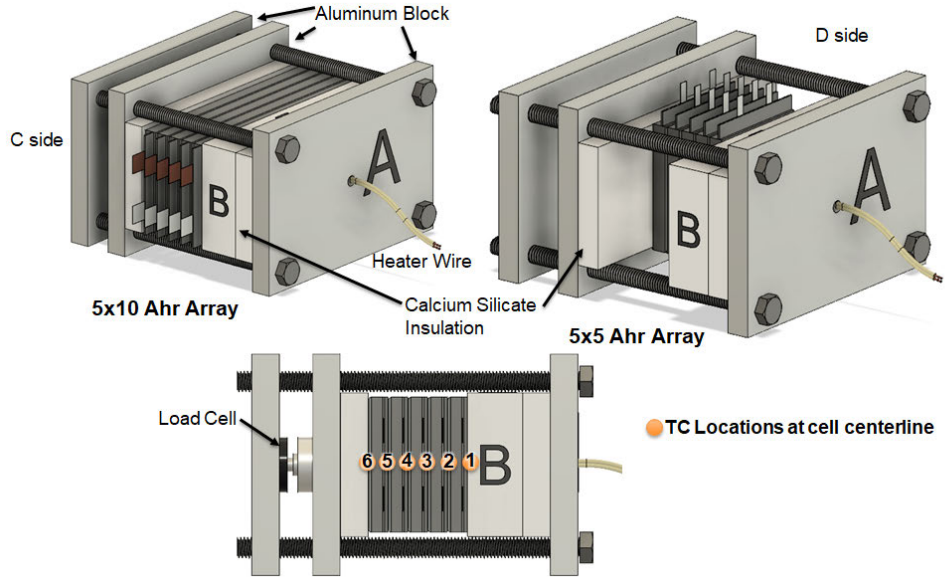

Figure 2.13: Diagram showing 5 cell array test setup with aluminum plates, clamping bolts, insulation and cells. A, B, C, D labels are used to indicate sides of setup.

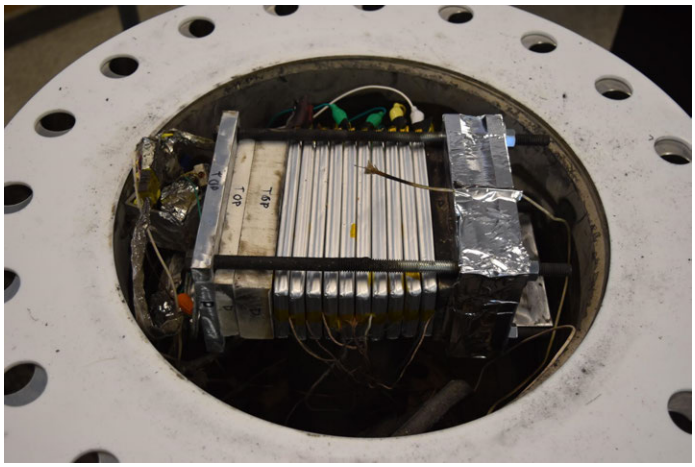

Figure 2.14: 10-cell 10 Ah array test setup in vessel before an experiment.

2.3.0.2 5 Ah Array Results

In the 5 Ah cell array experiments, surface temperatures were measured at the interface between two cells, or between a cell and boundary of the experimental setup, i.e. heater and insulation. In addition, cell voltage, vessel pressure, and several gas temperatures were measured, including the upper gas temperature at the highest point in the vessel.

Figure 2.15 shows the vessel pressure and upper gas temperature, as well as surface temperature measurements between cells from the 5-cell 5 Ah array test. Pressure rose in the vessel from cell venting with an increase in the upper gas temperature immediately following the first runaway event. The upper gas temperature trails the pressure because of the slower process associated with mixing time in the vessel. For the first cell the duration of the pressure increase is 6 seconds. For subsequent cells the pressure increased for an average of 11 seconds and decreased for an average of 4 seconds until the next cell goes into runaway. The duration of pressure increase

is indicative of thermal runaway causing intense venting. The period of pressure decrease occurs when the venting rate is very small and the cooling and mixing of hot gases causes the pressure to fall. In total, the average time between the initiation of runaway in one cell and the propagation to the next is 15 seconds.

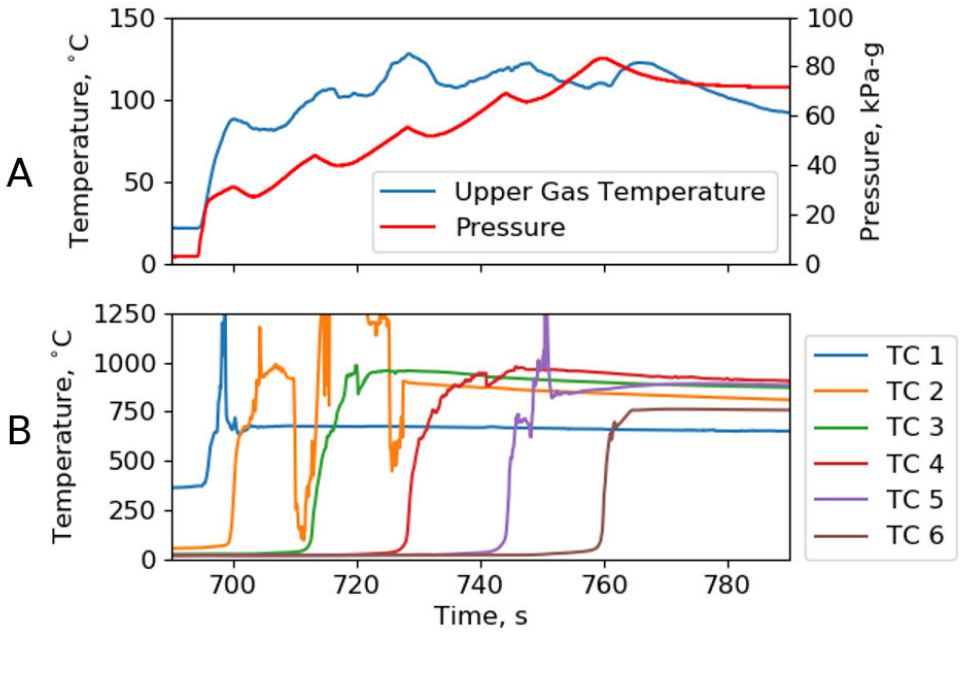

Figure 2.15: 5-cell 5 Ah array test data showing (a) pressure vessel gas temperature and pressure and (b) interface temperatures between adjacent cells.

Thermal runaway in each cell can also be inferred by the steep temperature increase at interfaces between cells. In the first cell, the steep increase occurs after a constant power heating process from a local point source. In the later cells which are triggered into runaway due to array propagation, the temperature initially increases due to heating in the last layers of the previous cell. The interface temperature then levels

off as the reacting (hot) cell preheats the unreacted (cooler) cell. Finally, another temperature increase occurs approximately 4 seconds later as a result of thermal runaway of the initially-unreacted cell. This is evident from the two sharp increases in temperature for each TC separated by a period of slower temperature increase.

The pressure increase also begins with the second surface temperature increase further showing thermal runaway. The cell interface temperature data also show that the propagation time was 15 seconds, but were unclear as to what constituted a starting or stopping point for thermal runaway, i.e. a critical temperature or time derivative of the temperature. This is made more challenging due to the thermal wave propagation marked by the first temperature increase which sometimes blends very closely with the second temperature increase from thermal runaway.

Figure 2.16 shows the same results as Figure 2.15, but for the 10 cell 5 Ah array. Very similar trends can be seen in both 5 Ah cell arrays. In this experiment, the pressure increase for the first cell is much faster than the other cells, occurring over only a 1.5 second interval. This is again followed by the upper gas temperature. Based on the pressure data, the propagated cells still vent over the course of 11 seconds with a 4 second delay for a 15 second propagation time.

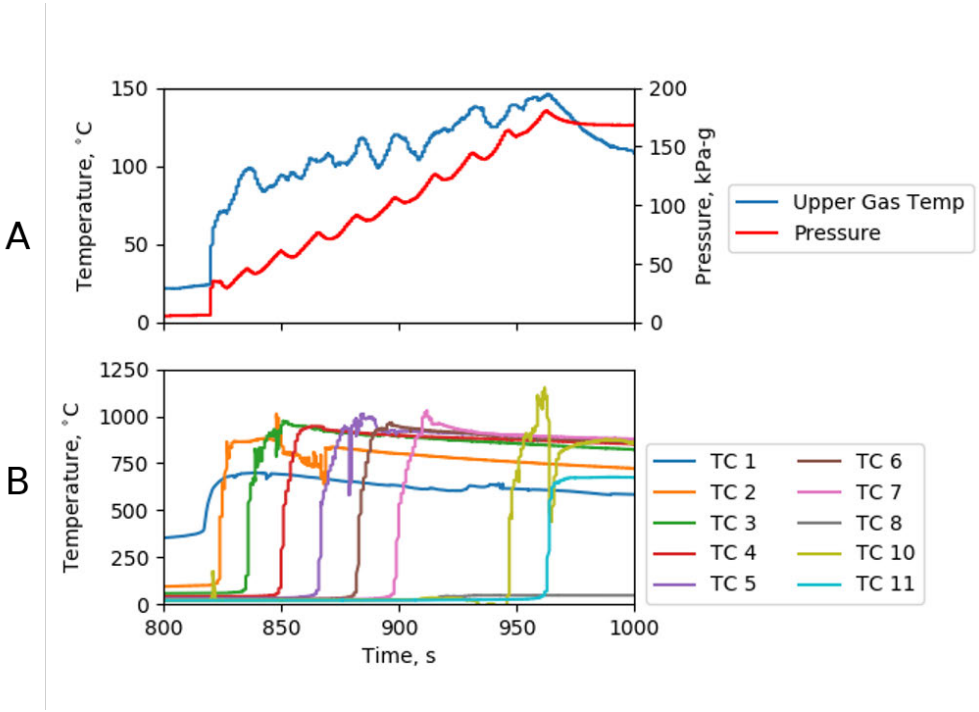

Figure 2.16: 10-cell 5 Ah array test data showing (a) pressure vessel gas temperature and pressure and (b) interface temperatures between adjacent cells.

The interface temperature data show a constant propagation time of 15 seconds. The secondary temperature increase and pressure rise are still in agreement with the start of the thermal runaway event for each cell. Overall there seems to be no significant differences between the two arrays, suggesting that larger arrays need not be tested for modeling propagation in a 1D array and that the first cell failure seems not to have influenced the results once the cells began propagating. This should be true as long as the heat released by already failed cells and runaway propagating to additional cells does not significantly change the environment temperature, causing preheating. However, more data are needed to confirm this trend. The thermocouples which would have shown runaway at approximately 915 and 930 seconds failed and are not shown. However, pressure data shows that these cells failed similarly to

the others. The average maximum interface temperature for TC 2 through TC 7 is 991°C.

2.3.0.3 10 Ah Array Results

The next experiments follow the same protocol as the previous but use 10 Ah cells. In these experiments, the interface temperatures, gas temperatures, cell voltage and vessel gas pressure were measured. In addition, the load cell as previously explained was also used to measure the clamping stress due to expansion and contraction of the cells.

Figure 2.17 shows data from the 10 cell array of 10Ah cells. As with the other array tests, the cells were not connected electrically. The vessel pressure and upper gas temperature show the same trends as the array of ten 5Ah cells, but with more vent gas produced, resulting in higher pressure and gas temperature. Based on the pressure data, the propagation time was approximately 22 seconds for the first 8 cells on average. Of this, pressure increased for 14 seconds and decreased for 8 seconds, corresponding to cell venting and subsequent gas cooling, respectively. This indicates that the venting time was 40 % longer than that of the 5 Ah cells while the delay between venting and thermal runaway propagation was 60 % longer. One reason the venting time is longer is because the 10 Ah cells are 18 % thicker than the 5 Ah cells and it will take the thermal runaway process more time to propagate through that thickness.

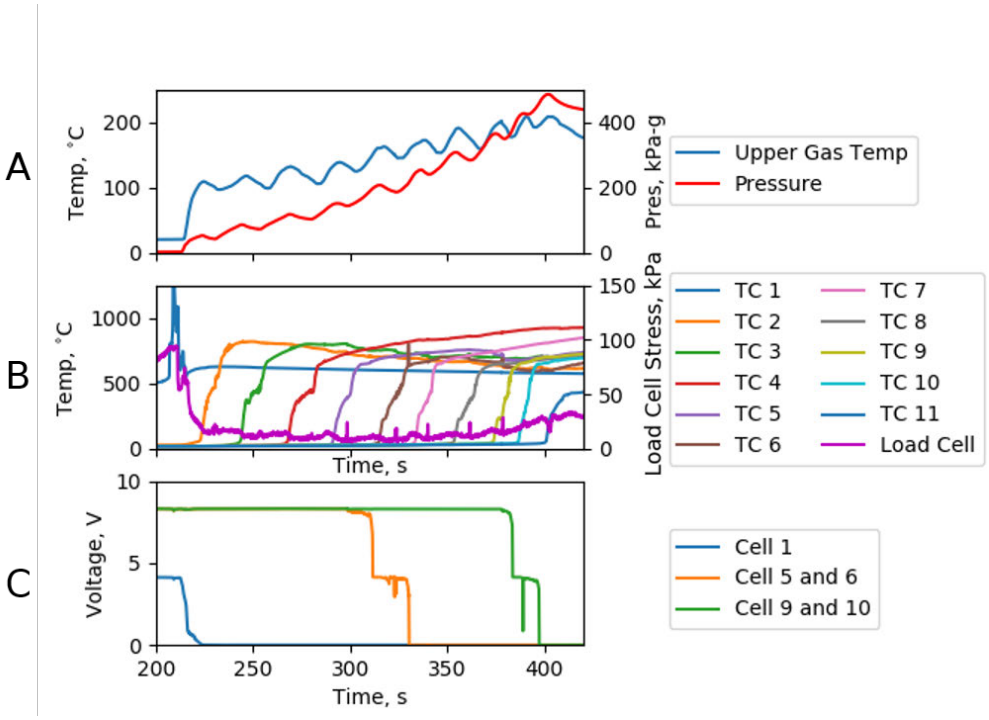

Figure 2.17: 10-cell 10 Ah array test data showing (a) pressure vessel gas temperature and pressure and (b) interface temperatures between cells and (c) voltages of cell 1, cells 5 & 6 in series and cells 9 & 10 in series.

The interface temperatures also show the same feature of a two-step increase separated by a short preheating time like the 5 Ah arrays. This feature can also be seen in the cell interface temperature in both Feng's and Li's work on array propagation in pouch cell arrays [37, 38]. Based on the interface temperature data, the propagation time was also approximately 22 seconds for the first 8 cells. The preheating time, or flat portion of the 2-zone increase, between the thermal wave propagation and the thermal runaway of the next cell is substantially longer than that of the 5 Ah cell arrays. The average maximum temperature for the cell interface temperatures (TC2 through TC10) is 876°C.

In this experiment, the cells seem to be propagating faster towards the end of the array. The last two cells propagate failure in 14 seconds on average. However, this trend was not seen in any other array test. This could be a result of higher chamber gas temperatures which would preheat the unfailed cells prior to propagation from the previous cell, thereby increasing the net heat flux into the cell. Higher chamber gas temperature also decreases the heat losses out of the cells. The pressure can also be seen increasing non-linearly for the last two cells as compared to other array tests where the pressure tends to increase linearly with time during the test. This could be a result of reduced cooling to the vessel walls as they increased linearly in temperature over the course of the experiment, reaching a peak temperature of approximately 120°C. It could also be a result of the reduction of cooling due to mixing with the initial cold gaseous nitrogen in the vessel as it becomes well mixed.

As observed in single cell tests, load cell peaks are markers of cell failure as the cell pressure reaches a maximum and is released through venting. This was used to calculate propagation time which was again found to be approximately 22 seconds. The clamping stress spikes in the load cell data aligns almost exactly with the beginning of the pressure rise and leads the second jump in each inter-cell temperature by approximately 2 seconds on average. The load cell disturbances are less pronounced in the 10 cell array due to the relaxation of the compression after the first cell fails. Overall, the load cell and pressure are better methods for determining the start of the event compared to temperature as they have faster response times and provide more clear signals than temperature data.

The voltages were measured for the first cell, cells 5-6 in series, and 9-10 in series. For

cell 6 at 325 seconds and cell 10 at 390 seconds, the voltage drops by a few volts and quickly recovers about 10 seconds before the thermal runaway event. This had been observed occurring 1 to 2 seconds before runaway in the 5 Ah tests. However, this effect is not reliably repeated for every cell. In both array experiments the voltage of a cell drops to zero approximately midway between the beginning and end of the runaway venting period. Compared to gas pressure, load cell and temperature data, the timing of voltage drop is less informative about the timing of the runaway process.

Figure 2.18 shows a zoomed in plot showing the failure of cells 5 and 6 from the 10-cell 10 Ah array test. This plot shows that the load cell clamping stress spike occurs at the same time the pressure vessel gas pressure measurement increase begins. This occurs because the clamping stress spike is a marker of the sudden pressure rise due to runaway reactions and the sudden pressure fall due to venting. The vessel pressure increase is a result of those vented gases being released into the vessel. Unlike the slowly heated single cell experiments where the clamping stress rises 20 seconds prior to venting, for propagating arrays the clamping stress leads the temperature rise by 2-3 seconds. Thus, the load cell and pressure are the most reliable ways of determining the propagation rate, as they are clear indicators of the event start and stop periods. The load cell spike and increase in gas pressure are good indicators of the rapid rise in internal pressure in the cell at the initiation of runaway and the subsequent release of gases.

The reason why the load cell and pressure gauge are more timely is due to the physics of what they are measuring more than each instrument's response time. The gas pressure gauge has a natural frequency of at least 1000 hz and the load cell has a

natural frequency of at least 100 hz. As the lithium-ion cell expands and contracts due to the generation and venting of gases, the resulting stresses in the cell propagate at the speed of sound in the battery cell. As these gases vent and are released into the vessel, the vessel gas pressure increases with changes propagating at the speed of sound through the gas. These processes are very fast and occur in much less than the 100 ms sample rate used for this experiment. Although this experiment uses very fine gauge (36 gauge) thermocouples which can respond very quickly to temperature changes, they lag because of the slow nature of diffusive heat transfer. In this case the heat must diffuse from the point at which the heat-generating reactions are occurring and then travel through the layers of the battery to reach the center of the end of the cell where the thermocouple is placed. The time it takes heat to diffuse through the thickness of the cell, is also seen in the single cell experiments, where temperature rises on the sides of the battery are seconds before the temperature rises seen through the thickness of the cell.

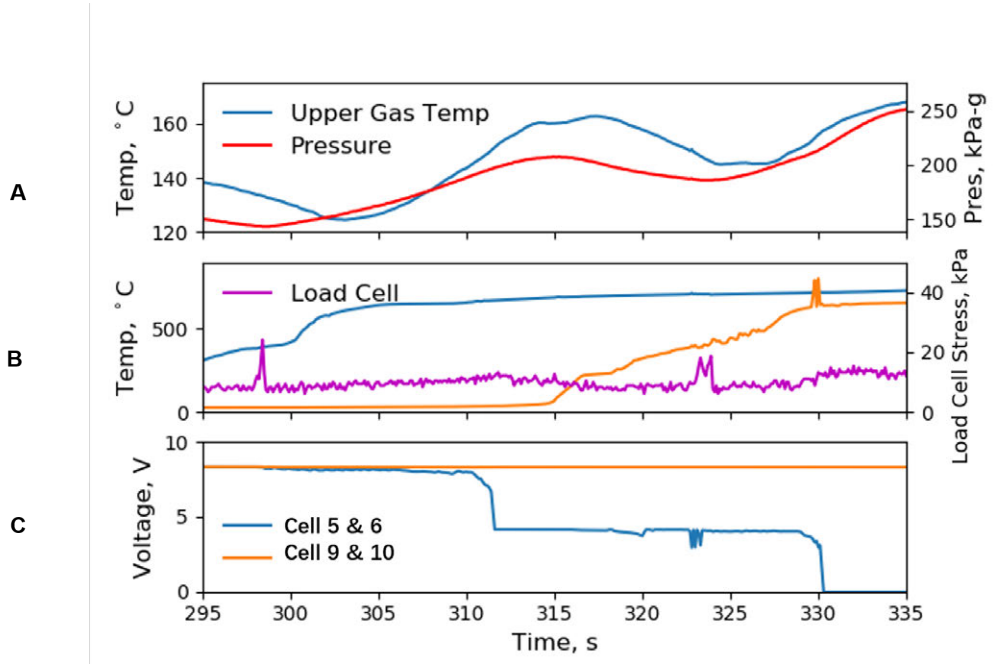

Figure 2.18: 10-cell 10 Ah array snapshot of failure of cells 5 and 6 showing (A) pressure vessel gas temperature and pressure and (B) interface temperatures between cells and (C) voltages of cells 5 and 6 in series and cells 9 and 10 in series.

Figure 2.18 also clearly shows the two-step temperature increase. This is shown in cell 5 as marked by the secondary temperature increase of the blue line at 300 seconds. The temperature shown in orange shows the interface temperature between cells 5 and 6. This temperature begins to rise as cell 5 runaway is nearly complete, then the rise continues slowly until the thermocouple senses the runaway of cell 6 about 2 seconds after cell 6 runaway is initiated.

An interesting result from Figure 2.18 is the lag seen in the voltage data. The blue trace in Figure 2.18 (C) shows the voltage of cells 5 and 6 cells in series. The first large drop occurs during the failure of cell 5 and the second is for cell 6. At the first spike in the load cell data, the voltage begins to waver. However, the voltage does not drop significantly until 10 seconds after the temperature jumps. Additionally, the

voltage does not fully fall for cell 5 until just before the gases stop venting as marked by the pressure signal. This pattern is seen again in the voltage for cell 6 as the voltage wavers again at the load cell spike, and only falling until well into the thermal runaway event. Overall, this shows that the voltage data is a poor marker of start and stop times, as well as propagation times. In this way, the voltage signal serves only to show whether thermal runaway has occurred barring all other measurements.

A 5-cell 10 Ah array was also tested and showed similar results with no significant differences to the first five cells in the 10 cell array. The final pressure and upper gas temperatures for the 5-cell 10 Ah array were almost identical to the 10-cell 5 Ah array, indicating that the volume of gas produced and heat released generally scales by watt hour capacity. However, more testing with varying state of charge and cell types is needed to confirm this trend and to measure precisely the amount of gas produced.

Figure 2.19 shows the propagated cell temperature profiles from the 10x 10 Ah cell array overlaid on idealizations for the temperature and load cell profiles of a thermal runaway propagating into a cell from a previous cell. The measured temperature profiles were aligned in time by aligning the spikes in the load cell data. This figure shows the stair step nature of interface temperature, where it first rises due to the previous cell runaway and then after a period, the temperature jumps again due to the next cell runaway. This stair step feature can be seen in the 10-cell 10 Ah, 5-cell 10 Ah and 5-cell 5Ah experiments here as well as in experiments by others [37, 38]. In this experiment the rate of temperature increase greatly decreases at about 660°C. This occurs because the pouch material is made from aluminum which melts at 660°C. Teardowns of cell arrays showed that most of the pouch material

between cells had been melted and ejected.

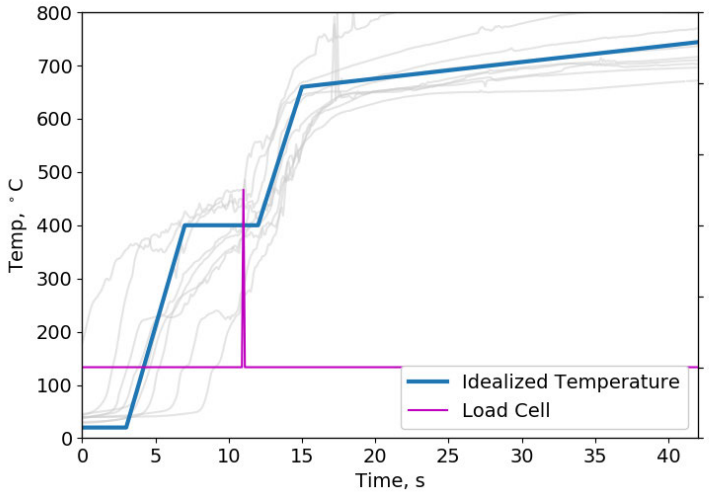

Figure 2.19: Temperature histories for 10 Ah cells, when aligned by time of runaway initiation as indicated by load cell spike show a two-step temperature profile which is idealized by the blue line.

Using the temperatures shown in Figure 2.19 along with pressure and load cell data, an idealized representation of the propagation process was created. Figure 2.20 shows the idealization of the temperature, pressure and load cell profiles for thermal runaway propagating from one cell to another. This shows the two components of the total propagation time: preheat or induction time and venting time. For the 10 Ah arrays the cell is first preheated for approximately 7 seconds from the thermal runaway of the previous cell as shown by the initial increase in temperature. During this time the vessel pressure decreases as the gases released from the previous cell mix and cool. Interface temperature then stagnates as the cell heats until it is ready for runaway to occur. Runaway reactions generate gas, increasing cell pressure and causing almost immediate venting as shown by the load cell which spikes and drops

almost instantly. Vessel pressure also begins to increase at this point, another indicator that thermal runaway has started and the cell is actively venting. The interface temperature takes approximately 2 seconds to reflect the temperature increase. The cell vents over the course of 13 seconds. As venting is concluding, one can see that thermal runaway has propagated to the other side of the failing cell by the initial rise in the next interface temperature, thus continuing the cycle.

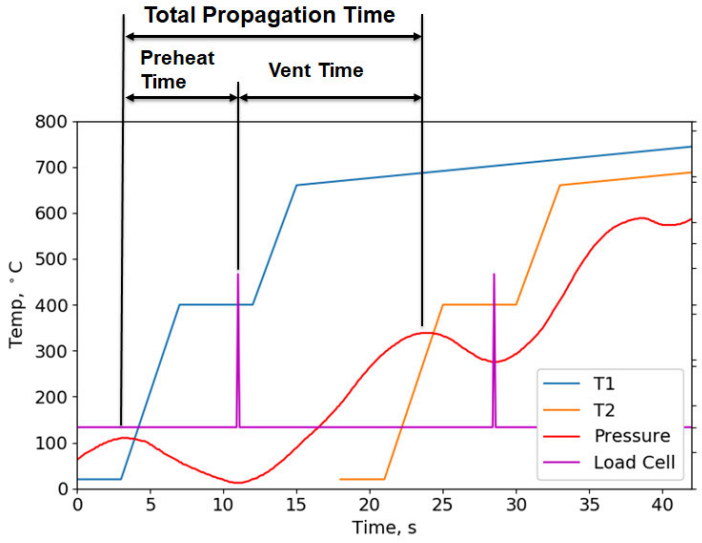

Figure 2.20: Idealization of propagation process showing idealized, interface temperatures on either side of the cell, pressure vessel gas pressure and load cell spike timing. After a period of preheating from the previous cell failure, a load cell spike (purple) indicates the beginning of thermal runaway and active venting. Vessel gas pressure (red) begins to increase at the same time as the load cell spike as gases are released. A decrease in vessel gas pressure indicates the end of the active venting period. Thermocouple measurements between previous cell and current cell (T1) and between the current cell and next cell (T2) are about 2 seconds behind in indicating the beginning and the ending of the vent time due to thermal runaway.

Table 2.2 shows the average and 95 % confidence intervals for preheat, venting and total propagation times for the 5 Ah and 10 Ah cells. These times are measured using peak to trough and peak to peak pressure data as illustrated in Figure 2.20. Each

Array	Preheat (sec)	95% CI (sec)	Vent (sec)	95% CI (sec)	Total (sec)	95% CI (sec)
5 Ah	4.3	± 1.4	11	± 2.7	15.4	± 2.5
10 Ah	7.4	± 5.1	13.2	± 4.1	20.6	± 8.0

Table 2.2: Propagation time Statistics for 5 Ah and 10 Ah arrays.

set of statistics comes from a sample of 13 cells which consist of the 4 propagated cells in the five cell array and the 9 propagated cells from the 10 cell array. The spread on the 10 Ah cells is much larger than that of the 5 Ah cells. This is due to the apparent acceleration at the end of the 10-cell 10 Ah array test.

One can infer a reaction propagation rate from these data using the vent time (See Figure 2.20) and the characteristic length (cell thickness). As an example, for the 5 Ah cells, there is an average through-thickness propagation time of 11 seconds. Using the thickness of the 5 Ah cells, the propagation rate is approximately 0.8 mm/s. For systems with convection-diffusion-reaction, one estimate for the reaction propagation speed is given by the scaling law:

$$u = \frac{(T_b - T_{ig})}{(T_{ig} - T_u)} \frac{\alpha}{\delta_R} \tag{2.1}$$

Representative values for thermal diffusivity (α), unburned temperature (T_u), ignition temperature (T_{ig}), adiabatic cell temperature (T_b), and preheat thickness (δ_R), can be used to find a propagation velocity (u) that is consistent with the measured values. Assuming this fundamental propagation speed, the differences in vent time between the 10 Ah and 5 Ah propagation cases are easily explained. The effects of thermal conductivity in the in-plane and through-plane directions have significant

effects on the rate at which the reaction wave propagates across the cell relative to through the cell. these observations are also consistent with temperature measurements made in the single cell failure cases in Section 2.2.

2.3.0.4 Cell Array Teardowns

In the cell array teardowns, the initiating cells are very different than the cells which runaway by propagation. Even though the initiating cells are heated much faster than the single cell experiments and are only heated at a single point, damage looks very similar to the single cell experiments. Figure 2.21 shows the photo from the post experiment teardown of the initial cell in the array of five 10 Ah cells. Figure 2.22 shows the teardown of the initial cell in the 10 cell 5Ah array. In the center a circular indent is left where the heater was compressed against the cell. In the 10 Ah cell, two regions of heavy damage show where jets left the cell while for the 5 Ah there is just one. On the 5 Ah cell, the single area of damage is more significant. Radial striations again mark the flow path for the vaporized electrolyte, vent gas, and melted aluminum which is forced out of the cell and beads up as seen on the sides of the pouch. One can also see where the jets of gas were strongest for the initiating cell, as the beads of aluminum are absent from having been blown completely out as seen in the middle of the pouch side in Figure 2.23.

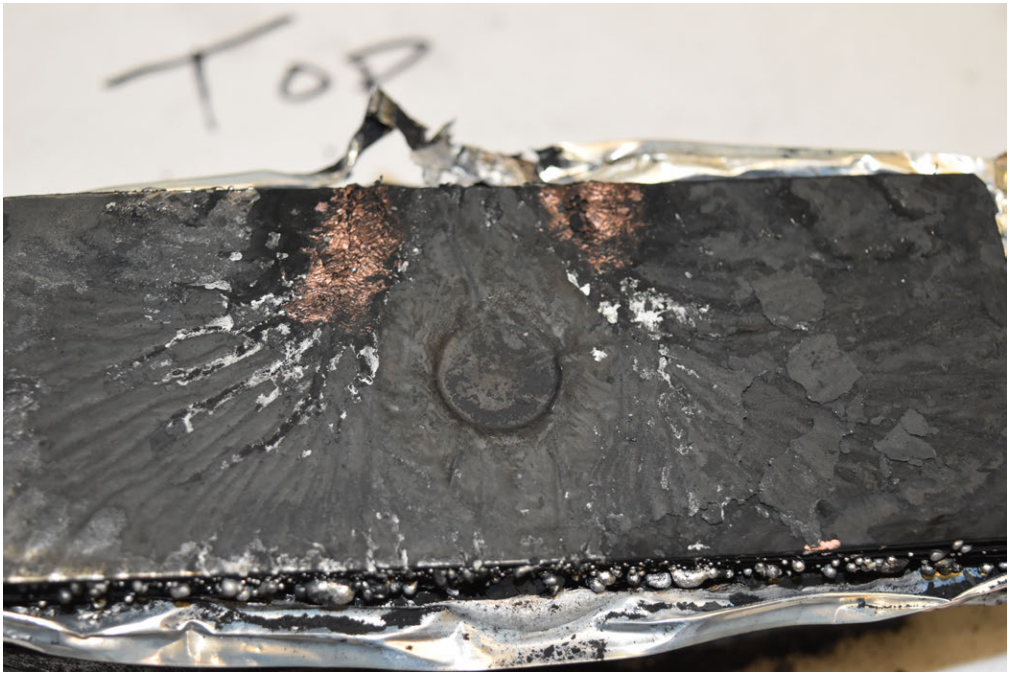

Figure 2.21: 5-cell 10 Ah array initiating cell teardown

Figure 2.22: 10-cell 5 Ah array first cell teardown

Figure 2.23: 10-cell 10 Ah initiating cell jet region.

Figure 2.24 shows 5 Ah cells that failed due to propagation. These cells have more noticeable striations. Cells 2 and 3 show striations originating from very close to the center. While in later cells the arrangement looks more random. The center pattern may be because the initiating cell was initiated near the center and central initiation passed on to the first few cells in propagation.

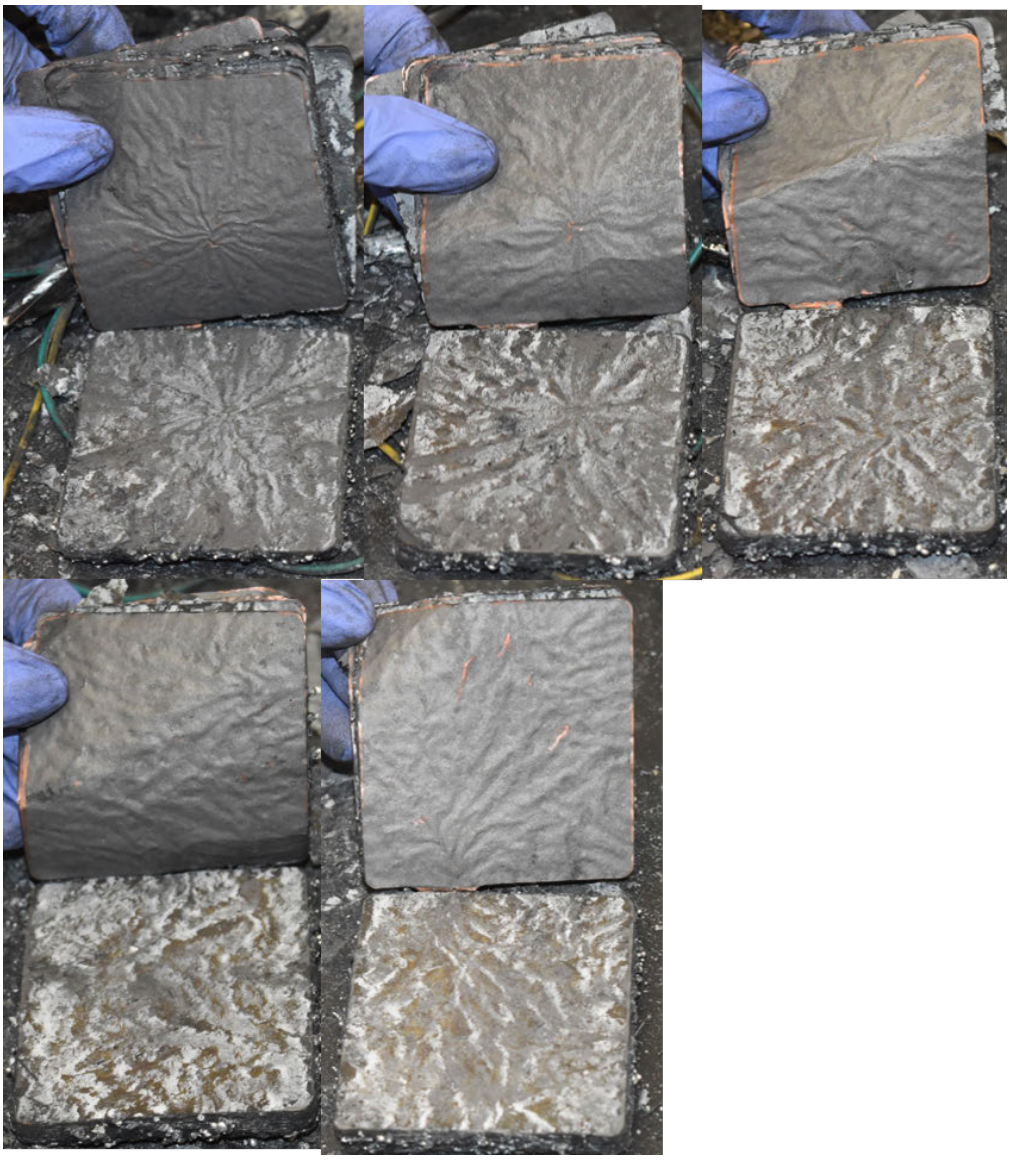

Figure 2.24: 5-cell 5 Ah array teardown.

Figure 2.25 shows the teardown of the second cell in the array and is representative of all of other 10 Ah cells failed by propagation. Propagated cells all lack regions of heavy damage as seen before. Cells are roughly uniformly heated to failure in a matter of seconds. As a result, striations are more subtle and there are not strong jets to

remove the aluminum beads from the perimeter of the cell. This indicates that the propagated cells failed more uniformly, thereby releasing their contents more calmly through multiple sides at once, instead of a rapid vent through a single point. Much of the aluminum current collectors in each of the cells were melted and beaded up on the sides of the pouch, or in fragments as a result of the measured temperatures in excess of 750°C melting the aluminum at 660°C. Pouch material between cells in every case was completely gone. However, the pouch material not directly between adjacent cells typically remained intact.

Figure 2.25: 5-cell 10 Ah array, second cell teardown.

2.3.0.5 Conclusions

This work compares the thermal runaway failures of pouch cells initiated by heaters with those initiated by thermal runaway propagation from adjacent cells. These differences are important for modeling cell failure in propagation, understanding the hazards of propagation and conducting battery failure forensics. Cells which failed after being slowly heated followed a slow process in which the cells gradually built up internal pressure until the cell ruptures and light venting occurs. After further heating the cell reactions eventually become fast enough to build up internal pressure rapidly, further rupture the cell and cause intense venting and rapid temperature increase (self-heating). Damage from these cells show localized regions of heavy damage where jets of hot material exit the cell. In contrast, cells initiated by propagation have only a few seconds between the time they are at ambient temperature and the time at which thermal runaway causes peak temperatures in the cell. This causes them to fail differently. Since there is less time for them to heat up, these cells do not have time to release gases by lightly venting before the intense runaway event. Since the cell has not been fully preheated, the period of significant venting and temperature increase lasts longer. Examination shows that the propagated cells have less damage inside and gas is released out of a greater surface area. A much great length of pouch seam failed in the propagated cells creating a larger vent area, likely due to the speed and intensity of the runaway reactions. While the initiation of runaway appears to occur at a random location near the center of the slowly heated cell, in a propagated cell it appears to begin on the side being rapidly heated and subsequently move across the cell to the other side.

These differences are important to notice for those who are trying to model and pre-

dict the effects of thermal runaway in battery modules. Since the process of thermal runaway is different for cells failing in propagation, it may be incorrect to apply single cell experiment results to try to predict the response of arrays of many cells. From a timing perspective, the single cell preheat period is much longer (which can be many minutes) than the propagated cell preheat time period (only a few seconds). For the period of intense venting, the single cell vents more quickly than a propagated cell. In this experiment the single cell also vented gases before the intense runaway venting period. Since the timing is different and the damage pattern is different, it is likely that the species of the gases produced is also different. This is important to note for safety designs. It may not be conservative or appropriate to design systems to mitigate explosions using species data produced by single cell tests as the volume and species produced by an array of cells is likely different.

The observation of major differences in damage between propagated cells and slower heated cells is important for those trying to understand forensics and can be used to identify how different cells are initiated. This work has illustrated different failure patterns for heater versus propagated cell failure characteristics. Heater failed cells have localized regions of heavy damage, while cells failed due to propagation have a more uniform damage throughout. When combined with work illustrating other failure patterns, this can be used to help determine which cell initiated thermal runaway and how a failure incident began.

This work is useful to experimentalists in battery research. A major contribution of this work is demonstrating the utility of using load cell clamping stress and gas pressure data to monitor thermal runaway of both individual cells and cell arrays. Load

cell clamping stress data is interesting and useful because it allows the experimenter to observe the initiation of runaway in multiple cells using only one sensor. It also has a much faster response than thermocouples. The load cell data provide insight into the pressure generation within the cell associated with the various reaction steps. Rising clamping stress is an indication of increasing reactions producing gas while falling load cell clamping stresses are indicative of venting. Vessel gas pressure data can be used to determine the time period over which cells are actively venting as they undergo thermal runaway. It is also useful to identify the time period between when one cell ends venting and the next one begins. Together with temperature data, these can be used to more clearly define the induction or preheat time needed to initiate runaway and the time it takes for runaway to travel through the cell.

This work also compares different sizes of similar pouch cells. The 10 Ah cells which are 18 % thicker than the 5 Ah cells, had a total cell to cell propagation time which is on average 33 % longer. Two mechanisms are believed to affect this time difference. The first is a fundamental propagation speed which is associated with the venting process. A convection-diffusion-reaction formalism was used to describe this process. The preheat process scales with the overall thermal diffusivity of the system. The combined effects of the vent and preheat processes are believed to describe observations in the array propagation tests.

Chapter 3

Thermal Runaway Propagation within a Module inside a Compartment

In Chapter 2, the propagation of thermal runaway was characterized for a simple 1D system. However, many real systems are much more complex and involve 3d geometry and heat transfer via radiation, convection and conduction. The objective of this work is to characterize the thermal runaway propagation process for a more complex commercially available energy storage module. To accomplish this objective, we first perform experiments. Next the experimental results are analyzed to observe the thermal runaway propagation process and its effects on the compartment. Then the timing of the thermal runaway propagation process will be used to generate an estimate of the gas release rate and heat release rate time histories. To validate the gas release rate time history, it is used in a CFD model and the resulting temperatures are compared with the actual experiments.

3.1 Introduction

Lithium-ion battery technology is being rapidly and widely adopted to provide energy sources for consumer devices, electric vehicles and fixed location energy storage systems. With the widespread use of this technology, comes increased exposure to hazards from lithium-ion battery thermal runaway failure which causes rapid heating and the release of flammable and toxic gases. This can be especially dangerous for large systems such as battery energy storage systems (BESS) which are used to store energy to meet residential, commercial, industrial or utility electricity needs.

There are many studies documenting abuse conditions which can lead to thermal runaway as well as the reactions which cause thermal runaway, these are reviewed in a number of articles [43, 45, 46]. The largest consequences of thermal runaway generally happen when many individual lithium-ion cells go into thermal runaway in quick succession, causing a much larger release of gases than a single cell.

There have been very few large experiments involving entire systems documented in the published literature. One of the earliest studies was in 2017 when DNVGL performed a study for Consolidated Edison and NYSERDA. This study examines NMC, LFP and other chemistries in experiments ranging from single cell to module. They measured concentrations of gases produced, but this data is of limited use without knowing the ventilation conditions. They also tried different suppression methods[47].

Exponent and FM Global in cooperation with the NFPA Fire Protection Research Foundation conducted a study examining sprinkler protection of energy storage sys-

tems. In these experiments they performed experiments using single modules, six modules and racks of batteries. The LNO/LMO rack system tested consisted of 16 modules and had a capacity of 82 kWh. The LFP rack system tested consisted of 16 modules and had a capacity of 125 kWh. For each system they compared sprinklered systems with those that are allowed to burn freely. These tests were performed in a well ventilated environment and were used to measure peak heat release rate as well as temperatures and heat fluxes in and around the system [48, 49].

In 2019, DNVGL released a report focused on energy storage fire and explosion risks for the maritime battery industry. This report measures vent gas compositions from various cells using FTIR. They also perform larger system experiments and test a number of different fire suppression methods[50].

Although much work has been done to characterize the failure of individual cells and small arrays of small cells, much less has been done to characterize the behavior of full-scale systems. A major challenge for system designers is characterizing the fire and explosion hazards from system thermal runaway without having to destroy large systems in experiments. A major objective of this study is to take results about the flammable gas release for a single cell and to apply them to predict thermal runaway behavior for a module in a compartment.

3.2 Experimental Setup and Model Development

For this study, single cell experiments were performed both in a burn structure compartment as well as in an inerted pressure vessel to understand the behavior of a single failing cell. Three experiments are then conducted to observe compartment

conditions in response to propagating thermal runaway in a module comprising 14 cells. One of these experiments uses a module in the open and two of them use the same module placed in a non-combustible steel rack enclosure. Finally, a computational fluid dynamics (CFD) model is presented to predict compartment conditions based on the experimentally measured mass loss due to plastic burning and the timing of lithium-ion cell intense gas venting observations.

3.2.1 Burn Structure Setup and Instrumentation

All of the compartment experiments for this work were conducted in a burn structure facility. The burn structure has interior dimensions of 5.7 m x 4.6 m with a ceiling height of 2.17 m. The interior of the burn structure is constructed using 5/8" fire resistant gypsum board. For these experiments the only major vent opening was the door which remained open for the experiments. The burn structure is instrumented with 8 thermocouple trees containing 36 type T thermocouples and 2 type K thermocouples. The burn structure also contains 28 directional flame thermometers (DFTs) which are used to measure heat flux on the ceiling and on a portion of the walls. The burn structure also has bidirectional probes to measures flows into and out of the door by measuring differential pressure. A more complete description of the burn structure facility is provided by Kurzawski [15].

3.2.2 Single Cell Open Air Experiment Setup

The cell used in these experiments is a NMC (Nickel Manganese Cobalt Oxide) prismatic cell with a nominal minimum capacity of 94 Ah and a nominal average capacity of 95.6 Ah. The cell has a nominal voltage of 3.68 V and a maximum

charge voltage of 4.15 V. The cell is rectangular shaped with dimensions 173 mm x 125 mm x 45mm as shown in Figure 3.1. The cell has a mass of 2.01 kg. For single cell experiments the cells were charged using a constant current, constant voltage scheme with a maximum current of 10 A and a maximum voltage of 4.2V. Charging was terminated when the current at 4.2V was less than 0.01C. The modules were charged to 51.8 V using a similar process for the 14 cells in series.

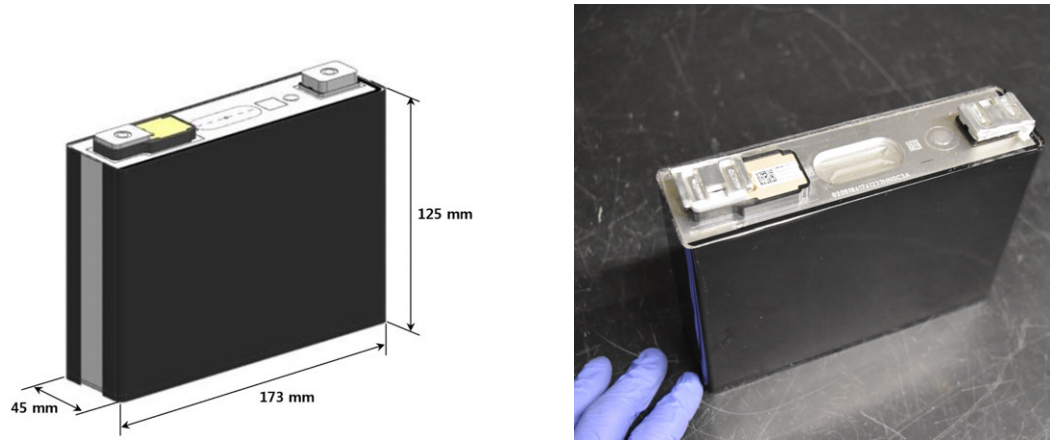

Figure 3.1: Single 94 Ah Cell Dimensions and Photograph

Three experiments were conducted in open air in the burn structure compartment. In the first experiment, the cell was heated from below using cartridge heaters embedded in an aluminum block. For the other two experiments, the cell was heated on one of the large faces using electric heaters which are cycled such that the heater-cell interface heats at 5 °C/min.

3.2.3 Single Cell Pressure Vessel Experimental Setup

To measure the volume and species of gases produced during thermal runaway, the last single cell experiment was conducted in the 53.5 L LIB-VeGA (Lithium-Ion Battery Vent Gas Apparatus) pressure vessel at the University of Texas at Austin. This apparatus and instrumentation is described in more detail by Kennedy et al [40]. The vessel was also used for the array experiments in Chapter 2. The vessel was initially filled to atmospheric pressure with nitrogen. The cell was failed thermally by heating one side of it at 5 °C/min with an electric heater. The pressure vessel setup is shown in Figure 3.2. During the experiment, cell surface temperatures along with gas temperatures throughout the vessel and vessel gas pressure are recorded. After the experiment, 3 samples of the gas were collected and analyzed using a gas chromatography thermal conductivity detector (GC-TCD) to determine the major components of the gas mixture released by the battery. Gas was collected approximately 24 hours after thermal runaway to allow gas temperatures to cool and vapors to condense to measure the total dry gas volume of the release. The GC-TCD unit is calibrated to measure H_2, N_2, CO, CH_4, C_2H_2, C_2H_4, C_2H_6, C_3H_6, C_3H_8 and H_2O. The GC-TCD peaks for C_3H_6 and C_3H_8 overlap and the sensitivity to each is similar, so they are reported together.

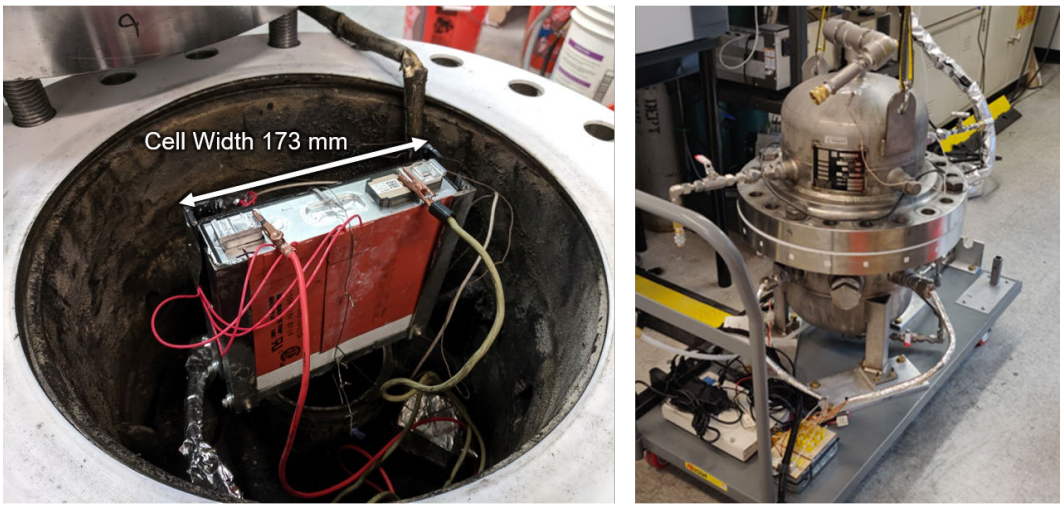

Figure 3.2: Single 94 Ah Cell in Pressure Vessel Prior to Experiment

3.2.4 Module and Rack Experiments Setup

Three experiments were completed using a full commercially available ESS module. The module consists of 14 of the previously described cells which are housed inside a polycarbonate casing and connected in series with aluminum tabs. On the front of the module is a circuit board for module management, this however was removed prior to experiment. This leaves the polycarbonate housing and the cells as the only flammable materials in the setup. Thermal runaway was initiated using a heater on the large face of a single cell similar to the single cell experiments. Each module was disassembled to insert the heater on cell 1 and to place thermocouples on each cell. A photo of the module along with the heater and thermocouples on the inside is shown in Figure 3.3.

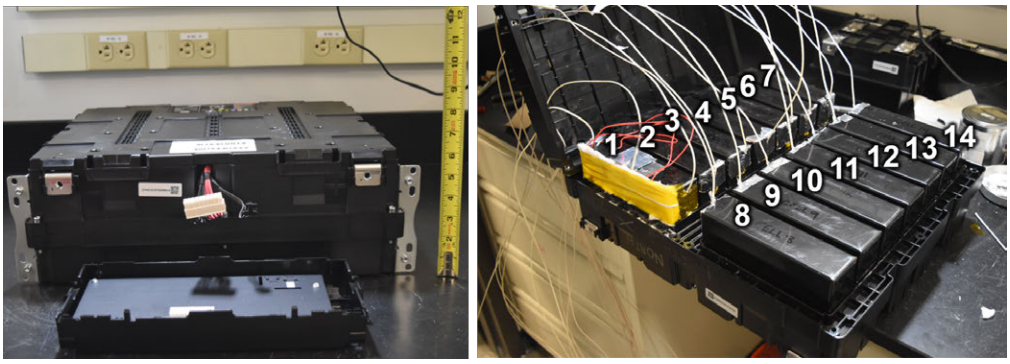

Figure 3.3: Module shown before opening and open with thermocouples placed on each cell and heater placed on cell 1 for experiment.

The module was reassembled and placed on a stand for the first experiment and placed inside a rack for two rack experiments. These experiments were conducted in the same burn structure facility as the single cell experiments. Figure 3.4 shows the module placed on a stand in the burn structure for the first experiment.

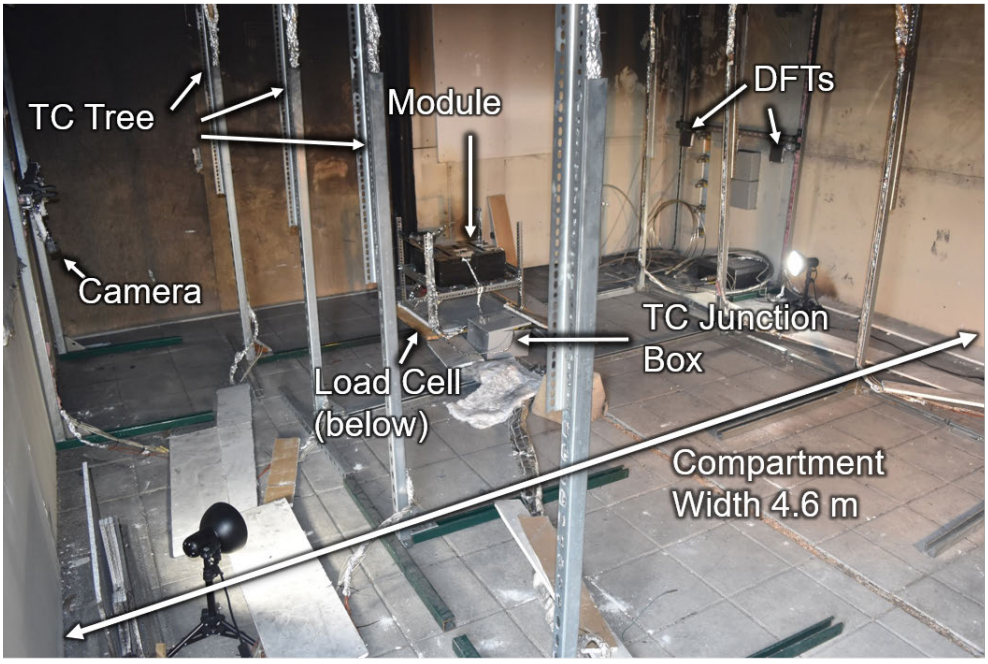

Figure 3.4: Burn Structure Setup for Open Air Module Experiment

Two experiments were conducted with the module inside of a steel rack enclosure. These experiments follow the same process as described previously with the only exception that for these experiments the module is placed in a steel rack. The steel rack is enclosed on 4 sides and on the top. The front of the rack has areas at the top and bottom which allow air to flow in and out of the rack. Two steel rack-mount server cases were used as dummy modules and placed above the module to simulate the presence of other equipment in the rack without adding to the fuel load. These steel server cases contained thermocouples to measure the exposure of above equipment to module failure.

Figure 3.5: Burn structure setup for rack experiments. The back of rack was removed to show module placement inside. Before the experiment, a steel sheet was placed to cover the entire back as shown by the red dotted line.

3.3 Experiment Results

3.3.1 Single Cell Open Air Results

Three experiments were conducted in which a single cell goes into thermal runaway in the middle of the burn structure compartment. For the first experiment with a single cell in open air, the cell was heated with constant power cartridge heaters placed in an aluminum block beneath the cell. The heaters were turned on full power to initiate thermal runaway. Due to the uncontrolled nature of the heating in this experiment the aluminum heater blocks ended up melting. This experiment caused the cell to rupture as it went into thermal runaway. The cell ruptured and the metal cell casing was thrown 2.3 meters across the room at about 8.7 m/s. The current collectors and active material were thrown 2.3 meters to the opposite side of the room where they burned.

Figure 3.6: In the first single cell experiment, the cell ruptured and was thrown across the compartment.

Since the investigation of catastrophic cell rupture is not a primary objective of this work, the heating protocol was changed for all subsequent tests to avoid this outcome.

In the other two single cell experiments, the vent on the top of the cell opens to relieve pressure when the temperature of the bottom of the cell is approximately 150 °C. Figure 3.7 shows data from a representative experiment during the time at which the vent opens and when intense venting occurs. This figure shows the temperatures as measured on various surfaces of the battery along with the cell mass.

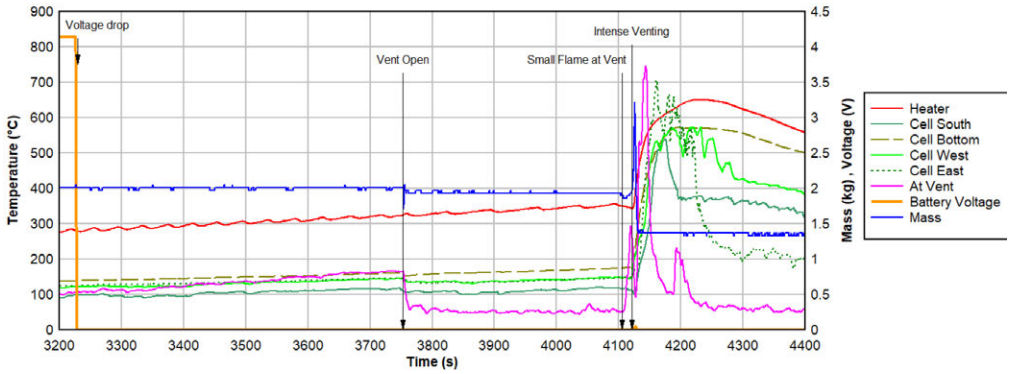

Figure 3.7: Single Cell Temperatures and Mass at Time of Vent Opening and Intense Venting

In this experiment the vent opens at 3753 seconds after the beginning of the experiment as shown in Figure 3.7. When the vent opens, a small cloud of liquids and gases is released as shown in Figure 3.8. Immediately after the vent opens, the decrease in internal cell pressure causes a small decrease in the cell temperature as measured on the cell surfaces and a larger decrease in the temperature of the gas immediately above the vent, which is now mixed with ambient air. This temperature decrease is shown at approximately 3760 seconds in Figure 3.7. In this experiment the gases exiting the battery ignited at 4105 seconds and the resulting flame can be seen at 4108 seconds in Figure 3.8. In the other very similar single cell experiment, ignition did not occur until after intense venting due to thermal runaway.

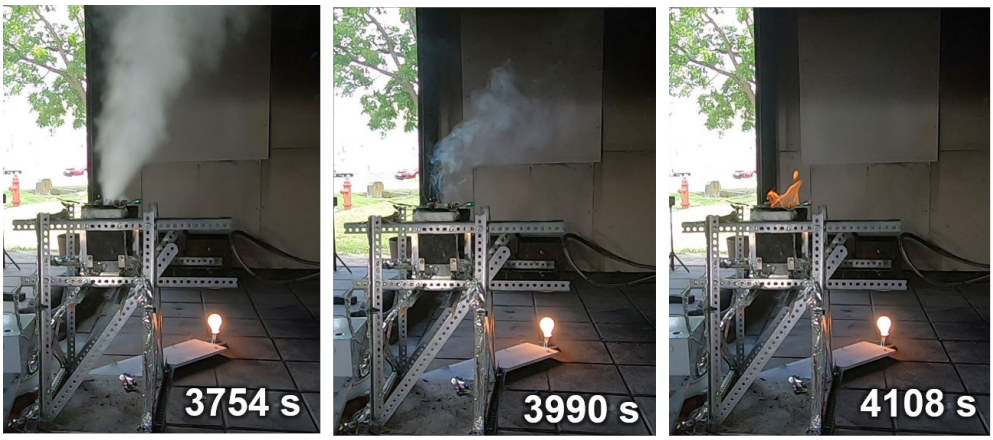

Figure 3.8: Single Cell Vent Opening Sequence

For the experiment in Figure 3.7, the vent opened at 3753 seconds and intense venting occurred 368 seconds later at 4121 seconds into the experiment. The other experiment had a similar response, with intense venting occurring 292 seconds after vent opening. Visually the intense venting process begins as a black turbulent jet. This jet contains both flammable gases as well as hot solid particles which at first causes intermittent ignition and later develops into a sustained jet flame. The intense venting sequence for this experiment is shown in Figure 3.9.

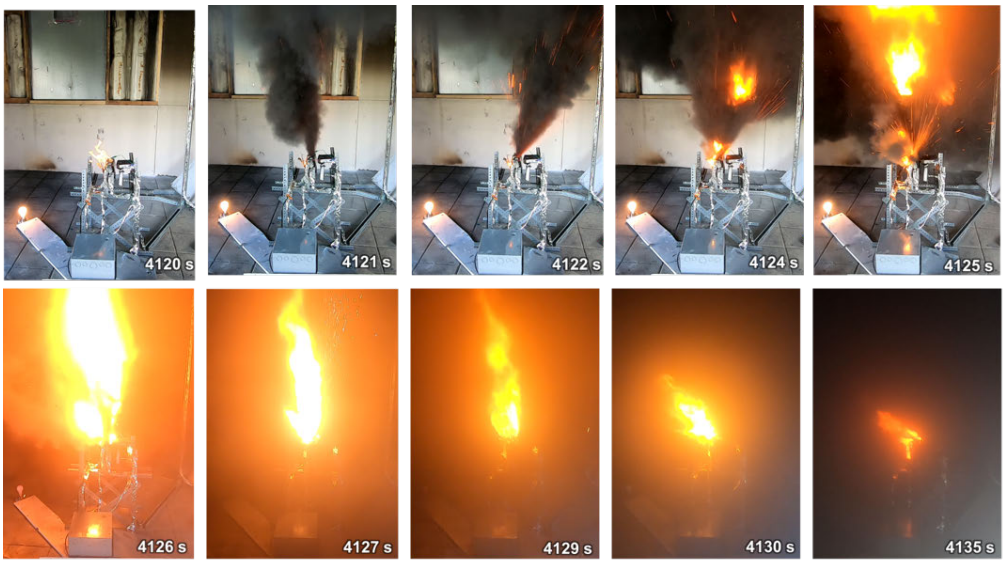

Figure 3.9: Single cell intense venting event is marked by the release of a turbulent plume of hot gases and solids which eventually ignite and form a jet flame.

Looking at the cell after the experiment, the pressure relief vent is seen to be open. The metal cell casing is still intact, however it is noticeably bulging by about 10 mm due to the pressure as shown in Figure 3.10. This bulging is significant because it could allow a hot cell to touch adjacent cells. This would allow heat to conduct into adjacent cells and could propagate the thermal runaway into other cells.

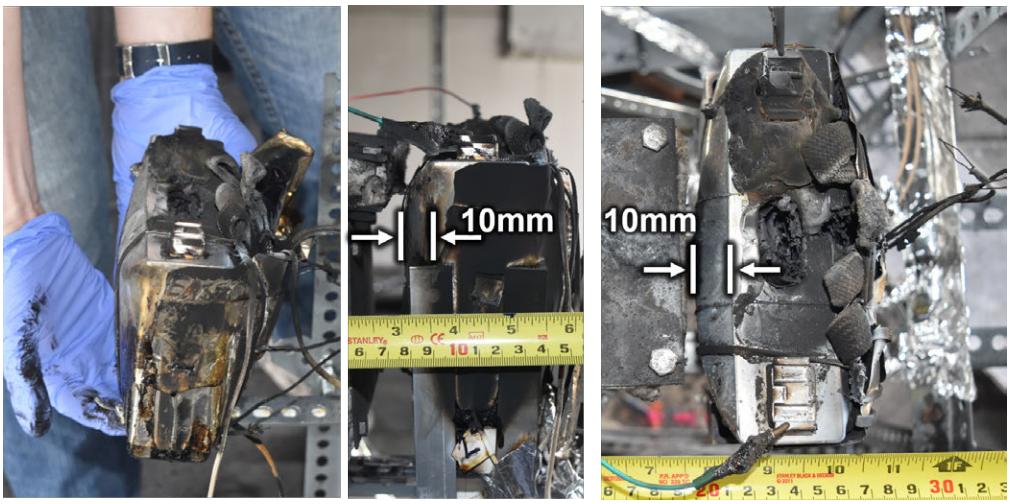

Figure 3.10: Single Cell Bulging After Experiment

3.3.2 Single Cell Pressure Vessel Results

The experiment in the pressure vessel allows for the measurement of the gases observed in the open experiments. This experiment was conducted using the same heating protocol as the used for the other two successful single cell experiments that didn't result in cell rupture. The pressure vessel gas temperature and pressure was used to determine the gas release rate and total volume released. This was done using the same techniques as described in [40]. The cell released 221.6 L of dry gas at standard pressure and temperature. Normalized by the nominal energy capacity of the cell, the cell produced 0.64 liters of gas per Watt-hour of energy stored. The volume fraction of each of the major species was measured by analyzing 3 samples with the GC-TCD instrument and then taking the average and normalizing while excluding the volume of nitrogen. The volume percentage by species of the gas released by the cell is shown in Table 3.1.

Species	Volume Percent
Hydrogen	30.6%
Carbon Dioxide	29.9%
Carbon Monoxide	21.3%
Methane	7.2%
Ethylene	5.6%
Propane or Propylene	2.0%
Ethane	1.8%
Other	1.6%

Table 3.1: Species Volume Percentage for gases released by NMC cell

The gas release rate is estimated based on the pressure and temperature time history for the gases in the pressure vessel. The volume release time history is shown in Figure 3.11.

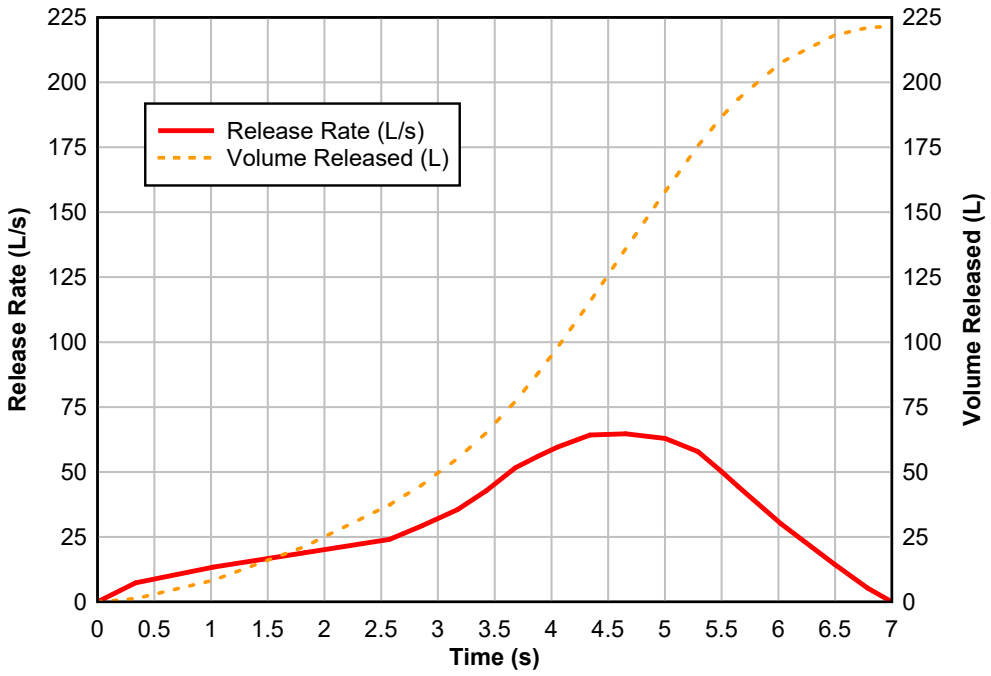

Figure 3.11: 94 Ah Prismatic Gas Release Rate

3.3.3 Open Air Module Experiment

In the open air module experiment, the cell 1 as shown in Figure 3.3 was heated at 5 °C per minute until the cell went into thermal runaway. After the first cell went into thermal runaway, thermal runaway naturally propagated into the remaining cells. The runaway propagation process was observed in audio, video, module and room temperature data, cell voltages and mass data. Generally, the failure of the cells inside the module appears to be similar to those of individual cells. Some of the clearest indications of vent opening and intense venting events are in the audio and video data of the event. Audio and video data indicate when the first cell vent opens allowing pressure to be released. After 77 seconds, reactions inside the cell reach a critical point and intense venting occurs in which a large amount of flammable gas and other materials are ejected from the cell at high speed in a period of several seconds. Figure 3.12 shows the intense venting period for cell 1 of the module.

Figure 3.12: Image sequence from video of cell 1 venting

The failure of each cell is observed to produce a short period of intense venting. The beginning of each intense venting event was determined by observing the audio and

video for the duration of the experiment. The intense venting events are noticeable in the audio data as short periods of loud squealing or hissing. Figure 3.13 shows that the audio amplitude clips during periods of intense venting. In the video, these same periods are characterized by large, bright jet flames extending to the ceiling. Figure 3.14 shows the percentage of the video image that exceeds a brightness threshold. The brightness threshold is set as a HSV value greater than or equal to 254 out of 255. In both Figures 3.13 and 3.14, identified intense venting events are marked with a dashed vertical line. For the first 5 cells to go into thermal runaway, the intense venting events are very easy to identify with audio and video. As the intensity of the fire increases and more cells become involved it becomes more difficult to identify exactly when an intense venting event is occurring. It is clear however, that all remaining have gone through thermal runaway by 2900 seconds.

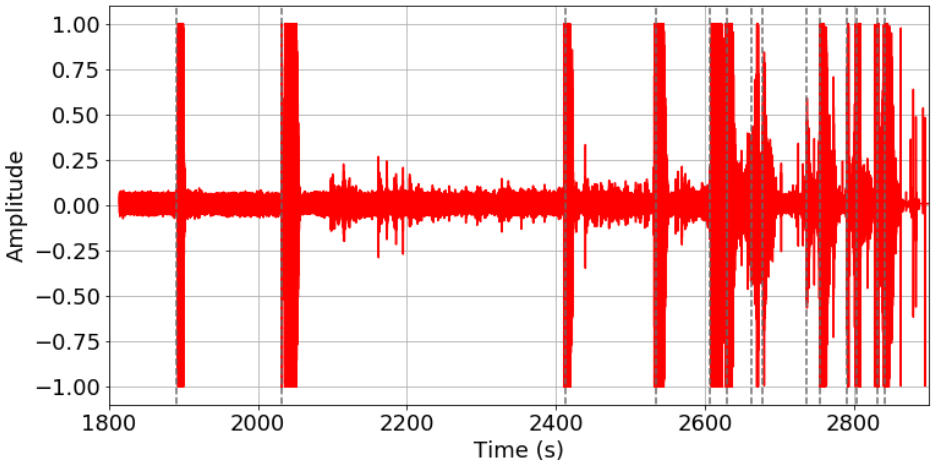

Figure 3.13: Audio amplitude shows clipping during periods of intense venting. Start of intense venting events are identified with dashed lines.

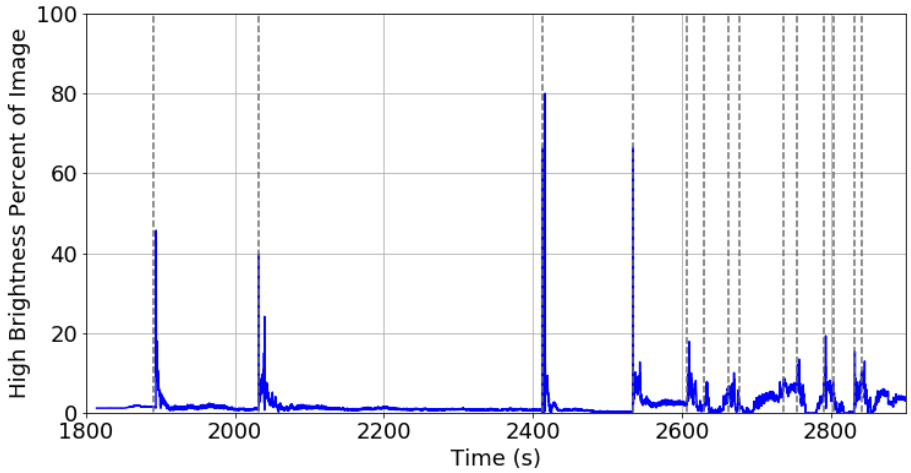

Figure 3.14: Plot of percent of video image exceeding brightness threshold of value ≥ 254. Intense venting events are identified with dashed lines.

The voltage data turned out to be of little use because shortly into the experiment the voltage wires were burned and shorted. The thermocouples attached to individual cells provided in Figure 3.15 give another perspective on the thermal runaway propagation process. Cell temperature data shows that runaway started with cell 1 at 1891 seconds into the experiment and then progressed to cell 2 at 2032 seconds. After the runaway of cell 2, the adjacent cell 3 as well as nearby cells 7,8 and 9 begin to heat significantly. As more cells go into thermal runaway it becomes more difficult to tell which cell is in runaway and by 2600 seconds, all of the cells are very hot and intense venting events become very frequent.

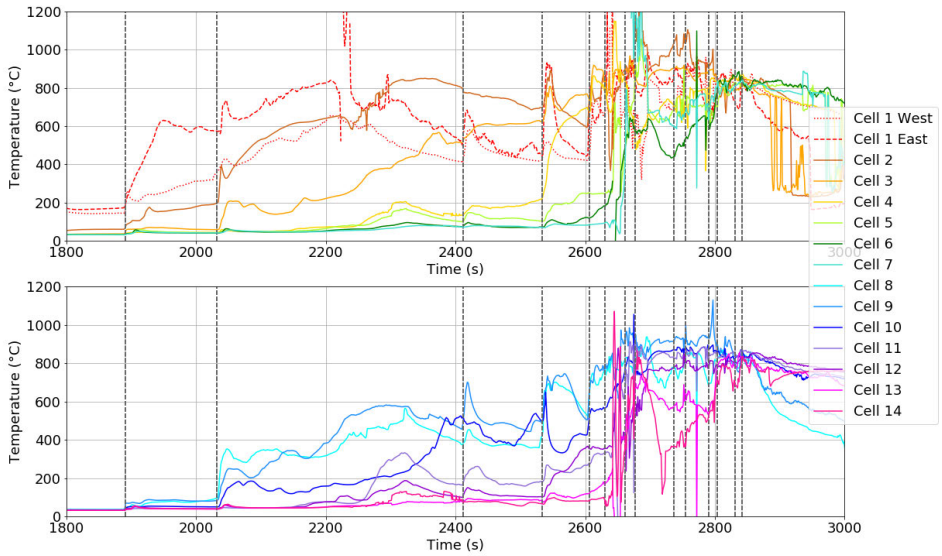

Figure 3.15: Cell temperatures for 14 cells show thermal runaway initiate in cell 1 and propagate to cell 2. By 2600 seconds all cells experience high temperatures and cells are going into thermal runaway in rapid succession.

It is also worth noting that throughout the course of the experiment, the attachment of the thermocouples on the cells changes. At the beginning of the experiment each thermocouple is taped to bare metal on the sides of each cell and the cells are enclosed in the polycarbonate module housing. Thus at the beginning of the experiment, the thermocouples are considered to measure the temperature of individual cells. By the end of the experiment, the thermocouples are in a pile of cell wreckage as most of the metal casings from the cells has melted and all that remains of the cells is the burned insides. Also by the end of the experiment, much of the polycarbonate has been consumed. Figure 3.16 shows the remains of the module after the experiment.

Figure 3.16: Module remains after experiment

Mass loss data of the event is also a useful means to understand the thermal runaway propagation process and also to observe the burning of solid materials like polycarbonate. Figure 3.17 shows the change in mass throughout the course of the experiment and 3.18 shows the mass loss rate. Initially there is negligible mass change until the first period of intense venting. Due to the downward thrust of the jet, this briefly appears as a mass gain for a couple seconds, before the scale registers that this period of intense venting caused the first cell to lose about 915 grams of mass in a period of about ten seconds. After this initial event, the jet flame from the venting event caused sustained burning of the polycarbonate module housing. This sustained burning introduces another source of mass loss. Polycarbonate burning continues to cause mass loss at a slow rate until at 2032 seconds the next cell experiences intense venting. This causes an additional 900 grams of mass loss and

results in visibly more burning in the video which can be seen as a higher mass loss rate in the mass data.

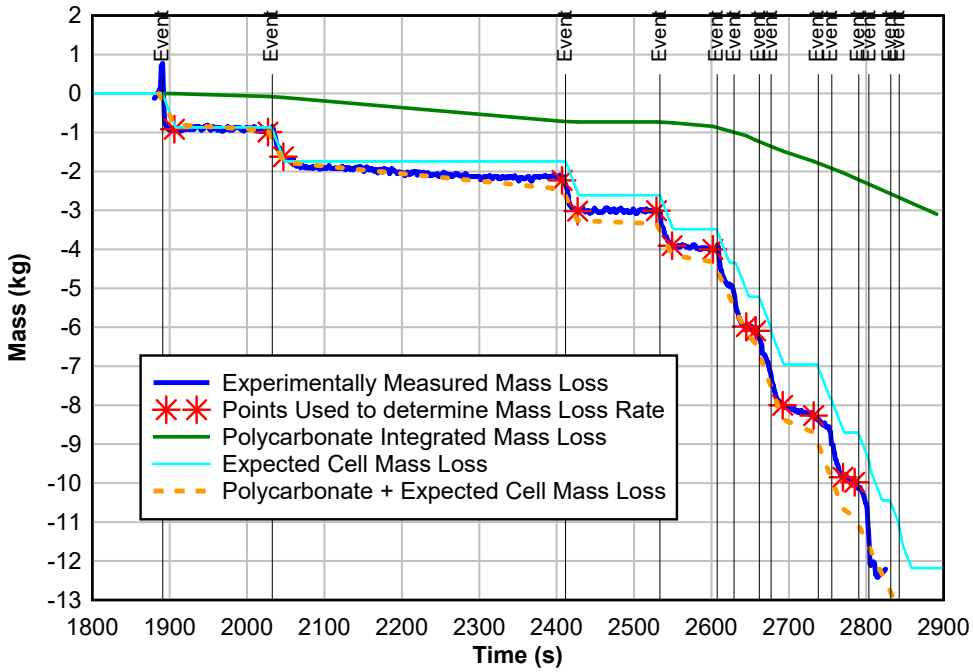

Figure 3.17: Cell mass loss over time shows 0.9 kg drops in mass at the time of each intense venting event. Cell intense venting events based on audio/video observations are labeled.

Analysis of this mass loss data can be used to inform computational fluid dynamics (CFD) model development of similar situations in which cells go into thermal runaway and module plastic material burns. Taking the first derivative of mass loss with respect to time produces a very noisy function which can be seen as the light blue line Figure 3.18. This function is very noisy due in part to measurement noise and also due to both large downward thrust and very fast mass loss as each cell undergoes a brief period of intense venting.

To model this process, it is important to distinguish lithium-ion cell mass loss due to intense venting from the mass loss associated with the burning of polycarbonate. This can be done by recognizing that the mass loss due to cell venting occurs in a very small window. As seen in the single pressure vessel experiment (Figure 3.11), the gas release associated with cell venting lasts about 7 seconds. As seen in the single cell in the open experiments (Figure 3.7), the period where most the cell mass loss occurs goes from about 5 seconds before runaway until 15 seconds after. To isolate polycarbonate mass loss from cell mass loss, points 5 seconds before and 15 seconds after each intense venting event are identified by audio and video indicators. Once these points are selected, the mass loss rate is linearized between each of these points. This process is used to generate the blue line shown in Figure 3.18. From this line it is evident that the mass loss rate due to cell thermal runaway is an order of magnitude greater than the mass loss rate due to polycarbonate burning. The polycarbonate burning rate can be approximated by using the mass loss rate between venting events and linearly interpolating between them for the periods of venting events. The mass loss rate of polycarbonate burning between intense venting events is useful to understand the heat release during the experiment and can be used in models of the process.

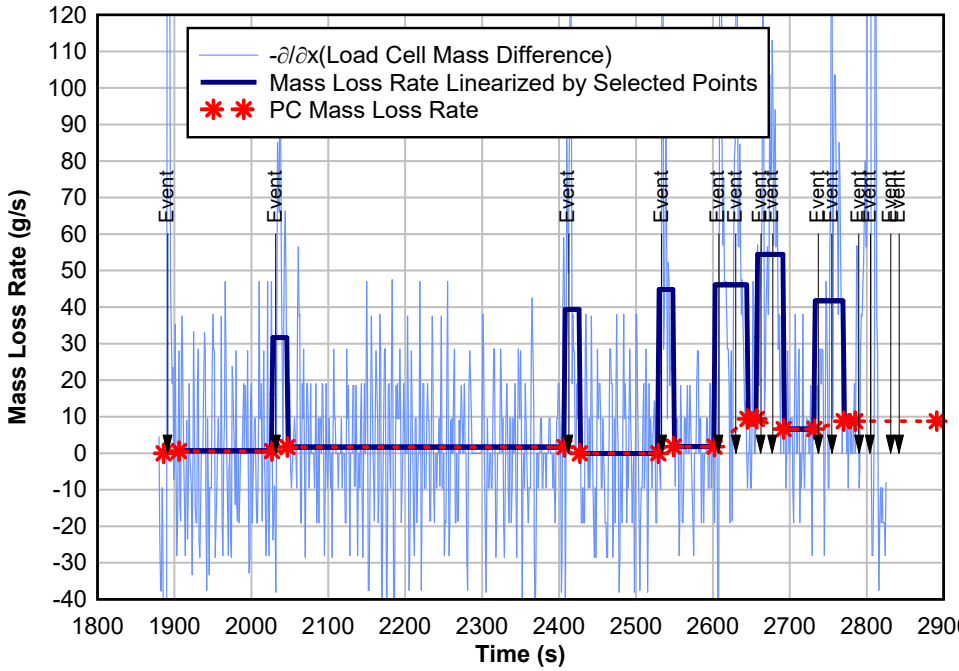

Figure 3.18: Cell mass loss rate as a function of time is very noisy with large spikes during cell intense venting. Linearizing mass loss rate using points before and after each runaway allows for the calculation of an average mass loss rate.

Temperatures and heat fluxes within the burn structure compartment were also measured. Figure 3.23a summarizes the compartment temperatures and heat fluxes during the course of the experiment. More detailed information can be found in the Appendix. Gas temperatures are reported at four levels (Ceiling, upper, mid and lower) on eight thermocouple trees. Heat flux measurements are taken at 16 points near the ceiling and also at 12 locations on the walls of the compartment facing the module. Generally, both temperature and heat flux see peaks each time a cell goes through intense venting. As an increasing number of cells go through intense venting in rapid succession, this leads to a buildup in temperature towards the latter half of the experiment. Since 8 of the ceiling level thermocouples are type

T, a number of thermocouples record maximum values at 400 °C. However, in two locations type K thermocouples are provided at the ceiling which shows that the temperature indeed exceeds 400 °C. From this data it is shown that the thermal runaway of just a single module in a compartment poses a significant fire hazard to the building. Temperatures in the upper gas layer reached at least 446 °C and the peak heat flux on the ceiling was 54 kW/m^2. The peak heat flux on the walls located 1.9 m away from the module was 43 kW/m^2.

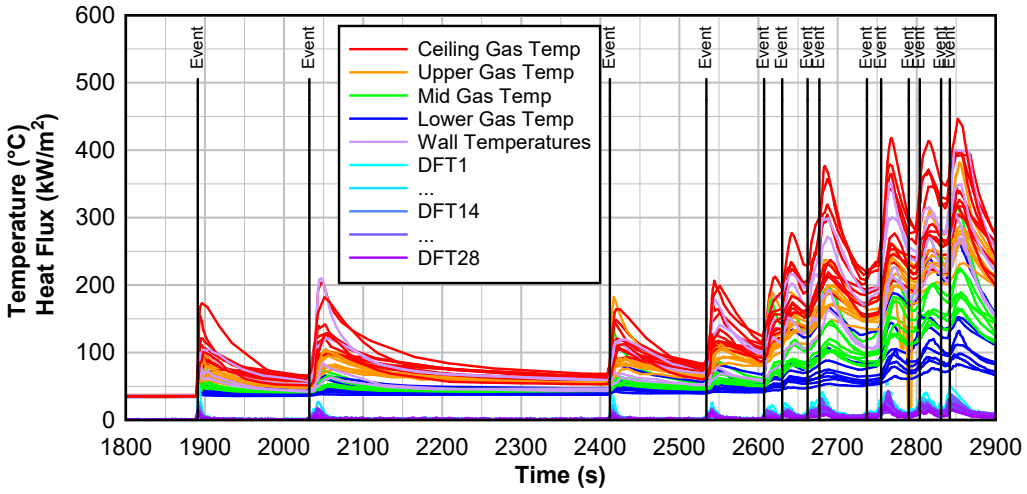

Figure 3.19: Experiment Compartment Temperatures

3.3.4 Rack Experiments Results

Two experiments were conducted using the same module placed inside a non-combustible steel rack. In these experiments, the module generally behaved in a similar fashion. The main difference between these experiments and the module in the open air experiment, is that due to the large amount of gas released, often the gases burn as the leave the top of the rack instead of immediately when they exit the module. This

causes the compartment gas temperatures to be more stratified.

In the first rack experiment, the runaway of the first cell caused a deflagration which made a loud bang and kicked up dust but did not cause overpressure damage. This event is shown in Figure 3.20

Figure 3.20: Sequence of images from deflagration following first cell runaway in first rack experiment.

The thermal runaway propagation within the module does appear similar. Figure 3.21 shows how many cells had failed in each experiment as a function of time, where the X-axis has been adjusted such that the intense venting of the first cell occurs at time 0. In this figure it can be seen that for all three modules, the final cell had intense venting between 959 and 995 seconds after the venting of the first cell. For all three experiments there was a large delay between the first and second cell intense venting. As more cells go through intense venting, the delay between events decreases. In all three experiments the last 3 cells undergo intense venting in a period between 20 and 38 seconds.

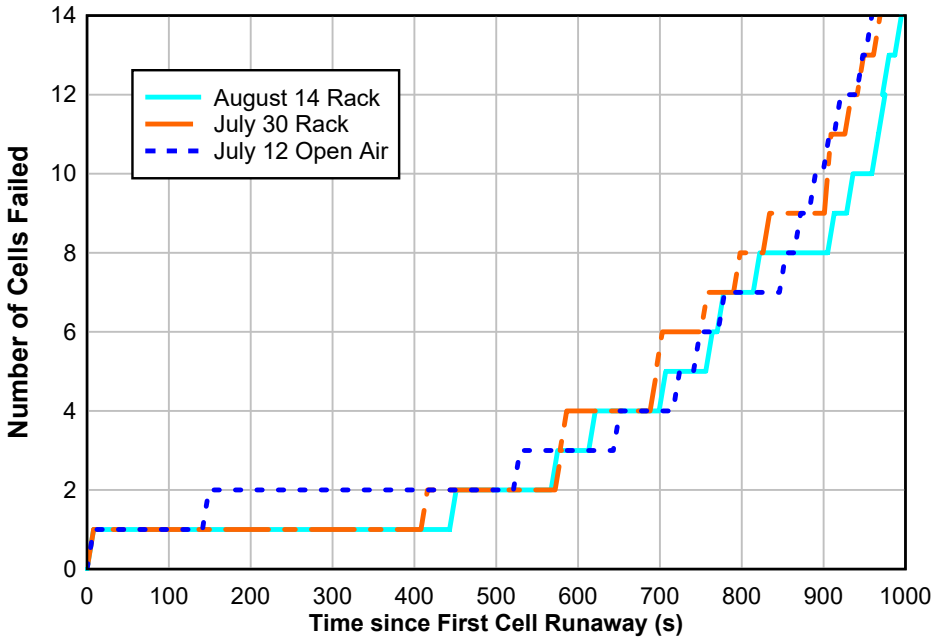

Figure 3.21: Number of Cells failed over time comparison for three different Experiments.

The first rack experiment featured very dense thermocouple instrumentation of the cells. Each cell had 3 thermocouples. Cell temperatures were recorded for both short sides (East and West) of each cell as well as the cell vent for each cell. Locations of the thermocouples are presented in Figure A.11 in the Appendix. Figure 3.22 summarizes the temperature data collected from all the cells. The first seven cells are shown above and the next seven are shown below.

From this detailed data, it is apparent that the side temperatures of each cell do not necessarily mimic each other. For example, at about 2200 s, the Cell 2 East temperature and the Cell 9 West temperature both peak. This peak is not registered on the Cell 2 West and Cell 9 East thermocouples. Since cells 2 and 9 are next to

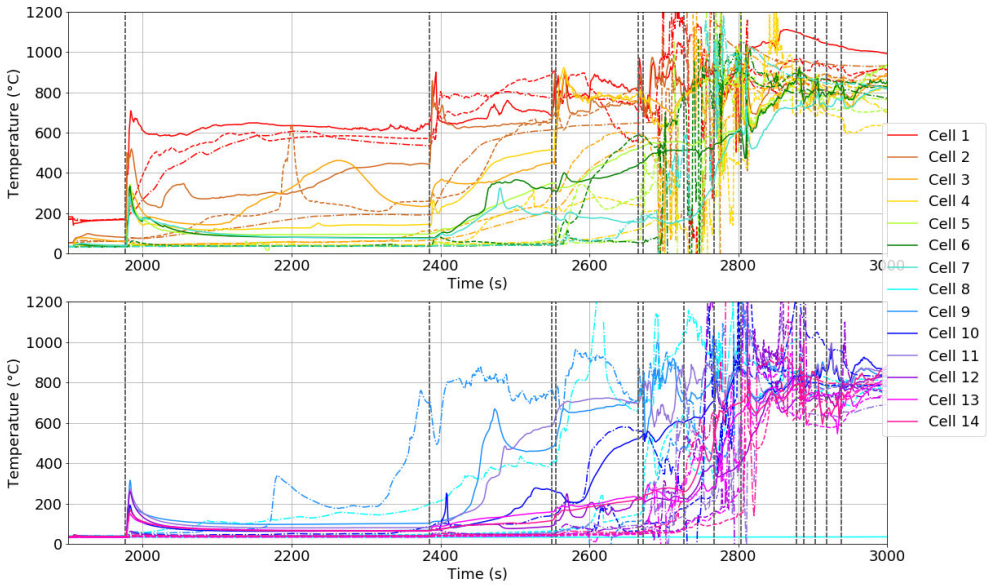

Figure 3.22: First Rack Experiment Cell Temperatures

one another, they are apparently both responding to heating occurring between the two of them. Since these are surface measurements, they are naturally influenced by gases surrounding them and multiple surface temperatures of the same cell can vary significantly.

Even with more densely instrumented cell temperatures it can be difficult to tell which cell is undergoing intense venting. It is more clear for the first several cells to undergo intense venting. However as time progresses, eventually the entire module becomes full of hot gases and cell side temperatures and vent temperatures are not only indicative of a particular cell venting, but also are responding to neighboring cell venting as well as the burning of polycarbonate all around the cells.

3.4 Computational Fluid Dynamics Model

3.4.1 Model Setup

Computational fluid dynamics (CFD) models of the module in open air and the module in a rack were created using Fire Dynamics Simulator (FDS). FDS is a Large Eddy Simulation CFD code created by NIST to model fires[51]. The particular geometry and material properties in the CFD model were based off the models developed by Kurzawski [15] who did extensive work developing the burn structure facility and CFD models to model it.

The domain of the CFD model includes the interior of the entire burn structure and a small region in front of the open door. The walls are modeled as obstructions with the thermal properties of the walls and the external boundary conditions are open on the sides outside the door. The model uses a grid size of 0.15 m.

The heat release rate in the model comes from the combination of flammable gases released by cells in thermal runaway and burning of the polycarbonate module. In the model, the heat release is represented by two different vents which release flammable gas. One vent is used to represent the hot flammable gas release from the lithium-ion cells in thermal runaway. This vent releases hot gases due to thermal runaway based on the gas species, volume and release rate that are measured from the single cell pressure vessel experiment. The temperature of the released gases is based on measured temperatures at the vent during the single cell in burn structure

experiments. In the model, this gas release occurs at the time of each intense venting event observed in the video and audio of the experiment.

The other vent releases gas corresponding to the heat release due to the polycarbonate burning. The gas release rate for this vent is based on measured mass loss of the module as described previously.

Once the polycarbonate mass loss rate and the heat release rate due to thermal runaway of batteries was estimated, then it was possible to build a CFD model of the event. Two different versions of the CFD model were created. In the Equivalent HRR FDS Model the combustion of polycarbonate and lithium-ion battery vent gas is approximated by using methane with the same heat release rate time history. In the Battery Gas FDS Model, a more complex model is developed which models the combustion of polycarbonate and battery vent gas using the properties of each material. In this model the unique combustion characteristics of each type of fuel was developed and used.

3.4.2 Model Results

3.4.2.1 Open Air Module Experiment

For temperature predictions inside the compartment both models perform fairly well. Figure 3.23 compares the compartment temperatures for the CFD model with the open air module experiment. In the models as well as the experiment, the temperature time history shows the same trend, in which the temperature increase spikes occur shortly after each runaway event. The increased frequency of runaway events

later in the experiment lead to significant temperature increases. One notable difference between the experiment values and the model predictions is that in the model each gas layer has largely the same temperature at any given time. In contrast, in the experiment thermocouples from the same layer have a wider spread of temperatures.

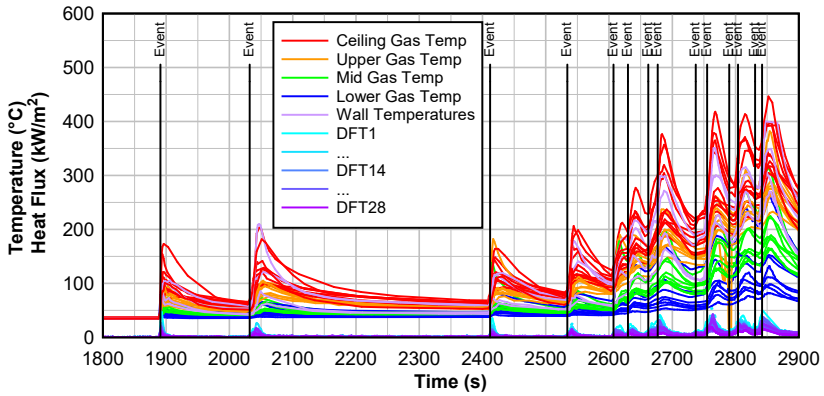

(a) Experiment Compartment Gas Temperatures and Heat Fluxes

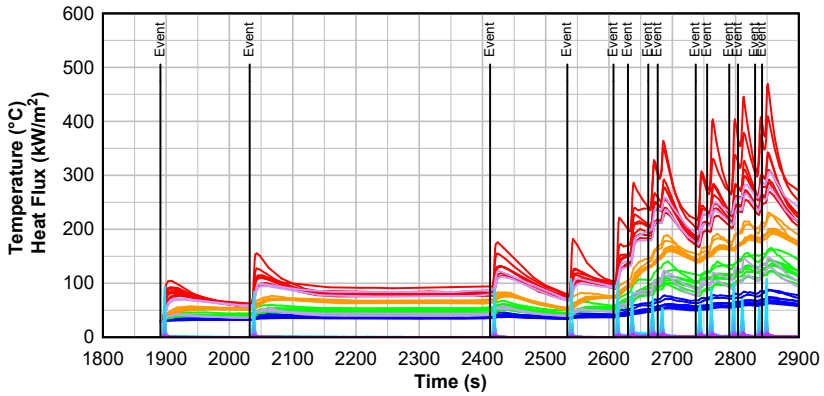

(b) Battery Gas FDS Model Temperature and Heat Fluxes

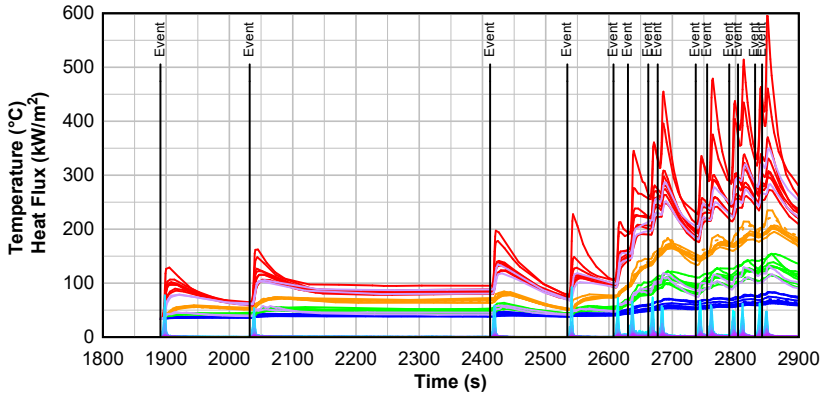

(c) Equivalent HRR FDS Model Model Temperature and Heat Fluxes

Figure 3.23: Experiment and model results from open air module experiment

Figure 3.24 compares the experimentally-measured and model-generated temperatures in the compartment for the Battery Gas FDS model. In Figure 3.24a maximum temperatures are compared for each thermocouple. In Figure 3.24b the entire time history of temperatures is compared.

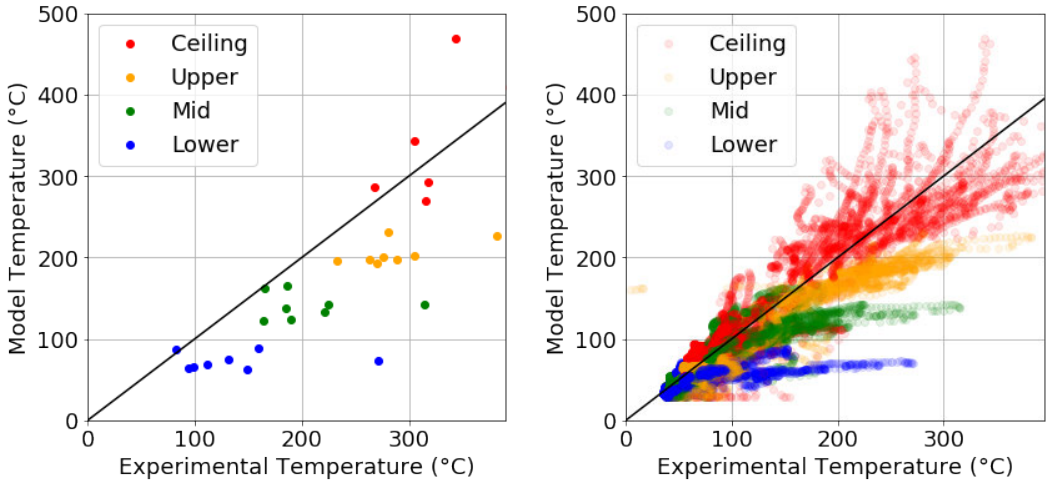

(a) Comparison of maximum compartment gas temperatures for each location

(b) Comparison of all compartment gas temperatures over time

Figure 3.24: Comparison of compartment gas temperatures for model and experiment

The actual experiment exhibited greater spread in lower and mid level gas temperatures than the model. The model shows temperatures as generally more stratified. In the model the thermocouples at each layer have values very close to one another. In the experiment, temperatures near the module are higher even at lower elevations. The contour plots in Figure 3.25 shows how in the model high temperatures stay up high, while in the experiment higher temperatures exist at lower levels in the region closest to the module. This difference seems to be due to greater mixing occurring in the experiment than what is accounted for by the model.

Figure 3.26 compares experiment and model gas concentrations in the upper layer

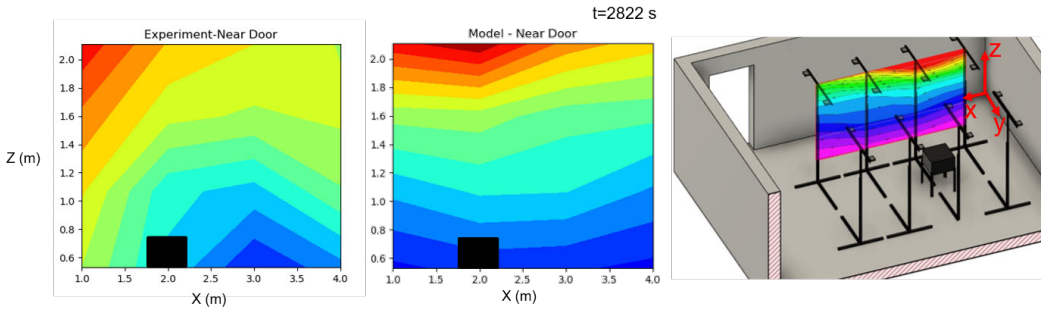

Figure 3.25: Contours of temperature for experiment and model for a slice taken along thermocouple tree plane near door. Module location shown by black box.

away from the module. Generally, both models performed well at predicting gas concentrations in the compartment. Since the Battery Gas Model takes into account the fact that a significant fraction of the released gas is carbon dioxide, it provides better predictions for carbon dioxide concentrations than the Equivalent HRR Model which assumes that all heat release is due to burning methane. However, since they have the same heat release rate, they both predict nearly the same values for oxygen concentrations.

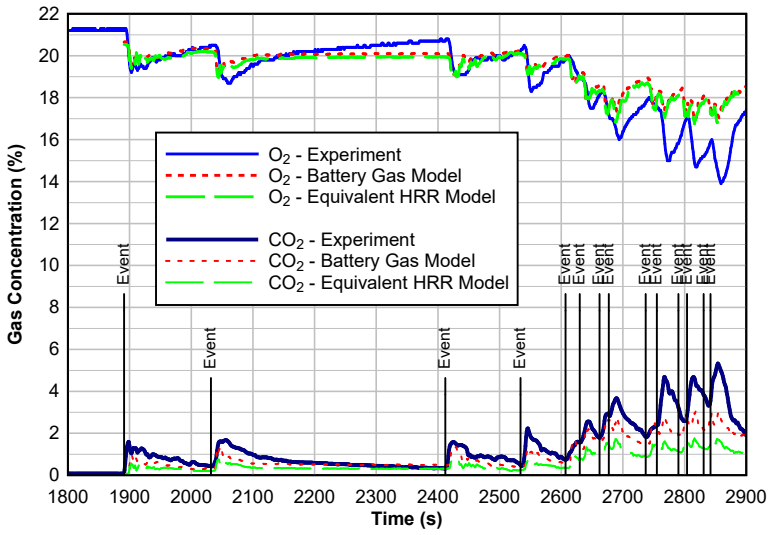

Figure 3.26: Comparison of experiment gas concentration measurement with concentrations predicted by battery gas CFD model and equivalent HRR model.

3.4.2.2 Rack Experiments

The same technique used to produce the open module CFD model was used for the rack experiments. These CFD models used the time of runaway data from the rack experiments. However, they used the polycarbonate mass loss rate from the open air module experiment because it was not measured for these experiments. Since the Battery Gas FDS model performs better, only it will be presented here. Predicted temperatures throughout the compartment are compared for the FDS model and the experiment. Temperatures are shown in Figure 3.27 for the first rack experiment and Figure A.20 for the second rack experiment. These temperature predictions show the same trends as those for the open module experiment.

Figure 3.28 compares the experimentally-measured and model-generated temperatures in the compartment. In Figure 3.28a maximum temperatures are compared for each thermocouple. In Figure 3.28b the entire time history of temperatures is compared. Temperature predictions are slightly better for the rack CFD models than for the open air module CFD model. This can be seen in Figures 3.27 and 3.28b. For the rack experiments, the spread in the measured temperatures for the mid and lower gas temperatures is greatly reduced. Since the rack chimneys most of the flame directly onto the ceiling, the gas temperature of the compartment is more stratified. Since the model shows more stratification, it has less error for these rack experiments.

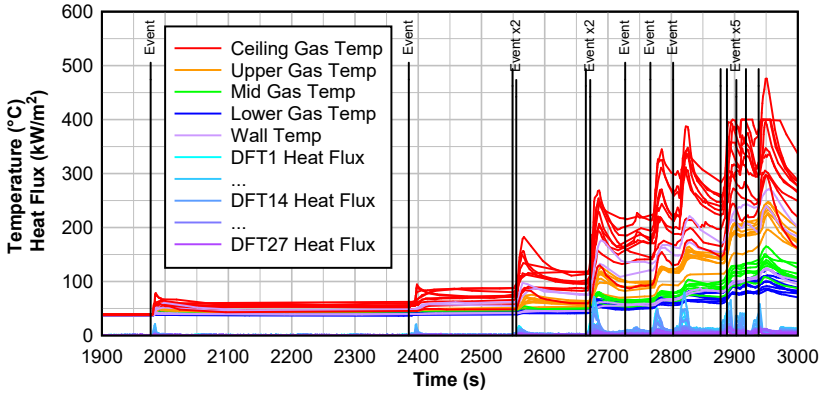

(a) Experiment Compartment Gas Temperatures and Heat Fluxes

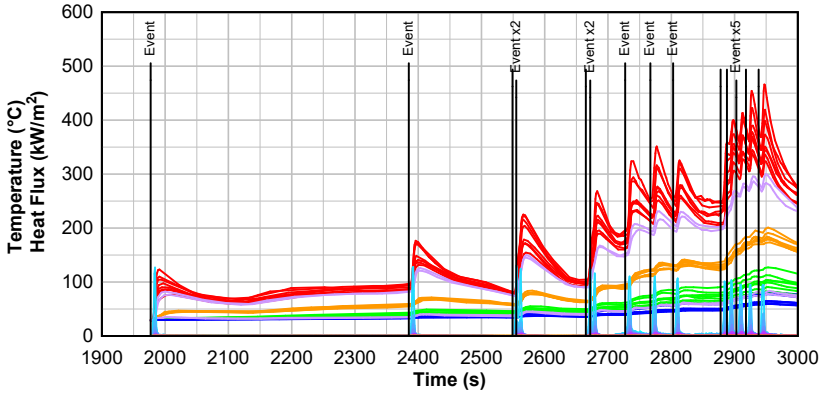

(b) FDS CFD Model Temperature and Heat Fluxes

Figure 3.27: Experiment and model results from first rack experiment

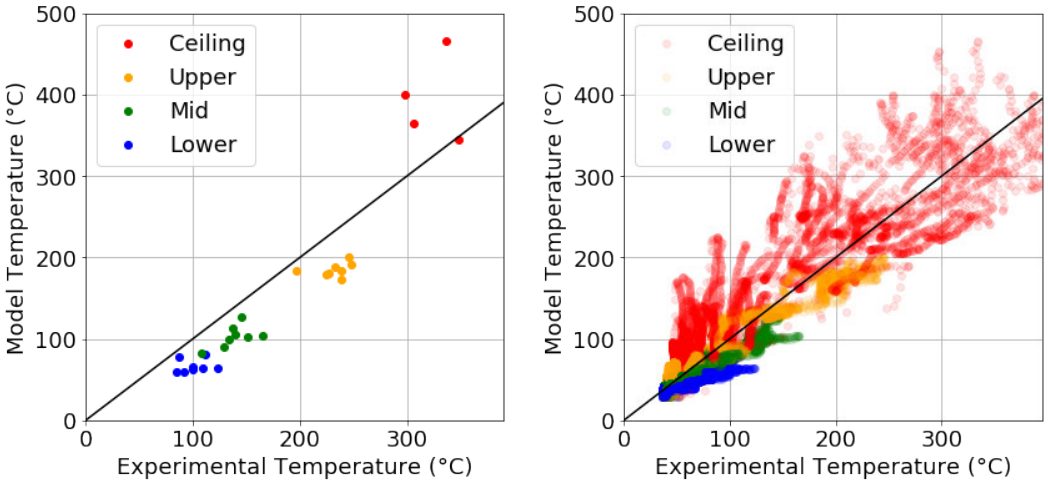

(a) Comparison of maximum compartment gas temperatures for each location

(b) Comparison of all compartment gas temperatures over time

Figure 3.28: Comparison of compartment gas temperatures for model and experiment

3.5 Conclusions

This chapter has examined thermal runaway propagation using commercially available ESS modules in a compartment. Multiple failure outcomes were observed for a single cell exposed to heating. Under one heating condition, the cell ruptured and was thrown across the room while in other circumstances the vent activates and releases pressure. Single cells were failed to characterize the gas release rate, gas species, temperature and mass changes associated with thermal runaway of a cell. Cells were observed to bulge after thermal runaway. For cases in which air gaps between cells is small (such as in the module tested), this bulging can allow failed cells to come into contact with adjacent cells.

A commercially available ESS module was tested for thermal runaway propagation. After heating a single cell to thermal runaway, thermal runaway propagated and eventually caused all 14 cells to experience thermal runaway. Some of the clearest indications of intense venting due to thermal runaway are through audio and video. Visually, intense venting is observed as jet flames which can reach the ceiling and cover a significant fraction of the image with nearly overexposed pixels due to high brightness. The audio indicates cell intense venting through squealing, hissing and roaring noises which are of sufficient amplitude to cause audio clipping. For these cells and modules, intense venting due to runaway can be identified in mass data as short periods ($\sim$ 15 sec) in which approximately 0.9 kg is lost. Mass loss rate can also be used to estimate module plastic material burning rates.

The same module was tested for thermal runaway propagation inside a rack enclosure. Cell surface temperatures and cell vent temperatures provide additional

information about the runaway propagation process but can be very difficult to interpret. The same cells may have very different temperatures on opposite surfaces and cell surface and vent temperatures may be strongly influenced by nearby cell failures as well flaming combustion.

Single cell gas release, the timing of cell thermal runaway intense venting and plastic mass loss rate can be used to develop a heat release or gas release time history for a module. This time history can be used to develop a CFD model of the event and to predict temperatures, heat fluxes and gas concentrations within a compartment. The model performs well at predicting temperatures throughout the compartment with the exception that near the module the model predicted more stratification than occurred in the experiment. The model is also useful for prediction of heat fluxes and gas concentrations in the compartment.

Future work is needed to develop models which will allow the prediction of the time of thermal runaway for each cell. These models will need to account for heat transfer to each cell and the runaway process in each cell. Based on these experiments, there are many challenges to getting such models to behave properly. A major challenge with such models is trying to characterize the geometry inside the module. Throughout the course of the experiment the module changes significantly. At the beginning, there are 14 cells each separated by about 8 mm air gap and surrounded by a polycarbonate housing. At the end of the experiment the geometry has changed significantly as the cells have swelled and melted and are all touching in the end. The polycarbonate housing geometry also changes significantly as in the end much of it has been consumed. These changes in geometry will make it more difficult to

predict the times of thermal runaway using a CFD model.

Chapter 4

Explosion Hazard Experiments

4.1 Introduction

Although explosions of lithium-ion battery vent gas are very dangerous and are of great interest, there have been very few published experiments involving battery gas explosions. Larsson observed gas explosions after failing lithium-ion cells in thermal runaway using an oven[52]. The FAA encountered some explosions unintentionally during a number of fire tests involving batteries. In one experiment, 4800 123A small lithium metal cells were exposed to fire in a compartment of an aircraft and the fire was controlled with Halon. Initially thermal runaway propagated but explosion was avoided due to Halon activation and low oxygen levels. Towards the end of the experiment, Halon concentration approached zero and oxygen levels increased. Then a single cell in thermal runaway ignited flammable gases and caused an explosion. The explosion blew open the floorboards, damaged the cockpit bulkhead and threw the cockpit door into the cockpit[53].

In another experiment the FAA tested a fire resistant cargo container which contained 5000 lithium-ion 18650 LCO cells packaged in boxes. They initiated thermal runaway on a single cell and allowed runaway to propagate throughout. In this experiment an aerosol fire-extinguishing agent was activated 20 minutes into the experiment when smoke was first detected. At this time the oxygen in the room dropped drastically. Over time oxygen levels increased in the container until at 45 minutes into the experiment, an explosion occurred and blew open the container's doors[53].

These two experiments demonstrate the danger of lithium-ion battery explosions. Due to the added danger and complexity of lithium-ion explosion experiments, intentional lithium-ion battery explosion experiments are largely absent from the literature. Engineers performing work for battery system manufacturers have observed explosions, but manufacturers are not keen to share these publicly.

In this section a number of explosion experiments are described. The intent of these experiments is to observe the process leading up to an explosion. One of the goals of these experiments is to better understand the explosion hazard that firefighters may face when confronting lithium-ion battery hazards in a small space such as a closet. Since a closet is a small volume, it is possible for even a small amount of lithium-ion batteries to produce an explosion. Battery systems ranging from laptops to scooters, e-bikes and even home energy storage systems can be increasingly found in home closets.

The end goal of this experiment series was to develop a closet-sized explosion exper-

(a) 1 ft steel cube experiment setup

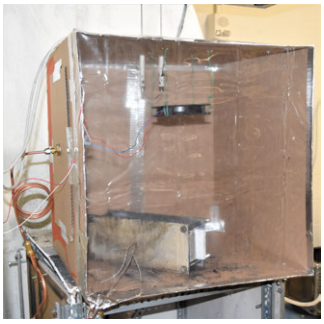

(b) Cardboard box experiment setup

(c) Closet experiment setup

Figure 4.1: Three experiment setups used for various scales of explosion experiments.

iment. To accomplish this, several smaller explosion setups were built for various scales of explosion experiment. A steel cube explosion setup was constructed which measures 1 ft x 1 ft x 1 ft (0.31 m x 0.31 m x 0.31 m). A cardboard box explosion setup was used as a low-cost intermediate scale setup and for field demonstrations at fire departments in Hawaii and Arizona. The cardboard box has dimensions of 22 in x 22 in x 21 in (0.56 m x 0.56 m x 0.53 m). Finally, a full-size closet setup was constructed with gypsum walls and wooden framing to conduct larger experiments. Figure 4.1 shows the three experiment setups used for this series of experiments.

4.2 Experiment Support Systems

Ignition, gas measurement, gas collection, and control systems were developed. These systems were used at every scale of experiment. The execution of the smaller experiments gave opportunities to test and improve these systems in preparation for the larger closet experiment.

4.2.1 Ignition System

A simple ignition system was built to allow the remote ignition of the battery gases for explosion experiments. The ignition system is based on a Beckett 5177U transformer which has a 20 kV peak rating and a 35 mA RMS current. The arc is formed with Beckett 5780 electrodes separated by a gap of about 10 mm. The connection from the transformer to the electrodes uses 18 gauge high voltage wire with a 42 kV rating. The system is shown in Figure 4.2.

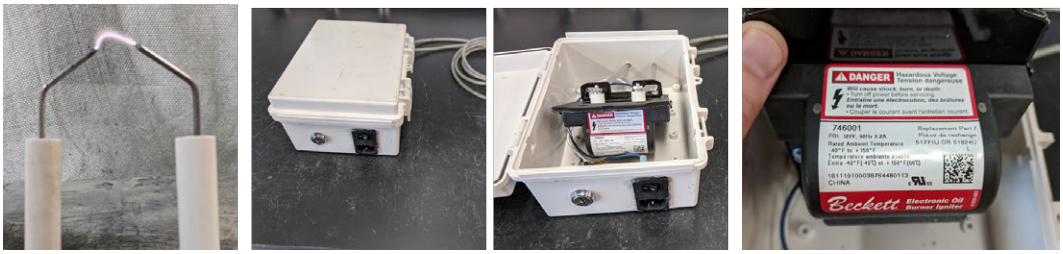

Figure 4.2: Igniter system consists of electrodes, high voltage wire and high voltage transformer.

4.2.2 Gas Measurement Systems

4.2.2.1 Gas Filtration, Pumping and Collection Systems

Gas filtration, pumping and collection systems were designed and built to allow the capture and measurement of gases during explosion experiments. These systems extract gas from the explosion compartment, filter out particulate matter and pump the gas into gas sensors and/or a foil bag for collection.

To accomplish this, the gases must first be pumped out and filtered. A series of four filters are used to remove particulates from the gases. The first level of filtering is done using a steel mesh over the gas intake and steel wool inside the intake. This

removes the largest particles and helps to prevent deflagrations from propagating into the sensor and collection systems. A series of 3 filters then removes the smaller particles. The first filter is a 51 micron fuel filter, the second filter is a 0.5 micron air filter and the final filter is a multipurpose filter that removes particles down to 0.01 microns in air. The filters and pumps are connected with 1/4" ID, 3/8" OD soft PVC tubing. The first two filters are extremely low cost and rapidly accumulate material so they are replaced after each experiment. The final filter is a higher quality filter that provides the level of filtration needed to protect the gas sensors and GC instrument. After the gases are filtered, they are clean enough and cool enough to pass through the pump. The 12V DC pump used is shown in Figure 4.4. After passing through the pump, the gases pass through the custom BlastDAQ gas sensor box described in Section 4.2.2.3. After passing through the gas sensors, the gas is either exhausted or pushed into gas bags for collection.

Figure 4.3: Filtering is accomplished by connecting low-cost disposable 51 micron and 0.5 micron filters in series with a 0.01 micron filter

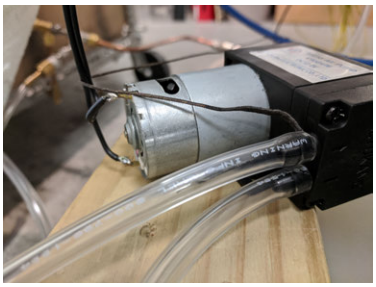

Figure 4.4: Pump used to extract gas samples

After passing through the sensors, the gas can be saved in a gas bag for later analysis with a gas chromatograph. This is accomplished by using a manifold and a series of solenoids which are operated to control whether the gas enters a designated bag or is exhausted. Manifold and solenoid setups were built to allow for three gas bags to be collected on one sensor line and a single gas bag to be collected for another. For the three-bag manifold, three normally-closed solenoids are used to control gas entry to each of the the bags. At the end of the manifold is a normally-open solenoid that allows the exhaust of gas when gas bags are not filling. In normal operation, the pump runs continuously and the exhaust solenoid is open to allow gas to flush the sampling line and filters. When a sample is taken, the exhaust solenoid is closed and the appropriate gas bag is opened to fill the bag. After between 8 and 15 seconds, the 0.5 L gas bag is full and the gas bag solenoid is closed and the exhaust solenoid is opened again. The manifold is designed such that the continuous flushing out the exhaust solenoid avoids the dilution of gas samples. The single bag manifold operates with one normally-closed valve which operates the gas bag along with one normally-open valve which allows for exhaust flushing. In the single bag configuration the two solenoids are wired together in parallel for easy control.

The gas bags are 0.5 liter multi-layer foil bags which are designed to contain gas

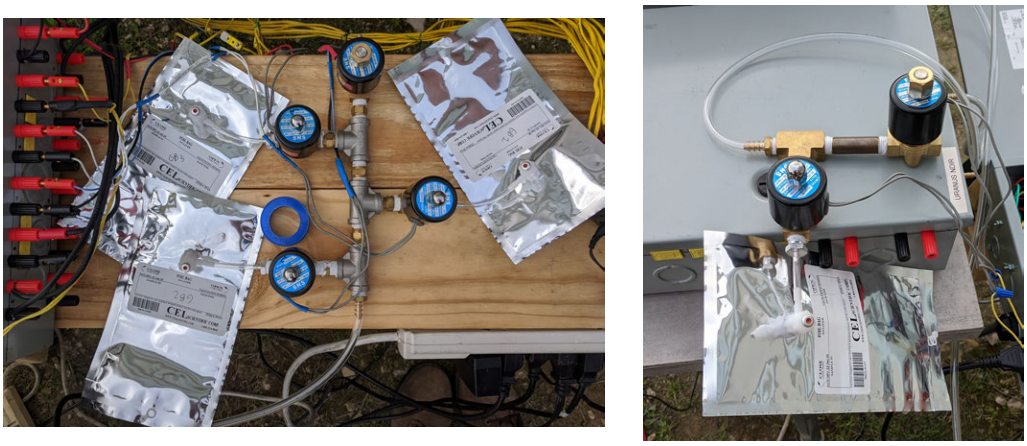

Figure 4.5: Manifold and solenoids used to control flow into gas bags.

samples. A concern with gas bags is the ability to hold gas samples over a long period without the escape of light gases such as hydrogen. Testing with a sample of battery gas showed that over the course of three days the hydrogen concentration changed by less than 1 % volume when taking repeated samples from the same bag. This gives confidence the bags can be used to analyze samples taken the previous day.

4.2.2.2 Gas Chromatography

After the gases are collected in the foil gas bags, their composition is analyzed (in the laboratory) using a Shimadzu GC-204 gas chromatograph thermal conductivity detector (GC-TCD). The gas chromatograph is calibrated to measure hydrogen, oxygen, methane, ethylene, ethane, propane, methane, carbon monoxide, carbon dioxide, oxygen, nitrogen and water. For the cells analyzed, this provides information for about 98% of the gas generated by the cell. When battery vent gas is mixed with air in an explosion compartment, the percentage of known gases is even greater.

4.2.2.3 BlastDAQ - NDIR and Electrochemical Sensor System

A custom internet of things (IOT) enabled sensor system was developed to facilitate the collection of gas concentration data. The system is built around a circuit board that I designed for this specific application. The circuit board features two ADCs (analog-digital converters), 4 thermocouple reading circuits and 3 circuits to control on-off operation of DC powered accessories. The circuit board design and final manufactured product are shown in Figures 4.6 and 4.7.

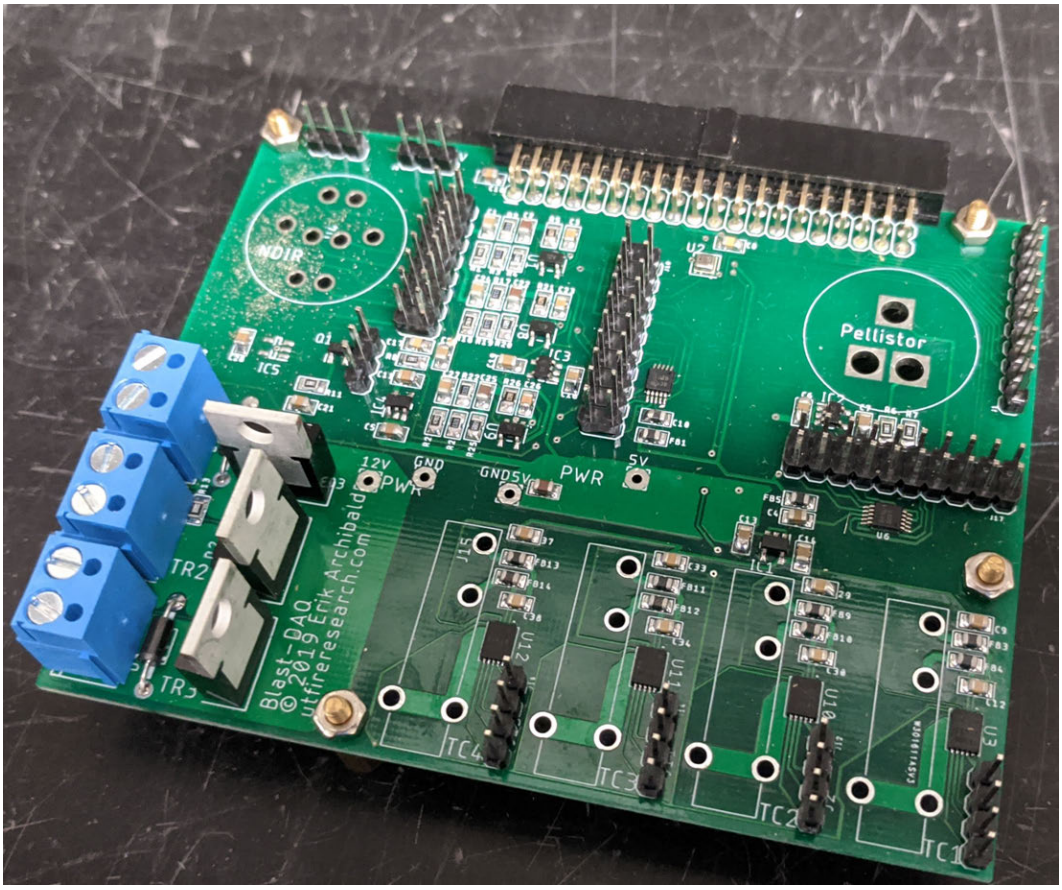

Figure 4.6: Custom designed printed circuit board can control DC powered devices and measure temperature and gas concentration.

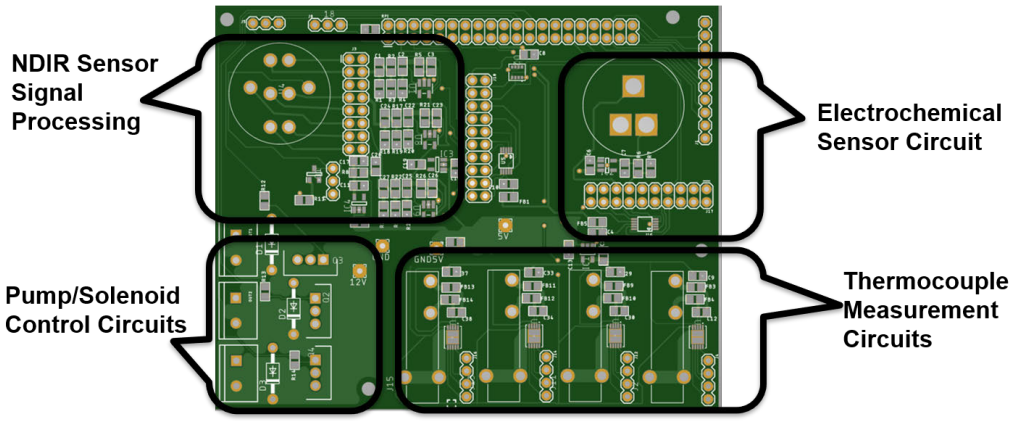

Figure 4.7: Custom designed printed circuit board to measure temperature, gas concentration and to control DC power devices.

To create a complete system, the custom printed circuit board was combined with other components and placed in a steel housing. The system uses a Raspberry Pi single board computer running Raspbian as the central control unit for the system. The final system also includes the oxygen sensor, NDIR sensor, a power supply and hardware and tubing to direct the gas flow across the sensors.

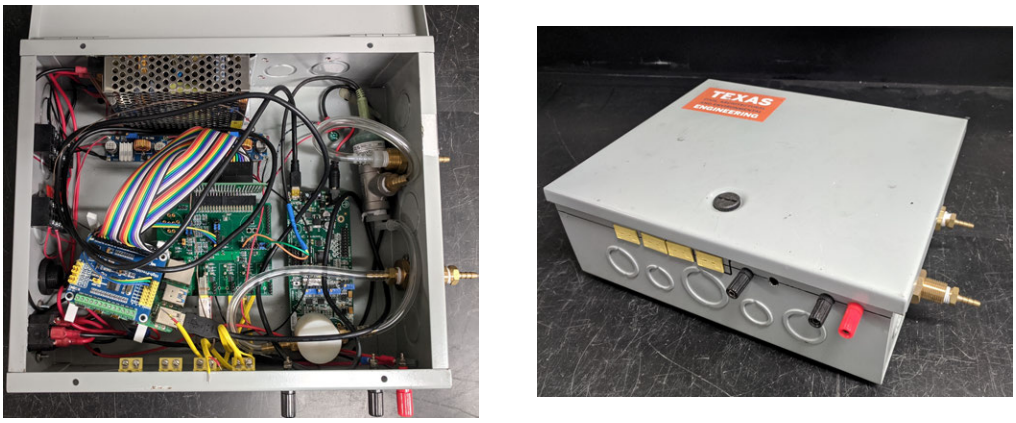

Figure 4.8: Gas Sensor Box with ports for gas sensing, thermocouples and power control.

Oxygen concentration is measured using a MaxTec Max-13 electrochemical sensor as shown in Figure 4.9a. The custom-built circuit board contains the circuitry and an analog-digital converter to measure the voltage on the sensor. Since electrochemical sensors are known to drift, each time the Raspberry Pi boots up it automatically calibrates the oxygen sensors for ambient oxygen concentration. This automatic calibration proved to be very effective for providing accurate oxygen measurements during experiments.

(a) Electrochemical Oxygen Sensor

(b) IR15TT-R NDIR Sensor

Figure 4.9: Gas sensors used in BlastDAQ System

The flammable gases and carbon dioxide in the battery vent gas are measured with a SGX SensorTech IR15TT-R non-dispersive infrared sensor attached to a SGX SensorTech EK-2 breakout board. This sensor is designed to measure methane and carbon dioxide gases by measuring changes in infrared absorbance of the gas. The sensor contains a lamp which is pulsed. The infrared absorbance of the gas is then measured using three detectors. The reference detector is not sensitive to any specific gas and responds in a sinusoidal pattern at the same frequency as the lamp. The active detector for carbon dioxide responds similarly with the exception that in the presence of carbon dioxide it will have decreased amplitude. The active detector for methane also works in the same manner. However, since many hydrocarbons have similar to absorbance to methane, the methane sensor will respond to any hydrocar-

bon gas.

The NDIR gas sensors were calibrated by flowing 99% purity methane, carbon-dioxide and nitrogen over the sensors and following the manufacturer recommended process to calibrate both zero and span (100 %) values.

When the system is plugged in, a custom python program running on the Raspberry Pi first checks for updates and then begins running the data collection process. The script saves the gas sensor data as a CSV and also publishes the data using the Thingsboard IOT protocol. A laptop is used as server to receive the data and is used to store and analyze the data from all the gas sensors. The laptop hosts a web interface which allows users to view data in real-time as well process and analyze data afterwards. The Thingsboard interface is shown in Figure 4.10.

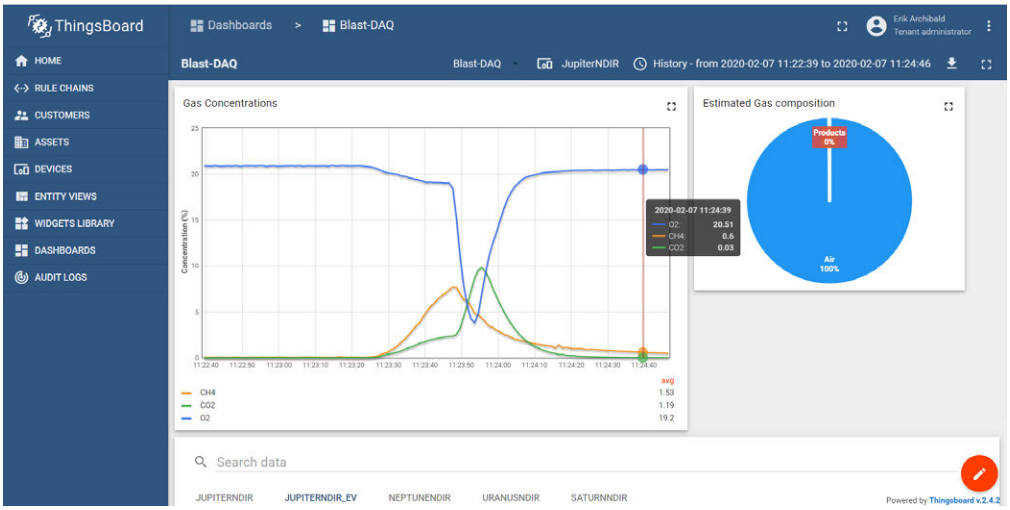

Figure 4.10: Internet of Things Dashboard for Real-time Data Collection System.

4.2.2.4 Gas Sensor System Testing Experiments

Seven gas sensor measurements from 2 steel cube experiments and 2 cardboard box experiments were used to test gas sensor performance and compare it against the gas chromatograph. For this process cells were put into thermal runaway in either the steel cube or the cardboard explosion apparatus as previously described. Gases were continuously pumped through the filters and into the NDIR and electrochemical sensors. For each experiment at one or two points in time a sample was collected by diverting the sensor vent flow into a gas bag. This was done at various points in time including immediately after runaway, 20 seconds after runaway, minutes after runaway and also after the explosion event. Gas samples were then analyzed using gas chromatography.

Figure 4.11 compares the results from the NDIR and electrochemical sensors when compared against the same samples later analyzed using gas chromatograph. For this comparison the electrochemical measurement of oxygen and the NDIR measurement of carbon dioxide are compared directly against the gas chromatograph values from the gas bag samples. Since the NDIR methane sensor is sensitive to wide array of hydrocarbons, the NDIR methane value is compared against the sum of all flammable gases measured using GC.

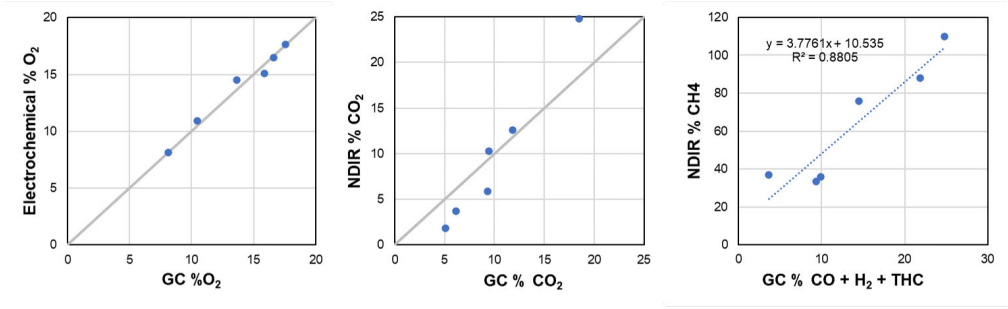

Figure 4.11: Comparison of NDIR and electrochemical sensor measurements with GC analysis performed on gas bag samples.

In Figure 4.11 it can be seen that the electrochemical oxygen sensor values were very close to those measured by GC. The NDIR carbon-dioxide sensor also performed reasonably well. The methane sensor gives readings exceeding 100 % methane because it is sensitive to a broad array of hydrocarbons. The intent is to use it as a proxy for the flammable gases released by a cell. The measured methane concentration does correlate with the sum of flammable gases measured by the GC although it does not perform nearly as well as the oxygen and carbon dioxide sensors. When used together these three sensors can provide insight into the mixture of gases present inside the explosion compartment. The oxygen value is informative as to how much air is present. The methane value is correlated with the amount of flammable gas released by the lithium-ion cell. And the carbon dioxide measurement is due to both carbon dioxide released directly by the cell as well as carbon dioxide formed by combustion.

4.2.3 Control System

A remotely-operated control system was developed to control the experiments. The system allows for manual control of the system as well as scripts and automatic PID

control. The system provides control to AC and DC outputs which control every aspect of the experiment. The first version of the control box contained seven 12V DC outputs and four 120V AC outputs and is shown in Figure 4.12.

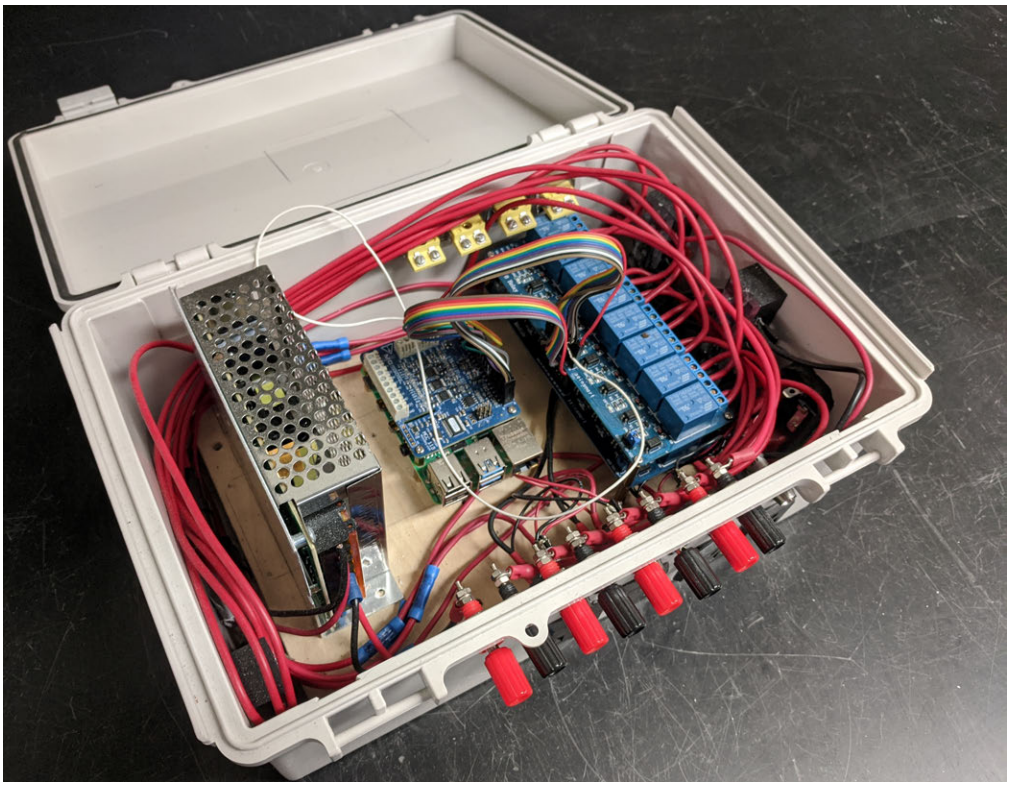

Figure 4.12: First version of control box used to control AC and DC outputs to run experiment.

The final version of the control box contains eleven DC outputs operating at 12V and five AC outputs operating at 120V. Each output is individually fused at 10A to ensure that the overload of any single circuit due to melting or fire would not trip breakers causing the entire system to go down.

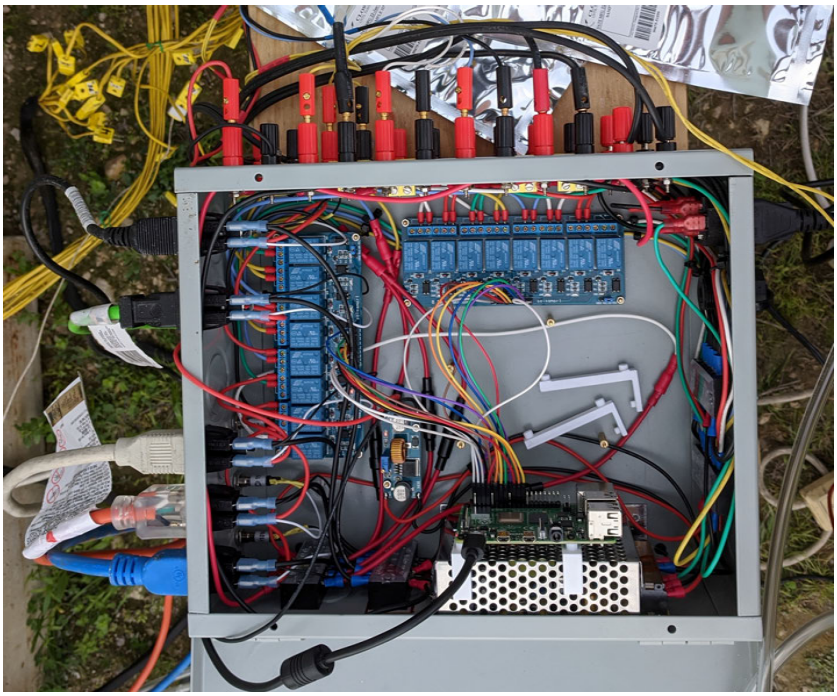

Figure 4.13: The control box consists of a single board computer, relays and power supplies needed to remotely control AC and DC systems used in the operation of an experiment.

The processing in the control box is done by a Raspberry Pi 4 single board computer. The Raspberry Pi GPIO ports are connected to 16 relays which can be used to control the AC and DC outputs. A 12V power supply provides DC power to the DC outputs. A 5V DC-DC voltage regulator is used to power the Raspberry Pi.

The Raspberry Pi runs the Raspbian operating system and uses Mycodo software. Mycodo is an open source software project that provides a web interface and framework for the Raspberry Pi to interact with inputs and outputs[54]. For this project Mycodo is configured to operate all of the AC and DC outputs connected to the relays which are connected to the Raspberry Pi's GPIO pins.

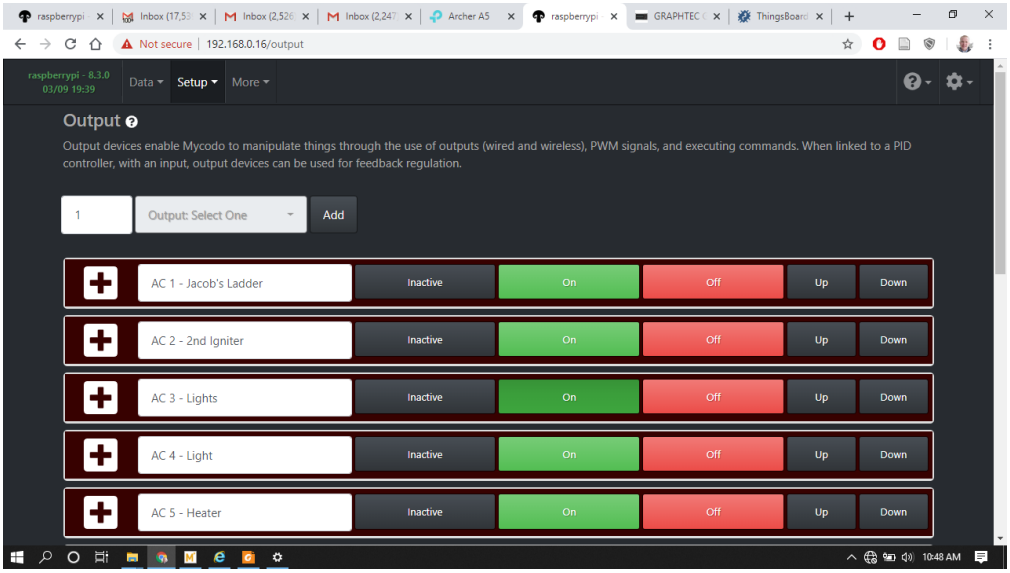

Figure 4.14: Mycodo web interface which allows for remote control of AC and DC outputs.

The AC and DC outputs in Mycodo can be controlled manually, controlled using a PID process or controlled automatically using scripts. For experiments that were highly repeated such as the cardboard box experiments, scripts were used to automate the collection of gas samples. For most other experiments the system was operated manually. Even when manually operated, the Mycodo system allows for the logging of output actions.

4.2.4 Small Steel Cube Setup

Early experiments were conducted in the 1 ft x 1 ft x 1 ft (0.31 m x 0.31 m x 0.31 m) steel cube. This cube has steel walls on all sides except for one which is a window. The top of the cube is made of plastic and fastened only on one edge, allowing it to open up to release pressure during an explosion. The explosion cube with a battery

setup inside of it is shown in Figure 4.15.

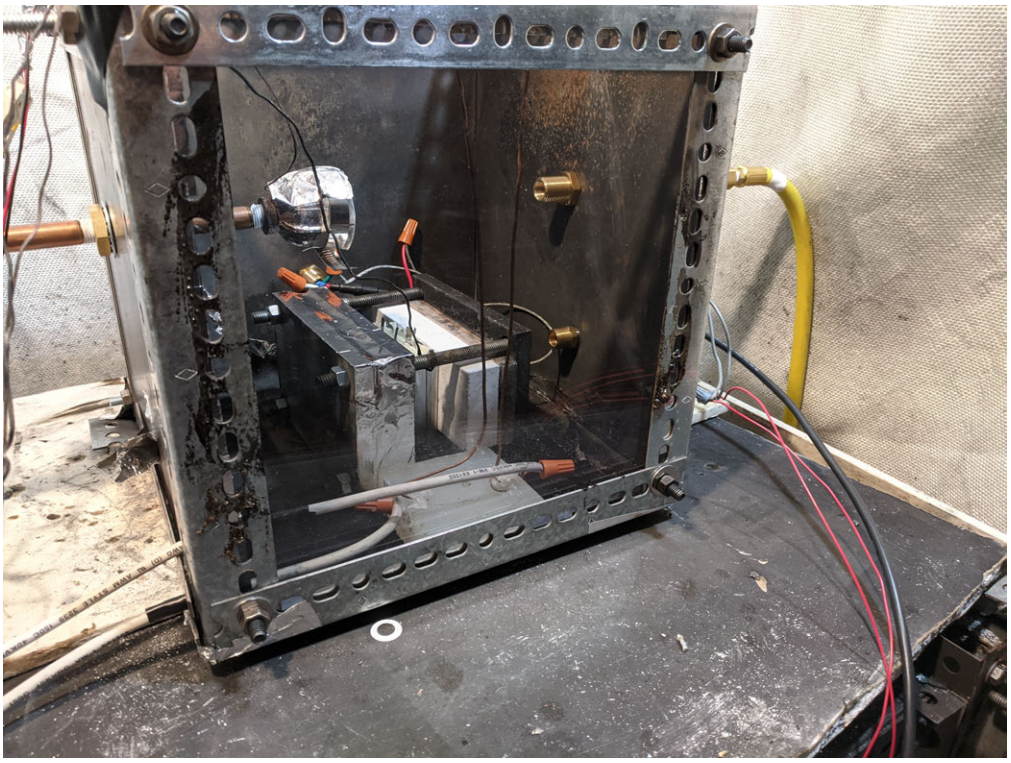

Figure 4.15: 1' x 1' x 1' (0.31 m x 0.31 m x 0.31 m) Explosion cube enclosure with cell clamping and heating setup

High speed video of the explosion process is recorded using a GoPro video camera. Gas temperatures are measured at two locations, just above the cells and in the center of the box.

ok

4.2.5 Cardboard Box Experiment Setup

A low-cost, disposable explosion setup was devised to perform intermediate experiments and also to be able to perform explosion demonstrations to help firefighters

understand lithium-ion battery hazards. The disposable setup is made using a heavy-duty extra large cardboard box with dimensions of 22 in x 22 in x 21 in (0.56 m x 0.56 m x 0.53 m). The cardboard box was closed off on one side with a clear shower curtain that allowed us to see into the box. When the explosion occurs, the shower curtain is ruptured.

Figure 4.16 shows the cardboard box with various systems connected inside. The cardboard box experiments made use of the gas measurement, ignition and control systems previously described. Cardboard box experiments also used 120mm 12V DC computer fans to promote mixing inside the box. In these experiments arrays of 18.5 Ah cells were failed using a similar setup as that used for the 5 Ah cells.

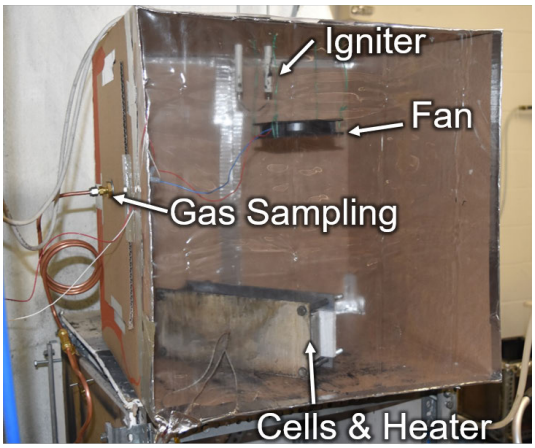

Figure 4.16: Cardboard Box explosion enclosure with fan, gas sampling, igniter and cell and heater setup.

4.2.6 Closet Experiment Setup

Two full-scale experiments were done using a commercially available lithium-ion cell in a closet. The experiment is demonstrative of the types of issues faced when ana-

lyzing explosion hazards of lithium-ion battery systems. In these experiments a cell is heated until runaway. After sufficient gas has accumulated for an explosion, the mixture can be ignited manually and the resulting pressure and impulse are measured. Temperature is measured throughout the compartment using thermocouples.

This setup uses a full-size closet which was constructed for full-scale explosion experiments. The closet is built out of 2x4 and 2x6 lumber and the walls are covered in 5/8" (16mm) fire resistant drywall. The closet is located inside of a steel shipping container, as shown in Figure 4.17. The closet is 1.11 m wide, 1.19 m deep and 2.13 m tall and has a volume of 2800 L. The door to the closet is 0.61 m wide and made from 1/2" (13mm) drywall which fails and opens during an explosion event.

Figure 4.17: Image showing the size, position and appearance of the closet in the shipping container.

A number of systems support the closet experiments. An Omega PX-309 pressure

transducer is installed in the north wall of the structure to measure the pressure-time history inside the closet. Pressure data is recorded at 1000 Hz using a MC Measurement Computing USB-204 12-Bit, 500 kS/s USB DAQ device. Temperatures are recorded at 5 hz with a Graphtec DAQ system. The closet has 11 thermocouples inside of it to measure gas temperatures at various points within the closet. Thermocouples trees are created by attaching thermocouples to cables which are anchored to the floor and ceiling. Additional thermocouples are attached to the battery cell. The two thermocouple trees and the positions of each thermocouple are shown in Figure 4.18.

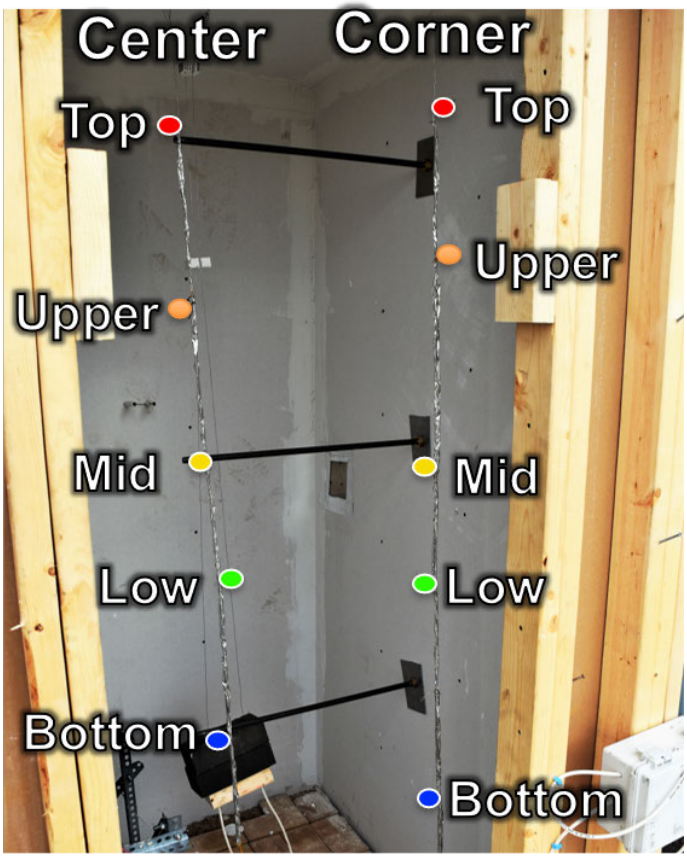

Figure 4.18: Closet thermocouples are hung off a wire near the center and a wire offset from a corner.

Two igniter systems use high voltage transformers to produce an arc to cause ignition inside the closet. One igniter system uses fixed electrodes from an oil-burning heater. The other igniter uses a Jacob's ladder which is hanging from the ceiling. The Jacob's ladder consists of two wires which hang close to each other. The wires support a brick which ensures that they are under a constant amount of tension. The wires vary in distance from each other. The high voltage from the igniter transformer is applied to the wires. An arc forms at the location where the wires are closest together. This arc causes heating in the air immediately above it, which then

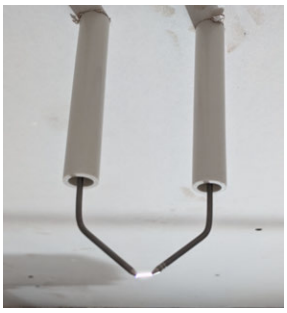

(a) Spark Igniter

(b) Jacob's Ladder Igniter

Figure 4.19: Closet igniter system uses both a fixed gap spark igniter and a Jacob's ladder igniter

weakens its dielectric strength. Since the dielectric strength is now less in the air above, the arc moves upwards. This allows for an arc to begin at a set location and then move upwards a foot (0.3 m) or so depending on the arrangement of the wires. This ignition setup makes it possible to provide ignition sources at multiple locations along a line using a single device.

Multiple cameras are used to monitor and record the experiment. Four security cameras provide live views on the inside and outside of the structure. In addition, two GoPro cameras placed in windows in the walls of the closet are used to record the explosion at 120 fps. Since the experiment is contained in a closed closet, lighting is also provided by a light on the floor of the closet and another pointing in through one of the camera windows. Figure 4.20 shows some of the systems installed in the closet.

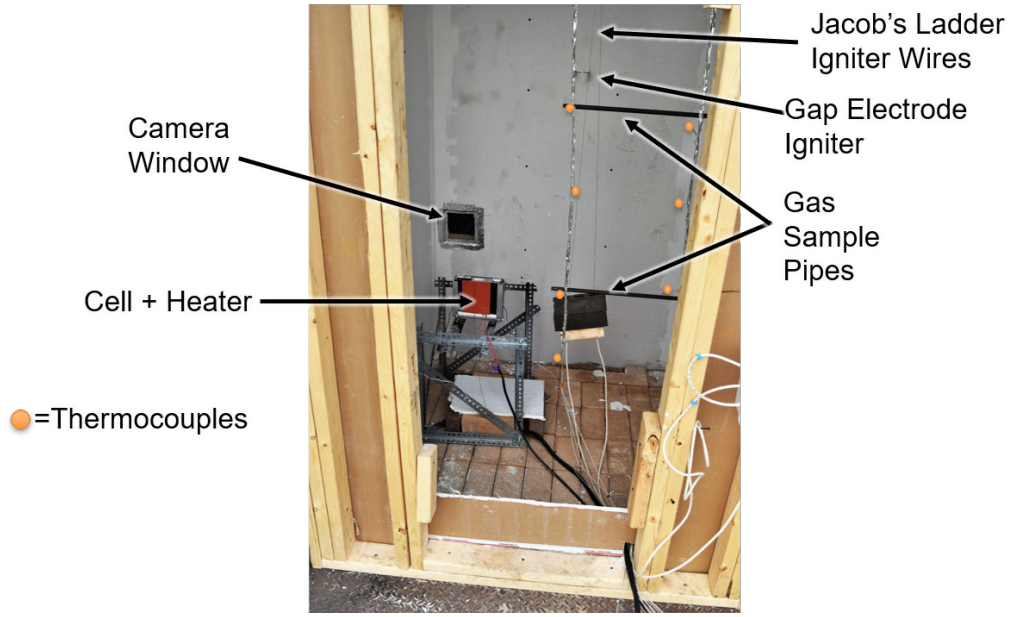

Figure 4.20: Equipment inside of closet experiment includes thermocouples, gas sampling pipes, cameras and igniter systems

The control of systems is performed using the custom-developed control box described in section 4.2.3. For this experiment, the control box controls 2 lights, 2 igniters, the cell heater as well as 4 pumps and 6 solenoids used for the NDIR gas measurement and gas bag sample systems. The control box is accessed remotely using a web browser and Wi-Fi during the experiment.

Gas composition in the compartment is measured using continuously running NDIR (Non-Dispersive Infrared) and electrochemical gas sensors as described in Section 4.2.2.3. The NDIR sensors are used to measure carbon dioxide and hydrocarbon volume fractions as a function of time at various fixed locations in the compartment. The electrochemical sensor is used to measure oxygen volume fraction as a function of time at those same locations. The NDIR and electrochemical sensors are useful for getting an approximate composition and seeing how it varies over space and time.

4.3 Experiment Results

4.3.1 Steel Cube Experiment Results

In total, five experiments were done in the small steel explosion box. These experiments were useful in understanding the nature of the explosion process. They were also useful in testing the gas bag sampling system, the NDIR gas measurement system, the ignition system and the control system. These experiments were also important in gaining experience preparing and running an explosion experiment.

This section describes in detail the results of one of these experiments. In this experiment a clamping setup with heater is placed to fail pouch cells. This setup is the same as the setup used in Section 2.3.0.1 with the five 5 Ah pouch cells placed inside. The setup consists of a heater, calcium silicate insulation and aluminum blocks used to clamp the five cells as shown in Figure 4.21. In an attempt to block immediate ignition, the setup is surrounded in steel mesh.

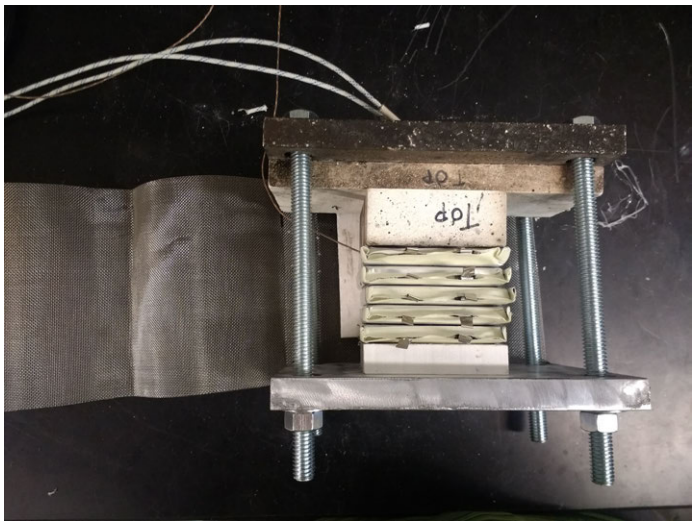

Figure 4.21: Aluminum blocks clamping calcium silicate insulation and 5 pouch cells

In the experiment, the heater is turned on and heats the first pouch cell until it is turned off manually when the first cell goes into thermal runaway. Figure 4.22 shows the sequence of images captured as the cell goes into thermal runaway and causes a gas explosion in the box. In the first image, the first cell can be seen venting a grey cloud. Less than 100 ms after the beginning of venting, the cell begins to eject hot particles. The steel mesh was not effective in blocking these particles. Less than 100 ms after the ejection of hot material, the hot material ignites released gases. From this point the flame propagates until eventually the flame travels throughout the entire cube, creating an overpressure sufficient to open the lid on the top of the cube. This entire process occurred in less than 1 second from the beginning of thermal runaway intense venting.

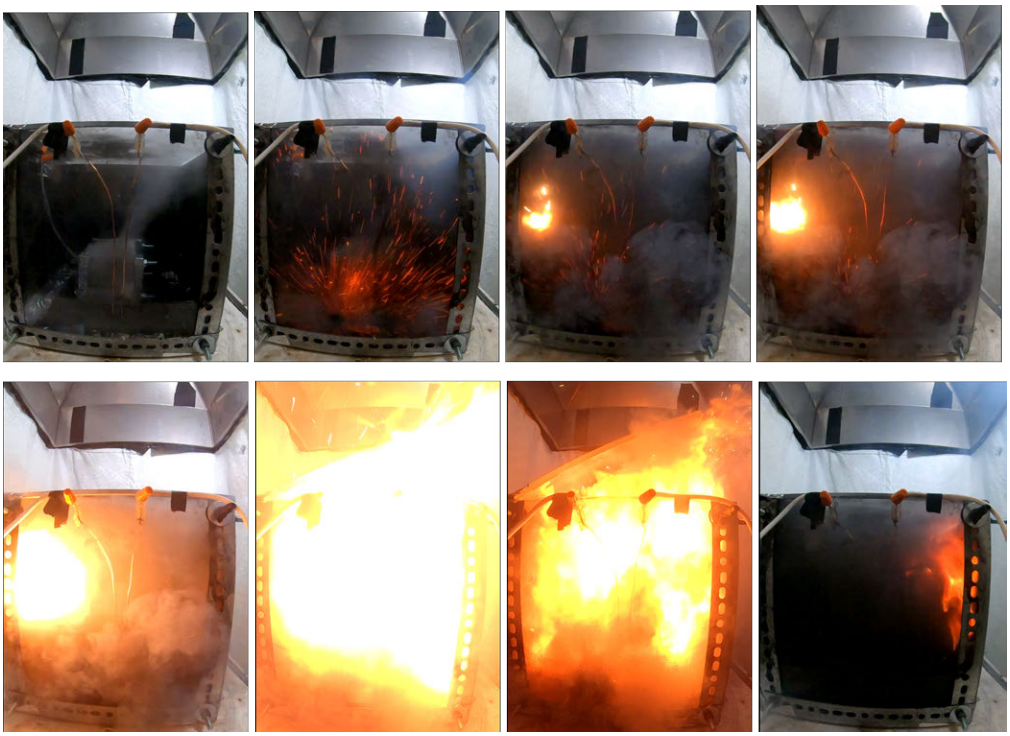

Figure 4.22: Sequence of images from first second after thermal runaway

A graph of the temperatures from the experiment and images at key times in the experiment are shown in Figures 4.23 and 4.24. As the first cell vents and causes the gas in the cube to burn, the heat propagates into the next cell causing it to go into thermal runaway. The runaway of the second cell did not trigger an explosion. An igniter was manually activated 18 seconds after the first runaway. In this case the ignition didn't cause a deflagration inside the cube sufficient to open the lid, but instead ignited a diffusion flame on the top of the cube. This diffusion flame was extinguished manually with nitrogen gas at about 65 seconds. At 156 seconds a lighter was used to try to attempt to light the vapors coming out of the top of the cube, to check if the mixture was still flammable. The mixture was still fuel-rich, and once again a diffusion flame burned on the top surface of the cube. This shows that at this point the mixture inside still had enough fuel to be flammable but not enough air to burn inside the cube. This diffusion flame was extinguished using nitrogen again at 175 seconds. At 206 seconds a lighter was used for ignition again and this time the mixture inside the cube had enough fuel and oxygen for a flame to propagate inside the cube. A slow flame crawled through the cube but did not burn fast enough to cause the lid to open like it did for the first explosion.

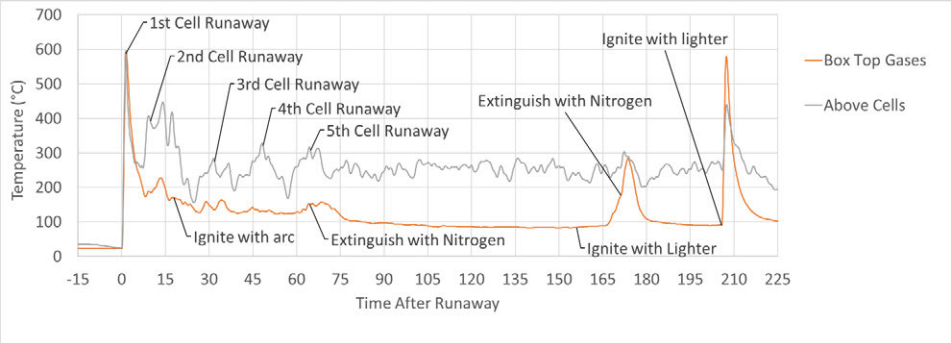

Figure 4.23: Temperature of gas in cube just above cells and near the top of the box.

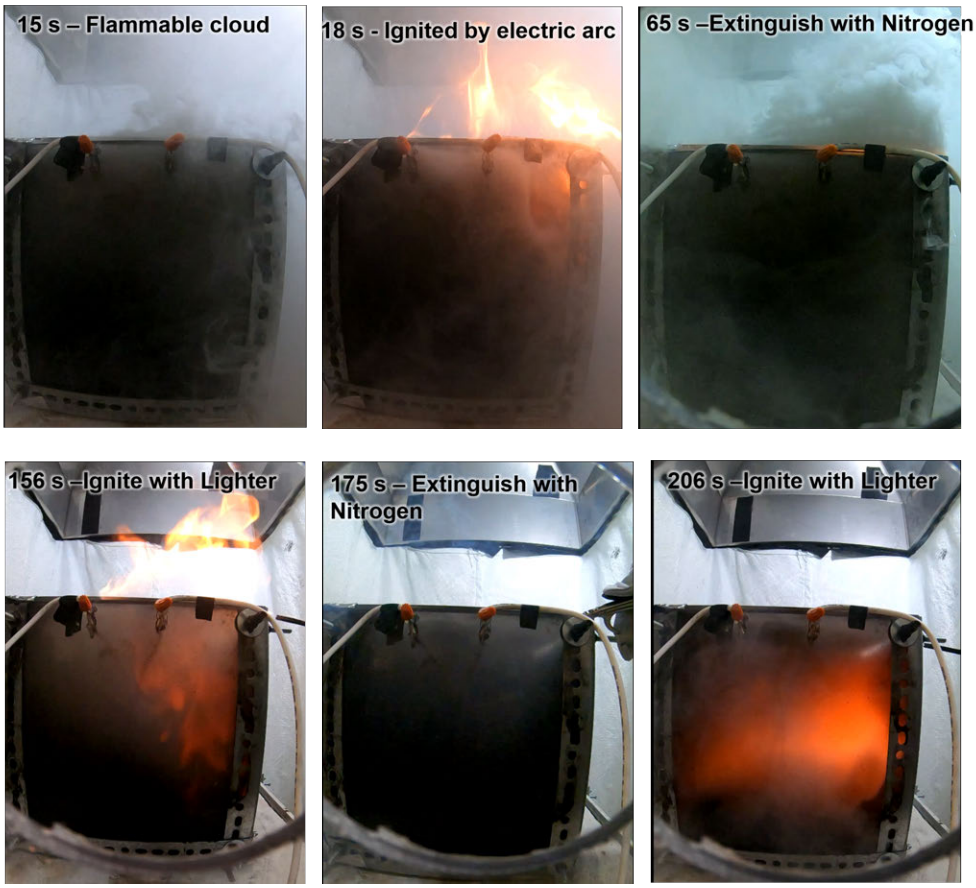

Figure 4.24: Sequence of images for events after explosion

This experiment demonstrates the complexity of the lithium-ion battery fire and explosion hazard. The batteries provide both a flammable gas source and an ignition source. However, in this case the ignition source was not observed to be reliable. This could be because the later cells failed differently than the first cell. It could also be because parts of the cube may have become oxygen deficient. It is also possible the the steel mesh intended to prevent ignition became more effective as it became clogged with particles. The cells did each vent flammable gas with about the same time delay between cells as observed in the 5 Ah array experiments in Section 2.

It is useful to keep track of the flammability of the gases in the compartment. Initially as the first cell goes into thermal runaway there was a localized region of flammable gas that was mixed appropriately with air to produce an explosion. The explosion consumed some of the fuel and produced a large volume of inert products. Shortly after the second cell releases gas, the activation of the igniter and the resulting diffusion flame is evidence that the gas mixture still contains fuel but is oxygen deficient except near the top where it has mixed with air. The later part of the experiment with repeated extinction and re-ignition demonstrates that even after minutes and repeated extinguishment with inert gas, the mixture has enough fuel to propagate a flame when mixed with air. The final ignition event that causes a slow flame to burn throughout the container is evidence that there is still enough fuel to burn and that it has finally been mixed with enough air to burn throughout the entire container. The slow propagation of this flame is evidence that at this point the mixture is suboptimal and results in a lower flame speed.

4.3.2 Cardboard Experiment Results

Eleven explosion experiments were conducted using a cardboard box setup. The cardboard box was also used for explosion demonstrations to educate firefighters in Hawaii and Arizona of battery system explosion hazards. These experiments allowed us to further test the gas bag sampling, NDIR and ignition systems and also gave us a chance to scale up to larger cells.

These experiments were conducted using 18.5 Ah LCO cells. Prior to these experiments, an array of five such cells was tested in the pressure vessel. The pressure

vessel experiment was used to measure the quantity and species of gases produced. The runaway of five 18.5Ah cells produced 118.2 L of gas, which is 23.6 L per cell or 0.35 L/Wh of energy storage. The composition of the gases is listed in Table 4.1:

Component	**Volume Percentage**
Hydrogen	26.8
Carbon Dioxide	31.9
Carbon Monoxide	23.9
Methane	4.8
Ethylene	7.1
Propane or Propylene	2.4
Ethane	1.3
Other	1.8

Table 4.1: Species Volume Percentage for gases released by 18.5 Ah LCO cell

Models for flammability and flame speed that will be described in Chapter 5 were run. This gas composition has a lower flammability limit (LFL) of 10% and an upper flammability limit (UFL) of 48%. Python scripts were used to run models to generate ternary plots of flammability and laminar flame speed as shown in Figures 4.25 and 4.26. In these figures the title identifies the person who analyzed the gas composition along with the date, chemistry and state of charge. This gas composition was measured in-house using cells from the same shipment as those used in these experiments. The ternary plots consist of three gas mixtures: fuel, air and inert. In this case the fuel is the gases released by the battery (which includes carbon dioxide). The inert gas mixture used is the products of this gas when burned in air at an equivalence ratio of 1. This was used because in instances without an inert gas suppression system, the mixture may become outside of flammability limits due to the mixture of burned products with the fuel and air mixture. These burned products may be produced in an initial diffusion flame or premixed flame. This construction

allows users of the ternary plot to follow the process of fuel being added through runaway, inert products being added through burning and air leaking in from the outside.

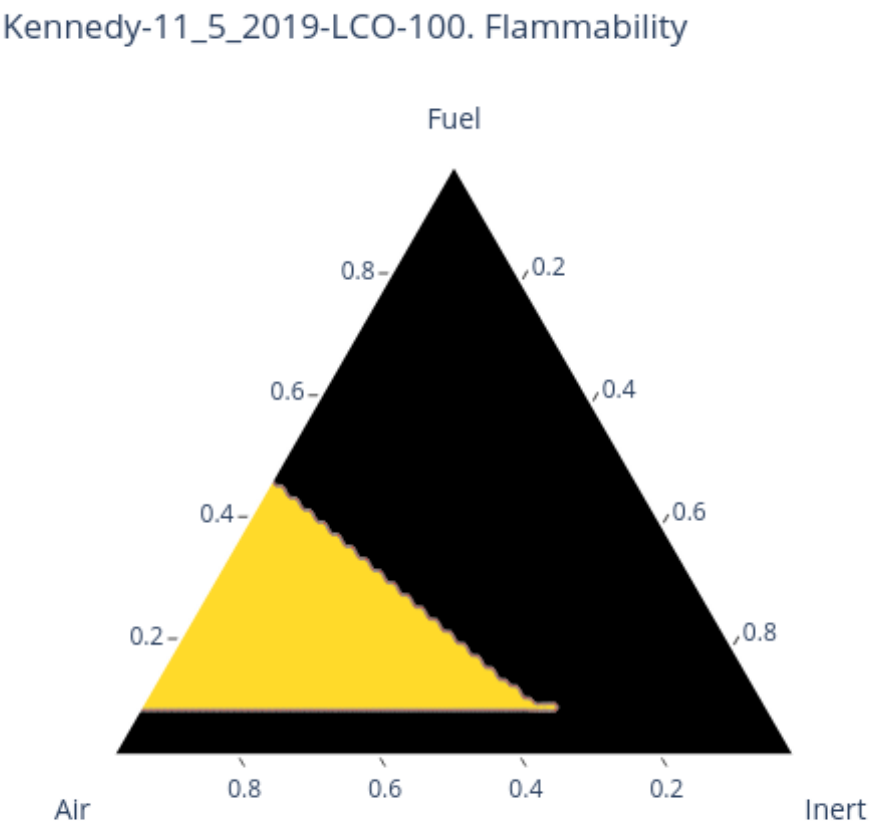

Figure 4.25: Ternary plot for Flammability of Battery Gas, Air and Burned Products Mixture

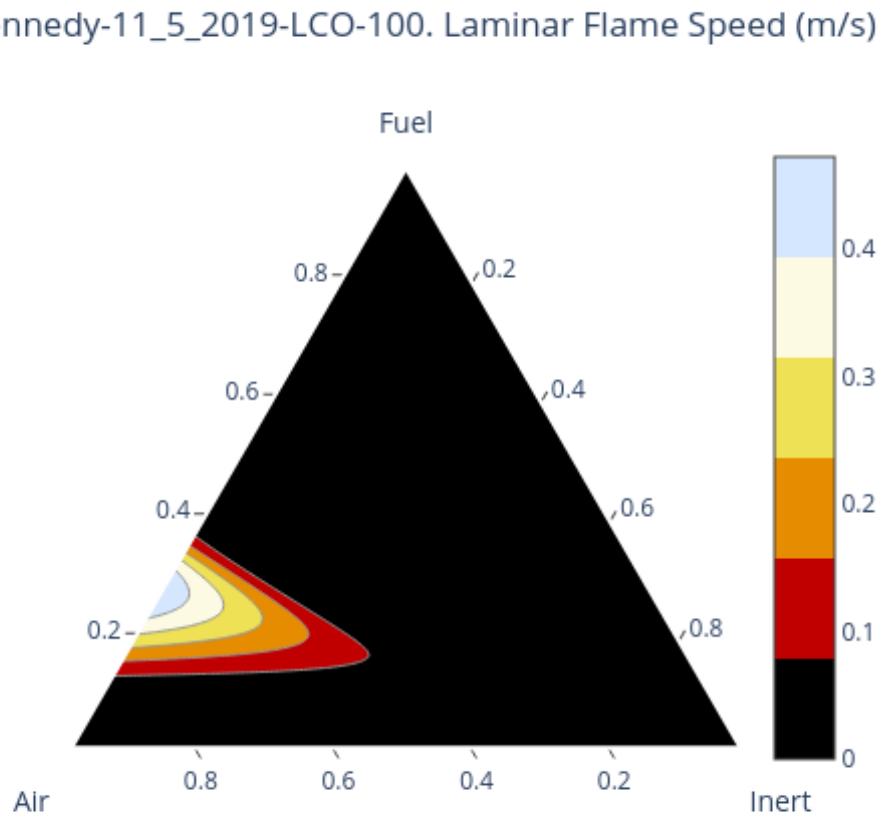

Figure 4.26: Ternary plot for Laminar Flame Speed of Battery Gas, Air and Burned Products Mixture

Many different experiments were carried out in the cardboard box setup. Some of the experiments used two 18.5 Ah cells while others used only one. For experiments that used two 18.5 Ah cells, thermal runaway did not spontaneously cause ignition. Instead an igniter would be triggered manually shortly after the gas release. However, the igniter was not successful at igniting the mixture at this time because the mixture was too rich. For these experiments, ignition would not occur until about 7 to 10

minutes after intense venting due to thermal runaway. At this point, enough air would mix in to allow an explosion to occur. The data for one such experiment is shown in Figure 4.27. In this experiment, intense venting due to thermal runaway occurs at 13:45 and causes increases in CH_4 and CO_2 concentrations immediately afterwards. As discussed in Section 4.2.2.4, the O_2 and CO_2 accurately represent the gas concentrations in the experiment. However, the CH_4 measurement is sensitive to a broad array of hydrocarbons and as such a reading of 80 % CH_4 is not indicative of exactly this much methane, but instead is correlated with increased amounts of battery gas hydrocarbons. After intense venting due to thermal runaway, the mixture is too rich and activation of the arc igniter will not cause a deflagration. After several minutes of leakage and mixing, ignition is possible as fuel concentration declines and oxygen concentration increases. In this experiment, ignition is triggered with an arc igniter at 13:53. At this time in Figure 4.27, oxygen and hydrocarbons rapidly drop as they are consumed while carbon dioxide is produced.

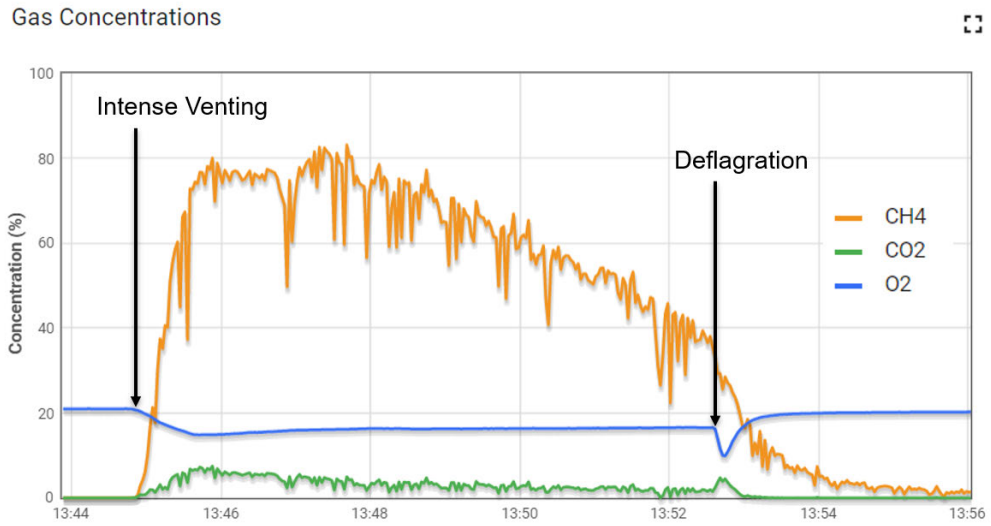

Figure 4.27: O_2, CO_2 and CH_4 sensor readings for inside box during experiment. Intense venting due to thermal runaway occurs at 13:45 and the deflagration is triggered by the igniter at 13:53

In experiments with a single cell, the amount of fuel released was more closely balanced with the amount of air inside the box. In these experiments activating the igniter shortly after runaway would cause a deflagration. A plot of gas data for one of these experiments is shown in Figure 4.28 and a sequence of photos showing the deflagration at 11:23:46 is provided in Figure 4.29.

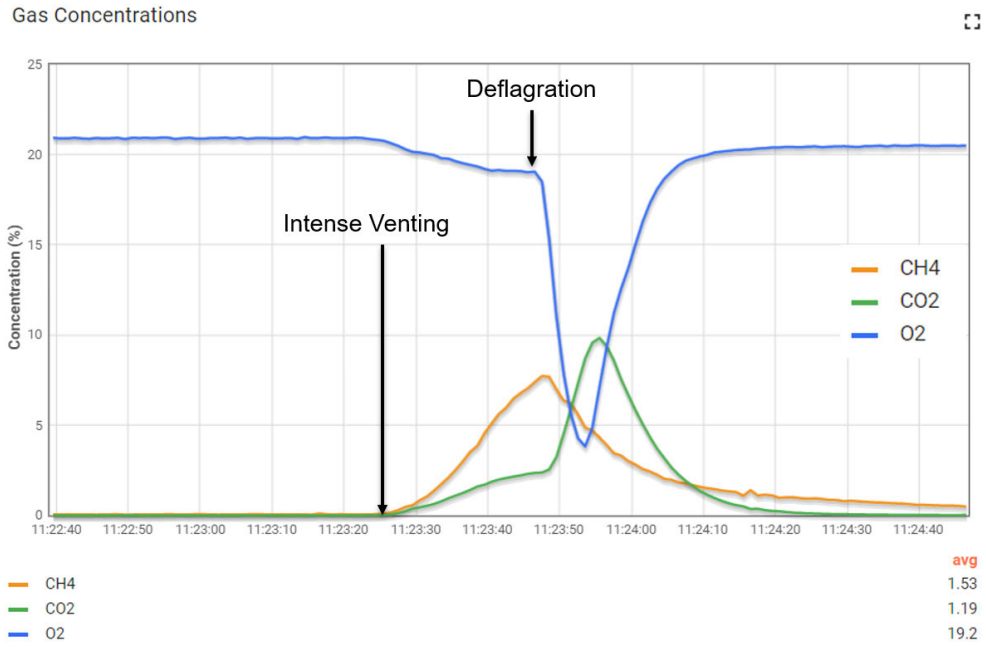

Figure 4.28: O_2, CO_2 and CH_4 sensor readings for inside box during experiment. Intense venting due to thermal runaway occurs at 11:23:25 and a deflagration is triggered by the igniter at 11:23:46

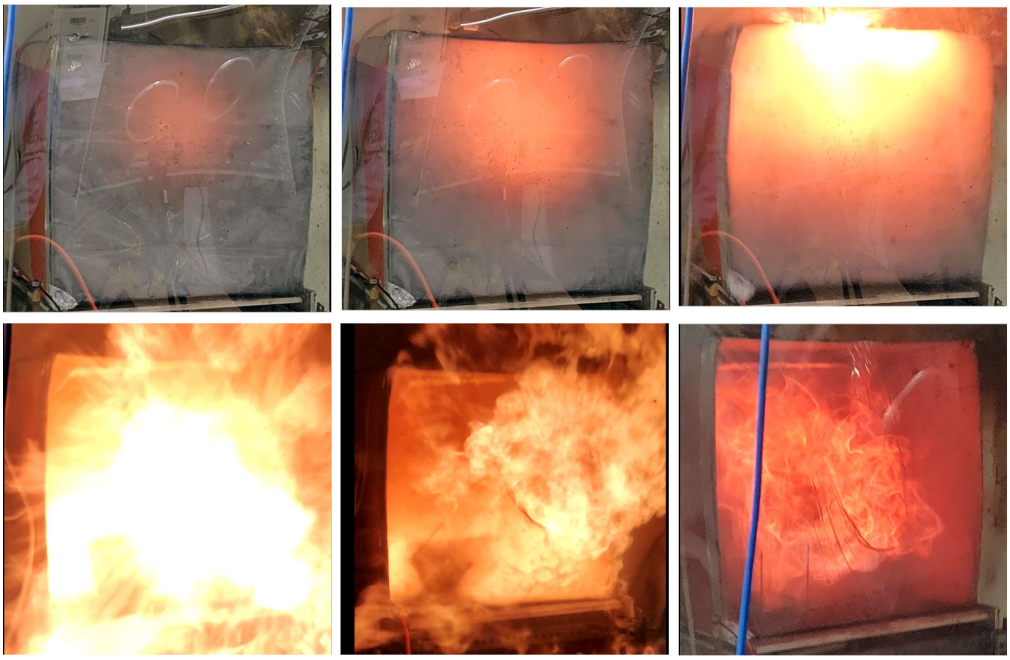

Figure 4.29: Cardboard Box Explosion Sequence in Laboratory

In this series of experiments we made a lot of observations about how different conditions affect outcomes. When multiple cells are used, enough gas is produced to cause the environment to be too rich to burn. This was observed on multiple experiments where activating the igniter soon after runaway did not trigger an explosion. In these experiments an explosion would occur when the igniter was activated after waiting several minutes until there was a sufficient quantity of air in the mixture. We also observed that the intensity of the explosion can widely vary. This is caused by the fact that mixtures with either too much or too little air and fuel have a much lower flame speed. These experiments also provided us with observations of the influence of venting conditions. If the integrity of the cardboard box or shower curtain is compromised before an explosion, then the severity of the explosion is greatly reduced and the outcome is a much less intense fire ball or in some cases just a fire. This

observation shows how deflagration vents that fail easily at a low pressure prevent the buildup of significant pressures inside. Another observation is that the instances that led to fires were ones in which air was more freely allowed to enter the box before ignition.

These experiments were very useful to better understand the conditions leading to explosions. These experiments were also instrumental in providing opportunities to test and improve control and gas measurement systems. Finally, the experiments were also beneficial in helping firefighters better understand the hazards posed by lithium-ion batteries. Figure 4.30 shows an outdoor demonstration of a cardboard box explosion.

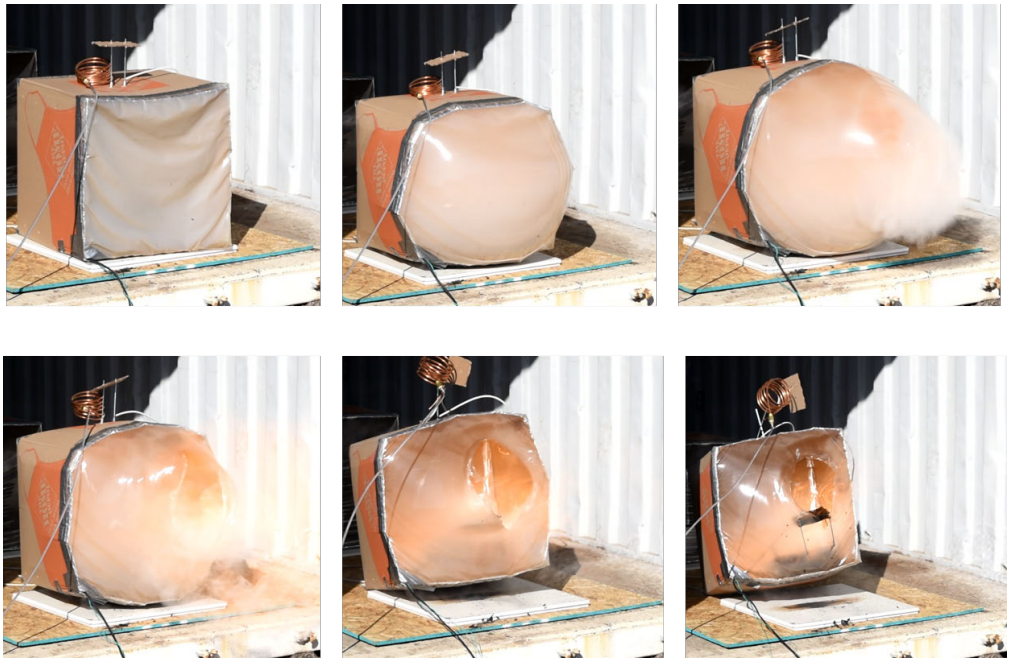

Figure 4.30: Cardboard Box Explosion Sequence Outdoor Demonstration

4.3.3 Closet Experiment Results

Two explosion experiments were conducted in the closet. In each experiment a single 94 Ah cell was put into thermal runaway using a heater. These experiments used the same 94 Ah cell described in section 3.3.2. The original intent of these experiments was to study the mixing of gases before the explosion event and then subsequently ignite the gas with an electric arc igniter. However in both cases an explosion occurred only a few seconds after the beginning of the gas release. This occurred because of the large amount of hot solid material being ejected by the cell. Even in the second experiment where insulation and steel mesh were placed to block hot material, this was not sufficient to prevent the ignition of the gases. Figure 4.31 shows the runaway and explosion inside the closet for the first experiment. In the first closet experiment, the cell first began to release a cloud of vapor and then after about 2 seconds began to release hot particles. After another 2 seconds, the particles ignite a flammable cloud which expands and eventually results in an overpressure which fails the drywall door panel.

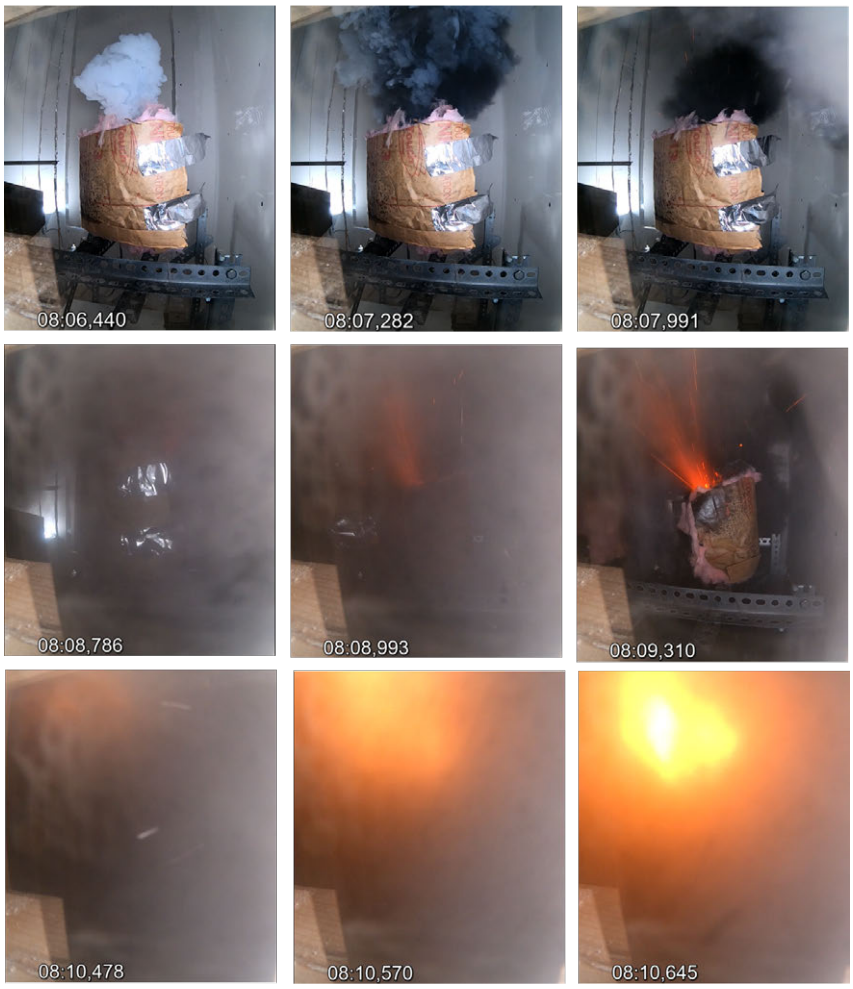

Figure 4.31: Sequence of video images shows the interior of the closet during the first explosion experiment. At 8:06.443 the first visible cloud of white material is ejected. The cloud rapidly turns black and begins to limit visibility in the closet. Hot material is ejected at 8:09 and causes ignition of flammable gases by 8:10.478.

Figure 4.32 shows the thermal runaway intense venting and subsequent explosion for the second experiment. In this experiment the cell was covered in ceramic fiber insulation and steel mesh in an attempt to prevent the ignition of gases. Despite the attempts to prevent ignition, the gases were ignited causing an explosion and failing the door drywall panel.

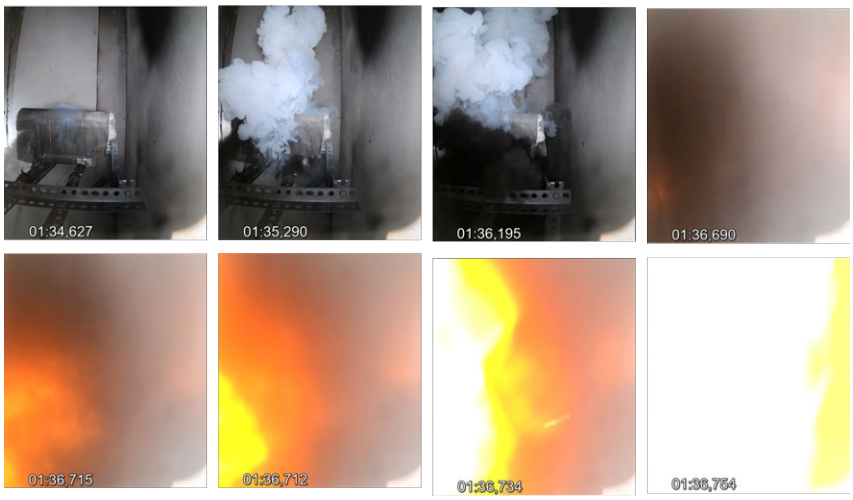

Figure 4.32: Sequence of video images showing the interior of the closet during the second explosion experiment with a single 94Ah cell.

Gas temperatures were recorded in the compartment for both experiments and are shown in 4.33. In both graphs, the x axis is offset such that time 0 is the time at which cell temperatures begin rapid rise due to thermal runaway self-heating. In the first closet experiment, top and upper gas temperatures in the center of the compartment begin to rise immediately after cell temperature begins rapid rise. This occurs because the vent was unobstructed in the first experiment and the intense venting of the cell was able to push hot flammable gases to the top of the compartment before the explosion. The dramatic temperature increase at about 2 seconds is due to the deflagration within the compartment. In this experiment, the highest temperatures are observed at the top and upper thermocouples. This is consistent with the video which shows burning initiating towards the top of the closet.

In the second closet experiment shown in Figure 4.33b, there is no thermocouple re-

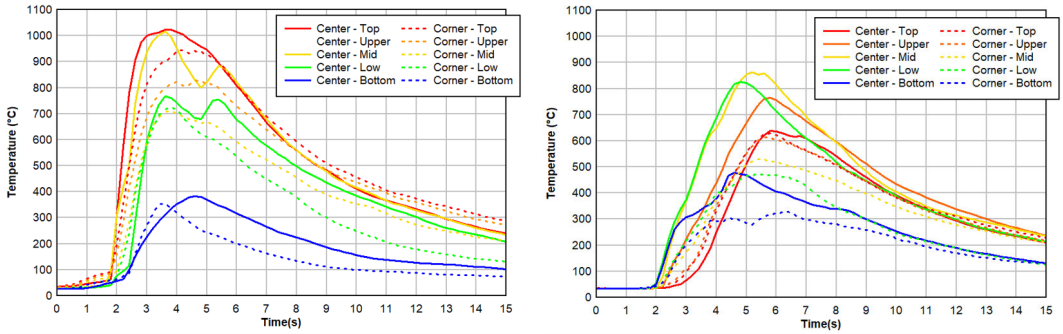

(a) First Closet Experiment (b) Second Closet Experiment

Figure 4.33: Gas temperatures in closet

sponse until after the deflagration at about 2 seconds. This likely occurred because in this experiment the vent is covered in multiple layers of mineral wool insulation and steel mesh which serves to reduce the jet velocity and cause the hot gases to diffuse more quickly. This effect is evident in the gas temperatures after the explosion. When the explosion occurs, peak temperatures are seen at the mid and lower layers. This suggests that much of the flammable gases involved in the deflagration were located closer to the mid and lower thermocouples in the compartment. This can also be seen in Figure 4.32 where the visible flames are much lower than they are in Figure 4.31 for the first experiment.

In both tests, small explosions were observed and sufficient overpressure was developed inside of the closet to fail the drywall door panel. Figure 4.34 contains a series of images taken during the second test showing the exterior of the closet during and immediately after the explosion.

Figure 4.34: Sequence of photographs showing an explosion and fire after a single 94 Ah cell fails within the closet. The mannequin was used to visualize the safety hazards to firefighters working in the vicinity.

For the second experiment, pressure time history data was recorded at 1000 hz, this data is shown in Figure 4.35. The pressure peaked at 1.2 kPa (0.17 psi). The duration of the pressure rise is approximately 200 ms. Integrating the pressure over time, the impulse is 140 kPa-ms (20.4 psi-ms). It is expected that this pressure time history is a function of both the fuel involved and the time and pressure at which the door failed and relieved the pressure.

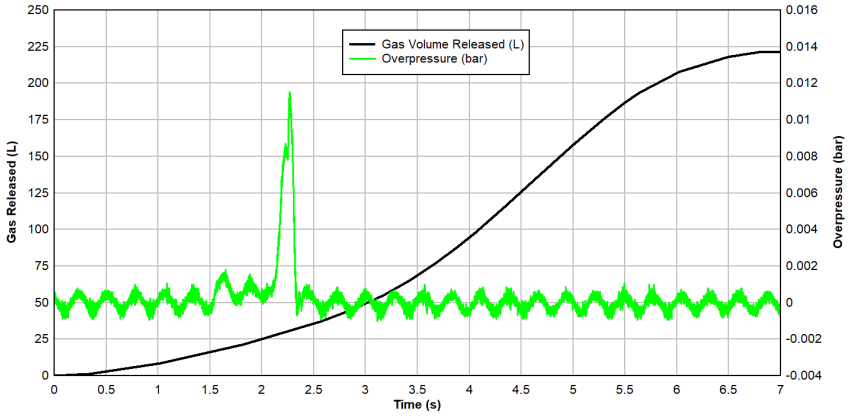

Figure 4.35: Pressure Time history inside closet for second experiment

Figure 3.3.1 also overlays the gas release time history obtained from the pressure vessel experiment in Section 3.3.2. In the second experiment, the hot particles ignite the hot gases and cause the pressure rise only 2 seconds after the onset of venting. Based on the release rate time history, this means that the explosion happened after the battery had released less than 50 L of the 221 L expected to be released. This volume of gas is less than 2% of the room volume. This value is well below the 9% required to reach LFL in a well mixed room. However, this deflagration was able to occur because it there was a localized region with a gas mixture within the flammability limits. This type of event is called a partial volume deflagration. Even though this gas mixture was much smaller than the room, it still produced an overpressure sufficient to break the drywall door off of the compartment. Although partial volume deflagration hazards are known in the literature [55], many people are either unaware of the hazard, or assume that partial volume deflagrations are unlikely or not significantly damaging. This experiment is evidence that partial volume deflagrations are quite possible for battery systems and can be very damaging even when the gas release is not sufficient to reach LFL in a well-mixed room.

4.4 Conclusions

In this chapter, systems were developed to perform lithium-ion battery gas explosion experiments. In particular, a low cost gas sensor system was developed to measure oxygen, carbon dioxide and hydrocarbons at multiple locations in real-time during an experiment. This system is useful to be able to estimate how much of a mixture is fuel, air and inert during an experiment. A gas collection system was developed to collect gas samples for later analysis. High voltage arc igniter systems including both fixed electrodes and a Jacob's ladder were employed to ignite gases.

A number of different explosion scenarios were observed experimentally. Both pouch cells and prismatic cells were observed to eject hot solid particles capable of igniting a deflagration. Pouch cells were capable of causing ignition, but do not reliably cause ignition. In contrast, even when covered in insulation and steel mesh, the prismatic cell was able to ignite a deflagration. It appears as though the ejection of hot particles occurs at a specific time during the intense venting process and for ignition to occur, the area surrounding the vent must have a flammable mixture. Explosions were observed immediately after cell venting due to the battery ejecting hot material which ignited the gases. Explosions were also observed shortly after cell venting when the cell failed to ignite the gases and the igniter system was used. In situations with too much fuel, ignition was not possible until air had mixed in and diluted the fuel. It was observed that even after a compartment has had an explosion, it may contain enough fuel to cause further deflagrations. Finally, partial volume deflagrations were observed. In the closet experiment, a damaging explosion was observed when the volume of gas released was less than 2% of the volume of the closet. This demonstrates the hazard that partial volume deflagrations are with

lithium-ion battery systems even when the volume of fuel is very small compared to the volume of the compartment.

Chapter 5

Explosion Hazard Models

In Chapter 2 and Chapter 3 the thermal runaway propagation process was characterized for simple 1-D arrays of pouch cells as well as a more complex commercially available module. Once the time of thermal runaway for each cell is determined, a gas release time history can be developed. This information combined with gas species and compartment properties can be put into models to determine if an explosion can occur and what the consequences may be. This chapter focuses on developing a set of models which can be used to evaluate the explosion hazard.

This work is a continuation of the work described in in *Explosion hazards from lithium-ion battery vent gas* which was published in the Journal of Power Sources in January 2020 [56]. This chapter covers many of the models in the original paper as well as some which are not included. This chapter uses the vent gas composition database developed in the original paper and builds upon it by adding more recent entries from literature. Finally, this chapter goes beyond the original paper, and describes a sensitivity analysis on the explosion model using ranges of possible values

from the vent gas composition literature review.

5.1 Explosion Hazard

Before looking into how to model the explosion hazard from lithium-ion battery systems, it is important to first consider what factors lead to explosions. Like any fire or explosion, a lithium-ion involved explosion requires an appropriate mixture of fuel and oxidizer as well as an ignition source. The fuel source provided by lithium-ion batteries is the flammable gas mixture ejected by the cell during thermal runaway. Fuel release for a thermal runaway event continues as long as cells are going into thermal runaway and venting flammable gases. Depending on the design of the system, this may continue until cells are sufficiently separated to avoid runaway propagation or until all the cells have gone into runaway and vented. Although lithium-ion batteries can produce a small amount of oxygen during thermal runaway, the majority of the oxygen used in an explosion comes from the air.

The ignition source for a lithium-ion battery explosion could be hot particles which are ejected from the battery such as those seen in Figure 4.31. Since these systems are always energized, electrical arcing is another possible ignition source as seen in Figure 3.8. Finally, explosions may be ignited by a smaller pilot flame that may already be burning.

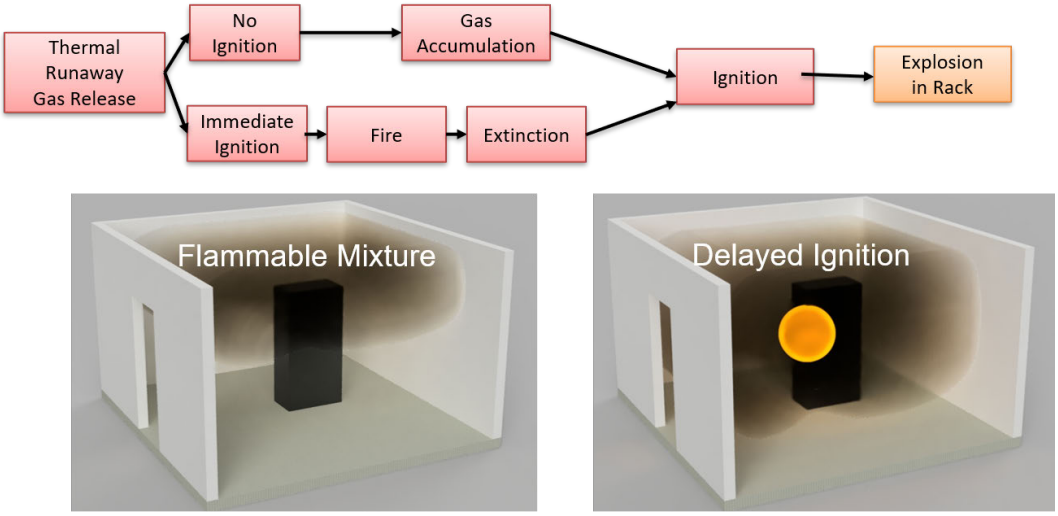

Figure 5.1: Sequence of events leading to a lithium-ion battery explosions

Figure 5.1 shows two sequences of events that can lead to an explosion. For every lithium-ion battery involved explosion, the first requirement is for a lithium-ion cell to go into thermal runaway. The thermal runaway process will release heat, flammable gases and sometimes hot material that can provide an ignition source. If the cell is large enough and the containing compartment is small enough, a single cell may be capable of causing an explosion. For typical cells in typical rooms, multiple cells must go into thermal runaway for a damaging explosion to occur. To make this possible, thermal runaway must progress from cell to cell as heat is transferred as shown in Chapters 2 and 3.

After flammable gases have been released, it is possible that they do not ignite. This could be due to a lack of ignition sources, oxygen deficient atmosphere, fire suppression systems or high velocity gases that cannot propagate a flame. Without adequate ventilation, these gases may accumulate. If later an ignition source

is provided, it can cause an explosion. Depending on the volume of gas released and the geometry of the enclosures, this could cause an explosion either inside the module, inside the rack or within the entire compartment. In some cases flammable gases may even accumulate and cause an explosion outside the battery compartment.

Another sequence of events that can lead to an explosion occurs when there is an ignition and an initial fire. While a flame is present, it is unlikely that enough gas can accumulate to cause an explosion. However, this initial fire may be extinguished due to fire suppression or oxygen deficiency. Once the fire is extinguished, remaining gases may still be capable of forming an explosive mixture. Once these gases are mixed with a sufficient quantity of air and are provided an ignition source they may cause an explosion.

These two pathways to an explosion may also be represented as a fault tree as shown in Figure 5.2 or an event tree as shown in Figure 5.3. The benefit of the fault tree is that it shows the events which lead up to an explosion and can be used to calculate the probability of an explosion. The fault tree is useful to see the relationships between events leading to an explosion[57]. The and and or gate structure of the fault tree makes it clear what events need to happen to produce an explosion. The nature of the fault tree also makes it more natural to consider what events may cause ignition or lead to the formation of a flammable mixture. The event tree is useful to see the sequence of events which can lead to an explosion [57]. An advantage of the event tree is that it allows the user to follow each event to other possible consequences such as fire and toxicity hazards.

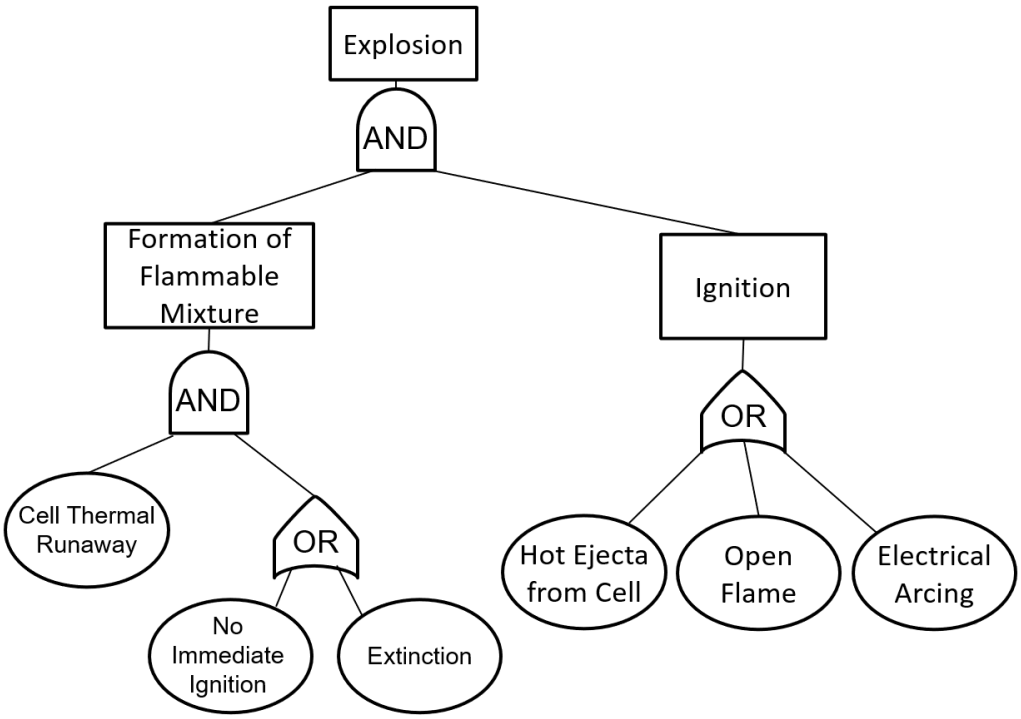

Figure 5.2: Fault tree showing factors leading to lithium-ion battery explosions

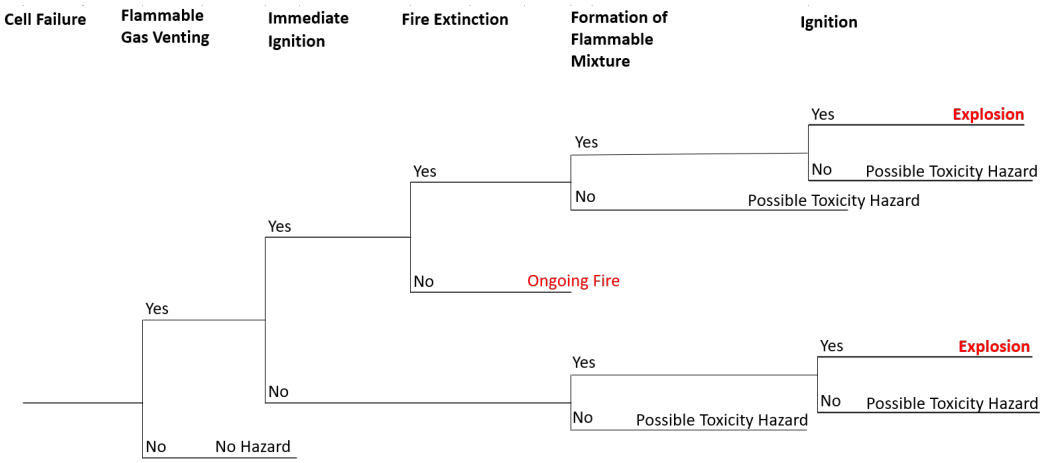

Figure 5.3: Event tree showing factors leading to lithium-ion battery explosions

When an explosion occurs, it presents a variety of different hazards to building occu-

pants, outside personnel and especially firefighters who have been called to respond to the fire. Historical events demonstrate the severity of the hazard to firefighters. In April 2013, ten firefighters were killed in an explosion when they were attempting to extinguish a fire at an ammonium nitrate storage facility in West, Texas. Firefighters are especially at risk with explosions since they are often the only people nearby as they carry out fire suppression activities. This can be a problem with battery incidents as these may first present as a fire or toxicity hazard with no obvious connection to batteries and then may result in an explosion later on.

There are several different hazards due to explosions. The rapidly expanding flame of the explosion can burn anyone in its path and even people farther away with thermal radiation. The rapidly expanding flame generates an overpressure inside of a compartment. This overpressure can cause a blast wave to propagate outside of the compartment as well. The increased pressure may cause hearing damage. The pressure over time creates an impulse which can act on people and debris and throw them large distances. The overpressure can also fail building components and injure people with missiles or fragments of building materials. Finally, the overpressure may cause a structural collapse which can injure occupants.

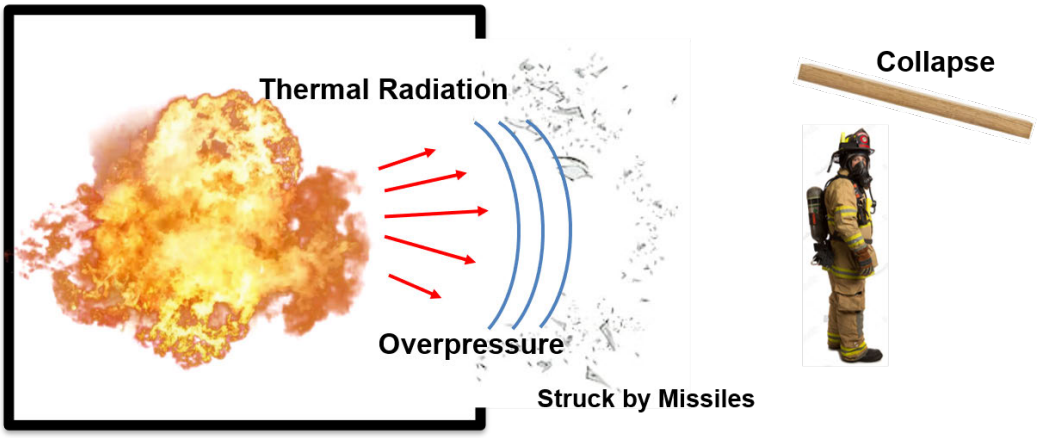

Figure 5.4: Firefighter hazards during an explosion.

5.2 Gas Composition

The first step to understanding the hazard is to characterize what flammable gases are produced by thermal runaway. Many experiments have been performed to measure the species of vent gas from lithium-ion cells in thermal runaway. In our paper [56] we reviewed all the data on vent gas compositions for lithium-ion cells in thermal runaway up until 2019. In this section, more recently available studies are added along with additional measurements which have been performed more recently by the University of Texas Fire Research Group. Figure 5.5 shows all the species composition from the originally reviewed literature by volume fraction.

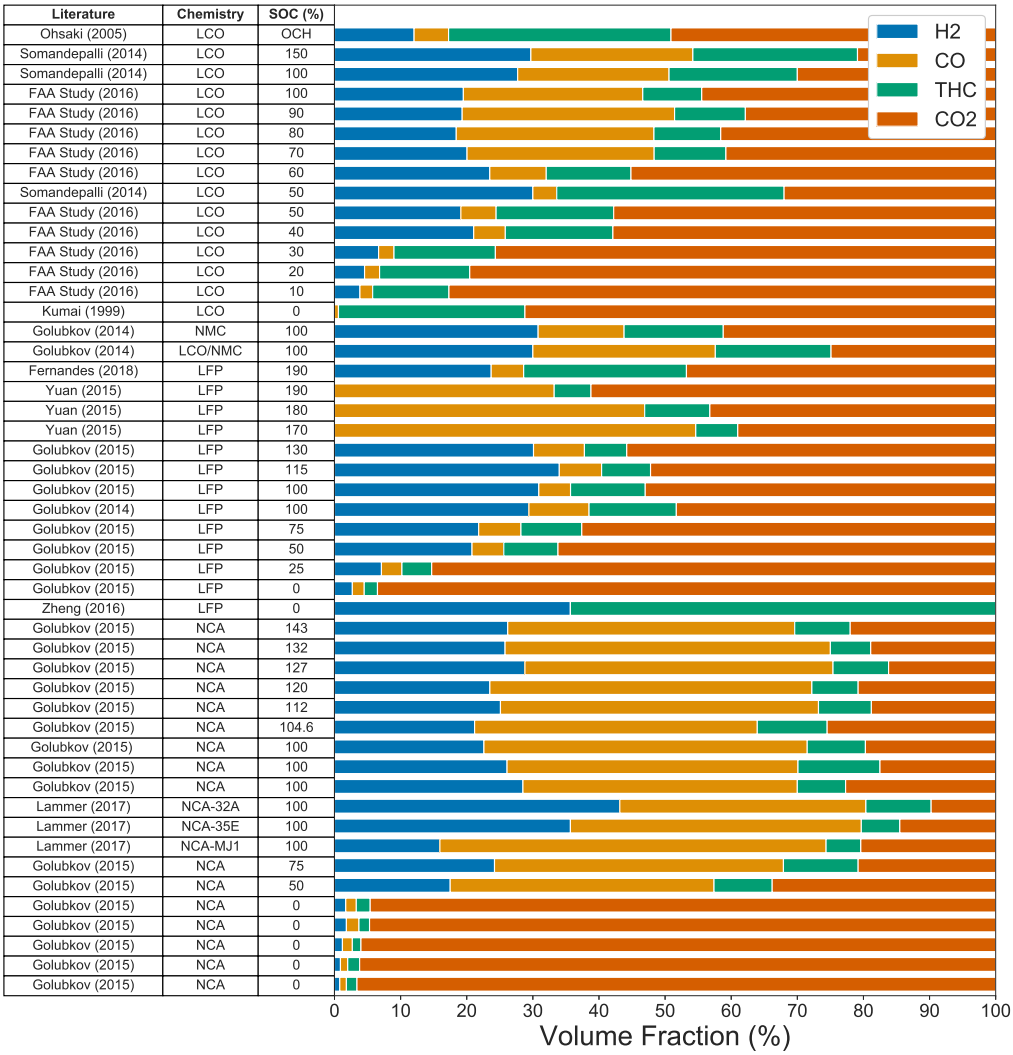

Figure 5.5: Battery Vent Gas Species Compositions from Literature [8]

Somandepalli et al. [58] failed a lithium cobalt-oxide (LCO) pouch cell in an argon filled test chamber and used gas chromatography to determine composition. Golubkov et al. [59, 60] performs similar tests for different cell chemistries at different states of charge (SOC) using 18650 cylindrical cells. The 2016 FAA study by Maloney et al. [61] was done at 10 psia in an inert environment. They test LCO cells at

various SOC. One problem with this data is that the sum of the gas compositions does not add up to 100 % and this changes with SOC. Lammer et al. [62] conducted experiments with 18650 cells from different manufacturers which provided different results.

In the literature, some of the experiments fail cells by overcharging. The first of which was Kumai et al. [63] in 1999, where an 18650 was overcharged and overdischarged until failure. In 2005, Ohaski et al. [64] failed a prismatic LCO cell using overcharging at 1 C until failure. Gas compositions were determined with gas chromatography. In 2015 Yuan et al. [65] failed overcharged prismatic LFP cells. They reported between 5% to 18% air, which we normalized out in Figure 5.5. In 2016, Zheng et al. [66] failed over-discharged LFP pouch cells and provided the gas composition. In 2018 Fernandes et al. [67] overcharge cylindrical LFP cells. Kennedy et al. provides gas compositions for both single lithium cobalt oxide (LCO) pouch cells as well as arrays [40]. Essl et al. compares NMC cell failures for pouch cells and prismatic cells when failed by heating, overcharging and nail penetration. They find that the initiating event causes variation in both the quantity and species of gas produced [1, 68]. In many areas of the United States, energy storage systems must be tested according to UL 9540A. This testing requires the characterization of gas composition for cells failing in thermal runaway. Most of these experiments are confidential, however Viswanathan and Paiss provide UL 9540 A data for LFP and NMC cells from an unspecified manufacturer [2].

In addition to the literature values, gas composition was also measured as part of this work. In Section 3.2.3 the species, volume and release rate was measured for a

prismatic 94 Ah cell which is used in both ESS and EVs. In Appendix 7 species and volume were measured for an LFP module consisting of cylindrical cells.

Although none of the studies produce nearly identical results, it can be seen that for cells that are charged to more than 50 % SOC, both thermally failed and overcharged lithium-ion cells produce mostly hydrogen, carbon monoxide, carbon dioxide and an assortment of hydrocarbons. When burned these gases pose a fire hazard, when unburned and released into a confined space, these mixtures pose an explosion hazard.

5.3 Models

Once the gas composition is known, models can be used to provide information about explosion hazards. The purpose of this effort is to create a set of simple models that when used together can be used to estimate if an explosion is possible and what worst-case explosion consequences could be. There are several sub-models which when used together make this possible. Figure 5.6 shows the relationships between the inputs and outputs of each model.

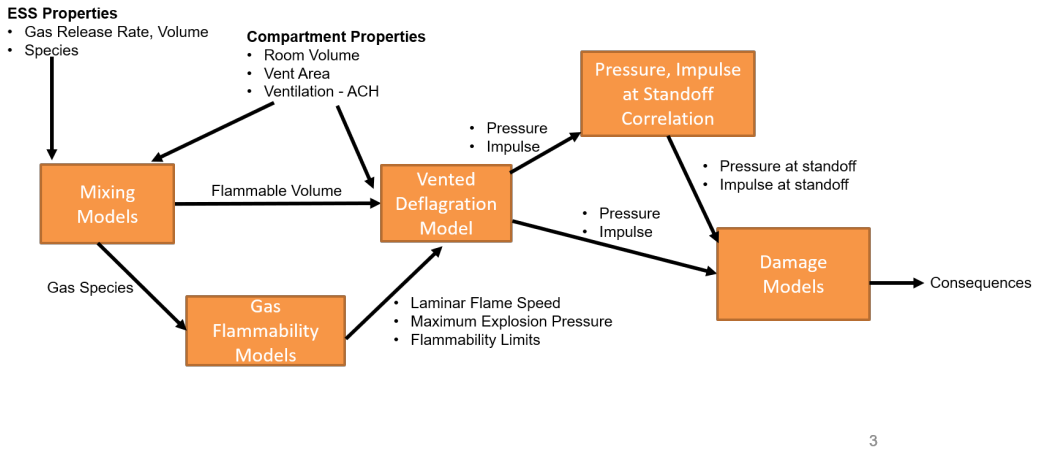

Figure 5.6: A combination of several simple models makes it possible to estimate possible explosion consequences based on compartment properties and ESS properties

The inputs for the entire set of models consist of ESS properties and compartment properties. For ESS properties, the inputs are the gas release rate, volume and duration along with the gas species. Compartment properties include the compartment dimensions, deflagration vent areas, deflagration vent failure pressure and the ventilation rate which will be expressed in ACH (air changes per hour).

5.3.1 Gas Mixing Models

A number of models can be implemented to calculate possible mixture conditions for explosion scenarios. A CFD model of flammable battery gas mixing with air in a closet is shown in Figure 5.7. The domain for this model is 1.12 m wide, 1.19 m deep and 2.13 m tall and uses a grid of 1 cm, 2 cm and 4 cm. The smaller grid sizes are used within the turbulent plume region. The mass release is 2.6 kg of battery vent gas released in 8 seconds. The gas released is the 100 % SOC NMC

composition described in Table 3.1 released at 700 °C from an orifice of 4 cm x 8 cm. A 1.12m long and 0.08 cm tall crack has an open condition to ambient pressure to represent a crack under a door. The distribution of gases in the compartment varies over time. Early on, gases within the flammability limits exist only in a small jet immediately above the battery. Since these gases are hot and directed upward, they start to form a layer at the top of the compartment which then folds down into the compartment. Since the velocity of the release jet is quite high and the volume of the room is small, enough mixing occurs such that towards the end of the simulation there is a more homogeneous mixture of gas in the flammable range throughout the entire compartment. In the last image, although the gas release has stopped, the concentrations begin to slowly change as air leaks in the bottom of the door and into the compartment. This mechanism makes it possible that even if there wasn't an explosion initially and the compartment is too rich, later on air can be introduced to produce a flammable mixture.

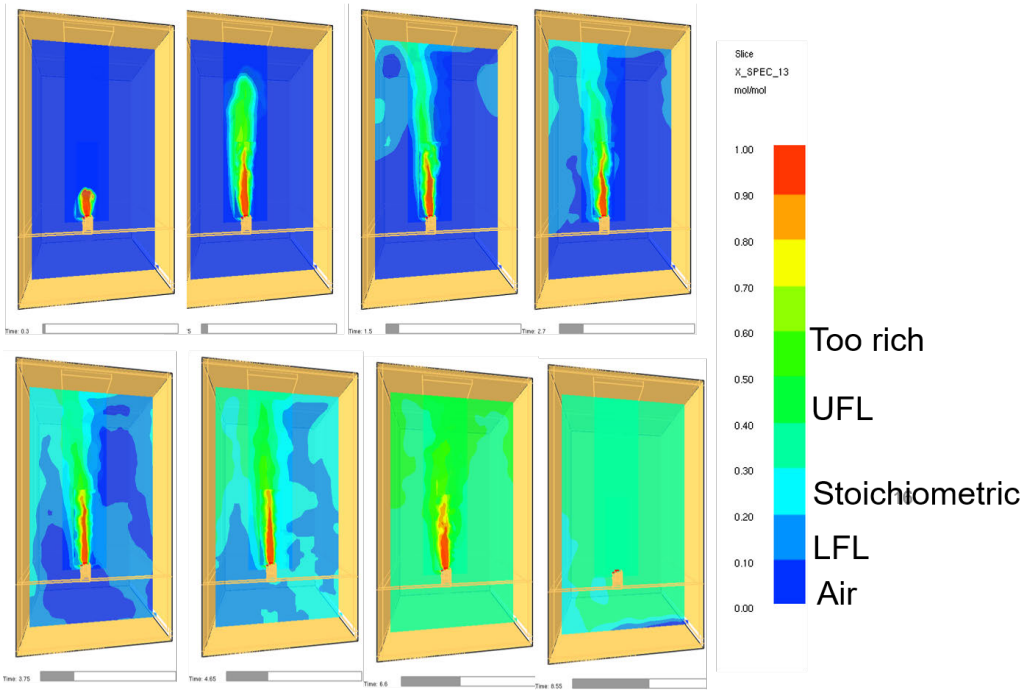

Figure 5.7: CFD Model results for battery vent gas concentration for thermal runaway gas release in a closet

For the purposes of many explosion analyses, the use of CFD models may be too detailed for the application. In accidental explosions there are often numerous ways in which gas can be released, mixed and ignited to cause a deflagration. The intent of explosion hazard analysis is to identify what conditions can cause an explosion and what the worst-case consequences might be. To accomplish this there are a number of simple models that can be used to approximate possible conditions leading to an explosion and worst-case mixtures leading to worst-case explosions.

Figure 5.8 represents three idealized mixing models. In the premixed or well-mixed case it is assumed that the gases are well mixed such that the same concentration of fuel exists throughout the entire compartment. The partial volume deflagration

case assumes that the fuel released forms a sphere or layer which is a homogenous stoichiometric flammable mixture. The partially premixed model assumes that there is a gaussian distribution of concentrations in which not all of the released flammable gas lies within the flammable region.

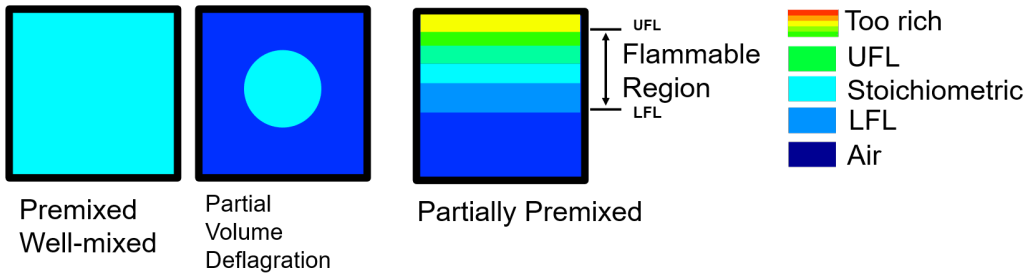

Figure 5.8: Idealized mixing models include assuming that the entire mixture is homogenous, assuming that a partial volume of flammable mixture exists and assuming that the mixture is partially premixed.

5.3.1.1 Perfectly Mixed Model

The perfectly mixed model is useful for developing an estimate of the worst case explosion consequences when a large amount of gas is released. As seen late in time in the closet mixing model (Figure 5.7), conditions can become well mixed when there has been sufficient velocity driving the mixing and enough time has elapsed to allow this to occur. The motion of gas due to thermal runaway or forced ventilation systems may cause a well-mixed condition. If the compartment is well-mixed then the concentration (X) at any point equals the average concentration (X_{ave}) of the compartment which can be calculated by dividing the volume of fuel (V_f) by the volume of the compartment ($V_{compartment}$), $X_{ave} = V_{fuel}/V_{compartment}$. For such a uniform concentration, an explosion can only occur when $X_{ave} \geq X_{LFL}$

. The worst case explosion will occur when the average concentration is such that

the laminar burning velocity is a maximum. When the well-mixed assumption is appropriate this mixture condition is used for NFPA 69 analysis to prevent a deflagration by ensuring that the average concentration is less than 25% of LFL[69]

5.3.1.2 Partial Volume Deflagration Model

In some cases not enough gas is released to form a well-mixed flammable mixture throughout the entire compartment. However, even though the average concentration in the compartment may be less than LFL, it is still possible for a damaging explosion to occur. In this case explosions may occur when a localized region of gas forms a flammable mixture. This partial volume may be considered to be either a volume of gas surrounding the release location, trapped gas in a rack or a layer of gas accumulated at the top or bottom of the compartment. Partial volume mixing is used by Ogle to determine the minimum concentration of gas to cause a damaging explosion [70].

To evaluate the hazards associated with partial volume deflagrations, it is assumed that there is some limited volume of perfectly mixed flammable mixture and the remainder of the compartment is filled with air. In this case the average concentration remains $X_{ave} = V_{fuel}/V_{compartment}$ while for the flammable volume the concentration is generally assumed to be mixed to a stoichiometric volume fraction (X_{st}) or the volume fraction associated with the highest adiabatic explosion pressure (P_{max}). This model is described in detail by Ogle [70]. In this model the minimum volume of fuel capable of causing a damaging explosion with a pressure exceeding (P_{dam}) can be found using the stoichiometric volume fraction (X_{st}) and the maximum pressure (P_{max}) as shown by Zalosh in the SFPE Handbook chapter on gas explosions [71].

$$X_{ave} = \frac{V_f}{V_{compartment}} = X_{st}\frac{P_{dam} - P_0}{P_{max} - P_0} \tag{5.1}$$

5.3.1.3 Partially Premixed Model

In reality, many explosions are caused by non-homogenous mixtures with concentrations at different locations ranging anywhere from nearly 100 % air to 100 % fuel. One way to approximate these concentrations is by assuming that they are layered at the floor or ceiling according to a Gaussian profile. This Gaussian profile will have layers of varying concentrations ranging from $X_{fuel} = 0$ up to some maximum concentration $X_{fuel} = X_{max}$. In this idealization there exists a flammable region where $X_{LFL} \leq X \leq X_{UFL}$. The flammable volume is maximized where $X_{max} = X_{UFL}$ This model is described in detail by Jo and Park [72]. One challenge associated with implementing this model is the determination of the parameter that describes the Gaussian distribution.

5.3.2 Gas Flammability Characteristics Models

The explosion potential of a gas mixture is a function of a number of flammability properties of the mixture. Gas flammability properties depend on the mixture of flammable gases as well as their mixture with air. Mixtures which have too little air or too much air cannot cause an explosion. The amount of air mixed with the battery vent gas can be quantified with the equivalence ratio (ϕ). The battery gases coming off the cell consist of mostly hydrogen, carbon monoxide, carbon dioxide and various hydrocarbon gases. This mixture can be specified using volume fractions.

There are a number of important flammability characteristics. The first of which are the lower and upper flammability limits. The flammability limits define the maximum and minimum concentrations of fuel that will propagate a flame when mixed with air. The flammability limits are used to determine if a given fuel and air mixture can produce a deflagration. If a deflagration can occur, the overpressure generated inside a constant volume is defined thermodynamically by the maximum pressure. This is an important input to explosion overpressure models. In practice, almost all confined explosions become vented through either existing openings, the activation of deflagration vents or the failure of building components. Overpressure generation in a vented structure depends primarily upon the burning velocity of the gases and the vent area through which pressure is relieved. There are a host of other gas properties required to predict the pressure generated in an explosion. Although overpressure calculations are not as sensitive to them, they have been computed and tabulated to facilitate the calculation of overpressures for a variety of experimentally measured battery vent gas mixtures.

5.3.2.1 Flammability Limits

The upper and lower flammability limits describe the maximum and minimum concentration of fuel that can propagate a flame. For this work, it will be assumed that battery vent gas mixture is mixed with air at a temperature of 300 K and an absolute pressure of 101.325 kPa. Upper and lower flammability limits are typically measured experimentally using standard test methods such as those described in ASTM E681.

Unfortunately, battery gas mixture composition has significant variation and mea-

sured flammability limits are not published for most battery gas mixtures. Because of this, models will be used to estimate the flammability limits of these gas mixtures.

The most common approximation for flammability limits is Le Chatelier's mixing law [73], which is shown in Equation 5.2. This allows the calculation of LFL for a mixture (X_{L}) using the volume fraction (X_{i}) and LFL of each of the components ($X_{\mathrm{L_i}}$) of a mixture.

$$\frac{1}{XL} = \sum_{i=1}^{fuels} \frac{X_{\mathrm{i}}}{X_{\mathrm{L_i}}} \tag{5.2}$$

Another method to estimate flammability limits is the calculated adiabatic flame temperature method which has been described in various articles[74]. In this method the adiabatic flame temperature is calculated for a mixture. The calculated flame temperature is then compared against a critical temperature to determine if the mixture is flammable or not. Different sources have different estimates of the critical temperature for flammability with values ranging from 1000 K to 1600 K [75, 76, 74]. Instead of using a single value for critical adiabatic flame temperature, Bounaceur et al. describe a method to calculate LFL and UFL for gas mixtures by using different critical temperatures for each gas [77]. These critical temperatures can be found by calculating the adiabatic flame temperature for a gas when it is mixed such that it is at LFL.

The first step to accomplish this is to calculate the threshold adiabatic flame temperature at which a flame will propagate. The threshold temperature for LFL depends on the gas involved. For example, hydrogen reaches LFL at a concentration of 4%, at which concentration the adiabatic flame temperature is 629 K. In contrast methane reaches LFL at a concentration of 5% and at this concentration the mixture has an

adiabatic flame temperature of 1480 K. The same process can be used to determine a critical adiabatic flame temperature associated with UFL [77]. Using published LFL and UFL values along with a software such as Cantera[78], it is possible to determine critical adiabatic flame temperatures for LFL and UFL for any gas that has published LFL and UFL volume fractions.

To find the critical temperature ($T_{L,blend}$) at which LFL occurs for a mixture of gases, a weighted average of critical temperature ($T_{L,i}$) and volume fraction (X_i) of each component can be used as shown in equation 5.3:

$$T_{L,Blend} = \sum_{i=1}^{N} T_{L,i} \cdot X_i \tag{5.3}$$

In this equation volume fraction of each component (X_i) is calculated based on all of the flammable gases and excludes any inert gases such as carbon dioxide which may be in the mixture. For this project critical temperatures were tabulated for hydrogen, carbon-monoxide, methane, propane, and ethane. Any other hydrocarbons are treated as propane. This assumption is used because most hydrocarbons will generally be similar to propane. It is acceptable to use this assumption as long as other hydrocarbons account for a relatively small concentration compared to the five known gases. This assumption is reasonable in the case of battery vent gas which is typically mostly hydrogen, carbon monoxide and carbon dioxide. This method is implemented for both lower and upper flammability limits. This method will not be validated here. Bounaceur et al. and Baird et al. provide validation for this method [77, 8].

5.3.2.2 Laminar Burning Velocity

The laminar burning velocity is an important property of gas mixtures when predicting deflagration hazards. The laminar burning velocity is the velocity at which a flame propagates through a premixed fuel and oxidizer mixture relative to the velocity of the unburned mixture. Laminar burning velocity is primarily dependent on the reactivity, diffusivity and exothermicity of the fuel and oxidizer mixture. Laminar burning velocity is generally increased by increasing temperature and decreased with increasing pressure. Since most explosions involving lithium-ion batteries generally happen at approximately atmospheric pressure and much of the reactants are air at ambient temperature, the effects of temperature and pressure will not be considered here. There is not a single accepted method for measuring laminar burning velocity, several have been used. Non-stationary methods measure the velocity of a flame front in a spherical bomb or a tube while stationary methods may use a burner [79].

Lithium-ion battery thermal runaway produces a mixture of gases for which burning velocity may not have been measured. In the absence of measured burning velocities, models can be used to estimate the burning velocity based on the properties of the gases which comprise the mixture. For this work, three different methods are utilized and compared against experimental data.

The first model used to estimate burning velocity uses Cantera which is an open-source software package for solving chemical kinetics and thermodynamics problems[78]. Cantera uses the GRI-Mech 3.0 database which contains 53 species and 325 reactions [80]. GRI-Mech has been used extensively for modeling problems involving natural gas. Several others have investigated the burning velocity of lithium-ion battery

vent gases using Cantera and GRI-Mech[8, 40, 81]. Others have used the GRI-Mech database to model flame speed of syngas flammable gas mixtures [82, 83].

In Cantera burning velocity is calculated using a 1D premixed flame model. In this model the mixture is defined by species mass fraction of the species (Y_i), pressure (P) and temperature (T) of the unburned mixture. For this work it is assumed that gases are at a temperature of 298 K and an absolute pressure of 101.325 kPa.

There are also correlation models which can be used to estimate burning velocity. Lapalme developed a correlation for burning velocity based on experimental data with gases mixtures of hydrogen, carbon monoxide, carbon dioxide and methane [10]. The Lapalme correlation equations are described as follows. The effect of CO_2 dilution and temperature is reflected in the correlation similar to that from Turns [84] as shown in equation 5.4.

$$S_u = SL_{ref} \cdot (1 - c \cdot X_{CO2}]) \cdot \left(\frac{T_i}{300}\right)^a \tag{5.4}$$

The maximum burning velocity ($S_{L,max}$) and the equivalence ratio at which this occurs (ϕ_m) are described in Equations 5.5 and 5.6.

$$SL_{max} = 2.1 \cdot exp(-5.9 \cdot X_{CH4}) \cdot (R - 0.5) + 1.4 \cdot exp(-3.97 \cdot X_{CH4}) + 0.4 \tag{5.5}$$

$$\phi_m = -0.905 \cdot exp(-13.4 \cdot X_{CH4}) \cdot (R - 0.5) + 1.05 \cdot exp(-7 \cdot X_{CH4}) + 1.07 \quad (5.6)$$

The correlation assumes that the base fuel is a mixture of hydrogen and carbon monoxide. The ratio of hydrogen to the total hydrogen and carbon monoxide (R) is calculated in equation 5.7:

$$R = \frac{X_{H2}}{X_{H2} + X_{CO}} \quad (5.7)$$

Other parameters are as follows:

$$a = (1.28 + 0.24 \cdot X_{CH4}) + 0.54 \cdot (\phi - (1.85 - 3.45 \cdot X_{CH4}))^2 \quad (5.8)$$

$$c = 0.028 \cdot exp((2.5 \cdot X_{CH4}^2 + 1) \cdot \phi + 0.5) + 1.23 \quad (5.9)$$

$$B = (-10.5 \cdot (X_{CH4} - 0.2)^2 + 1.5) \cdot R + 3.1 \cdot X_{CH4} + 0.035 \quad (5.10)$$

The correlation is good for mixtures where the base fuel is a mixture of hydrogen and carbon monoxide. For methane volume percentages less than 20% the correlation is good for equivalence ratios from 0.7 to 2.0.

Laminar Burning Velocity Validation Unfortunately there are very few published experiments in which the burning velocity of battery vent gases is measured. The only published study found measures the vent gas composition from an LFP

Source	Name	Max S_u	H_2	CO	CH_4	CO_2	C_2H_4	Data Points
Liu[11]	LFP	0.46	29.6	22.3	6.9	35.5	5.7	9
Lapalame[10]	H_2-CO	1.90	50.0	50.0	0.0	0.0	0.0	20
Zhou[9]	Basis	0.93	40.0	40.0	20.0	0.0	0.0	18
Zhou[9]	CH4-80	0.39	10.0	10.0	80.0	0.0	0.0	14
Zhou[9]	CO-60	1.00	26.7	60.0	13.3	0.0	0.0	20
Zhou[9]	CO-80	0.92	13.3	80.0	6.7	0.0	0.0	20
Zhou[9]	H2-60	1.27	60.0	26.7	13.3	0.0	0.0	20
Zhou[9]	H2-80	2.04	80.0	13.3	6.7	0.0	0.0	20
Lapalme[10]	S50C10	1.53	45.0	45.0	0.0	10.0	0.0	20
Lapalme[10]	S50C20	1.30	40.0	40.0	0.0	20.0	0.0	24
Lapalme[10]	S50C30	0.98	35.0	35.0	0.0	30.0	0.0	20
Lapalme[10]	S50C40	0.64	30.0	30.0	0.0	40.0	0.0	20
Lapalme[10]	S50M20	1.03	40.0	40.0	20.0	0.0	0.0	18
Lapalme[10]	S50M40	0.66	30.0	30.0	40.0	0.0	0.0	16
Lapalme[10]	S50M5	1.70	47.5	47.5	5.0	0.0	0.0	26

.0

Table 5.1: 14 gas compositions were used to validate burning velocity models

cell and then produces a custom mixture of gases to match the measured values. The flame speed of this gas mixture was then measured using a bunsen burner apparatus at equivalence ratios from 0.7 up to 1.5[11]. To supplement this data and expand the validation data set, models for laminar burning velocity can be validated using experiments with similar syngas mixtures which are available in the published literature. Like battery vent gas, these syngas mixtures consist of mostly H_2, CO, CO_2 and CH_4. Unlike these syngas mixtures, battery vent gas also consists of a variety of other hydrocarbons in small amounts. However, this validation set should be sufficient because it contains three most abundant species (H_2, CO, CO_2) and because flame speed is more sensitive to hydrogen variation [85].

Each of these mixtures had the burning velocity experimentally measured at be-

tween 9 and 26 different equivalence ratios. These experiments covered a range of equivalence ratios such that the peak laminar flame speed would be measured. The GRI-Mech based model in Cantera along with the Lapalme correlation were used to calculate the burning velocity for each mixture at each equivalence ratio. The Lapalme correlation was developed using the Lapalme data and so other data must be added in for better validation. Data from Liu and Zhou are included to show that the correlation works on other data. The results for the mixtures in the Zhou paper[9] are shown in Figure 5.9.

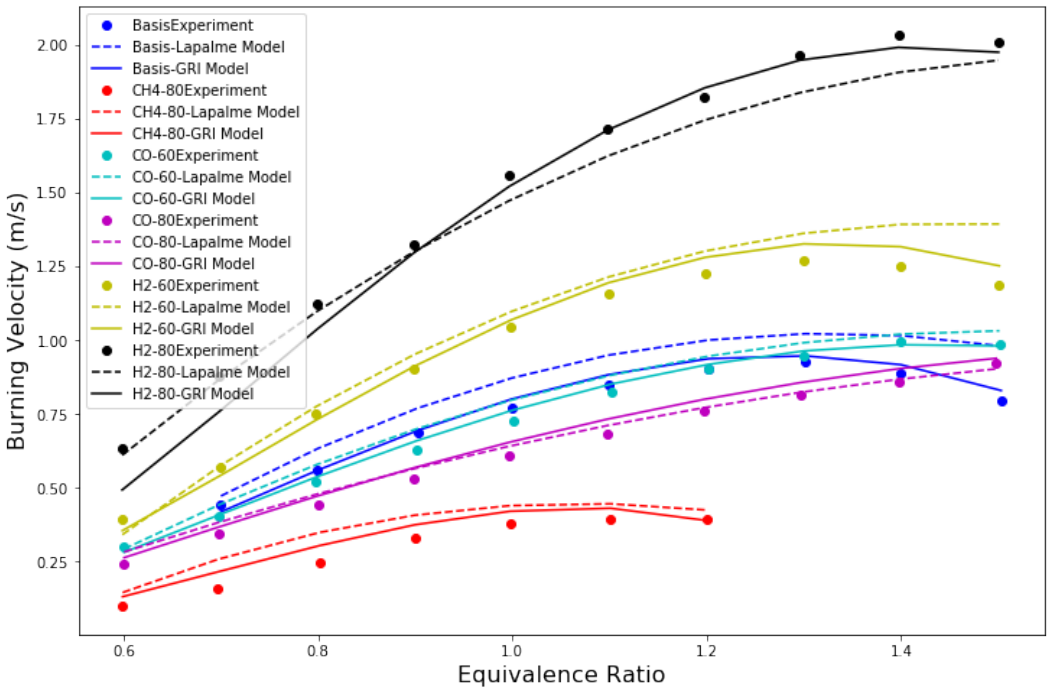

Figure 5.9: Comparison of Burning Velocity values for GRI-Mech model and Lapalme Model with experimental data from Zhou [9]

In total there were 14 different gas mixtures at various equivalence ratios used for validation. Using all of the different equivalence ratios, there are a total of 147

Model	Mean Percent Error	Percent Error Standard Deviation
Cantera/GRI	4.25%	10.57%
Lapalme Correlation	3.06%	8.77%

Table 5.2: Summary Statistics for Percent Error of Flame Speed Models

points that were used to compare measured burning velocities with those predicted by GRI-mech and the Lapalme model. The percentage error for these predictions was calculated and can be represented as a normal distribution. The mean and standard deviation of the percent error for the Cantera/GRI Mech model and the Lapalme correlation are presented in Table 5.2.

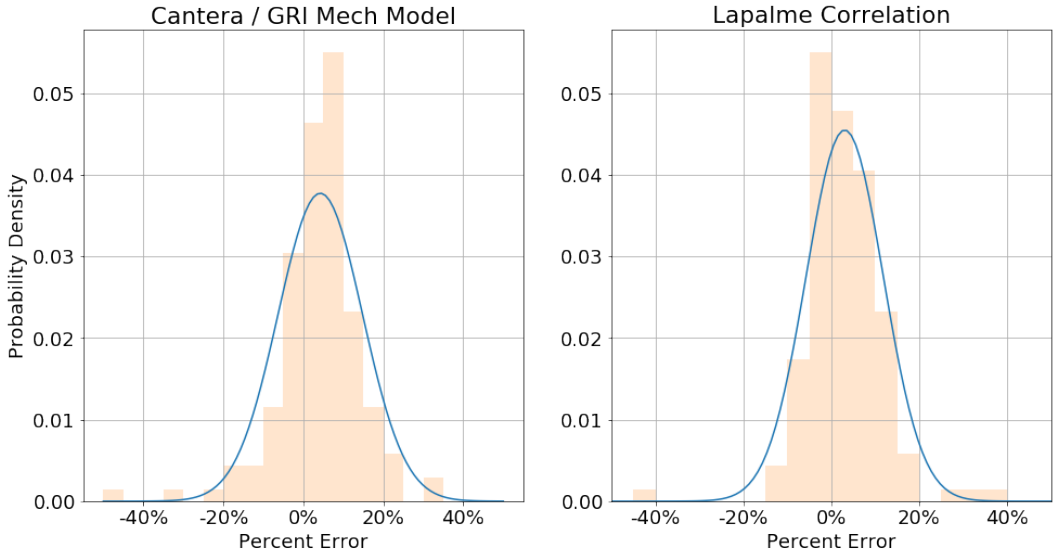

Figure 5.10: Distribution of Percent Error for 147 Burning Velocity predictions and 14 different fuel mixtures using GRI-Mech and the Lapalme model compared against experimental values from Lapalme [10], Zhou [9] and Liu[11]

5.3.2.3 Maximum Pressure

P_{max} is the pressure that is generated when the gas is combusted in a perfectly adiabatic, constant volume process. This pressure defines the maximum possible pressure that the gas could possibly generate. Cantera uses thermodynamic properties of the mixture to calculate P_{max}. P_{max} depends on the composition of gas produced.

Maximum Pressure Validation The adiabatic constant volume maximum pressure was calculated using Cantera to compare with experimental data. Experimental data comes from Somandapelli et al.[58] where they mixed battery vent gas with air at different equivalence ratios and measured the peak overpressure as well as the peak rate of pressure rise in a 20L spherical vessel. The Cantera model was used to analyze a variety of different fuel concentrations to evaluate the impact of different mixtures with air. Figure 5.11 shows our (UTFRG) predicted values for maximum pressure calculated using Cantera compared to experimental data. For lean concentrations where the fuel concentration is less than about 20%, the calculated maximum pressures are close to experimental values. However, for fuel rich concentrations, the pressure is much lower in the experiment. The calculated values are the maximum possible thermodynamic values, and the experimentally measured pressures should be lower because of incomplete combustion and heat losses.

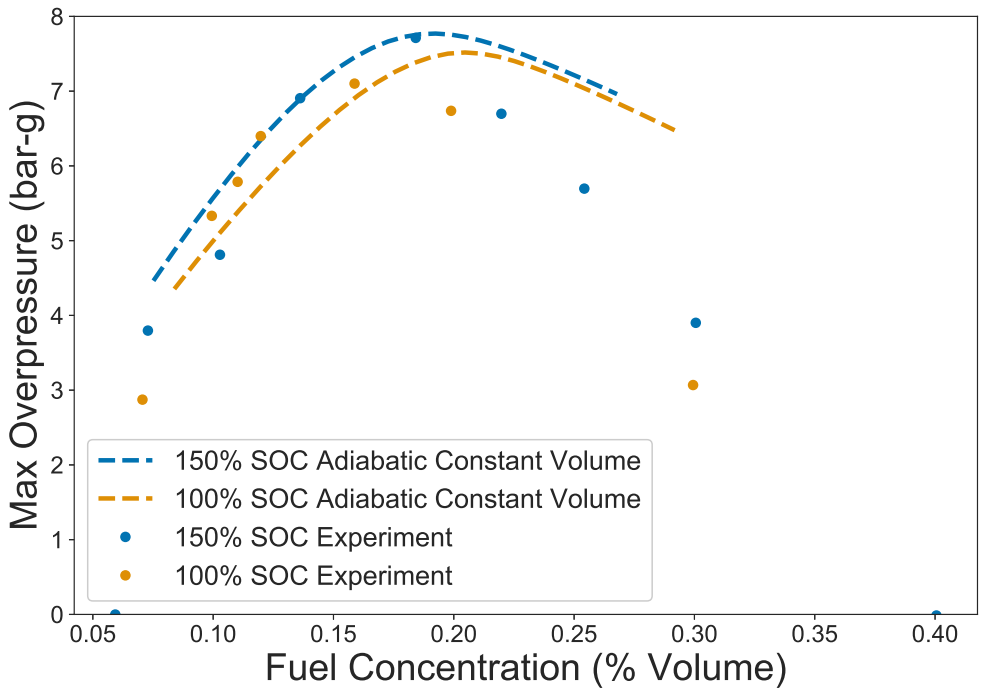

Figure 5.11: Maximum Overpressure Model Data Compared against Experimental Data

5.3.3 Vented Deflagration Models

The greatest pressure and impulse from a deflagration is generally experienced inside the compartment which confines the deflagration. Although it may be possible for detonation of battery vent gases to occur, it is unlikely that gas mixtures, confinement and congestion conditions will lead to a detonation. In this analysis, it is assumed that the combustion of battery vent gases leads to only deflagration events. Since deflagrations are slower than detonations and the prediction of pressure is only approximate, it is assumed that the pressure and impulse experienced throughout the compartment is the same.

If the deflagration occurs in a confined space and no vent is available to relieve pressure, the pressure would theoretically rise to the adiabatic maximum explosion pressure, P_{max} which is an absolute pressure between 5 and 9 bar, depending on the gas mixture. In reality, all typical structures fail at an absolute pressure well below 2 bar. To prevent structural failure and collapse, some facilities have deflagration vents which allow gas venting to occur when the pressure rises beyond some activation pressure. When properly designed, these vents will vent the high pressure from the compartment, greatly reducing the overpressure inside the compartment and either eliminating or greatly reducing the structural damage from the deflagration. If deflagration vent openings are not provided or are insufficient, the overpressure inside the structure may make windows, doors and other openings into unintentional vent openings. If the area of the intended or unintended vent openings is sufficient and they fail at a low enough pressure, this may be effective in preventing structural damage. If designed or unintentional vents openings are insufficient, then pressure will continue to rise until it is relieved by the failure of structural components such as walls, roof and floor systems. For compartments with no natural vent openings such as ISO shipping containers, this can lead to catastrophic destruction of the compartment and cause very high overpressure and structural collapse inside the compartment as well as high-velocity missiles and significant overpressures outside of the compartment. For the models presented in this section, it is assumed that deflagrations are adequately vented to prevent catastrophic structural failure of the compartment.

To determine the consequences of an indoor explosion in terms of maximum pressure or pressure-time history, a deflagration model is needed. These models rely on both

properties of the gas mixture and the geometry and venting of the enclosure. Key gas property inputs are laminar burning velocity and maximum constant-volume adiabatic pressure or P_{max}. As the burning velocity increases due to turbulence, the parameters β and $R0$ can be used to represent the exponential flame acceleration and critical flame radius.

There are a number of models available to predict overpressures in vented gas deflagrations. These models range in complexity. There are several analytical models available. In industry there are standards for vent sizing which can be used to solve for the pressure due to a vented gas explosion. Standards for vent sizing include NFPA 68 in the US and EN 14994 in Europe[86, 87]. In 2015 Molkov developed a model for vented deflagrations of hydrogen in air[88]. In 2011 Bauwens and Chao from FM global presented an analytical model and validated it with a series of propane, methane and hydrogen experiments in the FM global 64 m^3 explosion facility[89, 90]. Sinha and Wen developed an analytical model and validated it using methane, propane and hydrogen explosion data from the FM global facility as well as others[91, 92, 93]. Sinha evaluated performance of NFPA 68, EN 14994, Molkov, FM Global and their own model when compared against experimental data from the literature[92]. They observed that for hydrogen EN-14994 underpredicts for low concentrations and overpredicts for high concentrations and that NFPA 68 consistently overpredicts pressure[92]. The behavior of NFPA 68 could stem from its use as a design tool, which is intended to be conservative. The FM Global, Molkov and Sinha models did better at predicting pressures.

The previously described analytical models only provide peak pressure information

for inside the compartment and cannot provide the impulse or a pressure-time history. To better predict structural response to blast, a time history is required. To accomplish this the Mulpuru 0D vented deflagration model based on conservation and burning rate is used. This model solves a system of ODEs to determine the pressure time history[94].

More advanced models exist to model the pressure-time history of vented gas explosions. There are a number of computational fluid dynamics tools which have been used to predict pressure-time histories for vented deflagrations of flammable gases. One common tool for the prediction of gas deflagrations is FLACS. FLACS is a CFD software widely used in industry for the prediction of gas dispersion and gas explosion pressure-time histories[95]. Another tool is CEBAM, which is a finite volume CFD code used for detonations and deflagrations[96]. The open source CFD software suite OpenFOAM has also been used to predict explosion pressures and has been modified for the prediction of hydrogen gas deflagrations[97]. There are a number of challenges that come with the use of these models. Firstly these models are much more detailed than engineering models and as such require much more detailed information about the geometry and conditions of the case. Another challenge is that they require more modeling time and computational time to produce results. This increased time limits the number of cases that can be explored. This is problematic for explosion modeling, since for any given facility there can be a very large number of possible scenarios based on different release, ignition and ventilation conditions.

Recently there has been a renewed interest in gas explosion modeling with hydrogen explosions. The hydrogen work demonstrates the wide range of engineering models and CFD models that can be used and provides some insight into the performance of

these models. In a blind prediction versus experiments series, modellers used various CFD models and engineering models to predict the maximum pressure and impulse inside a 20 ft shipping container filled with a hydrogen-air mixture. Repetitions of the same single experiment were found to vary by more than 30% while variations between experiments and models often exceeded 100%. The ratio of the highest and lowest predictions was about 23[98]. Blind studies using inhomogeneous hydrogen-air mixtures also showed great variation in the results[99]. In this case, the models had to first predict the stratification of gases and then the deflagration process. This increases uncertainty, as many of the models did not capture the stratification process correctly. Similar to the homogeneous study, the simplified engineering models showed less variation [98, 99].

Going forward, this work will use two different models. The Sinha and Wen engineering model is a very fast model which can be used to calculate only maximum pressures. The Mulpuru 0D model will be used to determine pressure-time histories. Advanced CFD models were avoided due to the level of detailed information needed as well as the modelling and computational time demands that would make using the model for many scenarios not feasible.

Both of these models rely on the turbulent burning velocity. As gases burn, a flame front forms which moves into the unburned gases at some velocity. This velocity is initially the laminar burning velocity. However after the flame reaches some critical radius, then turbulence causes this velocity to increase. Bauwen's work provides data on the burning velocity acceleration for propane, methane and hydrogen vented gas deflagrations [100, 101, 102]. This work will use the Bauwen's equations and data

to represent flame acceleration for both the Sinha and Mulpuru models.

5.3.3.1 0D Vented Deflagration Model

A vented enclosure explosion model was developed by Mulpuru et al. working with the Atomic Energy of Canada [94] and has later been implemented and improved by others [103, 104, 105]. The model is a 0D physics model based on burning rate and conservation of momentum and energy. The model assumes that the gases are premixed, homogeneous, ideal gases. The properties of the burnt and unburnt mixtures are assumed to be spatially uniform. The model assumes an infinitely thin, smooth flame front. Burning is assumed to be slow such that the pressure in the volume is spatially uniform but temporally evolving. Compression and expansion of the unburnt mixture are isentropic. The model consists of three ordinary differential equations which are solved simultaneously.

The first equation is the conservation of mass. In this equation m_i is the initial mass of unburned gas, m_u is the mass of unburned gas, m_v is the mass of the vented gas and n is the ratio of the mass of burned gas to the initial mass.

$$\frac{d}{dt}\left(\frac{m_u}{m_i}\right) + \frac{d}{dt}\left(n\right) + \frac{d}{dt}\left(\frac{m_v}{m_i}\right) = 0 \tag{5.11}$$

The conservation of energy equation is similar, where E_b is the energy of the burned mixture and E_u is the energy of the unburned mixture.

$$\frac{d}{dt}\left(\frac{m_u}{m_i}E_u\right) + \frac{d}{dt}\left(nE_b\right) + E_u\frac{d}{dt}\left(\frac{m_v}{m_i}\right) = 0 \tag{5.12}$$

The rate of burned gas production is based on the laminar burning velocity S_L, and area A of the flame front and unburned gas density ρ_u.

$$\frac{dn}{dt} = \frac{1}{m_i}\rho_u S_{\mathrm{L}} A \tag{5.13}$$

For this work, the equations from Mulpuru [94] were coded in Python and solved using the RK45 Explicit Runge-Kutta method with a maximum timestep of 0.001 s. More details of the formulation of equations for use in the model can be found in the original paper by Mulpuru et al. [94]. Two modifications were made to the original equations. First, the code was altered such that the vent area can start out as zero and then the vent area goes to the prescribed value when the pressure reaches some threshold value. This allows for modeling the effects of vent opening on the pressure time history. The second adjustment was for the turbulent burning velocity. The turbulent burning velocity was modified to use the β and $R0$ values as well as the equation provided by Bauwens for flame acceleration [100, 102, 101].

5.3.3.2 Vented Deflagration Model Validation

One validation case was performed by comparing model results against results from experiments performed by Kumar et al. [106] using 20% and 29.5% hydrogen mixed with air at a temperature of 373 K. For this validation, the burning velocity for hydrogen is calculated using equations provided in Mulpuru et al. [94] and the β and

$R0$ parameters for flame acceleration are not used. In the experiments the pressure time history was recorded for well-mixed, centrally ignited hydrogen-air mixtures in a 6.37 m^3 spherical vessel. Model results are compared against the experiment in Figure 5.12. From this comparison, the maximum pressures are comparable (less than 10% error), while the predicted rise rate is faster for the stoichiometric (29.5%) mixture of hydrogen and slower for the 20% hydrogen case.

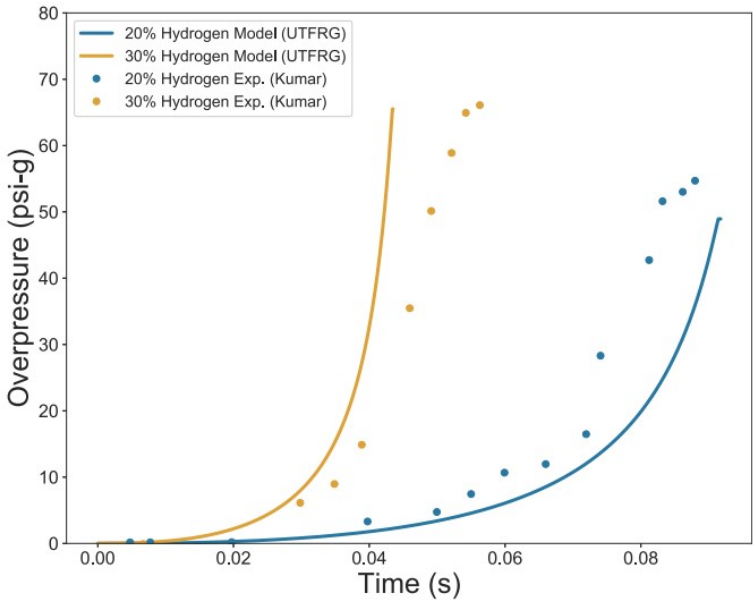

Figure 5.12: Comparison of vented deflagration model results with hydrogen experiment.

Validation for the vented deflagration model described in 5.3.3.1 was performed using 31 data points from published explosion experiments. The experiments were performed by Harrison & Eyre, Chao, and Bauwens. The 14 Harrison & Eyre experiments are performed with near stoichiometric mixtures of propane or methane in a 5.92m x 2.38m x 2.2m compartment with vent areas ranging from 0.58 m^2 to

2.74 m^2[107]. The Bauwens and Chao experiments also use nearly stoichiometric mixtures of propane or methane and are performed in the FM Global 4.6m x 4.6m x 3m explosion facility with vent areas of 2.7 m^2 and 5.4 m^2 [108, 90]. The experiments include center and back ignitions and occur in rooms without obstructions. A graph comparing the experimental max pressures with the model is shown in Figure 5.13. The percent error was calculated for each experiment and the distribution of percent error is shown in Figure 5.14.

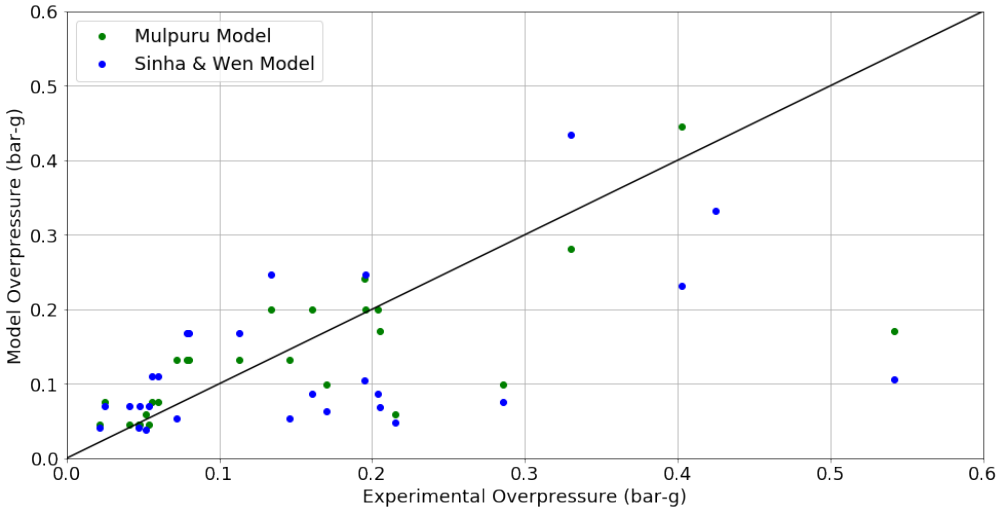

Figure 5.13: Mulpuru 0D ODE Model and Sinha/Wen Model Results Compared against Experimental Data

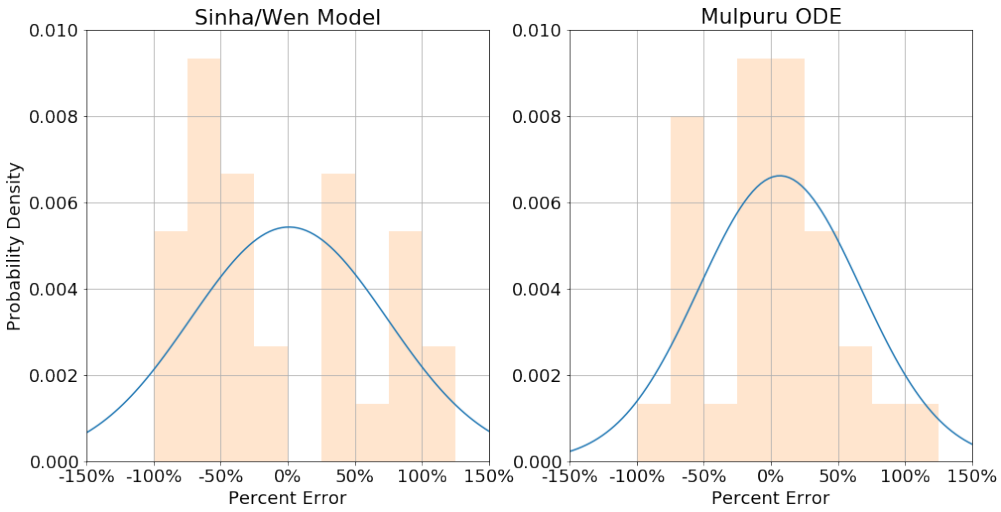

Figure 5.14: Histogram of max pressure percent error for vented gas explosion models compared against experimental data

5.3.4 Pressure at Standoff Model

Outside the explosion compartment, damaging overpressures can still exist. Once the pressure and impulse has been calculated for the compartment, models can be used to calculate the pressure for locations at standoff. For the purposes of this model it is assumed that the explosion compartment is outdoors and that locations at standoff are also outdoors and at ground level. It is also assumed that the explosion is a vented gas deflagration as opposed to a vapor cloud explosion, detonation or pressure vessel burst.

Forcier and Zalosh [109] review several models which can be used to determine the external pressure experienced by structures outside after a vented gas explosion. In 1980 Hattwig proposed a correlation which can be found in a Eckoff's dust explosion book[110].

$$P = P_{red}\frac{C_1 C2}{d} \tag{5.14}$$

This model will be used to calculate peak pressures for outdoor locations at a standoff from the vent. Validation of this model with experimental data can be found in Forcier and Zalosh's paper [109].

5.3.5 Damage Models

Once the pressure and impulse are known for both inside the explosion compartment and for locations at standoff, damage models can be used to predict the consequences. Damage to due to overpressure depends on the time-history of the pressure load on the object. Summary measures of the pressure-time history include maximum pressure and impulse. Impulse can be calculated as the integral of the pressure-time history curve. There are several different ways to estimate damage. Simple methods to estimate damage include tables of overpressure at failure and pressure-impulse diagrams.

5.3.5.1 Simple Structural Damage Models

There are many tables available in the literature for damage due to overpressure. These tables are often fairly generic and may not be specifically applicable to each object of a certain type. Since these tables have been simplified to include only pressure, they neglect to include the effect of the impulse or the shape of the pressure-time

history. Since only pressure is included, this data is more applicable for quasi-static loads for [111]. Quasi-static loading occurs when inertial effects are negligible, this generally occurs when the duration of the blast event is long compared to the natural period of the structure. In contrast, impulsive loading depends on the total impulse delivered to the structure and occurs when the duration of the blast load is smaller relative to the natural period of the structure.

A simple way to consider both the influence of pressure and impulse is through the use of P-I (pressure-impulse) diagrams. These diagrams have pressure and impulse on the X and Y axes with a curve representing the performance of a given structure or component. The curve represents the pressure and impulse at which a certain level of damage is achieved. Any pressure, impulse loading above the curve indicates that the object will be loaded beyond that level of failure.

The main limitation of P-I diagrams is that there is not enough of a database of them to be able to use to predict the performance of most systems. Additional P-I diagrams may be developed by testing a system to failure repeatedly, but due to the expense of many destructive experiments, are more commonly developed through the use of models.

5.3.5.2 SDOF Models

A common modeling approach to develop P-I diagrams is the use of single of freedom (SDOF) models. SDOF models are very commonly used in structural dynamics for both blast and earthquake loadings. With the SDOF approach a real system such as

a beam or a frame can be represented as an equivalent mass-spring-damper system as shown in Figure 5.15. The response of a spring-mass-damper system is described by the equation of motion which is derived from Newton's second law of motion [112, 113] as shown in Equation 5.15.

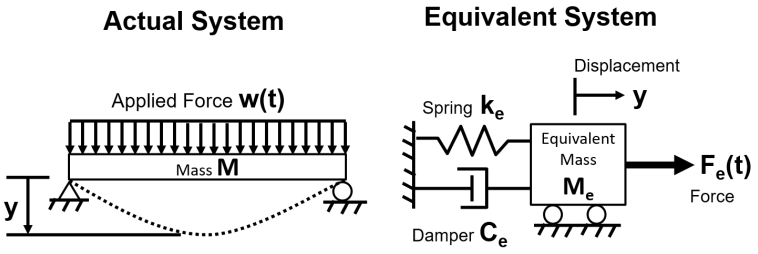

Figure 5.15: Actual structural systems such as a simply supported beam may be approximated by a mass, spring, damper system

$$M_e\ddot{y} + C_e\dot{y} + k_e y = F_e(t) \tag{5.15}$$

The equation of motion is written such that the displacement, (y) of the actual system equals the displacement in the equivalent system. In the equation of motion, M_e, C_e, k_e are respectively the mass, viscous damping constant and spring constant in the equivalent system. On the right hand side, $F_e(t)$ is the load history on the equivalent SDOF system which comes from the vented deflagration analysis. Factors can be derived to represent the relationship between the mass, stiffness, and load in the actual system and the equivalent system as shown in Equation 5.17 and 5.16.

$$K_M = \frac{M_e}{M_t} \qquad \text{Mass Factor} \qquad (5.16)$$

$$K_L = \frac{F_e(t)}{F(t)} = \frac{k_e}{k} \qquad \text{Load Factor} \qquad (5.17)$$

Values for K_L and K_M depend on boundary conditions of the actual system (pinned, fixed, pinned-fixed, cantilevered) as well as the loading (point load, uniform load, etc.). Values for K_L amd K_M are tabulated in textbooks [112] or Department of Defense manuals such as the SBEDS methodology manual [114] or UFC 3-340-02 [113].

In an SDOF system the spring force which tends to restore the element to its original position is also known as the resistance. Using $k_e y$ as the resistance in the equation of motion assumes that the structure exhibits a constant stiffness and remains elastic during response. This assumption is not acceptable for most blast design problems in which it is common for nonlinear stiffness due to the formation of hinges and yielding. To account for changes in resistance as load is applied, resistance functions are often developed. The resistance function relates the resistance of the structure to the deflection. It is common to replace the term $k_e y$ in the equation of motion using a term called resistance $R_e(y)$.

Resistance functions depend on the behavior of the actual system. Resistance functions have been developed for various systems including metal panels, metal beams, concrete members, masonry, pre-stressed concrete. For simplicity, this work will fo-

cus on implementing the SDOF approach for analysis of one-way corrugated steel panels, such as those which are used for walls and roofs of low-rise lightweight steel buildings often used as warehouses and garages.

Metal panel wall systems subjected to blast loading are typically treated as a beam which is loaded by a time-varying uniform load. The beam is analyzed on a unit width basis. The time-varying uniform load on the actual system is the pressure-time history of the blast load applied to the structure. For a beam subjected to a blast load the resistance function for the actual system can be determined by dividing the response into the elastic and plastic regions. During elastic response the spring constant is equal to the equation for deflection divided by the applied load. For example, for a simply supported beam:

$$y = \frac{5wL^4}{384EI} \quad \text{Elastic Displacement for Uniformly Loaded Simple Beam} \quad (5.18)$$

$$k = \frac{384EI}{5L^3} \quad \text{Stiffness for Uniformly Loaded Simply Supported Beam} \quad (5.19)$$

For this simply supported beam, the elastic response continues until the moment at the center of the beam exceeds the moment capacity of the beam. The moment capacity of the beam can be written as $M_p = f_{dy} \cdot Z$ where f_{dy} is the dynamic yield stress of the material and Z is the plastic section modulus. From statics, the moment as a function of static loading is $M_p = wL^2/8$. Knowing that the beam resistance $R = wL$, this equation can be solved to determine the maximum resistance $R_m = 8M_p/L$ which occurs as beam yields at the center. This resistance occurs be-

yond the yield deflection. The yield deflection can be calculated using the stiffness and the maximum resistance which produces $y_{yield} = R_m/k$. These values can be assembled to produce a resistance function curve such as that shown in 5.16.

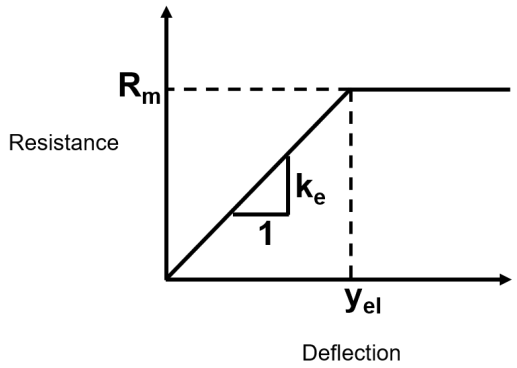

Figure 5.16: Resistance function characterizes the restoring force a structure will apply as a function of displacement.

There are several tools available to perform SDOF analysis for structures subjected to blast loads including SBEDS which is provided by the Protective Design Center of the US Army Corps of Engineers[114] and DCMS which is developed by Applied Research Associates (ARA). For the purposes of this research, a simple SDOF solver was developed using the same approach as described by the SBEDS manual [114]. For simplicity, the SDOF solver was developed for only one-way metal panel systems. SBEDS and DCMS provide a greater range of available materials that require more effort to model the more complex resistance functions such as those of concrete, masonry and two-way systems.

Once the terms in the equation of motion (Equation 5.15) have been found, it then can be solved as an ordinary differential equation. In the simple SDOF solver de-

veloped for this work, it is solved using the odeint function of the Python package Scipy which is a Python interface of the odepack FORTRAN library. The result of integrating the equations is $y(t)$, the displacement time history for the component. From this time history the maximum displacement can be extracted and used to calculate the maximum angle of rotation which is $\theta = tan^{-1}(2 \cdot y_{max}/L)$. The ductility ratio can be calculated as the ratio of the maximum displacement to the yield displacement, $\mu = y_{max}/y_{yield}$. Once the maximum deflection and angle of rotation have been found they can be compared to response limits which defines different levels of damage. Response limits for accidental explosions in the petrochemical industry are found in the ASCE book [115] while response limits for antiterrorism design are in PDC-TR 06-08 [116] and UFC 3-340-02 provides response limits for accidental explosions for the US Department of Defense.

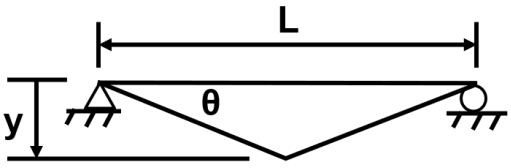

Figure 5.17: The angle of rotation of a member is a function of displacement and member length.

5.3.5.3 SDOF Model Validation

Single-degree-of-freedom structural dynamics models have been used extensively for blast response to both weapons and accidental explosions for structural response to overpressures generated by both detonations and deflagrations. For the purposes of this work, a code was developed which uses the same method as SBEDS to calculate the response of one-way supported corrugated metal panels. SBEDS has already

been extensively validated against experiments for corrugated steel panels, one-way reinforced concrete walls, one-way reinforced masonry walls, two-way unreinforced masonry walls, prestressed concrete panels and cold-formed steel beams[117, 118]. There is no need to repeat this validation, however here the results of the previously performed validations will be analyzed to determine the error associated with SDOF models. Analysis is conducted for two systems that had a large number of experimental data points: corrugated steel panels and reinforced concrete walls. For these systems, the validation data[117, 118] is analyzed to assess the modeling error associated with SDOF structural damage models. Using these data the distribution of percentage error was calculated for corrugated panels and reinforced concrete walls. Figure 5.18 compares the experimental and model maximum displacements directly. Figure 5.19 shows the distribution of the percent error for the measurements. Summary statistics are shown in Table 5.3.

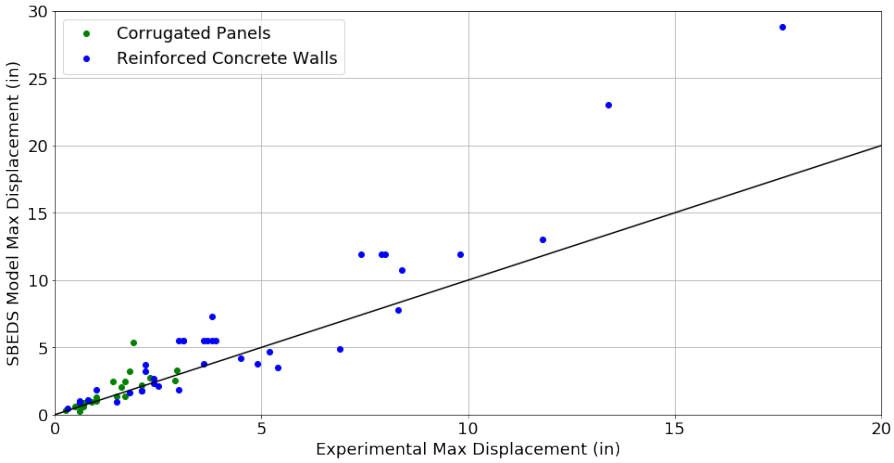

Figure 5.18: SBEDS model predicted displacements compared to experimental displacements for concrete wall and corrugated panel response to blast

Table 5.3: Summary statistics for distribution of percent error for SBEDS SDOF models of corrugated panels and reinforced concrete walls

Component	Mean	Standard Deviation	Tests	Test Series
Corrugated Steel Panels	23.7 %	46.7 %	22	3
Reinforced Concrete Walls	28.3 %	40.1 %	38	5

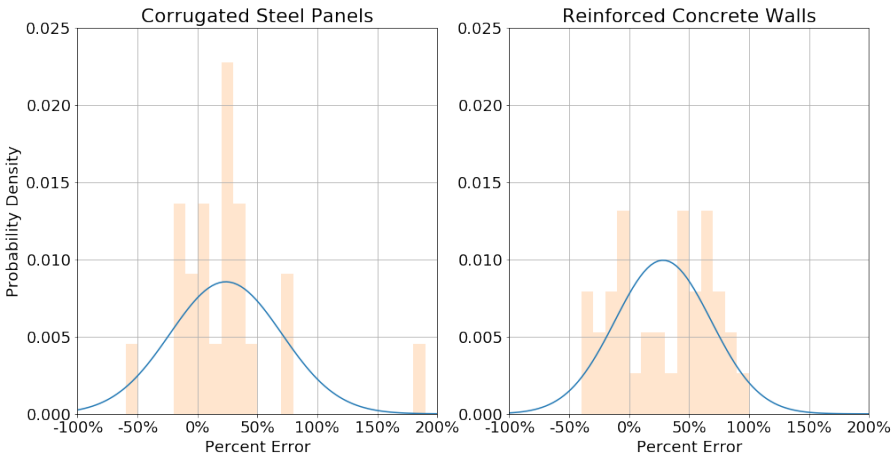

Figure 5.19: Distribution of percent error for SBEDS SDOF models of corrugated panels and reinforced concrete walls

5.3.5.4 Other Damage Models

So far only simple structural damage models and SDOF models have been described here. In practice, there exist more types of damage and additional models to estimate damage. In addition to structural collapse, overpressures can throw structural and non-structural debris creating missiles that can be a severe hazard to people nearby. Missile hazards are examined in Lee's process safety book [111]. People can also be thrown due to overpressures as has occurred in the McMicken ESS incident, the Houston train car incident and Griffith University ESS incident[5, 119, 120]. This phenomenon depends on peak dynamic pressure and impulse and is explained

as whole body displacement in Lee's process safety book[111]. Other damage could include thermal damage both to structures as well as burn injuries to people. Damage models are the final piece to estimating possible consequences for explosions involving lithium-ion batteries.

5.4 Summary of Battery Vent Gas Fire and Explosion Properties

There are many ways in which the various models can be employed to assess hazards from lithium-ion battery vent gas. A knowledge of gas composition, combined with gas flammability models, vented deflagration models and damage models makes it possible to evaluate possible incidents. Before putting all of the models together, first the battery vent gas composition data will be paired with the gas flammability models to characterize the realm of battery vent gas properties relevant to fires and explosions.

As shown in Section 5.2, the gas composition for cells failed in thermal runaway can vary significantly. This variation in gas composition can lead to significant variations in the gas properties as calculated using the models described in Section 5.3.2. This section will summarize differences in flammability characteristics based on a dataset of 43 published gas compositions described in Section 5.2.

5.4.1 Gas Properties as a Function of State of Charge

The upper and lower flammability limits were calculated using Bounaceur's method described previously[77]. Figure 5.20 shows flammability limits for the battery vent

gas samples in the data set. Generally, the flammability range is smaller for lower SOC.

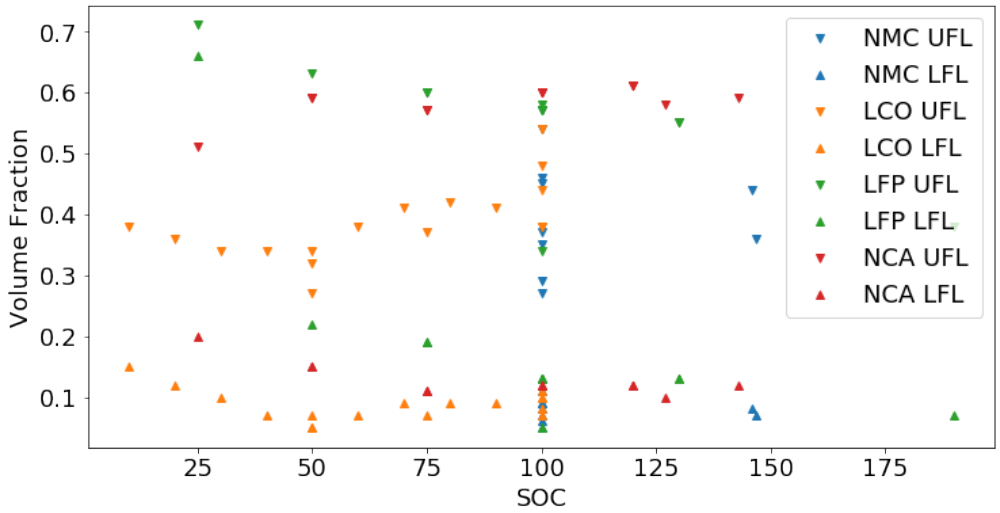

Figure 5.20: Upper and lower flammability limits and stoichiometric volume fraction as a function of state of charge.

The GRI-Mech model implemented in Cantera described in Section 5.3.2.2 was used to estimate the laminar burning velocity of the various compositions of battery vent gas. Laminar burning velocity is plotted against state of charge (SOC) in Figure 5.21. This data shows that the laminar flame speed of the produced gases generally decreases for lower states of charge.

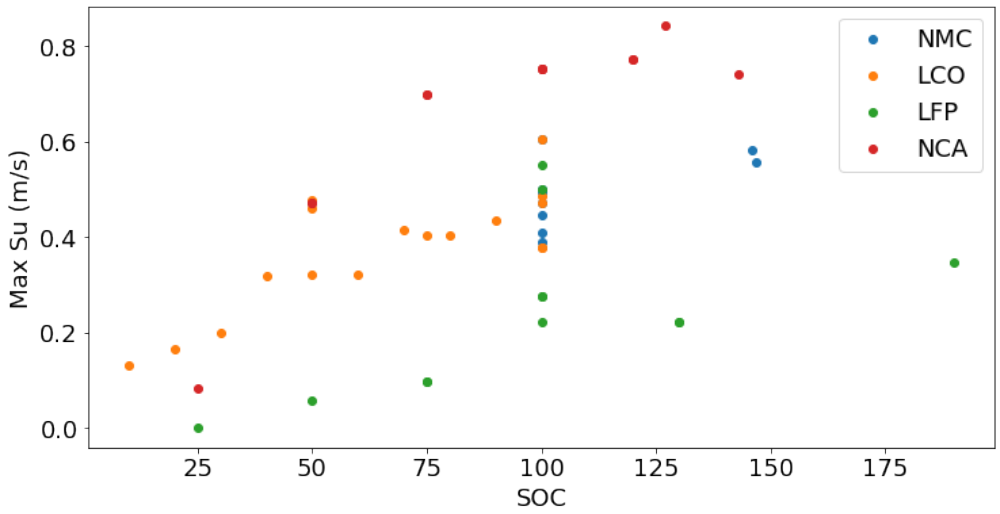

Figure 5.21: Maximum Laminar Flame Speed generally increases with state of charge

The reasons for these variations in properties can be understood by looking at compositions of the gas mixtures. The volume fraction of hydrogen generally decreases with decreasing SOC, while the volume fraction of carbon dioxide generally increases with decreasing SOC as shown in Figure 5.22.

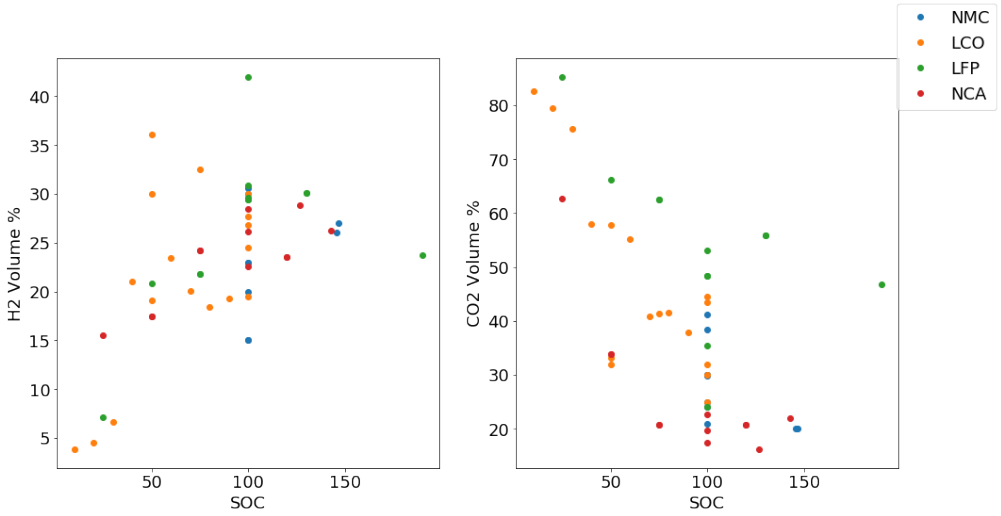

Figure 5.22: Volume fraction of hydrogen and carbon dioxide as a function of state of charge (SOC).

It can be seen in Figures 5.20 and 5.21 that 100 % SOC has the most observations. This is because many in industry consider 100 % SOC to be the worst case fire or explosion scenario. Although overcharge failures at above 100 % SOC can produce a higher burning velocity as seen in Figure 5.21 and more gas[1], these are often not considered because systems are designed to avoid overcharging cells. This may not be appropriate considering that improperly operating systems was a major cause of the ESS fires in Korea [19].

5.4.2 100 % SOC Gas Properties

Since there are the most experiments at 100 % SOC, and this is a commonly used composition for safety design, further description of these results is warranted. Lower flammability limits for the battery gas produced at 100 % SOC cells is shown in Figure 5.24. From the limited amount of data available, there doesn't appear to be any trend by cell chemistry. Regardless of chemistry, LFL values range from 5 % to

13%.

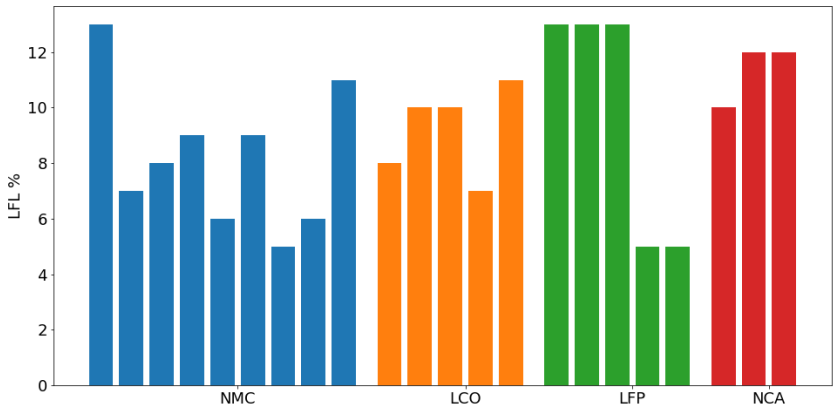

Figure 5.23: Lower flammability limits (LFL) for 100 % SOC battery gas compositions using various chemistries.

Upper flammability limits for the battery gas produced by 100 % SOC cells is shown in Figure 5.24.

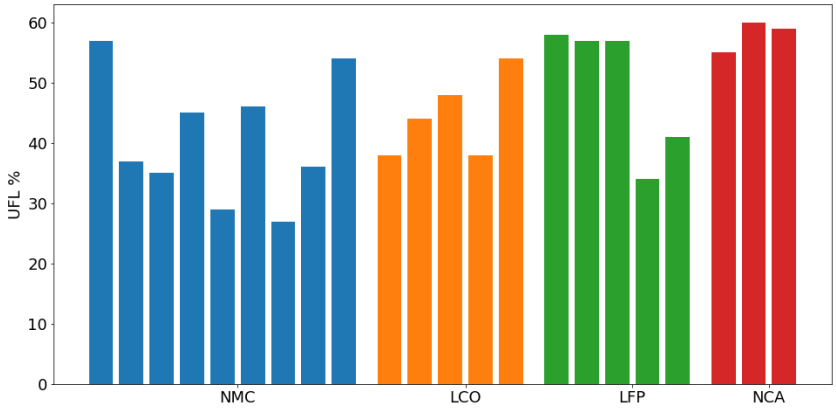

Figure 5.24: Upper flammability limits (UFL) for 100 % SOC battery gas compositions using various chemistries.

Cantera was used to determine the stoichiometric volume fraction for each gas composition. The stoichiometric volume fraction is the amount of battery gas required to evenly balance with oxygen. Worst-case burning velocities and explosion pressures occur at slightly above the stoichiometric volume fraction. Figure 5.25 shows the stoichiometric volume fraction for each gas.

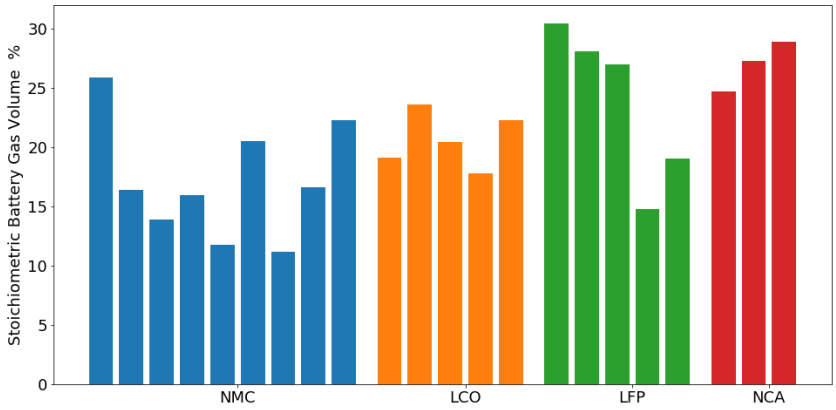

Figure 5.25: Stoichiometric volume percent for 100 % SOC battery gas compositions using various chemistries.

A key parameter for fire hazards is the heat of combustion. As shown in Chapter 3, the heat of combustion along with the release-rate profile for a set of cells can be used to define the heat release rate for CFD models of fire involving thermal runaway. Heat of combustion was calculated using Cantera to compute the difference in specific enthalpy between reactants and products. The heat of combustion calculated corresponds to the lower heating value (LHV) of the gas mixtures. Heat of combustion values are plotted in Figure 5.26. Although many consider LFP to be "safer" than other chemistries, the heat of combustion of LFP cells ranges from the lowest values to the highest values.

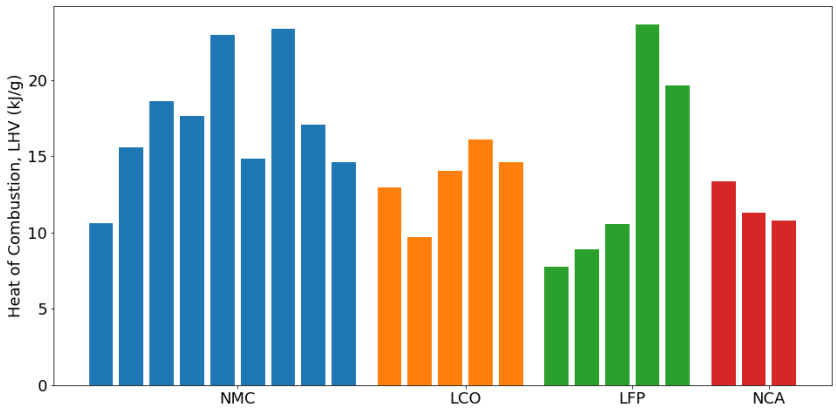

Figure 5.26: Heat of combustion for 100 % SOC battery gas compositions using various chemistries.

For many explosion models, the measure of the energy stored by the gas is the maximum adiabatic explosion pressure (P_{max}) which is calculated using Cantera as described in 5.3.2.3. Values for maximum explosion pressure are shown in Figure 5.27.

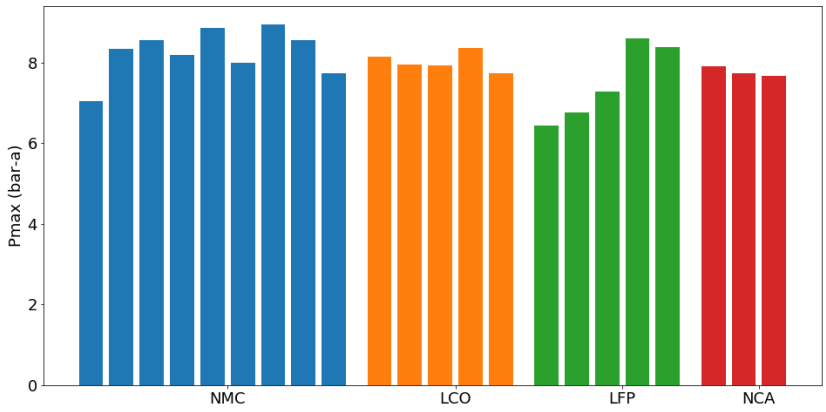

Figure 5.27: Maximum explosion pressure for 100 % SOC battery gas compositions using various chemistries.

Another key input to some explosion models is the expansion ratio, σ which is defined as the ratio of the unburned gas density divided by the burned gas density. This value is important because this expansion is a major factor in driving the velocity of the flame front and creating the overpressure. Expansion ratio is an input to the Sinha Wen model as well as the FM Global model for vented gas explosions[93, 89]. The Mulpuru and EVA models do not have expansion ratio as an input but instead use the burned and unburned gas densities directly along with P_{max} [94, 103, 104, 105].

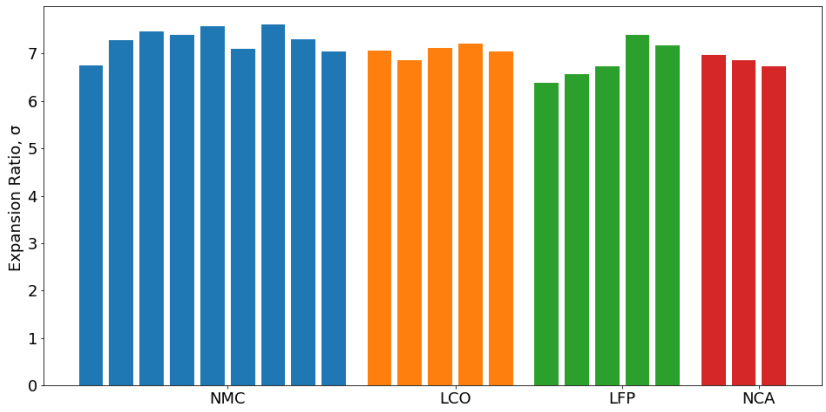

Figure 5.28: Expansion ratio for 100 % SOC battery gas compositions using various chemistries.

Finally, the laminar burning velocity is a very important input to all explosion models. Laminar burning velocity was calculated using the Cantera and GRI-Mech as described previously. Results for laminar burning velocity are shown in Figure 5.29.

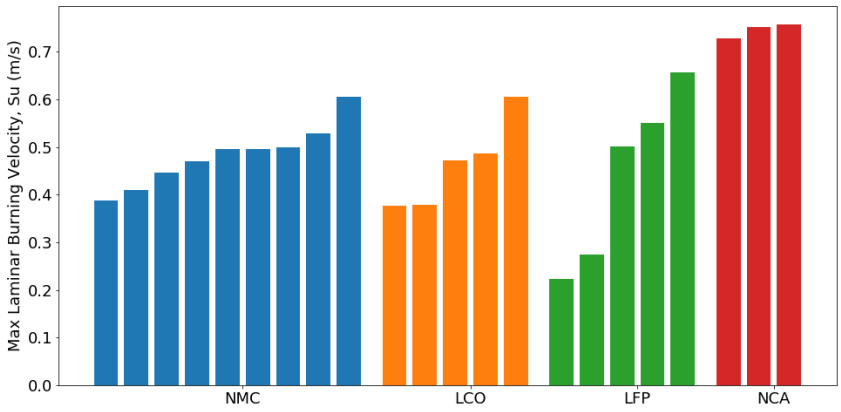

Figure 5.29: Burning Velocity for 100 % SOC battery gas compositions using various chemistries.

The properties above along with several other gas properties used in explosion models were summarized based on the 21 100% SOC battery compositions. This summary is useful to capture the range of values used in explosion models. Table 5.4 shows the mean, maximum, minimum, standard deviation for each gas property.

The battery vent gas composition database and the gas flammability models can be used to summarize the range of fire and explosion properties possible for the experiments available in the literature. This review includes battery vent gas composition from the four most common chemistries: NMC, LFP, LCO and NCA. It also includes data from the each major form factor: pouch, prismatic and cylindrical. Finally, it includes data from various SOC. As others have noticed, the laminar burning velocity can vary with SOC [40, 81]. This analysis shows that burning velocity generally increases with increasing SOC. This analysis also shows that flammability limits may widen for increasing SOC as shown by Ma et al [121].

Table 5.4: Summary of fire and explosion properties for 100 % SOC battery vent gas. Mean, minimum, maximum and standard deviations come from 21 published gas compositions.

Parameter		**Mean**	**Min**	**Max**	**Std**	**Units**
Gas Released per nominal capacity	r	0.40	0.12	0.63	0.13	L/Wh
Lower Flammability Limit	LFL	10%	5%	13%	3%	
Upper Flammability Limit	UFL	47%	27%	60%	11%	
Stoichiometric Gas Volume	X_{st}	21%	11%	30%	6%	
Heat of Combustion	Δh_c	14.3	7.8	23.7	4.88	kJ/g
Maximum Pressure	P_{max}	7.85	6.44	8.95	0.70	bar-g
Expansion Ratio	σ	7.03	6.38	7.62	0.35	
Burning Velocity	S_u	0.48	0.22	0.75	0.15	m/s
Unburned gas density	ρ_u	1.16	1.12	1.21	0.03	kg/m3
Burned gas density	ρ_b	0.17	0.15	0.18	0.01	kg/m3
Unburned Const Volume Specific Heat	$c_{v,u}$	779	765	794	8	J/kgK
Burned Const Volume Specific Heat	$c_{v,b}$	1189	1170	1208	11	J/kgK
Unburned Const Pressure Specific Heat	$c_{p,u}$	1072	1048	1093	14	J/kgK
Burned Const Pressure Specific Heat	$c_{p,b}$	1471	1444	1504	13	J/kgK
Unburned Ratio of Specific Heats	γ_u	1.38	1.37	1.39	0.01	
Burned Ratio of Specific Heats	γ_b	1.24	1.23	1.25	0.00	
Burned Gas Dynamic Viscosity	μ	69.9	66.3	71.4	1.51	$\mu Pa \cdot s$
Unburned Gas Sound Speed	a_u	347	339	355	5	m/s

5.5 Explosion Model Sensitivity Analysis

There are many gas properties that are important inputs to vented gas explosion models. And as can be seen in Section 5.4.1, these properties can vary greatly for the various compositions of gas released by batteries in thermal runaway. In this section a sensitivity analysis is conducted to determine the impact of these parameters on the explosion pressure generated. For this sensitivity analysis, a custom implementation of the Mulpuru / EVA model described in Section 5.3.3.1 will be used. The sensitivity of the Sinha/Wen model[93] is also compared. Ranges for input values come from the range of gas properties for 100 % SOC cells described in Section 5.4.

The sensitivity analysis was conducted using the Mulpuru and Sinha/Wen models to calculate maximum pressure. The execution of the Monte Carlo runs and the development of sampled inputs was performed using the Python package SALib [122]. The sensitivity analysis was used to determine global sensitivity indices using Monte Carlo methods as described by Sobol [123]. The Saltelli method was used to generate input parameters for the Monte Carlo runs [124]. The inputs to the sensitivity analysis consisted of ranges of gas properties. These ranges were taken from Table 5.4. Data for turbulent flame acceleration is not available for battery vent gas compositions. So, values for R0 were assumed to vary from 0.02 m to 0.20 m based on Bauwens data for Hydrogen and Propane respectively [101, 102]. Values for β were assumed to vary between 0.167 and 0.33 which corresponds to an α between 1.2 and 1.5 which is described as a typical range for hydrocarbon deflagrations as reported by Bauwens [102]. Results from the sensitivity analysis are shown in Figure 5.30.

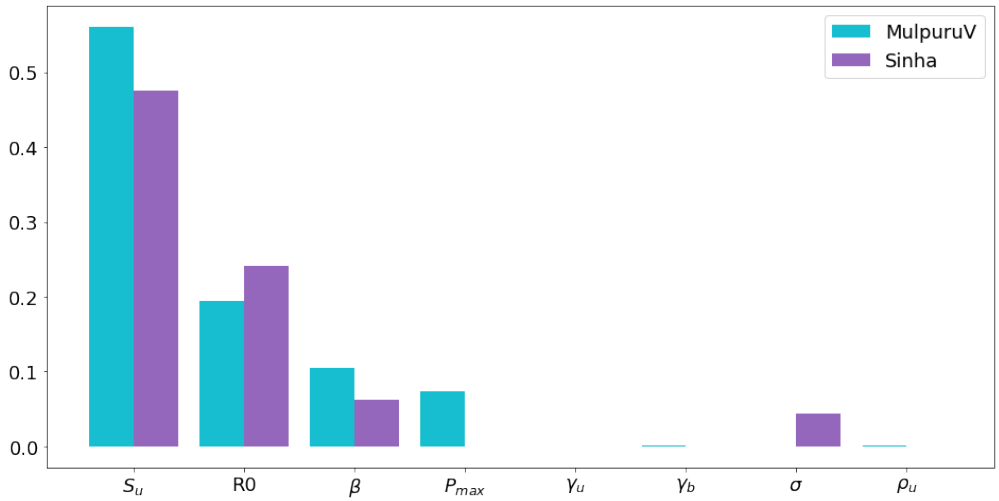

Figure 5.30: Sensitivity of modified Mulpuru vented deflagration model and Sinha/Wen model maximum pressure to various gas properties

As expected, the vented gas deflagration is most sensitive to the laminar burning velocity (S_u). The deflagration is also very sensitive to the parameters describing turbulent burning acceleration, β and $R0$. This is also expected. These parameters increase the burning velocity when the flame radius exceeds the critical radius. There is also a great deal of sensitivity to the variation in the parameters. The parameters β and $R0$ have not been measured for battery gas and these values are given wide ranges based on reported ranges for hydrocarbons and hydrogen. Other parameters that were important are maximum pressure (P_{max}) for the 0D Mulpuru model and expansion ratio (σ) for the Sinha/Wen model. These two parameters are different ways of capturing the same effect. The Sinha/Wen uses the ratio of burned and unburned densities to capture the pressure increase due to the heated products whereas the Mupluru model considers this as the ratio of maximum pressure to initial pressure.

5.6 Conclusions

This chapter has shown how multiple models may be used together to estimate the explosion hazards from lithium-ion battery systems. Furthermore, this section has validated these models against real data and collected information on model uncertainty. The distribution of percent error to represent model uncertainty was collected for laminar burning velocity models, vented deflagration models and a single degree of freedom (SDOF) structural damage model. To function, these models require battery vent gas composition information. A library of publicly available gas compositions was created. This library was used along with models to determine flammability limits, laminar burning velocity, heat of combustion and other gas properties for each composition of battery vent gas. A sensitivity analysis found that the maximum explosion pressure is most sensitive to battery vent gas laminar burning velocities and turbulent flame acceleration parameters.

Chapter 6

Application of Explosion Hazard Models

This chapter provides applications of the models described in Chapter 5. First, a sensitivity analysis is conducted with the burning velocity, vented deflagration and SDOF model. Next, case studies using the models are provided. Finally, some of the models and the gas composition database is applied to determine the minimum quantity of batteries in a given volume required to cause deflagrations.

6.1 Uncertainty Sensitivity Analysis

A sensitivity analysis was completed using several of the models together to investigate the effect of uncertainty on model results. For this exercise three models were used in conjunction. This exercise starts with a range of laminar burning velocities based on one standard deviation of burning velocities presented previously in Table 5.4. Uncertainty due to burning velocity model error is considered based on the per-

cent error calculated for the GRI-Mech burning velocity model. The burning velocity with error is an input to the Mulpuru vented deflagration model. The pressure-time history results are then multiplied by an error coefficient and then used as an input to calculate the maximum deflection of a metal panel using the SDOF model. Error on the output of the SDOF model is then considered.

As discussed in Chapter 5, each model has some uncertainty associated with it. In Chapter 5 the model uncertainty was summarized using the mean and standard deviation for percent error. The percent error is simply 100 % times relative error which is calculated as shown in Equation 6.1. The equation for relative error can be rearranged to calculate the actual value of a parameter given a model prediction for the parameter and a known relative error as shown in Equation 6.2. In Equation 6.2, the effect of the relative error can be rewritten as a coefficient, ε which can be calculated from relative error as shown in Equation 6.3. For uncertainty analysis, a range of possible ε values can be determined using plus or minus the standard deviation of relative error (σ_{δ_X}) as shown in Equations 6.4 and 6.5. The results for the maximum and minimum ε for each model based on the standard deviation of percent error for each model is shown in Table 6.1.

$$\delta = \frac{X_{model} - X_{actual}}{X_{actual}} \quad \text{Relative Error for parameter X} \quad (6.1)$$

$$X_{actual} = \frac{X_{model}}{1+\delta} = X_{model} \cdot \varepsilon_X \quad \text{Actual Value} \quad (6.2)$$

$$\varepsilon_X = \frac{1}{1+\delta} \quad \text{Coefficient representing model error} \quad (6.3)$$

$$\varepsilon_{X\_min} = \frac{1}{1+\sigma_{\delta_X}} \quad \text{Maximum coefficient} \quad (6.4)$$

$$\varepsilon_{X\_max} = \frac{1}{1-\sigma_{\delta_X}} \quad \text{Minimum Coefficient} \quad (6.5)$$

Table 6.1: Standard deviation of percent error for models was used to calculate maximum and minimum error terms (ε) to represent model errors in Monte Carlo sensitivity analysis

Parameter	**% Error Std**	**Min ε**	**Max ε**
Burning Velocity Model Error (ε_{Su})	10.6%	0.904	1.118
Mulpuru Model Error (ε_P)	60.3%	0.624	2.519
SDOF Model Error (ε_{SDOF})	46.7%	0.467	0.682

To propagate error through the models, appropriate coefficients (ε) are multiplied by the results of each model as shown in Equations 6.7, 6.9 and 6.11. In addition to the uncertainty due to model errors, this sensitivity analysis also considers uncertainty due to an unknown gas composition. To account for uncertain gas composition, the sensitivity analysis uses a range of laminar burning velocity values. The analysis uses burning velocity values ranging from 0.33 m/s up to 0.63 m/s which are calculated using Equation 6.6. These values were determined by taking one standard deviation above and below the mean of burning velocity reported in Table 5.4.

$$Su_{model} = Su_{mean} \pm \sigma_{Su} \quad \text{Burning velocity input range} \quad (6.6)$$

$$Su_{actual} = Su_{model} \cdot \varepsilon_{Su} \quad \text{Burning velocity with model error} \quad (6.7)$$

$$P_{model}(t) = f(Su_{actual}) \quad \text{Pressure-time history from Mulpuru model} \quad (6.8)$$

$$P_{actual}(t) = P_{model}(t) \cdot \varepsilon_P \quad \text{Pressure-time history with model error} \quad (6.9)$$

$$\Delta_{model}(t) = f(P_{actual}(t)) \quad \text{Max displacement from SDOF model} \quad (6.10)$$

$$\Delta_{actual}(t) = \Delta_{model}(t) \cdot \varepsilon_{SDOF} \quad \text{Max displacement with model error} \quad (6.11)$$

This sensitivity analysis is based on single reference scenario. In this scenario the compartment is 4.6m x 4.6m x 3.0m with a vent area of 5.4 m^2. The flame acceleration parameter β is fixed at 0.20 and $R0$ is set to 0.197 m. The SDOF model is run using a corrugated panel as shown in Figure 6.1. Properties of the panel are shown in Table 6.2.

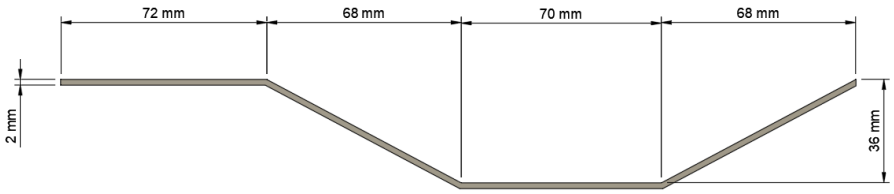

Figure 6.1: Steel cross-section used for SDOF analysis.

The sensitivity analysis was conducted using the Sobol [123] method and Saltelli [124] sampling. These calculations are performed by the SALib python package [122]. Values reported are first-order global sensitivity indices as described by Sobol

Table 6.2: Parameters used in SDOF model

Parameter	**Symbol**	**Value**	**Units**
Moment of Inertia	I	0.2976	in^4
Section Modulus	S	0.397	in^3
Area	A	0.9153	in^2
Span	L	118	in
Support		Pin-Fixed	
Tributary Width	t	10.94	in
Dynamic Yield Strength	Fdy	66550	psi

[123]. In total there were four uncertain parameters, laminar burning velocity (S_u), burning velocity model error (ε_{Su}), Mulpuru deflagration model error (ε_P) and SDOF model error(ε_{SDOF}). A Monte Carlo approach was used to run the model 10,000 times using values sampled between the upper and lower bounds provided for each input.

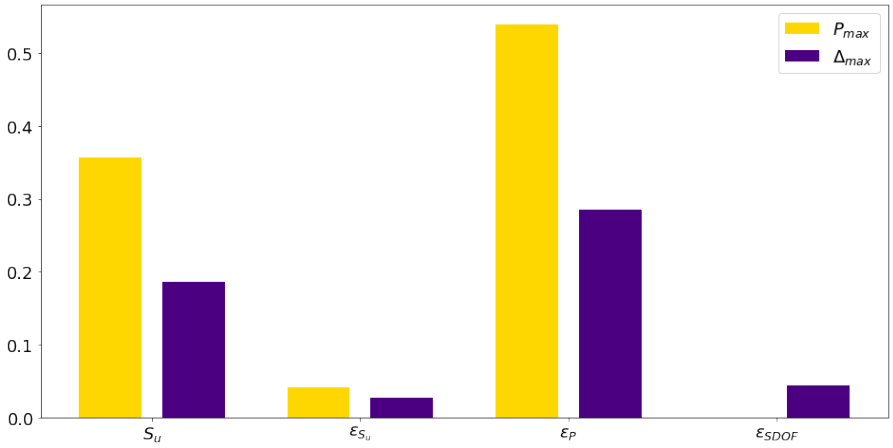

Figure 6.2: First-order global sensitivity indices from sensitivity analysis show that the dominant sources of variation in pressure results and structural deflection is uncertainty in the vented deflagration model and uncertainty associated with having a deflagration caused by a battery gas mixture with an unknown gas composition.

The results of the sensitivity analysis are first-order global sensitivity indices for each

uncertain input and are shown in Figure 6.2. These indices show that the dominant sources of variation in pressure results and structural deflection is uncertainty in the vented deflagration model and uncertainty associated with having an unknown gas composition. As expected, uncertainty in the SDOF model does not affect the maximum pressure. Uncertainty in the SDOF model plays a much smaller role in the maximum deflection than the larger uncertainties coming from the vented deflagration model. These results suggest that to reduce the uncertainty associated with damage it is very important to know the gas composition for the particular cells involved. These results also indicate that since the effect of burning velocity model error is small, it may be appropriate to use models for burning velocity and avoid the expense of conducting experiments. As expected, the uncertainty in vented gas deflagration pressure is the largest source of uncertainty.

6.2 Case Studies

The explosion models previously described can be used to explore the explosion incidents that have occurred.

6.2.1 Kona Electric Vehicle in Garage Case Study

In July 2019 in Montreal Canada the thermal runaway of a battery of a Hyundai Kona resulted in an explosion that launched the garage door across the street, totaled the car and damaged the garage. This incident can be used as a case study to demonstrate the usefulness of the explosion analysis approaches described previously.

The Hyundai Kona is a subcompact SUV which was released in 2017 with a gasoline

engine and in 2018 as an electric vehicle. The Kona is available with two different batteries, a short range version with a 39.2 kWh capacity and a long range version with a 64 kWh capacity. These capacities are typical for modern electric vehicles. The Tesla Model 3 for example has battery options ranging from 54 kWh to 82 kWh while the BMW i3, which is smaller, has options for capacity between 18.2 kWh and 37.9 kWh. The 2019 Kona involved in the incident likely had a 64 kWh battery pack, since this is the only battery pack available in North America[14]. Figure 6.3 shows a 2019 Hyundai Kona EV.

Figure 6.3: 2019 Hyundai Kona EV[12]

The battery pack for the Kona is located in a metal housing underneath the floor of the vehicle as shown in Figure 6.4. Inside the battery pack there are 5 modules as shown in Figure 6.5. These modules sit on top of cooling channels which circulate liquid coolant. The three modules side-by-side in the front of the vehicle each contain 20 cell groups. The two modules stacked towards the rear of the vehicle each contain 19 cell groups[14].

Each cell group consists of 3 pouch cells which are connected in parallel. The pouch cells are mounted with brackets which hold them in place[14]. The pouch cells are

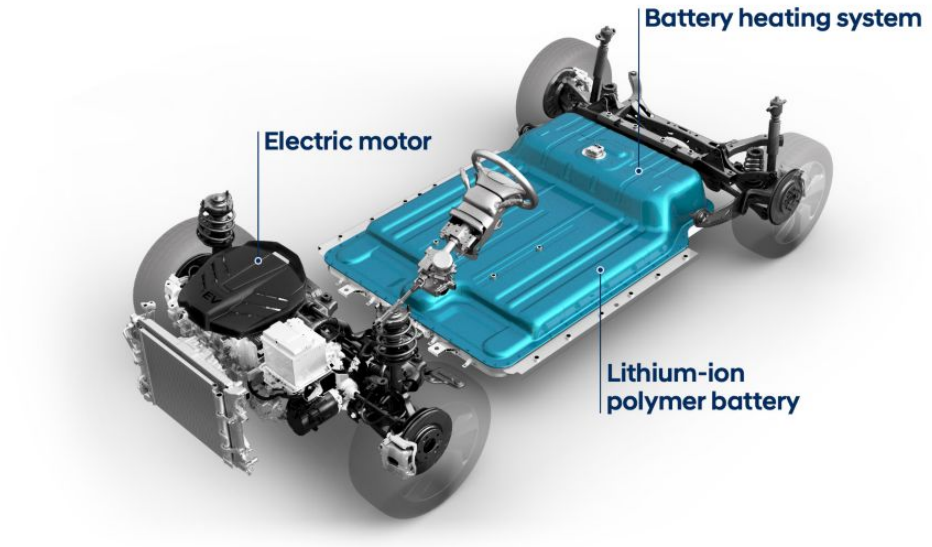

Figure 6.4: Hyundai Kona battery pack is located inside a metal housing underneath the floor of the vehicle[13]

packed closely together very similar to the cells used in the array experiments in Chapter 2. This packing is needed to reduce the volume of the battery pack and also serves to provide confinement to cells against swelling. However as seen in the array experiments, this arrangement makes it very easy for thermal runaway to propagate from one cell to the next. The cooling system, being located on the bottom surface of the cells is almost certainly designed for regular use and it is doubtful that it would provide much benefit in preventing runaway propagation.

In total there are 294 cells. Using the number of cells, a nominal voltage of 3.6 V and the total energy stored, the cell capacity is calculated to be about 60 Ah. The cells are LG Chem pouch cells with a NMC 622 chemistry and tabs on the two short ends. NMC 622 means that the cathode chemistry is 60% Nickel, 20% manganese and 20% cobalt [14]. A photograph of a similar cell is shown in Figure 6.6.

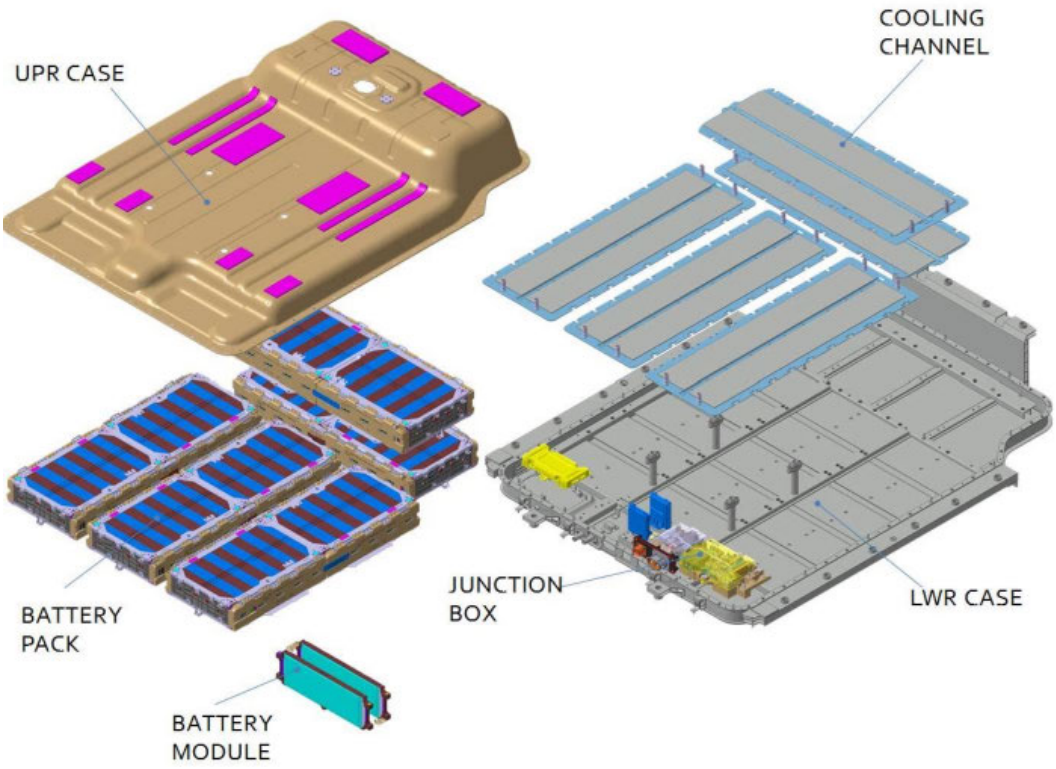

Figure 6.5: Hyundai battery pack consists of 5 modules, each module contains 19 or 20 cell groups (which are shown in alternating red and blue). Each cell group consists of 3 pouch cells connected in parallel. [14]

Figure 6.6: Cells are LG Chem Pouch Cells similar to this photo [14]

The cells described in the Kona [14] are very similar (or possibly the same) as the cells that have been tested by Essl et al. [1]. Essl performed overheating, overcharge and nail penetration runaway experiments on 60 Ah, NMC 622, automotive pouch cells with graphite anodes and 1:1 ratio of EC:EMC electrolyte. For the purposes of this analysis, it shall be assumed that the Kona cells failed similarly to the cell's Essl failed using overheating. In Essl's experiments, the cells were put into thermal runaway by heating and then the vent gases composition was measured using gas chromatography. In these experiments the cells produced 1.56 L/Ah or 0.43 L/Wh of gas when failed due to overheating [1]. This relation can be used to estimate the total volume of gas that can be produced if all of the cells failed due to overheating. The composition of this gas is shown in Table 6.3.

The models for laminar flame speed and flammability limits described in 5.3.2 were

Table 6.3: Species Volume Percentage for gases released by 60 Ah NMC 622 Pouch Cell from Essl et al. [1]

Species	**Volume Percent**
Hydrogen	15%
Carbon Dioxide	30%
Carbon Monoxide	26%
Methane	5%
Ethylene	10%
EMC	3%
Water	4%
Other	7 %

run with this gas composition to determine the relevant properties of this gas mixture. For this gas mixture LFL is 8% and UFL is 35%. The stoichiometric volume concentration of battery gas is 14 %. The maximum laminar flame speed is 0.45 m/s and the maximum explosion pressure is 8.6 bar. Ternary plots can be used to visualize the flammability limits and how laminar flame speed and maximum explosion pressure vary with the amount of air, fuel and inert products in the mixture.

The owner reported that the vehicle was not charging at the time of the incident [125]. Given that the vehicle was parked in the garage of the owner, it is reasonable to assume that since the owner was not charging it, it must already be at or near fully charged. Another evidence that the car was close to full charge is that the cells did go into thermal runaway. Essl's work on similar cells found that 30% SOC 60 Ah NMC 622 cells did not go into an intense thermal runaway when overheated[1]. Going forward in the review of this incident, it will be assumed for these reasons that the cells were fully charged and therefore failed in a manner similarly to Essl's 100% SOC overheating experiment.

Using the battery capacity of 64 kWh and a gas release of 0.43 L/Wh, the total volume of gas released is 27500 L or 972 ft^3. This gas release occurred in a typical-looking single car garage. Single car garage widths are typically 12 to 16 ft, typical lengths are 20 to 24 ft and heights are between 7 ft and 10 ft[126]. The volume of a 14 ft x 24 ft x 8 ft garage would be 2688 ft^3 or 76116 L. If as the gas is released only air is expelled from the garage the average concentration of battery gas in the garage after all is gas is released would be 36%. This puts the mixture just barely above the upper flammability limits of 35%. Since battery some gas escapes the compartment and new air will enter, this mixture will likely always remain within the flammability limits.

A vented gas explosion model can be used to approximate possible explosion scenarios. To approximate worst-case conditions, a homogeneous stoichiometric mixture of 14% battery vent gas is assumed. For comparison to a less than ideal mixture, a lean homogenous mixture of 10% battery gas will be used. The modified version of the Mupluru model described previously will be used. The model has been modified to allow for the vent to open a specific pressure. For this scenario, garage door dimensions of 7 ft x 12 ft will be used for the vent area. There is limited data as to the blast resistance of garage doors. However, for wind load pressures, garage doors have been found to be weaker than the rest of the structure. Based on data for garage door failures under wind pressures, a failure pressure of 0.018 bar is used [127]. Results of the model for the stoichiometric and lean mixtures are shown in Figure 6.7.

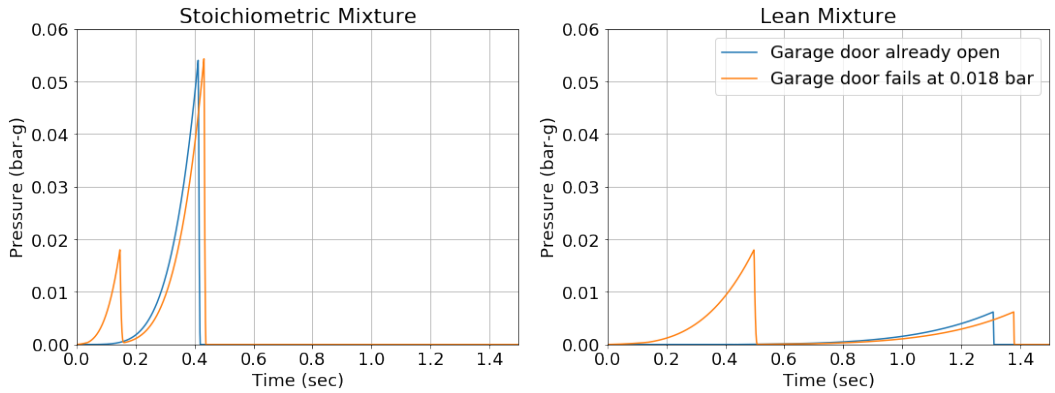

Figure 6.7: Pressure-time history for vented gas explosion in garage.

In Figure 6.7, it is apparent that the stoichiometric mixture produces a much higher maximum pressure. For the stoichiometric mixture with a garage door is already open, the pressure simply rises to a maximum value of 0.055 bar before rapidly dropping as the event ends. When the garage door begins closed there is a rapid-build up to 0.018 bar, which is then relieved when the garage door fails and becomes an open vent. After the garage door fails the pressure rapidly drops and then continues to increase to a maximum of 0.055 bar. For the stoichiometric case, having the garage door already open serves only to reduce the impulse, while the peak pressure remains about the same. For the lean mixture, whether or not the garage door starts open has a large impact on both the impulse and peak pressure. Since the lean mixture has a slower laminar burning velocity, the vent area of the garage door is sufficient to keep pressures much lower. However, if the garage door starts out closed, then the maximum pressure in the compartment is determined by the failure pressure of the door.

In the actual event, the explosion launched the garage door across the street[7].

The pressure reduction due to the venting likely made it possible for the rest of the building to remain standing. It is unclear whether the damaged roof was caused by the explosion, fire or firefighter intervention. As shown by the models, the failure of the garage door serves to lower the pressure inside the garage and thus prevent the structural collapse of the entire building.

Figure 6.8: Hyundai Kona on tow truck after incident (Mathiue Wagner - Radio Canada) [7]

Figure 6.9: Garage door thrown across the street after Hyundai Kona thermal runaway caused explosion. (Mathiue Wagner - Radio Canada) [7]

Figure 6.10: Garage after Hyundai Kona thermal runaway caused explosion which threw garage door across the street. It is unclear whether the damaged roof was caused by the explosion, fire or firefighter intervention. (Mathiue Wagner - Radio Canada) [7]

6.2.2 Surprise Arizona ESS Explosion Case Study

In April 2019, a 2 MWh ESS system in Surprise, AZ exploded resulting in 8 firefighters being injured [22, 23]. The explosion threw a firefighter 73 feet and another firefighter 30 feet, causing serious trauma in addition to chemical burns and chemical inhalation exposure [5]. This incident comes after a 2012 fire involving the same electric utility [24].

The ESS involved consisted of a 2 MW / 2 MWh system inside of a dedicated ESS building near a substation in Surprise, AZ. The system is owned by the electric utility APS, was integrated by Fluence and uses cells provided by LG-Chem. The building measures 15.2m x 3.96m x 3.66m (50 ft x 13 ft x 12 ft). The building does

not have any vents intended for deflagration venting[128]. In practice, the deflagration was vented by the failure of the two exterior doors. This produces a vent area of approximately 3.9 m^2.

The interior of the building is occupied by only the energy storage system and supporting equipment. The ESS consists of 27 racks, each rack containing 14 modules. Each module contains 28 cells arranged in a 2P14S configuration. The cells are LG Chem JP3 pouch cells[128]. These cells are intended for high-power applications. At the top of each rack are supporting electrical equipment including a battery protection unit (BPU), node controller and power conversion system (PCS).

On April 19, 2019 at 16:54:30 the first measured deviation occurred as the voltage of rack 15, module 2, battery 7 dropped by 0.24V. Within eight seconds the voltage dropped another 3.8V. At this time the total voltage drop is approximately equal to the operating voltage of a single cell. At 16:54:40, temperature increases were recorded at the rear of rack 15. Less than a minute after the first voltage drop, at 16:55:20 smoke alarms were activated and circuit breakers were opened. As designed, 30 seconds after activation at 16:55:50 the clean agent suppression system discharged NOVEC 1230 agent. Fluence sent a field service engineer who eventually called the fire department because of a suspected fire. Fire department personnel arrived at 17:48 [128]. 911 callers had reported smoke in the area and a bad smell [5].

Figure 6.11: ESS Building upon arrival of firefighters[5]

At 18:04, responding firefighters called for the HAZMAT (hazardous materials) team. Between 18:37 and 19:15, the HAZMAT team conducted three 360 degree size-ups of scene while taking gas measurements. During these size-ups, CO and HCN sensors were out of range with measurements greater than 500 ppm and 50 ppm respectively [5]. At approximately 19:50, the gas/vapor mixture was no longer observed to be coming out of the building, CO and HCN levels were heading towards safe levels and the firefighters made a plan to open the door.

Figure 6.12: Firefighters opening door a few minutes before explosion.[5]

The door was opened to the ESS at 20:00:54. A deflagration occurred which firefighters described as a loud noise and a jet of flame extending 75 ft outward and 20 ft vertically from the open door. During this event, the two firefighters by the door were thrown from their positions. One firefighter went through a chainlink fence and ended up in a bush 73 ft from the door. The flame extended such that the bush the firefighter landed in was burning after the deflagration. The other firefighter was thrown 30 ft. All four firefighters that had been in the area of the deflagration lost

consciousness. [5].

Figure 6.13: Rear door was blown off and wall was deformed after ESS explosion. [5]

Figure 6.14: Green side door was blown off the building and into the fence. [5]

Inside the ESS, it was found that only a single rack (rack 15) was involved in the incident. This rack was blackened and melted aluminum was found on the floor below it. Investigators determined that there was not evidence of significant flaming combustion within the compartment [128].

The events of this incident generally align well with experimental and modeling results of lithium-ion battery thermal runaway incidents. The voltage drop of 4.08V noticed at the beginning of the incident is consistent with observations of voltage dropping by the cell voltage for each that fails as seen in the experiments in Chapter 2. The propagation of thermal runaway from a single pouch cell into adjacent pouch cells was also observed in Chapter 2. In this incident runaway also propagated from module to module within the rack.

Gas release and gas properties is not publicly available for these cells, so the closest available data will be used. Viswanathan and Paiss report gas release data taken from a UL 9540A report [2]. This data is for a 72.5 Ah NMC pouch cell that is used for energy storage applications. The LG Chem JP3 pouch cells used in the McMicken facility are NMC pouch cells with a capacity of 64 Ah. The models previously described were used to calculate gas properties for the mixture. The mixture is given in Table 6.4 and the calculated properties used for explosion hazard analysis are provided in Table 6.5.

Using $r = 0.37L/Wh$ and the rack energy of 93.8 kWh, the volume of released gas is estimated to be 34.7m^3. With dimensions of 50 ft x 12 ft x 13 ft, the volume of the building is 220 m^3. The volume of gas is 15.7 % of the volume of the entire build-

Table 6.4: Species Volume Percentage for gases released by 72.5 Ah NMC Pouch Cell from Viswanathan [2]

Species	**Volume Percent**
Hydrogen	31.2%
Carbon Dioxide	28.9%
Carbon Monoxide	24.4%
Total Hydrocarbons	15.5%
Other	0 %

Table 6.5: Gas Release Properties based on NMC Cell described by Viswanathan[2]

Parameter	**Symbol**	**Value**	**Units**
Gas Released per nominal capacity	r	0.37	L/Wh
Lower Flammability Limit	LFL	6 %	
Upper Flammability Limit	UFL	36%	
Stoichiometric Volume Concentration	Xf	17%	
Heat of Combustion (LHV)	Δh_c	17.1	kJ/g
Maximum Pressure	P_{max}	8.54	bar
Expansion Ratio	σ	7.30	
Burning Velocity	S_u	0.53	m/s
Unburned gas density	ρ_u	1.17	kg/m3
Burned gas density	ρ_b	0.16	kg/m3
Unburned Ratio of Specific Heats	γ_u	1.37	
Burned Ratio of Specific Heats	γ_b	1.24	
Unburned Gas Sound Speed	a_u	345	m/s

ing. Given a LFL of 6 %, this means that it is possible for a well-mixed flammable mixture to fill the entire structure.

The ternary plot shown in 6.15 was created to describe the sequence of events that led to the explosion. The ternary plot represents the average composition of the air in the structure as a mixture between battery gas (fuel), air and inert. This ternary plot was created using combustion products of nitrogen, carbon dioxide and water as inert. Using NOVEC 1230 as the inert would produce different flammable ranges but follow the same general shape.

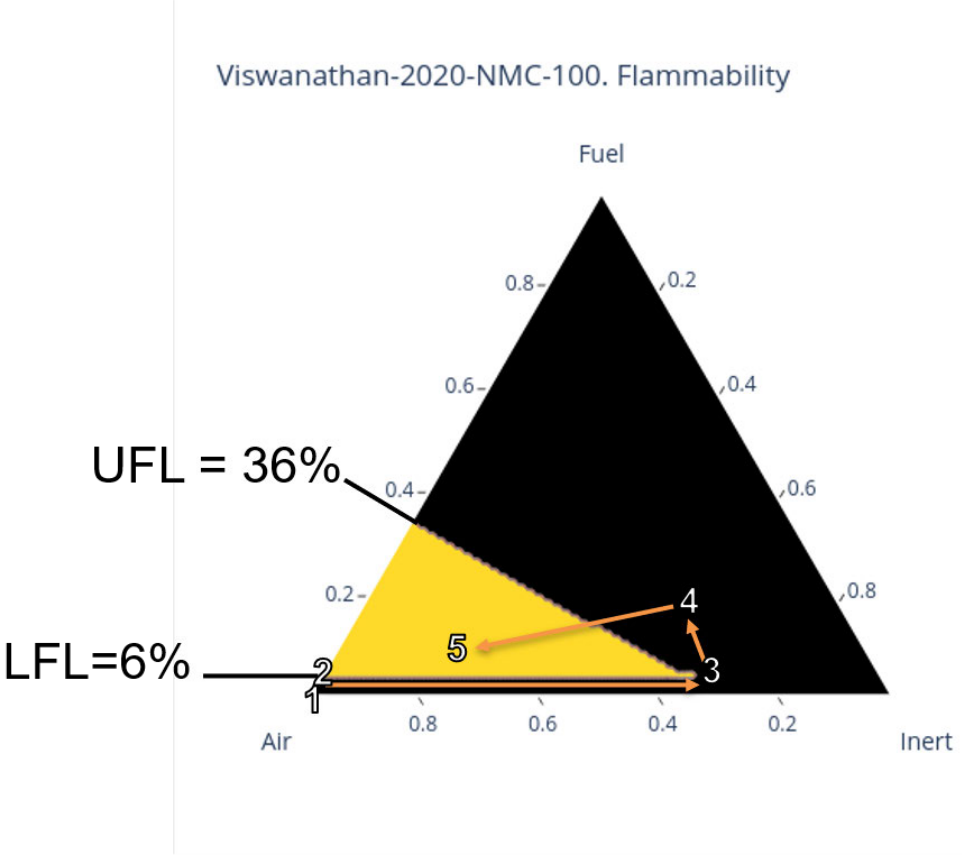

Figure 6.15: Ternary plot showing flammability ranges for NMC vent gas, air and inert products mixtures

The events of this incident are as follows:

1. Initially the compartment is full of air.

2. After thermal runaway of the first cell(s) a small amount of battery gas (fuel) is introduced into an environment which is still mostly air.

3. After activation of the smoke alarm system, the inert clean agent (NOVEC-1230) is released in an attempt to extinguish all combustion in the compartment.

4. As the cells continue in runaway, more flammable battery vent gas is released into the room.

5. Air is introduced into the building through leakage and eventually through the opening of the door by firefighters.

6. A flammable mixture now exists and can be ignited if put into contact with hot surfaces (which may exist due to runaway) or to electrical arcing (which may exist due to high voltage batteries and damage).

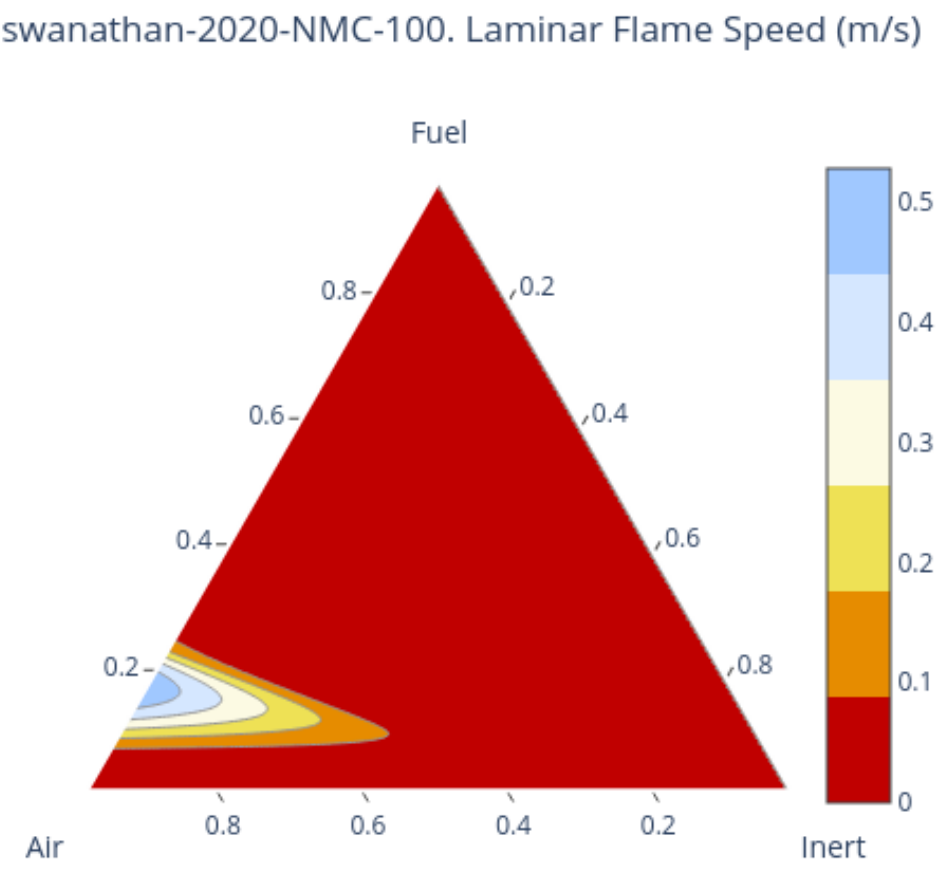

Figure 6.16: Ternary plot showing laminar flame speed for mixtures of NMC vent gas, air and inert products mixtures

6.3 Minimum Energy Storage to Produce Explosions

A common first step in explosion analysis is to determine whether or not an explosion can occur. As discussed in section 5.1, there are several pathways that can lead

to different explosion scenarios. There are three different explosion events that are of interest:

1. Sufficient gas is released and good mixing does not occur, which makes it possible for a partial volume deflagration to occur and cause damage greater than a threshold pressure, P_{dam}.

2. Sufficient gas is released and mixing occurs such that the entire volume can reach LFL. An explosion may occur when an ignition source is provided anywhere in the entire volume.

3. Sufficient gas, combustion products and suppression agents are released such that combustion in the entire volume is oxygen limited. Given a source of ignition, this makes it possible for an explosion to occur only after additional air has been introduced. If only battery vent gas has been released, this occurs at gas releases exceeding X_{UFL}.

In a single incident, explosions may be possible from each of these scenarios. Partial volume deflagrations are more likely early in an event before enough gas has been released to fill the entire volume and before the gases have time to mix well with surrounding air. As more gas is released it is possible to achieve an average concentration exceeding LFL in the entire volume. This larger volume of gas may reach any ignition source in the room. If the volume of released gases, combustion products and suppression agents exceeds UFL in a compartment then the explosion may be caused by the re-introduction of air. Generally, as the volume of released gas increases, the chances of explosion increase as more means to an explosion become

possible.

Three critical volumes of gas can be used to determine which types of explosion are possible. These critical volumes can be expressed as average concentrations by dividing by the compartment volume:

$$X_{ave} = \frac{V_f}{V_{compartment}}$$

$$X_{ave} \geq X_{pvd} = X_{st}\frac{P_{dam} - P_0}{P_{max} - P_0} \quad \text{Partial volume deflagration possible [71]} \quad (6.12)$$

$$X_{ave} \geq X_{LFL} \quad \text{Full Volume deflagration possible} \quad (6.13)$$

$$X_{ave} \geq X_{UFL} \quad \text{Oxygen-limited deflagration possible} \quad (6.14)$$

Using the library of gas compositions and gas properties it is possible to calculate the minimum average concentration X_pvd required to produce an explosion exceeding 0.02 bar. This can be done for each gas composition. Results are shown in Figure 6.21.

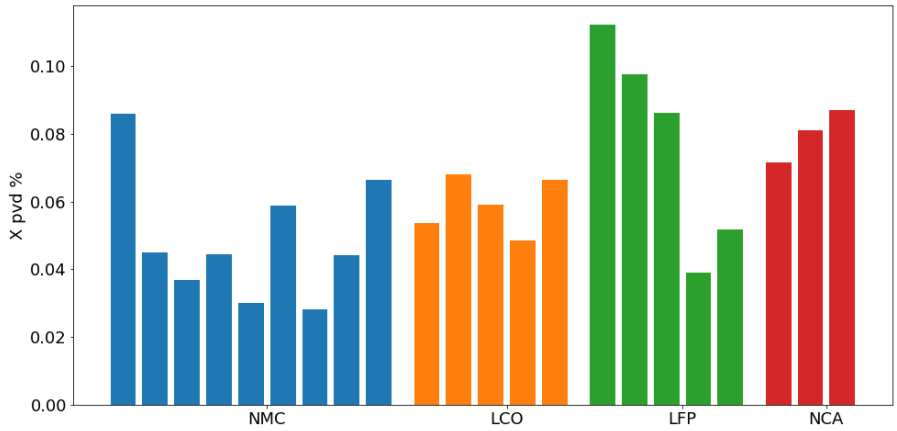

Figure 6.17: Minimum average concentration to cause a partial volume deflagration for various gas compositions from literature.

These concentrations can be converted to energy storage density using the gas release per watt-hour figure, r.

$$\frac{E_{stored}}{V_{compartment}} = \frac{1}{r}\frac{V_{fuel}}{V_{compartment}} = \frac{X_{ave}}{r} \tag{6.15}$$

Based on the gas composition data summarized in 5, the minimum amount of energy stored per volume required to reach partial volume deflagration, LFL and UFL concentrationsis summarized in Figures 6.21, 6.19 and 6.20.

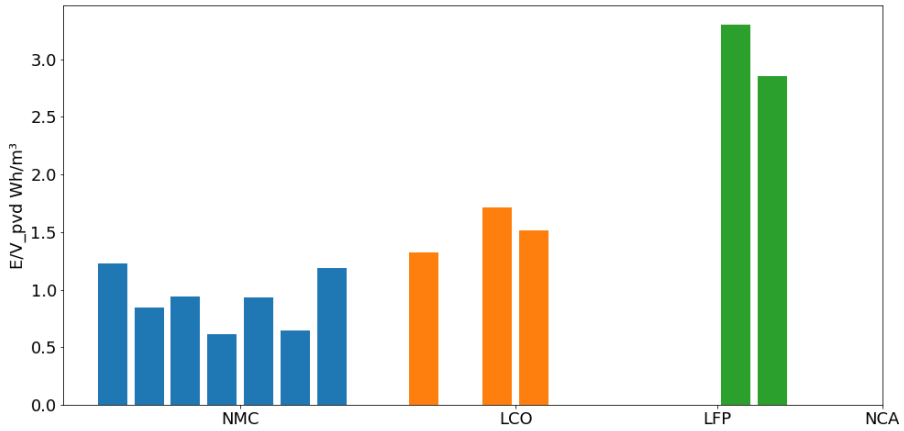

Figure 6.18: Minimum energy stored per unit volume required for partial volume deflagration

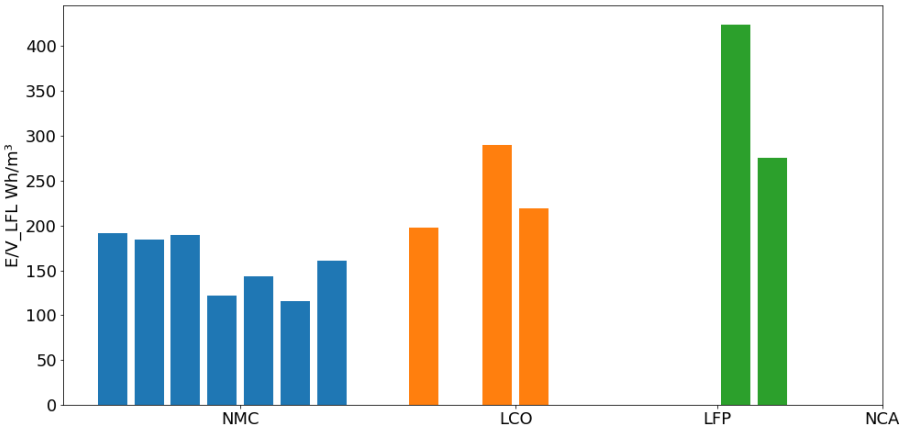

Figure 6.19: Minimum energy stored per unit volume required to reach LFL in full volume

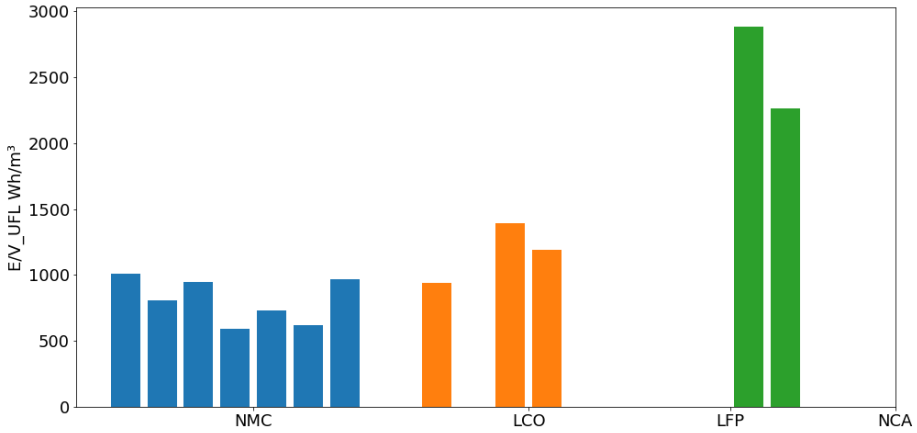

Figure 6.20: Minimum energy stored per unit volume required to exceed UFL in full volume

These minimum energy stored per volume can be used to develop a graph showing the limits for each type of explosion. This can be used to compare explosion hazards. It can also be used to determine what types of explosions are possible for a given energy stored and volume.

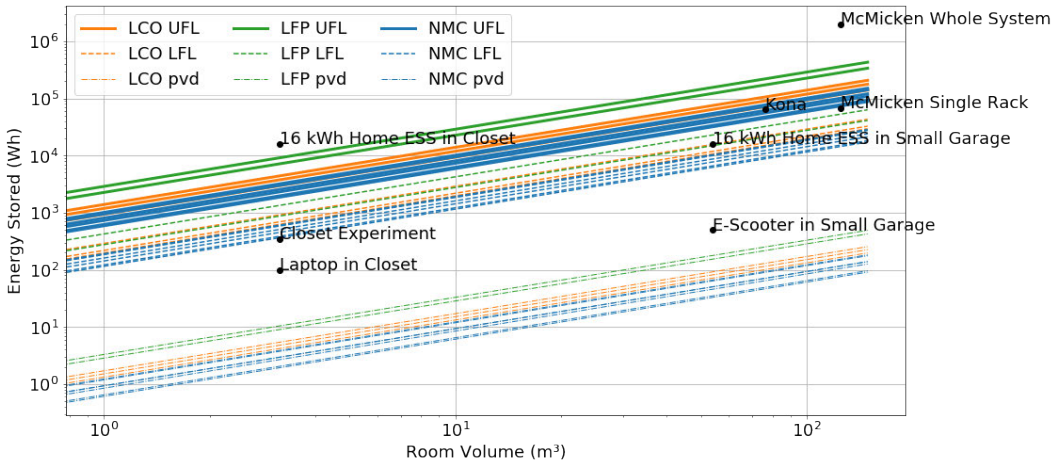

Figure 6.21: Minimum energy stored per unit volume required for partial volume deflagration

6.4 Conclusions

In this chapter the models from Chapter 5 were applied in various ways. A sensitivity analysis was used to determine the effect of unknown gas mixtures and model error to structural displacement and damage of a steel panel wall system. The wall's displacement and damage is most sensitive to the error in the vented deflagration model and the variation of burning velocity due to the range of possible battery vent gas compositions.

A case study was performed based on the Hyundai Kona explosion in Montreal Canada. This case study is evidence of how a typical car in a typical garage has enough energy stored to cause a serious explosion. This case study showed how effective the large garage door area was at reducing the overpressure in the garage and preventing the complete collapse of the entire garage.

The McMicken Arizona case study was useful to look at a series of events can lead to an explosion. A ternary plot was used to demonstrate how the gas composition in the compartment could have changed throughout the incident and made the explosion possible.

Finally, the concept of partial volume deflagrations is applied to battery systems to determine the quantity of energy storage required per volume to cause a deflagration. These values are compared against experiments and incidents to show how much fuel could have been available in each deflagration.

Chapter 7

Conclusions

This work has covered a broad range of topics spanning the breadth and depth of fire and explosion hazards associated with lithium-ion battery thermal runaway propagation.

Chapter 2 examined the thermal runaway process for both single pouch cells and arrays of pouch cells in direct contact. These experiments show that the thermal runaway process can be different in cells failed with heaters when compared to those failed to due propagation from other cells. Cells which failed due to runaway propagation exhibit less damage inside and fail more slowly. This chapter also highlighted the usefulness of load cells to measure the change in clamping stress during the course of thermal runaway experiments. The load cell clamping stress data is useful because it provides insight into the buildup of pressure within a cell as it heats up and goes into thermal runaway.

Chapter 3 looks at thermal runaway propagation in a more complex geometry. In

this chapter single cells are failed to better understand the behavior of a 4.8 kWh module during thermal runaway propagation. Three 4.8 kWh modules are put into thermal runaway and temperatures are recorded inside the module and rack as well as throughout the compartment. A CFD model is developed to be able to approximate the heat release from lithium-ion cell thermal runaway. An approach is demonstrated to use CFD modeling to model fires with thermal runaway propagation in a compartment. The model performs well at predicting temperatures throughout the compartment, although the model seems to underpredict lower level temperatures near the module. The model can also be used to predict heat fluxes and gas concentrations. A key limitation of this model is that it requires knowledge of the thermal runaway propagation times and the polycarbonate burning rate to be able to estimate heat release rate.

Chapter 4 describes the development of systems to conduct explosion experiments with lithium-ion batteries. These systems are used to conduct explosion experiments in enclosures from small laboratory scale up to full-sized closet scale. These experiments demonstrate the challenges associated with lithium-ion battery explosions. Pouch cells and prismatic cells are both observed to be capable of ejecting hot particles and igniting deflagrations on their own. Oxygen-limited explosions are observed in which ignition is not possible until after the gases have diluted with air. A partial volume deflagration is observed in a closet, which causes a sufficient overpressure to fail the closet door. This demonstrates the possibility of battery systems both releasing the flammable gas and providing the ignition source to cause a deflagration even before detection and ventilation systems can detect the hazard.

Chapter 5 describes a number of models that can be used to determine whether an explosion hazard exists and what consequences may occur. This chapter provides a comprehensive review of gas compositions produced by lithium-ion cells in thermal runaway. It uses models to determine a variety of properties for each vent gas mixture. Models are described for determining flammability limits, laminar flame speed maximum explosion pressure, heat of combustion and other gas properties. Experimental data is used to validate and characterize model error for two laminar flame speed models. Vent gas explosion models are also reviewed. A 0D ODE based model is modified to be able to predict pressure time histories including the effects of vent opening pressures and turbulent flame acceleration. Vented deflagration models are validated against experimental data and a model error is characterized. A single degree of freedom, structural response to blast model is also validated and its model error is characterized. These models can be used together to understand possible consequences due to a lithium-ion battery involved explosion.

Chapter 6 applies the models from Chapter 5. A sensitivity analysis shows that structural damage is most sensitive to model error in the vented deflagration model. Case studies of incidents are reviewed to understand how models can provide insight into their outcomes. The Montreal garage explosion incident is used to demonstrate the usefulness of the vented deflagration model. The incident and model show the importance of having a large vent area available which serves to reduce the pressure and reduce damage to other parts of the structure. The McMicken Arizona incident is used to demonstrate the usefulness of ternary plots in determining the flammability of flammable gas mixtures for battery incidents. Partial volume deflagration mixing models along with battery gas data is applied to determine the minimum

amount of gas required to cause a deflagration. This analysis reveals that damaging explosions are possible with rooms in which the volume of gas released is well less than 1 % of the volume of the compartment.

The experiments in Chapters 2, 3 and 4 along with the models discussed in chapter 5 and 6 provide insight into the unique hazard of explosions involving lithium-ion batteries. Unlike many flammable gas explosions, lithium-ion batteries are capable of producing both a gaseous fuel and an ignition source. The location and timing of these fuel and ignition sources along with the geometry of the system and its surroundings can have very large effects on the outcome of the incident. Incident outcomes can include gas release only (as seen in the LFP cells in Appendix B), fire only (as seen in NMC modules in Chapter 3) and explosion as seen in Chapter 4. It is also possible that in a single incident gas accumulation, explosion and fire can all occur for the same compartment at different times as shown in Section 4.3.1.

Lithium-ion cells and systems can provide multiple ignition opportunities. As shown in Figure 3.8, an ignition can occur due to an electric arc even before intense venting due to thermal runaway. In this case the 4.2 V of just a single cell was sufficient to ignite the flammable vapors coming from the cell. Later, as intense venting occurs, ignition is possible due to the ejection of hot solid materials. These materials may be glowing hot and can be seen in Figures 4.22 and 4.31. After a cell has gone into thermal runaway and produced a flame, this flame can cause piloted ignition to plastic housings and subsequent cells which in turn can pilot later gas releases due to runaway. Piloted ignition is evident in the continued burning of the module in open air described in 3.3.3. Although not observed in these experiments, it may

be possible that cells themselves may be hot enough to cause ignition after thermal runaway.

The flammable gas release profile for lithium-ion batteries is also unique. The release of flammable gas in a lithium-ion battery system depends on the kinetics of thermal runaway which drives the heat generation. As heat is generated, runaway reactions occur which release flammable gases. This heat may transfer into other cells and cause the propagation of thermal runaway as seen in Chapter 2 and 3. Having a gas release driven by heat generation is similar to solid and liquid fires in which the heat released by a fire causes vaporizaton or pyrolysis which produces more flammable gases. Most conventional fires can be extinguished through cooling or oxygen reduction because the fire needs heat and oxygen to grow. Unlike conventional solid and liquid fires, the reactions causing heat and gas generation in a lithium-ion cell are inside the cell. This makes them very difficult to cool sufficiently to stop runaway. Since the reactants for thermal runaway are all self-contained in the cell, the removal of oxygen may not stop the thermal runaway process either. For example, in the array experiments in Section 2.3, a single cell was failed in a nitrogen environment and thermal runaway propagated to the remaining cells in the array. The ability of lithium-ion cells to continue to produce flammable gases regardless of oxygen deprivation or external cooling makes them a unique fire and explosion hazard. The generation of gases is also different from most flammable gas explosions as well. Unlike a flammable gas pipeline leak, the flow of flammable gases cannot be turned off. Unlike the release of flammable gases from a container, it is usually not possible to plug or cool a cell to stop the release of flammable gases. Another key difference in fuel release for lithium-ion cells is the time profile. Lithium-ion cells often release no

gas or only small amounts of gas while heating, but then release a very large amount of gas in a short time period as they progress in thermal runaway. This unusual gas release time profile can also influence the outcome.

A key factor in the outcome of a runaway event is the timing of the ignition source and fuel release. For both the pouch cells and the prismatic cells used in this work, the hot particle ejection ignition source occurs early in the intense venting process. For the pouch cells, ignition may not have been reliable because the surrounding mixture of gases wasn't flammable. For the prismatic cells, ignition started out as intermittent as initially there was either too much shear or only pockets of gas were flammable. As thermal runaway propagates and more cells become involved, this will generate more flammable gas and more ignition sources and, unless oxygen deprived, would be expected to increase the chances of ignition.

Another factor which determines the outcome of a runaway incident is the geometry of the battery system and the compartment. As shown with the 94 Ah cell, it caused a jet flame when in a larger room (Figure 3.9), but caused an explosion with an overpressure sufficient to break the drywall door panel when confined in a smaller closet space. The same cell within a module inside a very leaky rack produced a deflagration with a audible bang which kicked up dust but did not cause any overpressure damage.

Available deflagration venting area is another factor in the consequences of explosions. This can be seen in real incidents. In the Houston rail car incident, the rail car did not have any weak area which could fail and act as a deflagration vent. Since

excess pressure could not vent, the car pressurized until the entire car ruptured catastrophically. In contrast, for the Montreal Hyundai Kona explosion, pressure vented through a large garage door, which reduced the pressure sufficiently to make it possible for most of the rest of the garage to remain standing.

This work has investigated the fire and explosion hazards of lithium-ion battery systems using a wide range of experiments and models. Thermal runaway of just a single cell in lithium-ion systems can, unless mitigated, propagate to entire systems and cause the release of large amounts of flammable gas. Depending on ventilation conditions, ignition sources and fire suppression these flammable gases can either cause a fire or an explosion. This work has demonstrated one way to develop a CFD model to replicate an experiment featuring a battery system in a compartment fire. This work has also described models that can be used to estimate possible explosion consequences. Models developed to estimate the minimum quantity of energy storage needed to cause an explosion show that even very small amounts of batteries when put in a small space are capable of causing explosions.

Appendix A

Module Experiments Supplemental Data

This appendix provides additional details from the module and rack experiments described in Chapter 3.

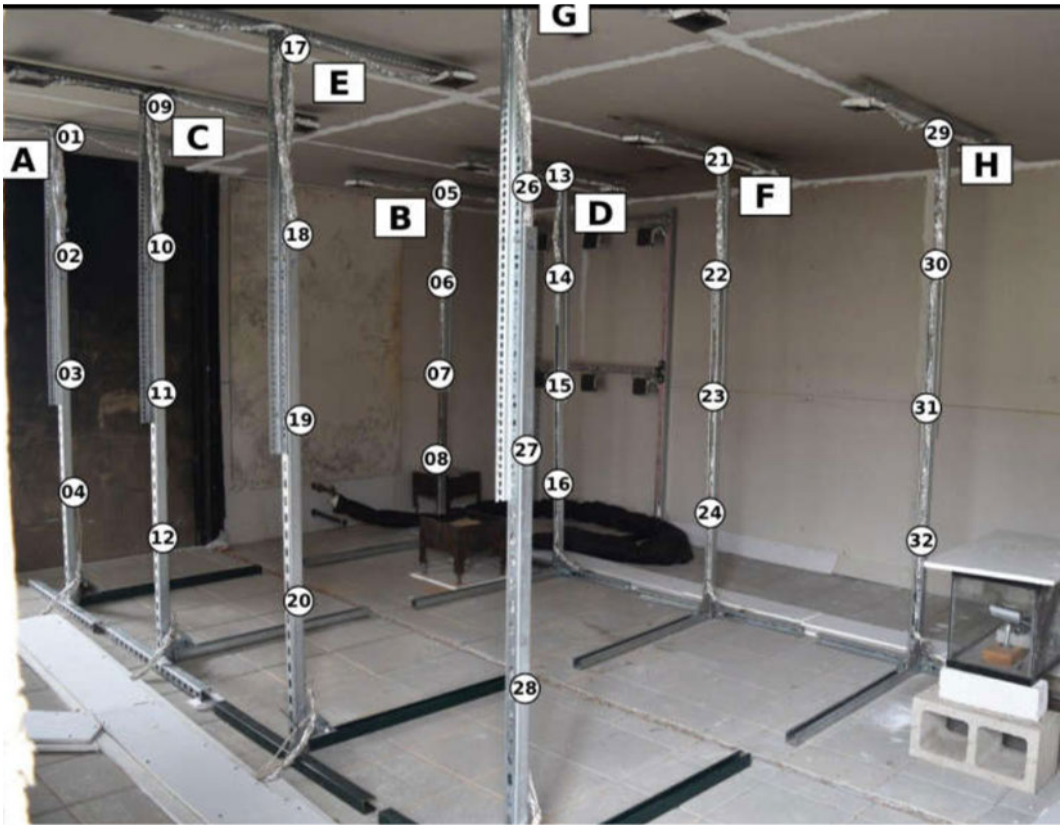

Figure A.1: Location of thermocouples in burn structure compartment [15]

Experiment Setup

Open Air Module Experiment

Cell Temperatures For the open module experiment, cell temperatures were recorded for both short sides (East and West) of each cell as well as the cell vent for each cell. Locations of the thermocouples are presented in Figure 3.3.

Figure A.2 summarizes the temperature data collected from all the cells. The first seven cells are shown above and the next seven are shown below.

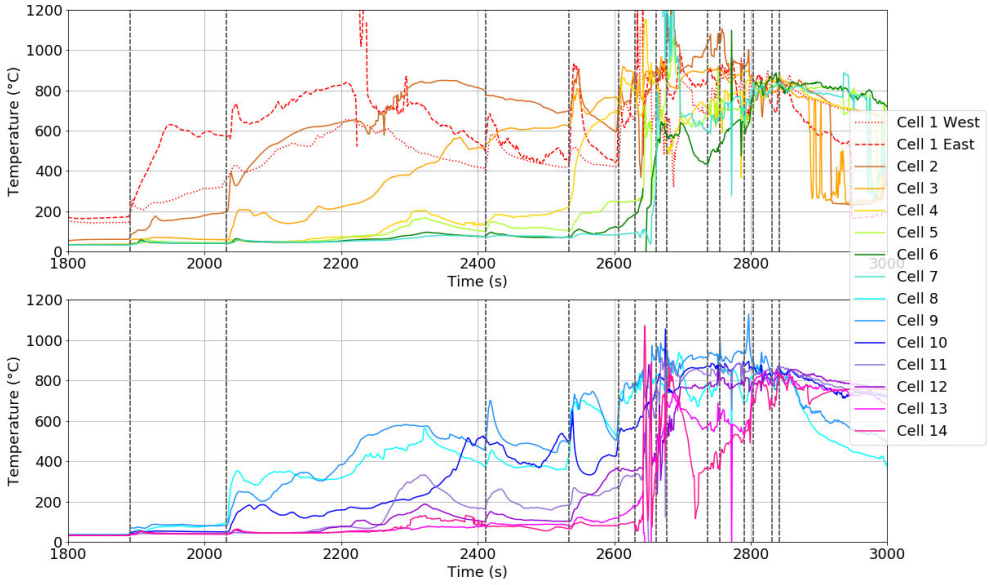

Figure A.2: Open Module Experiment Cell Temperatures

The temperatures for each cell are shown individually in Figures A.3, A.4 and A.5.

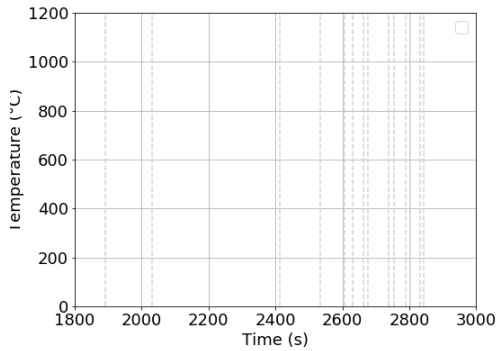

(a) Cell 1

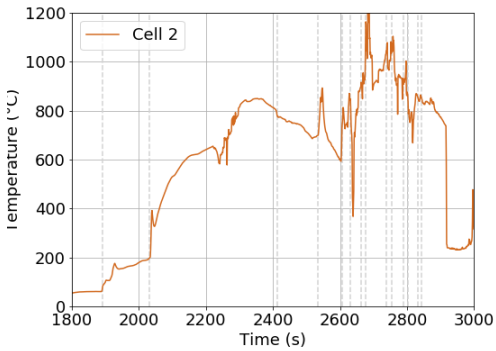

(b) Cell 2

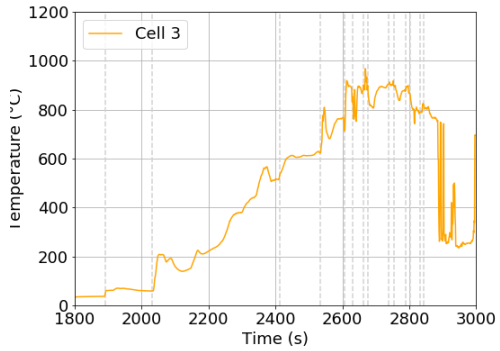

(c) Cell 3

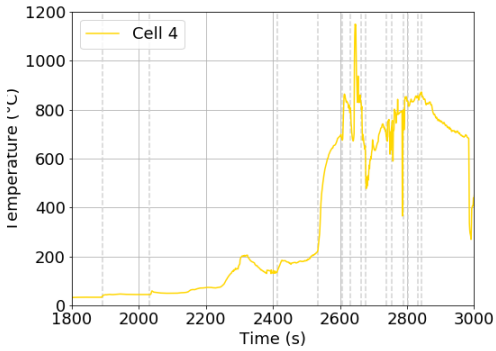

(d) Cell 4

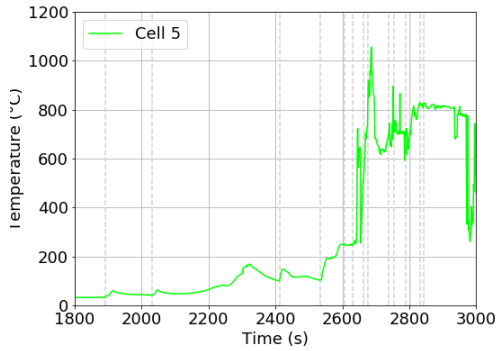

(e) Cell 5

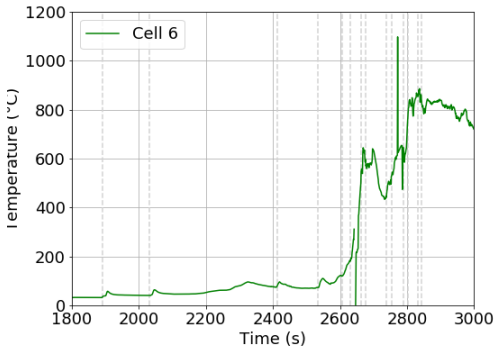

(f) Cell 6

Figure A.3: Open Module Experiment Cell Temperatures

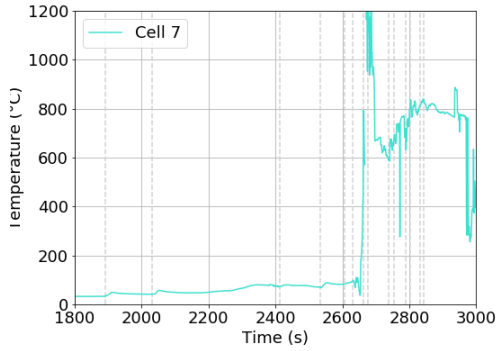

(a) Cell 7

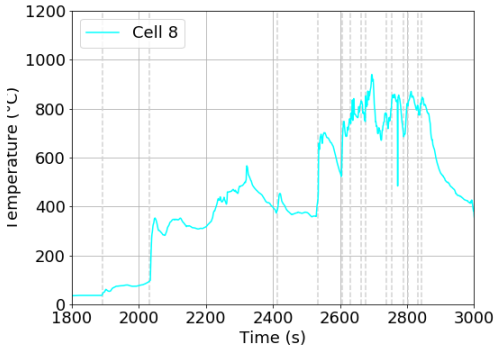

(b) Cell 8

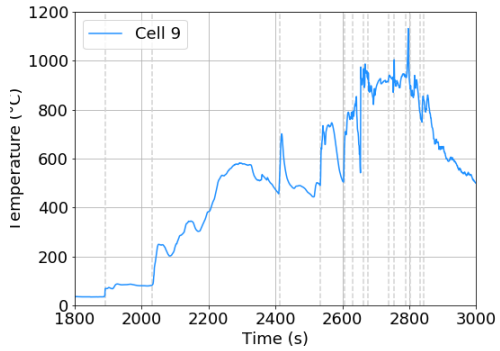

(c) Cell 9

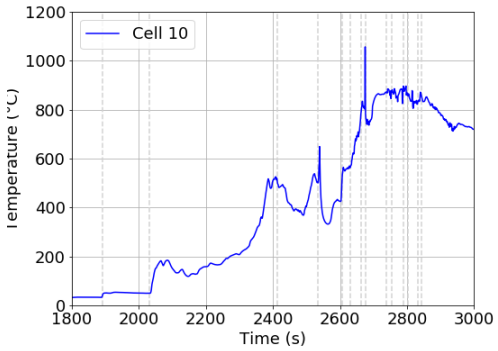

(d) Cell 10

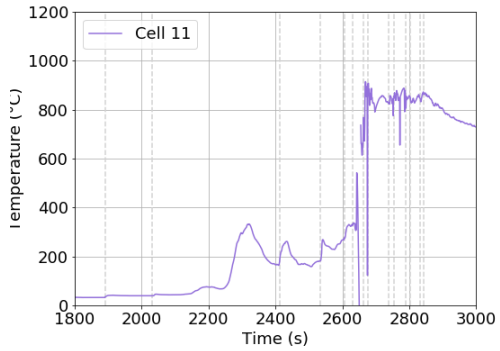

(e) Cell 11

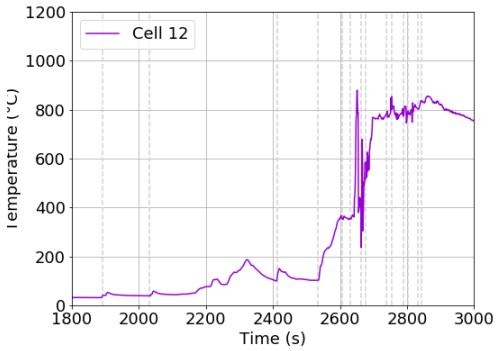

(f) Cell 12

Figure A.4: Open Module Experiment Cell Temperatures

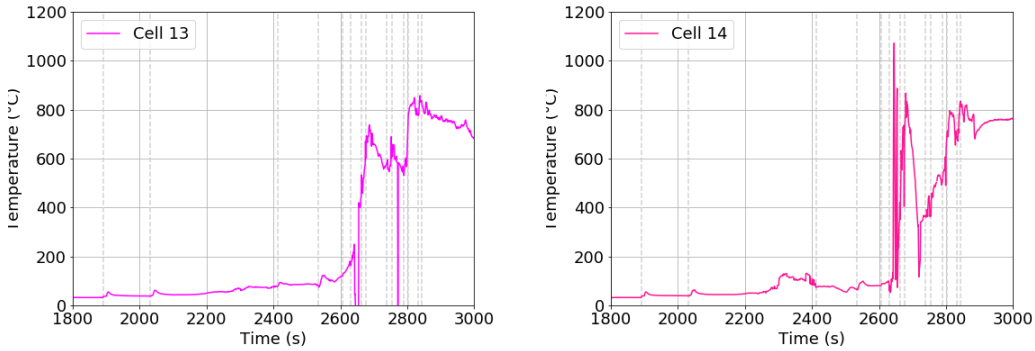

(a) Cell 13

(b) Cell 14

Figure A.5: Open Module Experiment Cell Temperatures

Module Gas Temperatures Gas temperatures were also recorded within the module.

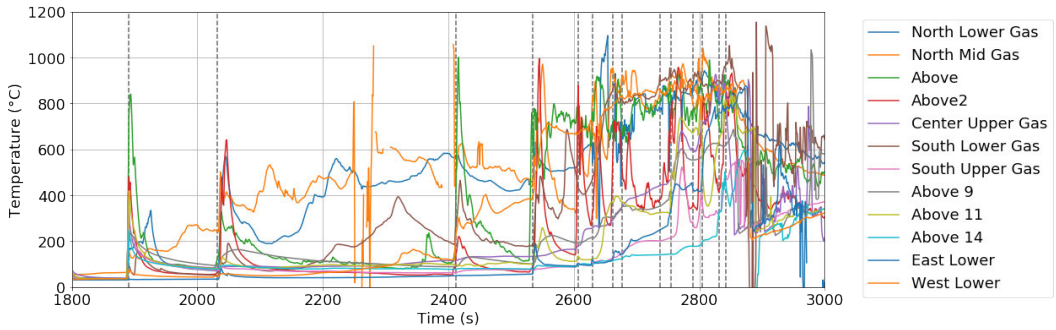

Figure A.6: Open Module Experiment Module Gas Temperatures

Compartment Gas Temperatures Gas temperatures were measured throughout the compartment using 32 thermocouples placed on 8 trees as shown in Figure A.1. Temperatures are measured at 4 different elevations, which are called ceiling, upper, mid and lower. Figure A.7 shows all the compartment gas temperatures over time from both the experiment and model. Figures A.8, A.9 and A.10 shows the gas temperatures for each tree individually for comparison between model and experiment.

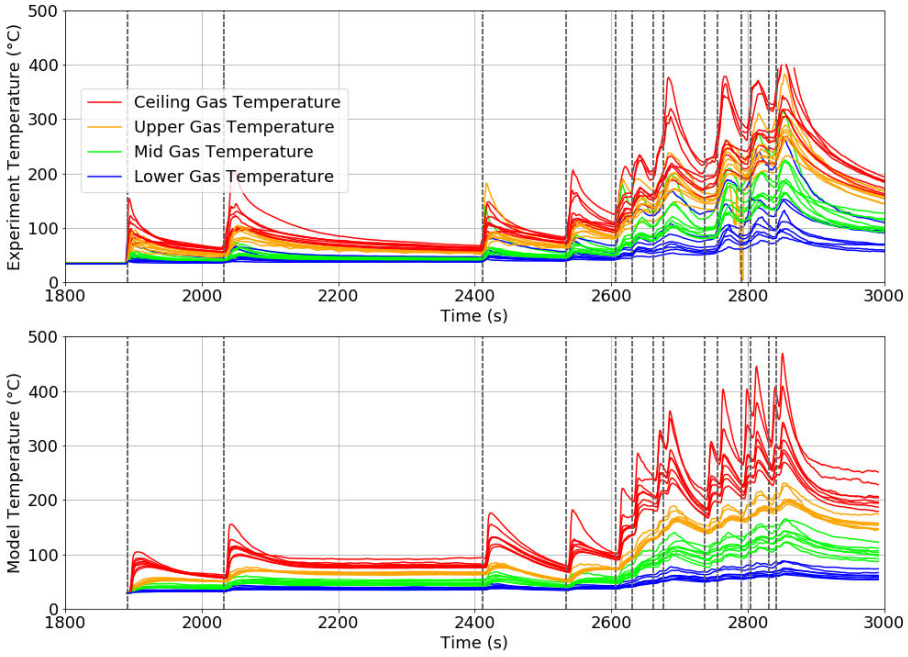

Figure A.7: Open Module Experiment Compartment Gas Temperatures from Experiment and Model

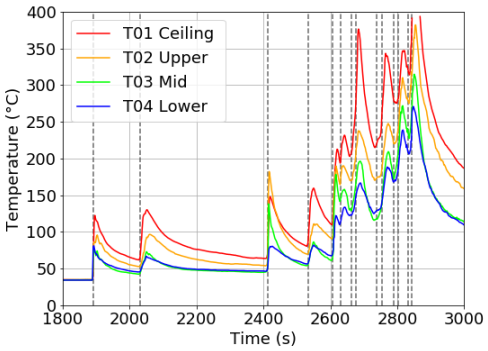

(a) Experiment Gas Temperatures TC 1-4

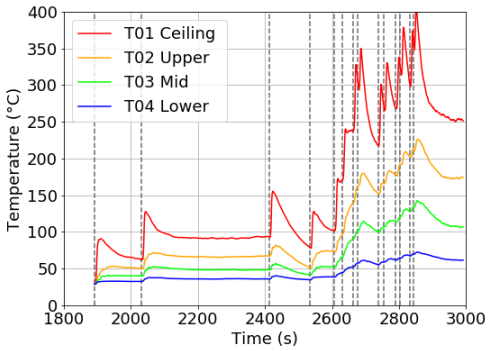

(b) Model Gas Temperatures TC 1-4

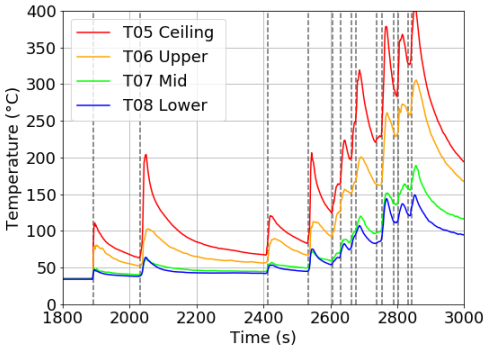

(c) Experiment Gas Temperatures TC 5-8

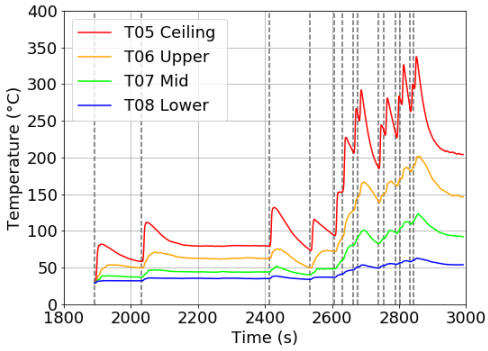

(d) Model Gas Temperatures TC 5-8

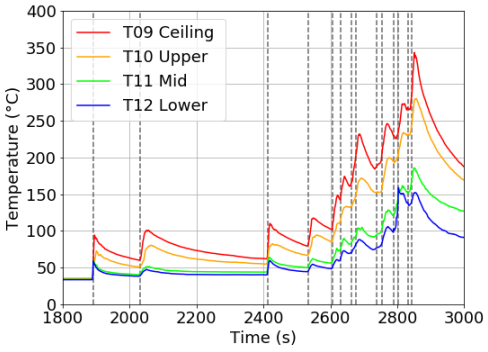

(e) Experiment Gas Temperatures TC 9-12

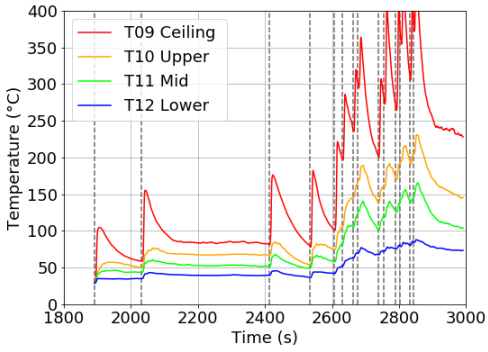

(f) Model Gas Temperatures TC 9-12

Figure A.8: Open Module experiment compartment gas temperatures from experiment and model.

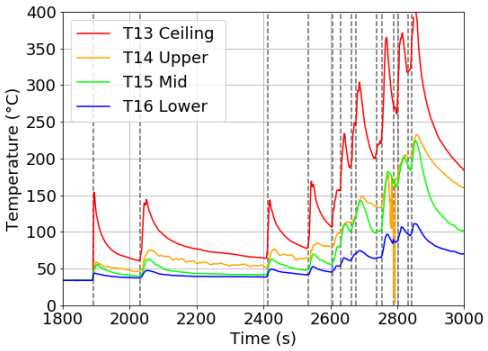

(a) Experiment Gas Temperatures TC 13-16

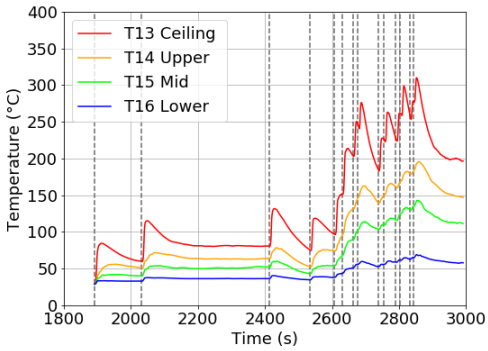

(b) Model Gas Temperatures TC 13-16

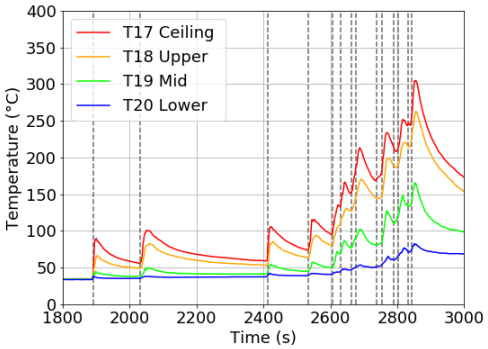

(c) Experiment Gas Temperatures TC 17-20

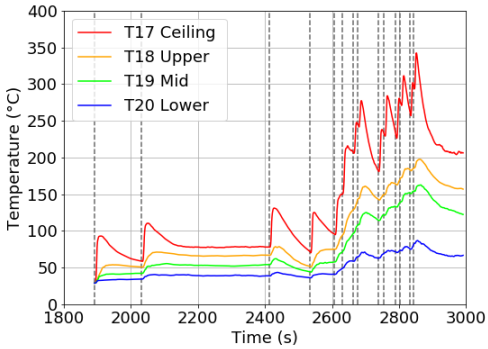

(d) Model Gas Temperatures TC 17-20

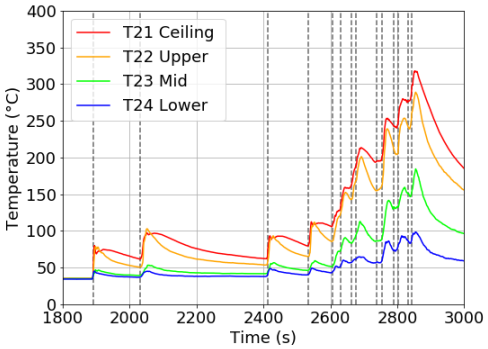

(e) Experiment Gas Temperatures TC 21-24

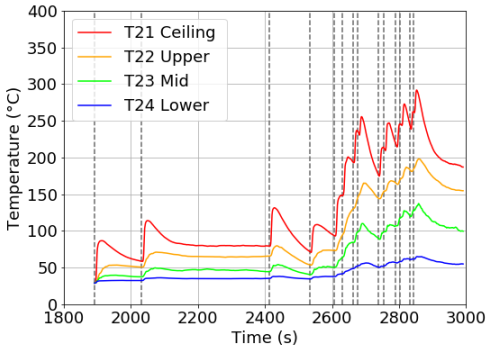

(f) Model Gas Temperatures TC 21-24

Figure A.9: Open Module experiment compartment gas temperatures from experiment and model.

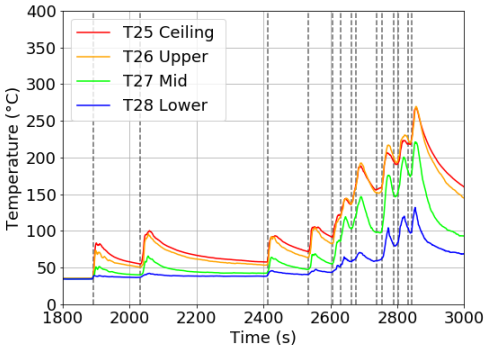

(a) Experiment Gas Temperatures TC 25-28

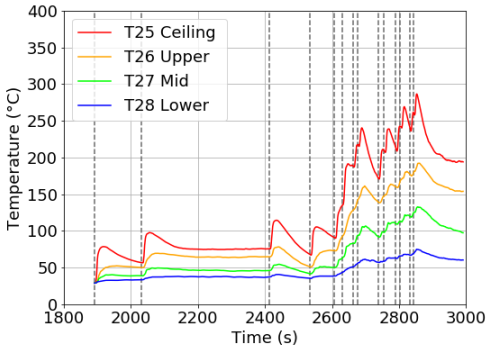

(b) Model Gas Temperatures TC 25-28

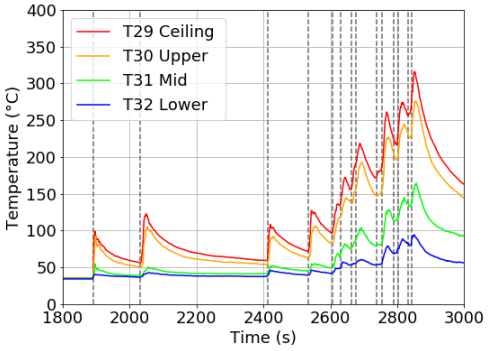

(c) Experiment Gas Temperatures TC 29-32

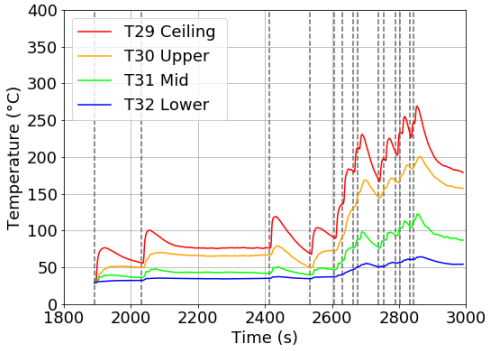

(d) Model Gas Temperatures TC 29-32

Figure A.10: Open Module experiment compartment gas temperatures from experiment and model.

First Rack Experiment

Cell Temperatures For the first rack experiment, cell temperatures were recorded for both short sides (East and West) of each cell as well as the cell vent for each cell. Locations of the thermocouples are presented in Figure A.11.

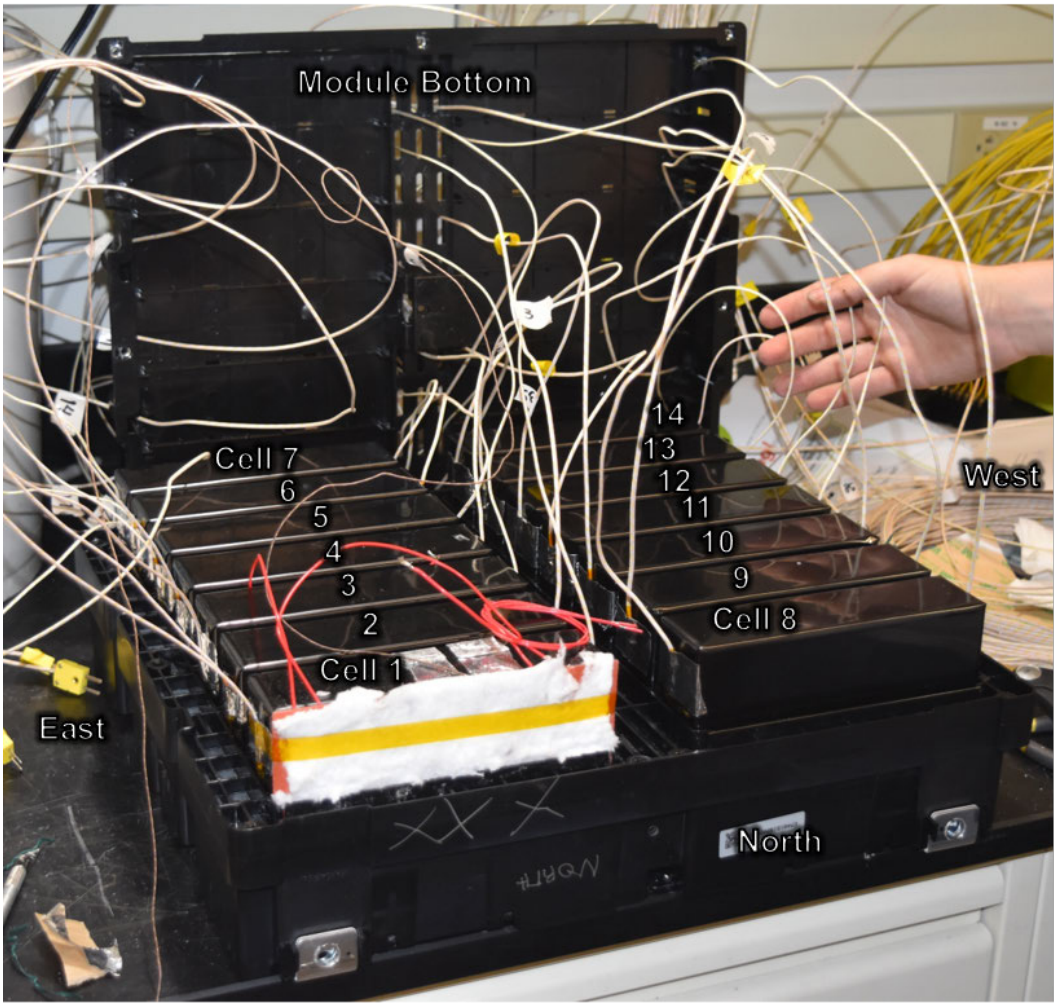

Figure A.11: First Rack Experiment Cell TC Locations

Figure 3.22 summarizes the temperature data collected from all the cells. The temperatures for each cell are shown individually in Figures A.12, A.13 and A.14.

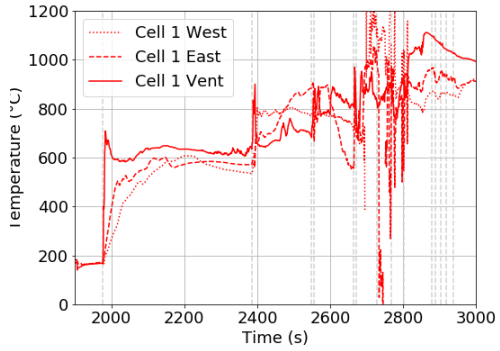

(a) Cell 1

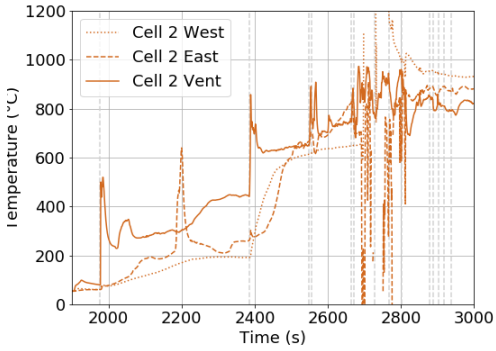

(b) Cell 2

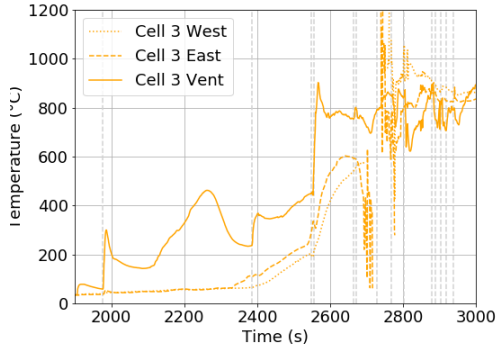

(c) Cell 3

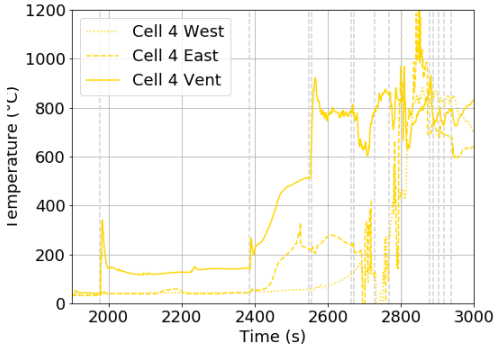

(d) Cell 4

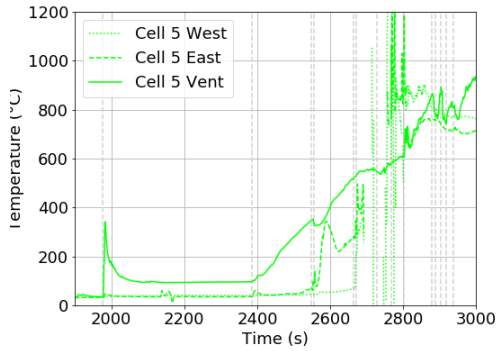

(e) Cell 5

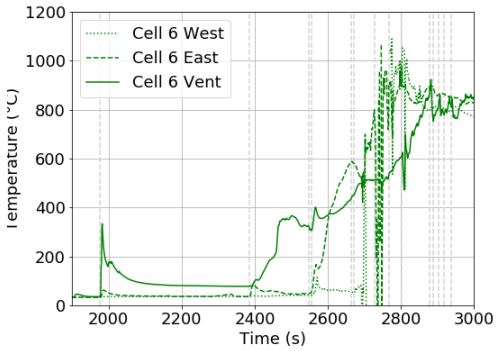

(f) Cell 6

Figure A.12: First Rack Experiment Cell Temperatures

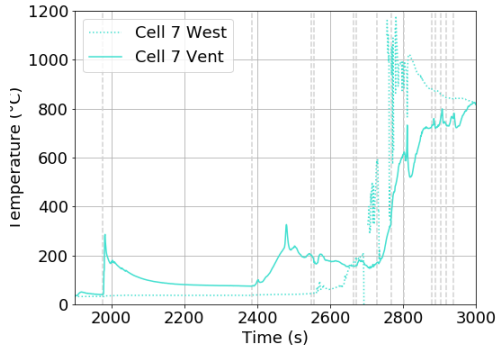

(a) Cell 7

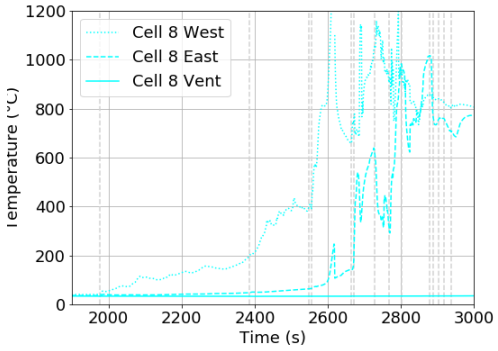

(b) Cell 8

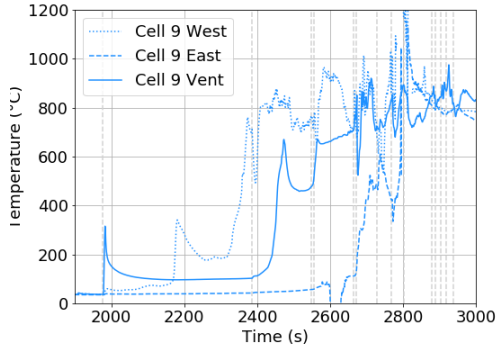

(c) Cell 9

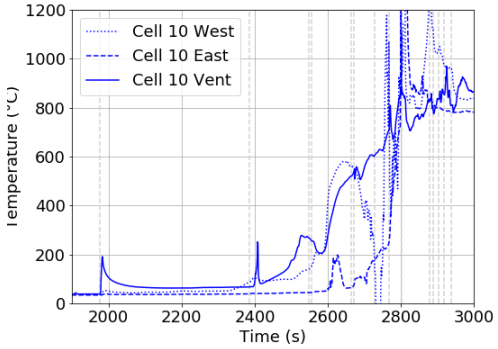

(d) Cell 10

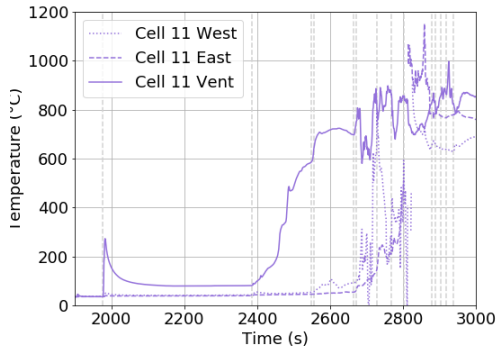

(e) Cell 11

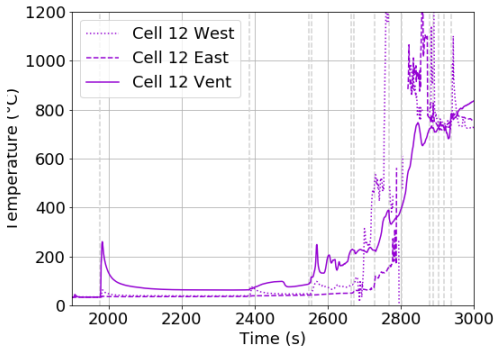

(f) Cell 12

Figure A.13: First Rack Experiment Cell Temperatures

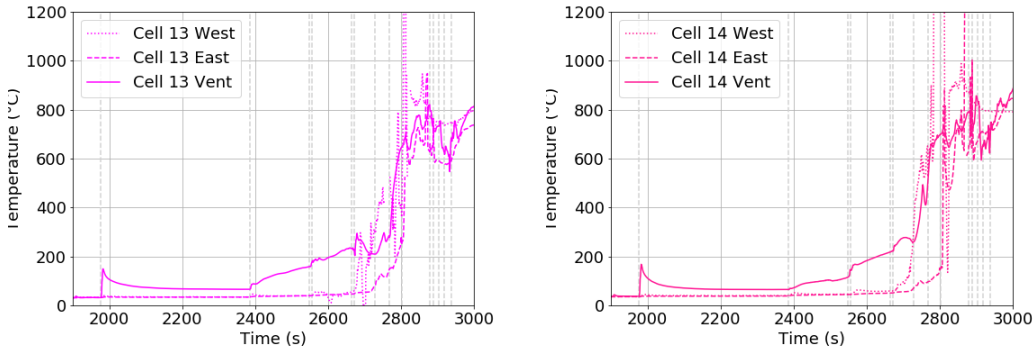

(a) Cell 13

(b) Cell 14

Figure A.14: First Rack Experiment Cell Temperatures

Module Rack Gas Temperatures Gas temperatures were also recorded within the module and within the rack.

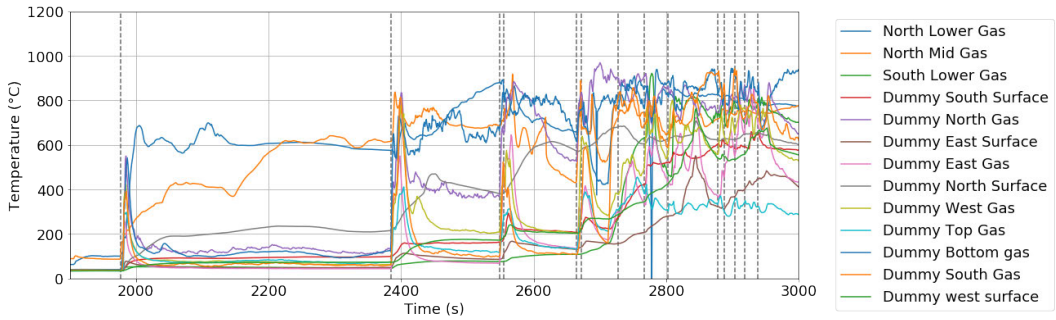

Figure A.15: First Rack Experiment Module and Rack Gas Temperatures

Compartment Gas Temperatures Gas temperatures were measured throughout the compartment using 32 thermocouples placed on 8 trees as shown in Figure A.1. Temperatures are measured at 4 different elevations, which are called ceiling, upper, mid and lower. Figure A.16 shows all the compartment gas temperatures over time from both the experiment and model. Figures A.17, A.18 and A.19 shows the gas temperatures for each tree individually for comparison between model and experiment.

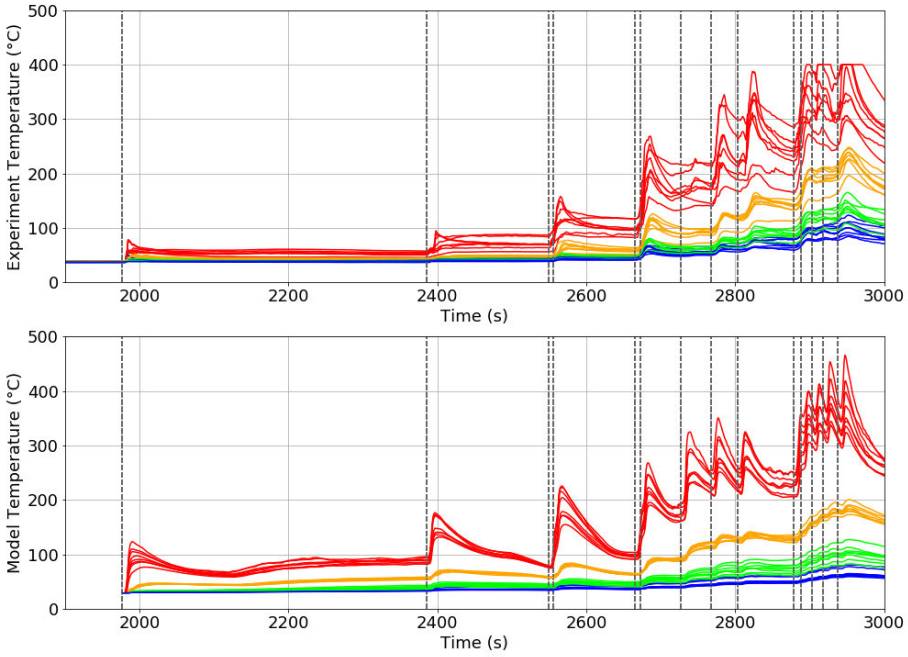

Figure A.16: First Rack Experiment Compartment Gas Temperatures from Experiment and Model

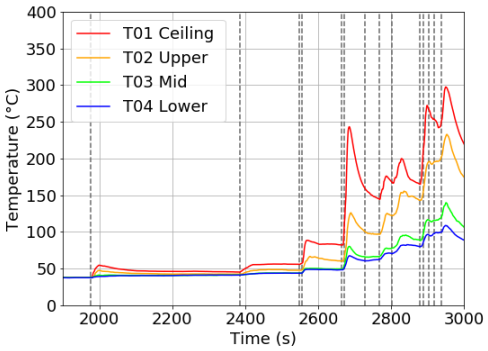

(a) Experiment Gas Temperatures TC 1-4

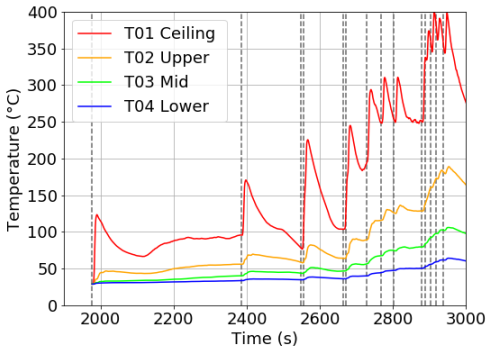

(b) Model Gas Temperatures TC 1-4

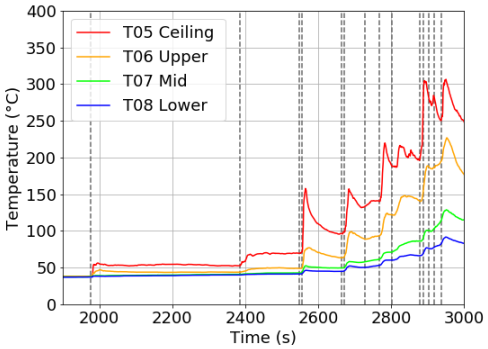

(c) Experiment Gas Temperatures TC 5-8

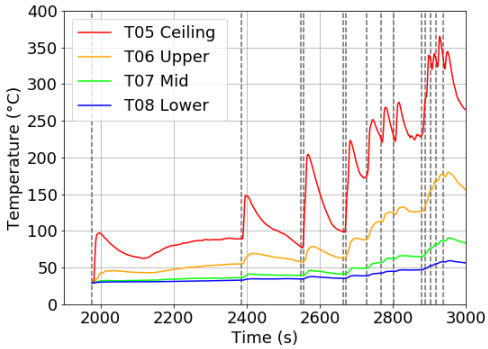

(d) Model Gas Temperatures TC 5-8

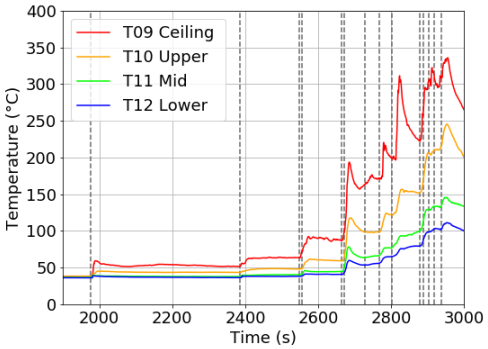

(e) Experiment Gas Temperatures TC 9-12

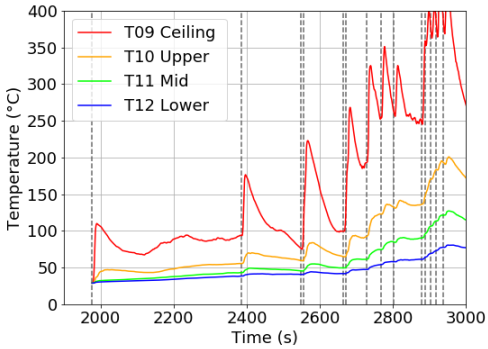

(f) Model Gas Temperatures TC 9-12

Figure A.17: First rack experiment compartment gas temperatures from experiment and model.

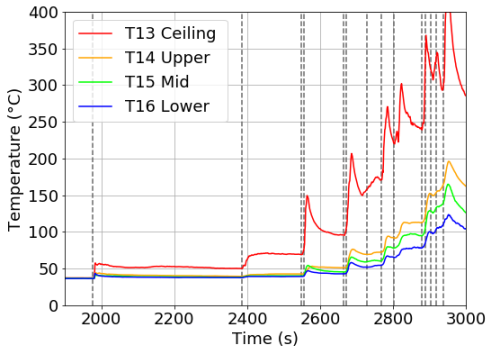

(a) Experiment Gas Temperatures TC 13-16

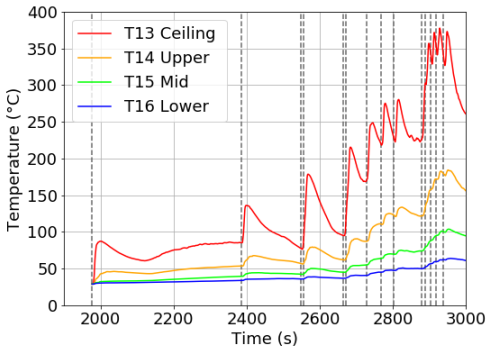

(b) Model Gas Temperatures TC 13-16

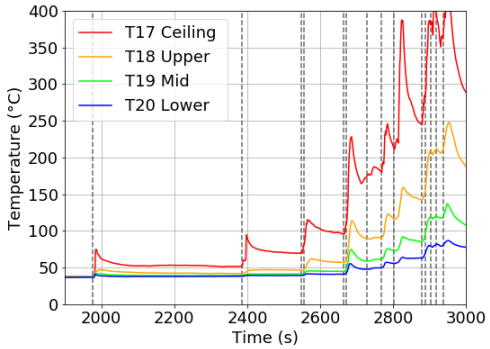

(c) Experiment Gas Temperatures TC 17-20

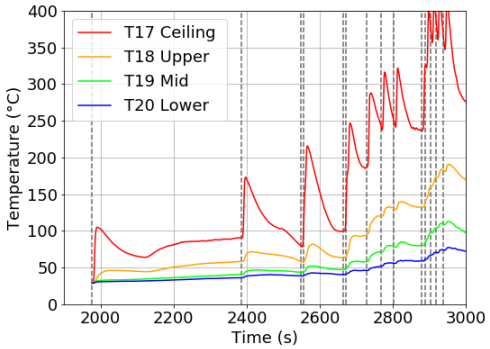

(d) Model Gas Temperatures TC 17-20

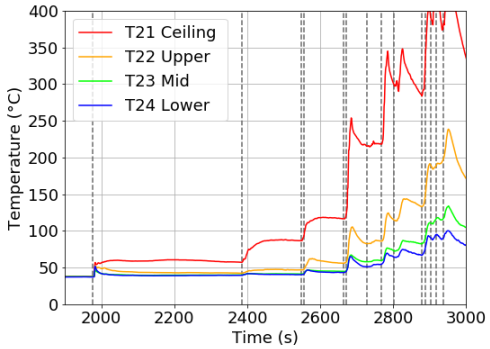

(e) Experiment Gas Temperatures TC 21-24

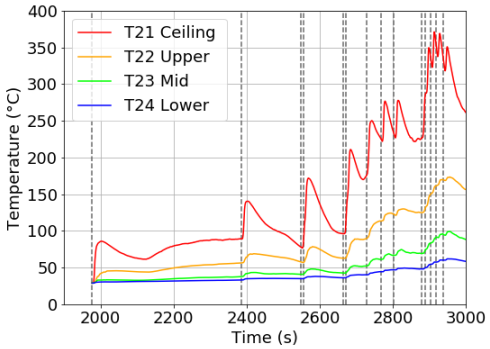

(f) Model Gas Temperatures TC 21-24

Figure A.18: First rack experiment compartment gas temperatures from experiment and model.

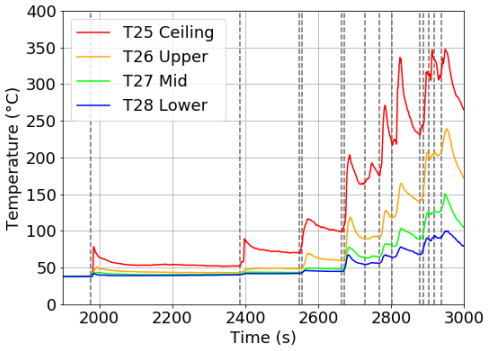

(a) Experiment Gas Temperatures TC 25-28

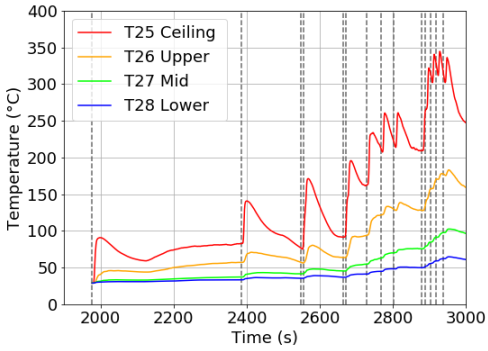

(b) Model Gas Temperatures TC 25-28

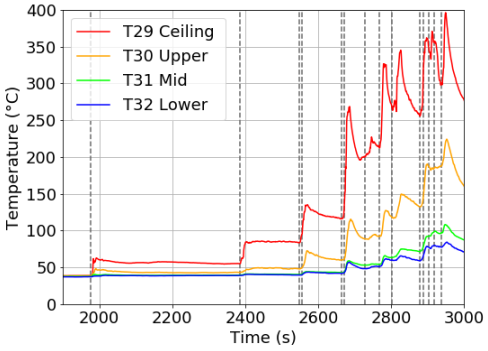

(c) Experiment Gas Temperatures TC 29-32

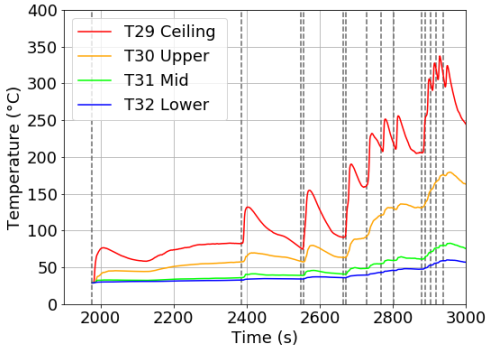

(d) Model Gas Temperatures TC 29-32

Figure A.19: First rack experiment compartment gas temperatures from experiment and model.

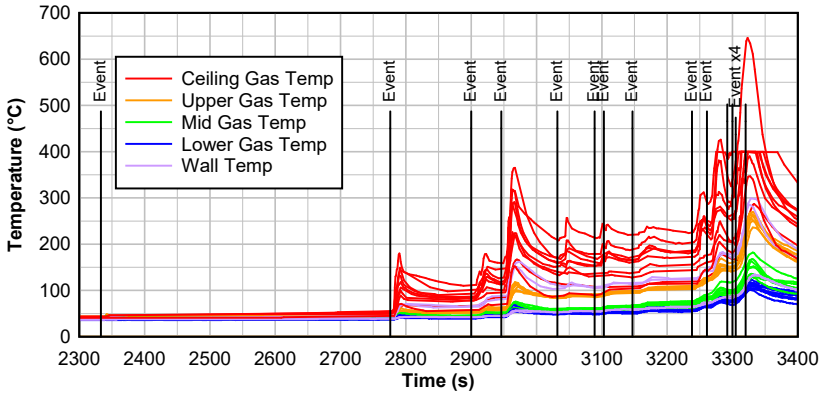

(a) Experiment Compartment Gas Temperatures and Heat Fluxes

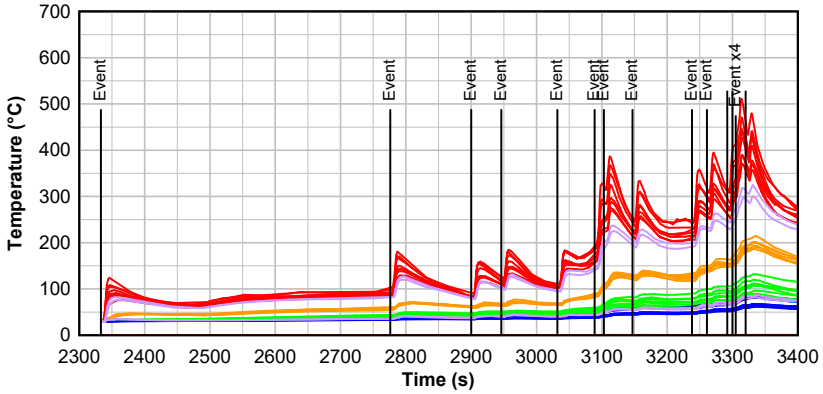

(b) FDS CFD Model Temperature and Heat Fluxes

Figure A.20: Experiment and model results from second rack experiment

Appendix B

LFP Module Experiments

There are many different chemistries and form factors for battery systems. While it is not possible to examine every combination of form factors and lithium-ion chemistries, an effort was made to at least briefly examine common types of systems. In this section thermal runaway, gas generation and thermal runaway propagation behavior is examined experimentally for a system comprised of arrays of cylindrical lithium-ion iron phosphate (LFP) cells.

These experiments are performed using commercially available LFP modules. The modules measure 197mm x 132mm x 173mm and have a mass of 5.3 kg. Each module contains 48 cylindrical 26650 cells. The cells are arranged 8s6p, meaning the cells are connected in parallel in groups of 6 and 8 of these groups are connected in series. Each cell has a nominal voltage of 3.2V and a nominal capacity of 11.84 Wh. As a whole the system has a nominal voltage of 25.6 V and a nominal capacity of 22.2 Ah or 568.3 Wh. Figure B.1 shows the module along with a module that has had sides cut off to show the cells inside of the module. Internally the cells are arranged in an array which is 6 cells long (cells connected in parallel), 4 cells wide and 2 cells high. Above the cell array is a circuit board which provides cell balancing, short circuit protection, high voltage cut off and low voltage cut off. On one side of the cell array are plastic spacer grids which fill the excess space in the module.

The objective of these experiments is to quantify the composition and volume of gases

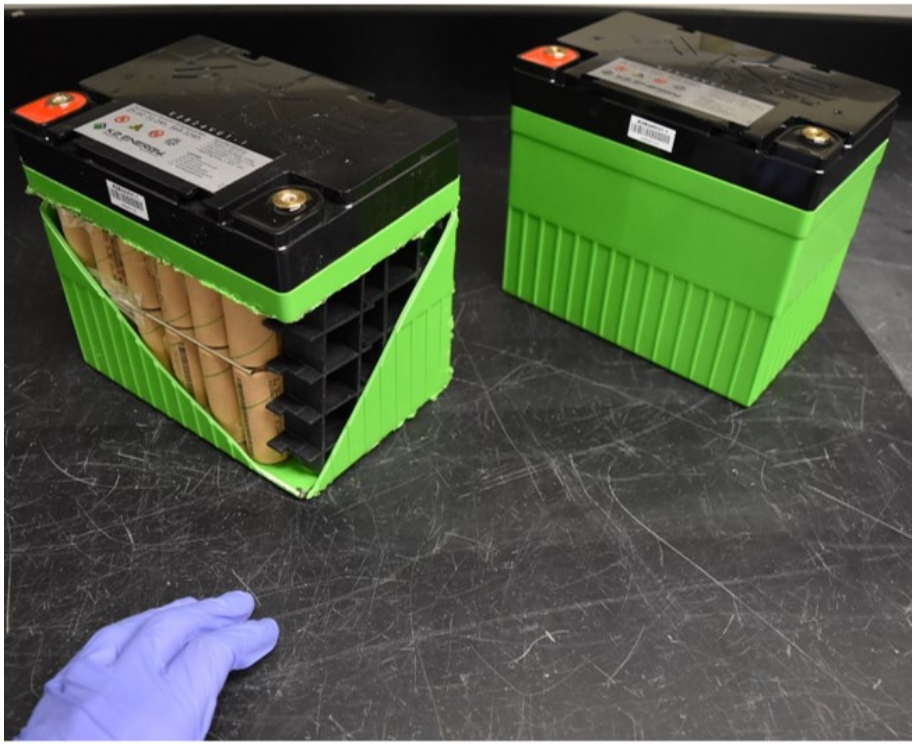

Figure B.1: LFP module and cut-open LFP module showing cylindrical cells array inside

produced when the cells go into thermal runaway. Another objective is to produce initial observations of the thermal runaway propagation process for a commercially-available LFP system. To accomplish these objectives, two experiments were executed. To observe how the thermal runaway propagation process could occur in an installation, the first experiment thermally fails the cell on a stand inside of a closet-sized test structure. To measure the volume and species of gas released during thermal runaway, a second experiment was performed inside of a pressure vessel which was inerted with nitrogen.

Closet Experiment

Experiment Setup For the closet experiment, the module was heated by placing it on top of heated aluminum blocks. The aluminum blocks measure 65 x 200 mm x 12 mm and each contain three 2 inch long, 0.25 inch diameter cylindrical cartridge heaters. Each cartridge heater has an output of 200 W at 120V. The setup uses two aluminum block heaters. Each aluminum block heater supports about half of the module. For this experiment, only one of the aluminum blocks was heated. The other was available as a backup in the event that thermal runaway did not propagate. The module can be seen on top of the aluminum heater blocks in Figure B.2.

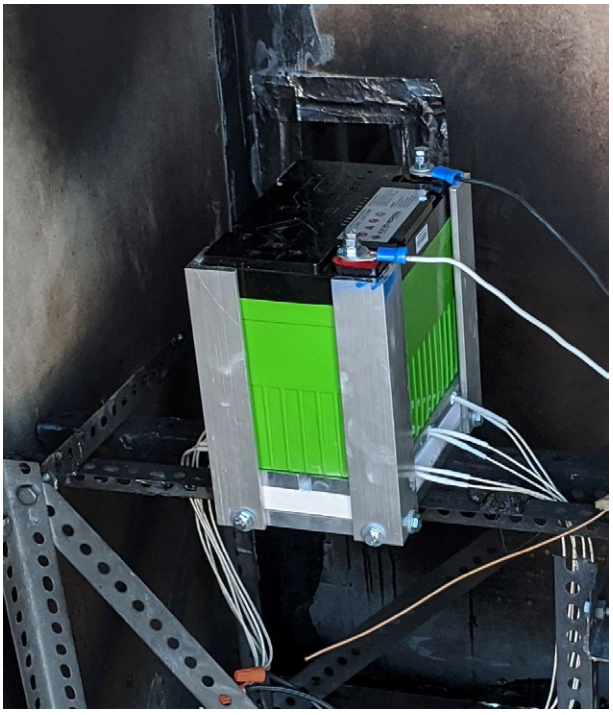

Figure B.2: Module on top of aluminum block heaters in closet before experiment.

The experiment was conducted in a closet constructed for the purposes of testing

fire and explosion hazards of lithium-ion battery systems in small spaces. The closet construction is described in Section 4.2.6.

During the experiment the module was heated using one of the aluminum block heaters until thermal runaway initiated. Afterwards thermal runaway was allowed to propagate from cell to cell. The heater was positioned such that half of the bottom cells were directly above it. The other half of the bottom cells were positioned on top of the other heater, which was not used since runaway propagated from one side to the other from cell to cell.

The module is supported by aluminum block heaters and surrounded by aluminum angle to prevent movement. This is mounted to stand which is placed on a load cell towards one side of the closet. Inside the closet there are two windows for cameras, two thermocouple trees, and two arc igniters to ignite flammable gases. The closet is closed with a door for the duration of this experiment.

During the experiment the compartment temperature was measured using two trees of 24 gauge type K thermocouples, one near the center of the compartment and another offset from one corner. The temperature of the aluminum heater blocks is also measured using thermocouples. The mass of the entire setup was also measured throughout the experiment using the load cell.

Results Audio and video taken during the experiment show that it takes about 2036 seconds from the time of the first cell runaway until the last cell runaway. Dur-

Figure B.3: LFP Module in closet before experiment.

ing this period, the thermal runaway propagation process through the cells results in about 42 audible popping, hissing or squealing noises. Video shows that these noises are associated with the release of a white cloud containing flammable gases, particulate matter and electrolyte.

Before the first noticeable popping noise and white cloud, the module produces a small amount of smoke. This could be due to melting and burning of the plastic casing exposed to the aluminum block heater. The first noticeable visual and audio cues of runaway occur at 1402 seconds when there are 5 popping noises in a 9 second period, each sound is accompanied by a release of a white cloud containing gases, liquids and particulate. Figure B.4 shows the module before the first popping noise, at the time just after a popping noise and ten seconds later after the 5

popping noises have occurred and a white cloud has been produced which mostly obscures view of the far wall. After the first few thermal runaway events, the room became obscured with the white/gray cloud caused by cell thermal runaway releases.

Figure B.4: LFP module before first popping noise, during first popping noise and after 5 popping noises which occur in a 9 second period.

In addition to audio and visual cues of thermal runaway, the process can be seen in the mass data. Figure B.5 shows the module mass as a function of time along with the first derivative of module mass. The spikes in the first derivative of mass show times when cells are rupturing and releasing clouds of gas and other material. In total there are 26 spikes that produce a mass loss rate greater than 1 g/s. These spikes vary in magnitude. Six of the mass loss spike events result in a mass loss of more than 3 grams in one second. The remaining 20 mass loss spikes cause only a little more than 1 gram of mass loss in one second. This is an indication that some runaway and mass loss events are more severe than others.

The mass loss events appear to be grouped. The first 12 mass loss spikes occur in 918 seconds from 1413 s to 2331 s. Then there are no mass loss spikes for a period of 305 seconds. The next 14 mass loss spikes occur from 2636 s to 3449 s. Since

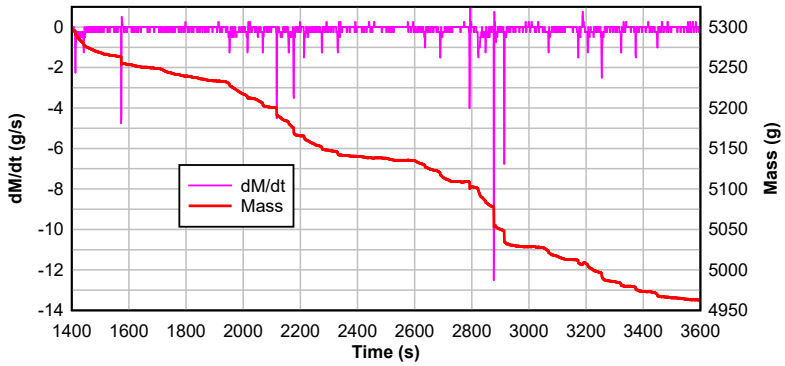

Figure B.5: Module mass and derivative of module mass as a function of time show that 26 mass loss spike events with a mass loss of 1 g/s, of which 6 mass loss events cause greater than 3 g/s of mass loss.

runaway was started by heating up 12 of the cells, it appears that the first 12 mass loss events are the 12 cells above the heater going into runaway and that the delayed mass loss events are the others.

Unlike the NMC experiments in Section 3.3 for this single module in thermal runaway, there was not any visible flaming combustion. Because of this, temperatures inside the compartment increased only slightly. Temperature increases do correlate with mass loss spikes and audible hissing and popping noises. Figure B.6 shows the closet temperatures alongside the mass loss rate (purple) and noticeable sounds (black).

After the experiment, the module was examined for damage. In the end only 24 of the 48 cells went into thermal runaway. The lower 24 cells went into thermal runaway while the 24 cells above did not. Even though only 12 of the bottom cells were directly above the heater that was turned on, thermal runaway propagated

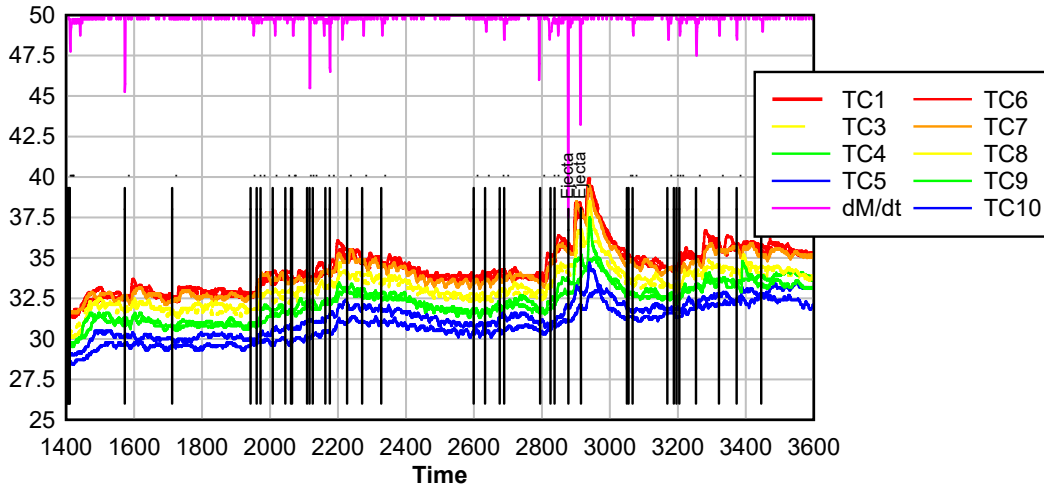

Figure B.6: Closet compartment temperatures, mass loss rate and audible noises (black lines).

from these 12 cells to the 12 cells next to them. However, thermal runaway did not propagate into the 24 cells above these. This is surprising as the cells above are separated from those below by only a thin plastic panel and thin foil current collectors. However, this was enough to prevent runaway propagation. The cells above appeared to be intact complete with the paper wrapping that they originally had. Even after 2 weeks, the voltage of the upper battery pack was measured at 13.3 V, which is indicative of still being nearly fully charged.

Pressure Vessel Experiment

Experiment Setup The pressure vessel experiment was conducted to provide measurements of the quantity and species of gas released by the cells during thermal runaway. Since in the closet experiment, the aluminum block heaters under the

Figure B.7: LFP Module after experiment

module were unable to cause runaway to propagate into the upper cells, the module was partially disassembled to allow for the testing of only the bottom 24 cells. For this experiment only the bottom 24 cells were used. The plastic housing, wires and circuit board were removed as shown in Figure B.10.

The experiment was conducted in the pressure vessel used for the pouch array experiments described in 2.3. During the experiment the vessel gas pressure was measured with a pressure transducer. Gas temperatures were measured at 9 locations throughout the vessel.

Figure B.8: Lower 24 cells did go into thermal runaway during experiment with several losing their top and and venting material.

Results The vessel gas pressure and gas temperature data can be used to observe the thermal runaway propagation process. Figure B.11 shows the temperature and pressure data along with the first derivative of the pressure data. From this data it can be observed that the thermal runaway propagation process proceeded over the course of 909 seconds from about 3401s to 4310s. Gas and temperature data were used along with a model to determine the volume of gas released. This 24 cell array generated 33.5 liters of gas at STP conditions.

Approximately 24 hours after the experiment, 3 gas samples were taken and analyzed using gas chromatography to determine composition. The composition of the

Figure B.9: Top 24 cells did not go into thermal runaway during the experiment

is provided in the Table B.1.

A photograph of the cell array after the experiment is shown in Figure B.12. After the experiment the mass of each cell was measured. Five of the cells had a mass between 23 and 36 grams while the remaining 20 cells had a mass between 72 and 82 grams. Undamaged cells have a mass of 86.7 grams. This shows that there are two different ways in which cells fail. The cells with a large mass loss have lost one of

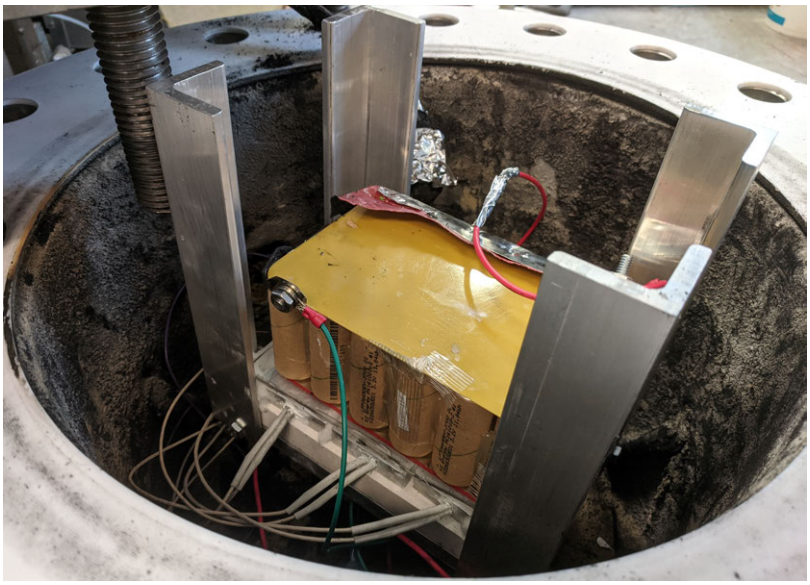

Figure B.10: 24 cell array in pressure vessel before experiment

the ends of the cell and eject or partially eject large amounts of cathode, anode and current collectors. Cells with smaller mass loss have their top and bottom in place and have lost only gases, liquids and small particles through the vent on the end of the cell. The five cells with a large amount of mass loss are also likely the five cells that led to larger pressure spikes in the pressure data. These pressure spikes were also accompanied by a clinking noise, which is likely the impact of the metal top on the vessel walls.

Discussion There are a number of common behaviors seen in both experiments. One major similarity is that in both experiments some of the cell failures were more severe than others. In the case of the closet experiment, the more extreme cell failures are those in which a large amount of the inside of the cell is ejected. In the video of the event the two most severe failures are obvious because they were the only two that visibly threw ejecta across the closet. These two failures were also

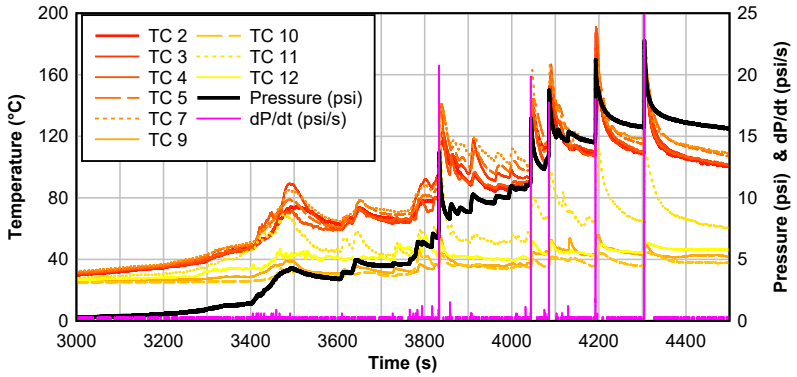

Figure B.11: Gas temperatures in higher (TC2-TC9) and lower (TC10-12) regions of vessel along with vessel gas pressure and first derivative of gas pressure.

Species	**Volume Percent**
Hydrogen	42
Carbon Dioxide	24
Carbon Monoxide	7.8
Methane	7.6
Ethylene	4.5
Propane or Propylene	3.7
Ethane	1.78
Other	8.62

Table B.1: Species Volume Percent for Gas Released by LFP Array

evident due to larger mass loss rates and total mass loss for these events. In the pressure vessel experiment, the more extreme cell failures are seen by the five times that there is a considerably larger pressure spike. These spikes also corresponded with clinking noises, likely caused by the impact of the cell top onto the vessel walls. Afterwards the cells that had more extreme failures were evident because they had lost significantly more mass than the other cells.

These two experiments demonstrate a number of differences when compared against

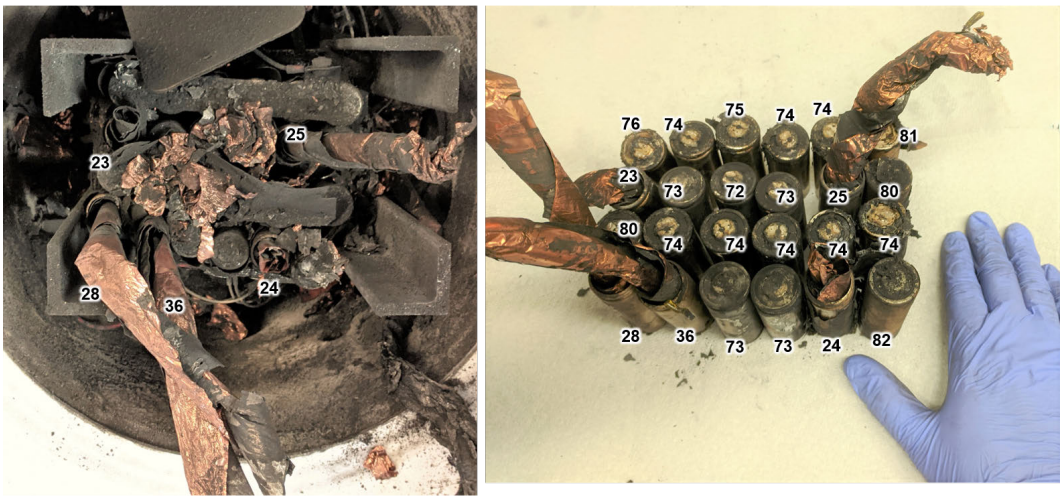

Figure B.12: 24 cell array in pressure vessel after experiment with mass in grams of lightest cells annotated

the LCO and NMC pouch cell and prismatic systems. One major difference is that the failing module never caught on fire. This is due to the fact that out of the 24 cells that went into thermal runaway, only one was observed to eject hot material which might cause an ignition. In contrast, both the LCO pouch cells in Section 4.3.1 and the NMC prismatic cells in Section 4.2.6, both consistently released a jet of glowing hot particles for a few seconds shortly after the beginning of the intense venting period.

Another major difference between the LFP cells and the LCO and NMC cells is the amount of gas generated. The LFP cells produced only produced 0.12 liters of gas at STP for every Watt-hour of nominal energy storage capacity. This is significantly lower than the 0.35 L/Wh for the 10 Ah pouch cell arrays and the 0.64 L/Wh produced by the 94 Ah prismatic NMC cell.

Although these cells seem to be more difficult to propagate thermal runaway and they produce less flammable gas than others, they are clearly still very hazardous. A major danger is that if a large energy storage system has a thermal failure that causes the thermal runaway of multiple cells and modules, it can still easily produce enough gas to cause a major fire or explosion, such as the Griffith University explosion. The vent gas generated by thermal runaway consists of 42 % hydrogen, which will cause it to have a high burning velocity and consequently makes it very dangerous for explosions.

Figure B.13: 24 cell array, removed cells with mass measurements

Bibliography

[1] C. Essl, A. W. Golubkov, and A. Fuchs, "Comparing Different Thermal Runaway Triggers for Two Automotive Lithium-Ion Battery Cell Types," *Journal of The Electrochemical Society*, vol. 167, no. 13, p. 130542, Oct. 2020, publisher: The Electrochemical Society. [Online]. Available: https://doi.org/10.1149/1945-7111/abbe5a

[2] V. Viswanathan and M. Paiss, "Safety Comparison of Li-ion Battery Technology Options for Energy Storage Systems - IEEE Smart Grid," Aug. 2020. [Online]. Available: https://smartgrid.ieee.org/newsletters/august-2020/safety-comparison-of-li-ion-battery-technology-options-for-energy-storage-systems

[3] A. Piffert, "Fire at ENGIE Drogenbos, 11.11.2017," Nov. 2017. [Online]. Available: https://www.youtube.com/watch?v=IElPzxj37dw&ab_channel=AsoPiffert

[4] "Rolling danger," Apr. 2017, section: Editorials. [Online]. Available: https://www.houstonchronicle.com/opinion/editorials/article/Rolling-danger-11101640.php

[5] M. B. McKinnon, S. DeCrane, and S. Kerber, "Four Firefighters Injured In Lithium-Ion Battery Energy Storage System Explosion - Arizona," p. 66.

[6] E. S. T. Australia, "Second alarm fire, 5th floor Griffith Uni Nathan QLD State of the art "Hydrogen Powered Building"," Mar. 2020. [Online]. Available: https://www.youtube.com/watch?v=H0MwP_aCJrw

[7] . . A. E. |. L. U. CBC News and 2019, "Electric car catches fire and explodes in Île-Bizard garage | CBC News," Jul. 2019. [Online]. Available: https://www.cbc.ca/news/canada/montreal/electric-car-catches-fire-and-explodes-in-%C3%AEle-bizard-garage-1.5227665

[8] A. R. Baird, E. J. Archibald, K. C. Marr, and O. A. Ezekoye, "Explosion hazards from lithium-ion battery vent gas," *Journal of Power Sources*, vol. 446, p. 227257, Jan. 2020. [Online]. Available: http://www.sciencedirect.com/science/article/pii/S0378775319312509

[9] Q. Zhou, C. S. Cheung, C. W. Leung, X. Li, X. Li, and Z. Huang, "Effects of fuel composition and initial pressure on laminar flame speed of H2/CO/CH4 bio-syngas," *Fuel*, vol. 238, pp. 149–158, Feb. 2019. [Online]. Available: http://www.sciencedirect.com/science/article/pii/S0016236118318313

[10] D. Lapalme and P. Seers, "Influence of CO2, CH4, and initial temperature on H2/CO laminar flame speed," *International Journal of Hydrogen Energy*, vol. 39, no. 7, pp. 3477–3486, Feb. 2014. [Online]. Available: http://www.sciencedirect.com/science/article/pii/S0360319913030735

[11] L. Liu, Z. Du, T. Zhang, Z. Guo, M. He, and Z. Liu, "The inhibition/promotion effect of C6F12O added to a lithium-ion cell syngas premixed flame," *International Journal of Hydrogen Energy*, vol. 44, no. 39, pp. 22 282–22 300, Aug. 2019. [Online]. Available: https://www.sciencedirect.com/science/article/pii/S0360319919323936

[12] A. Staff, "2019 Hyundai Kona EV Pictures," 2019. [Online]. Available: https://www.autoblog.com/buy/2019-Hyundai-Kona+EV/photos/

[13] Hyundai, "KONA Electric," 2021. [Online]. Available: https://www.hyundai.com/eu/models/kona-electric.html

[14] J. Nisewanger, "Exclusive: details on Hyundai's new battery thermal management design," Dec. 2018. [Online]. Available: https://electricrevs.com/2018/12/20/exclusive-details-on-hyundais-new-battery-thermal-management-design/

[15] A. J. Kurzawski, "Inverse modeling and characterization of an experimental testbed to advance fire scene reconstruction," Thesis, Dec. 2017, accepted: 2018-03-08T15:02:27Z. [Online]. Available: https://repositories.lib.utexas.edu/handle/2152/63814

[16] J. Deign, "Engie Investigates Source of Belgian Battery Blaze," Dec. 2017. [Online]. Available: https://www.greentechmedia.com/articles/read/engie-investigates-source-of-belgian-battery-blaze

[17] N. Hyun-woo, "Frequent fire raising concerns over safety of solar energy," Jan. 2019. [Online]. Available: https://www.koreatimes.co.kr/www/tech/2018/12/133_260560.html

[18] P. private joint investigation committee on energy storage system (ESS) fire accidents, "ESS accident cause investigation results and safety enhancement measures announced," Jun. 2019. [Online]. Available: https://www.gov.kr/portal/ntnadmNews/1897648

[19] S. Cummings, "South Korea Identifies Top 4 Causes that Led to

ESS Fires," Jun. 2019. [Online]. Available: https://liiontamer.com/south-korea-identifies-top-4-causes-that-led-to-ess-fires/

[20] K. Staff, "Neighborhood residents concerned following train car explosion," Apr. 2017. [Online]. Available: https://www.khou.com/article/news/local/neighborhood-residents-concerned-following-train-car-explosion/285-433810198

[21] S. Beausoleil, "Lithium batteries causes train car explosion in NE Houston," Apr. 2017. [Online]. Available: https://www.click2houston.com/news/train-catches-fire-in-ne-houston

[22] "Eight AZ Firefighters Hurt, One Critically, in Explosion." [Online]. Available: https://www.firehouse.com/safety-health/news/21077221/eight-az-firefighters-injured-one-critically-in-a-large-utility-battery-explosion

[23] "Injured firefighters identified from substation battery explosion in Surprise | Arizona News | azfamily.com." [Online]. Available: https://www.azfamily.com/news/firefighters-hospitalized-after-power-substation-battery-explosion-in-surprise/article_c28a7f1e-631c-11e9-9bf1-bfa00f273619.html

[24] H. Mai, "APS storage facility explosion raises questions about battery safety," Apr. 2019. [Online]. Available: https://www.utilitydive.com/news/aps-storage-facility-explosion-raises-questions-about-battery-safety/553540/

[25] M. Dennien, "Firefighter 'knocked on his back' in fire blast at Griffith University," Mar. 2020, library Catalog: www.brisbanetimes.com.au Section: Queensland. [Online].

Available: https://www.brisbanetimes.com.au/national/queensland/firefighter-injured-in-overnight-blaze-at-griffith-university-campus-20200316-p54aet.html

[26] E. Archibald, R. Kennedy, K. Marr, J. Jeevarajan, and O. Ezekoye, "Characterization of Thermally Induced Runaway in Pouch Cells for Propagation," *Fire Technology*, Mar. 2020. [Online]. Available: https://doi.org/10.1007/s10694-020-00974-2

[27] A. O. Said, C. Lee, X. Liu, Z. Wu, and S. I. Stoliarov, "Simultaneous measurement of multiple thermal hazards associated with a failure of prismatic lithium ion battery," *Proceedings of the Combustion Institute*, Jun. 2018. [Online]. Available: http://www.sciencedirect.com/science/article/pii/S1540748918300671

[28] S. Wilke, B. Schweitzer, S. Khateeb, and S. Al-Hallaj, "Preventing thermal runaway propagation in lithium ion battery packs using a phase change composite material: An experimental study," *Journal of Power Sources*, vol. 340, pp. 51–59, Feb. 2017. [Online]. Available: http://www.sciencedirect.com/science/article/pii/S0378775316315427

[29] J. Lamb, C. J. Orendorff, L. A. M. Steele, and S. W. Spangler, "Failure propagation in multi-cell lithium ion batteries," *Journal of Power Sources*, vol. 283, pp. 517–523, Jun. 2015. [Online]. Available: http://www.sciencedirect.com/science/article/pii/S0378775314016905

[30] C. F. Lopez, J. A. Jeevarajan, and P. P. Mukherjee, "Experimental Analysis of Thermal Runaway and Propagation in Lithium-Ion Battery Modules,"

Journal of The Electrochemical Society, vol. 162, no. 9, pp. A1905–A1915, Jan. 2015. [Online]. Available: http://jes.ecsdl.org/content/162/9/A1905

[31] G. Zhong, H. Li, C. Wang, K. Xu, and Q. Wang, "Experimental Analysis of Thermal Runaway Propagation Risk within 18650 Lithium-Ion Battery Modules," *Journal of The Electrochemical Society*, vol. 165, no. 9, pp. A1925–A1934, Jan. 2018. [Online]. Available: http://jes.ecsdl.org/content/165/9/A1925

[32] D. Ouyang, J. Liu, M. Chen, J. Weng, and J. Wang, "An Experimental Study on the Thermal Failure Propagation in Lithium-Ion Battery Pack," *Journal of The Electrochemical Society*, vol. 165, no. 10, pp. A2184–A2193, Jan. 2018. [Online]. Available: http://jes.ecsdl.org/content/165/10/A2184

[33] ——, "Thermal Failure Propagation in Lithium-Ion Battery Modules with Various Shapes," *Applied Sciences*, vol. 8, no. 8, p. 1263, Aug. 2018. [Online]. Available: https://www.mdpi.com/2076-3417/8/8/1263

[34] P. Huang, P. Ping, K. Li, H. Chen, Q. Wang, J. Wen, and J. Sun, "Experimental and modeling analysis of thermal runaway propagation over the large format energy storage battery module with Li4Ti5O12 anode," *Applied Energy*, vol. 183, pp. 659–673, Dec. 2016. [Online]. Available: http://www.sciencedirect.com/science/article/pii/S0306261916312697

[35] A. O. Said, C. Lee, S. I. Stoliarov, and A. W. Marshall, "Comprehensive analysis of dynamics and hazards associated with cascading failure in 18650 lithium ion cell arrays," *Applied Energy*, vol. 248, pp. 415–428, 2019.

[36] X. Feng, X. He, M. Ouyang, L. Lu, P. Wu, C. Kulp, and S. Prasser, "Thermal runaway propagation model for designing a safer battery

pack with 25Ah LiNixCoyMnzO2 large format lithium ion battery," *Applied Energy*, vol. 154, pp. 74–91, Sep. 2015. [Online]. Available: http://www.sciencedirect.com/science/article/pii/S0306261915005814

[37] X. Feng, L. Lu, M. Ouyang, J. Li, and X. He, "A 3D thermal runaway propagation model for a large format lithium ion battery module," *Energy*, vol. 115, pp. 194–208, Nov. 2016. [Online]. Available: http://www.sciencedirect.com/science/article/pii/S0360544216312075

[38] Q. Li, C. Yang, S. Santhanagopalan, K. Smith, J. Lamb, L. A. Steele, and L. Torres-Castro, "Numerical investigation of thermal runaway mitigation through a passive thermal management system," *Journal of Power Sources*, vol. 429, pp. 80–88, Jul. 2019. [Online]. Available: http://www.sciencedirect.com/science/article/pii/S0378775319305026

[39] E. Archibald, R. Kennedy, K. C. Marr, J. Jeevarajan, and O. A. Ezekoye, "Characterization of thermally induced runaway in pouch cells for propagation," *Fire Technology*, 2020.

[40] R. W. Kennedy, K. C. Marr, and O. A. Ezekoye, "Gas release rates and properties from Lithium Cobalt Oxide lithium ion battery arrays," *Journal of Power Sources*, vol. 487, p. 229388, Mar. 2021. [Online]. Available: http://www.sciencedirect.com/science/article/pii/S0378775320316724

[41] *Product Specification PL-896474-2C*, AA Portable Power Corp, 2010.

[42] "UL - 9540a Test Method for Evaluating Thermal Runaway Fire Propagation in Battery Energy Storage Systems | Standards Catalog." [Online]. Available: https://standardscatalog.ul.com/standards/en/standard_9540a_3

[43] Q. Wang, P. Ping, X. Zhao, G. Chu, J. Sun, and C. Chen, "Thermal runaway caused fire and explosion of lithium ion battery," *Journal of Power Sources*, vol. 208, pp. 210–224, Jun. 2012. [Online]. Available: http://www.sciencedirect.com/science/article/pii/S0378775312003989

[44] R. Spotnitz and J. Franklin, "Abuse behavior of high-power, lithium-ion cells," *Journal of Power Sources*, vol. 113, no. 1, pp. 81–100, Jan. 2003. [Online]. Available: http://www.sciencedirect.com/science/article/pii/S0378775302004883

[45] Q. Wang, B. Mao, S. I. Stoliarov, and J. Sun, "A review of lithium ion battery failure mechanisms and fire prevention strategies," *Progress in Energy and Combustion Science*, vol. 73, pp. 95–131, Jul. 2019. [Online]. Available: http://www.sciencedirect.com/science/article/pii/S0360128518301801

[46] D. Ouyang, M. Chen, Q. Huang, J. Weng, Z. Wang, and J. Wang, "A Review on the Thermal Hazards of the Lithium-Ion Battery and the Corresponding Countermeasures," *Applied Sciences*, vol. 9, no. 12, p. 2483, Jan. 2019, number: 12 Publisher: Multidisciplinary Digital Publishing Institute. [Online]. Available: https://www.mdpi.com/2076-3417/9/12/2483

[47] D. Hill, N. Warner, and W. Kovacs, "Considerations for ESS Fire Safety," DNVGL, Tech. Rep., Feb. 2017.

[48] R. T. Long and A. M. Misera, "Sprinkler Protection Guidance for Lithium-Ion Based Energy Storage Systems," p. 46, Jun. 2019.

[49] B. Ditch and D. Zeng, "Development of Sprinkler Protection Guidance for Lithium Ion Based Energy Storage Systems," FM Global, Tech. Rep., Jun. 2019.

[50] B. Gully, H. Helgesen, J. Skogtvedt, and D. Kostopoulos, "Technical Reference for Li-ion Battery Explosion Risk and Fire Suppression," DNVGL, Tech. Rep., Nov. 2019.

[51] K. McGrattan, S. Hostikka, R. McDermott, J. Floyd, C. Weinschenk, and K. Overholt, "Fire dynamics simulator user's guide," *NIST special publication*, vol. 1019, no. 6, 2013.

[52] F. Larsson, S. Bertilsson, M. Furlani, I. Albinsson, and B.-E. Mellander, "Gas explosions and thermal runaways during external heating abuse of commercial lithium-ion graphite-LiCoO2 cells at different levels of ageing," *Journal of Power Sources*, vol. 373, pp. 220–231, Jan. 2018. [Online]. Available: http://www.sciencedirect.com/science/article/pii/S0378775317314398

[53] H. Webster, T. Maloney, S. Summer, D. Dadia, S. Rehn, and M. Karp, "Summary of FAA Studies Related to the Hazards Produced by Lithium Cells in Thermal Runaway in Aircraft Cargo Compartments," US FAA, Tech. Rep. DOT/FAA/TC-16/37, 2016.

[54] K. Gabriel, *Mycodo Environmental Regulation System*, Jan. 2018. [Online]. Available: http://dx.doi.org/10.5281/zenodo.824199

[55] J.-W. Park, C. B. Oh, Y. S. Han, and K. H. Do, "Computational study of backdraft dynamics and the effects of initial conditions in a compartment," *Journal of Mechanical Science and Technology*, vol. 31, no. 2, pp. 985–993, Feb. 2017. [Online]. Available: http://link.springer.com/10.1007/s12206-017-0151-z

[56] A. R. Baird, E. J. Archibald, K. C. Marr, and O. A. Ezekoye, "Explosion hazards from lithium-ion battery vent gas," *Journal of Power Sources*, vol. 446, p. 227257, 2020.

[57] M. E. Paté-Cornell, "Fault Trees vs. Event Trees in Reliability Analysis," *Risk Analysis*, vol. 4, no. 3, pp. 177–186, 1984, _eprint: https://onlinelibrary.wiley.com/doi/pdf/10.1111/j.1539-6924.1984.tb00137.x. [Online]. Available: https://onlinelibrary.wiley.com/doi/abs/10.1111/j.1539-6924.1984.tb00137.x

[58] V. Somandepalli, K. Marr, and Q. Horn, "Quantification of Combustion Hazards of Thermal Runaway Failures in Lithium-Ion Batteries," *SAE Int. J. Alt. Power.*, vol. 3, no. 1, pp. 98–104, May 2014.

[59] A. W. Golubkov, D. Fuchs, J. Wagner, H. Wiltsche, C. Stangl, G. Fauler, G. Voitic, A. Thaler, and V. Hacker, "Thermal-runaway experiments on consumer li-ion batteries with metal-oxide and olivin-type cathodes," *Rsc Advances*, vol. 4, no. 7, pp. 3633–3642, 2014.

[60] A. W. Golubkov, S. Scheikl, R. Planteu, G. Voitic, H. Wiltsche, C. Stangl, G. Fauler, A. Thaler, and V. Hacker, "Thermal runaway of commercial 18650 Li-ion batteries with LFP and NCA cathodes – impact of state of charge and overcharge," *RSC Advances*, vol. 5, no. 70, pp. 57 171–57 186, Jun. 2015. [Online]. Available: http://pubs.rsc.org/en/content/articlelanding/2015/ra/c5ra05897j

[61] T. Maloney, "Home : FAA Fire Safety," Oct. 2016. [Online]. Available: https://www.fire.tc.faa.gov/systems/lithium-batteries

[62] M. Lammer, A. Königseder, and V. Hacker, "Holistic methodology for characterisation of the thermally induced failure of commercially available 18650 lithium ion cells," *RSC Advances*, vol. 7, no. 39, pp. 24 425–24 429,

May 2017. [Online]. Available: http://pubs.rsc.org/en/content/articlelanding/2017/ra/c7ra02635h

[63] K. Kumai, H. Miyashiro, Y. Kobayashi, K. Takei, and R. Ishikawa, "Gas generation mechanism due to electrolyte decomposition in commercial lithium-ion cell," *Journal of Power Sources*, vol. 81-82, pp. 715–719, Sep. 1999. [Online]. Available: http://linkinghub.elsevier.com/retrieve/pii/S0378775398002341

[64] T. Ohsaki, T. Kishi, T. Kuboki, N. Takami, N. Shimura, Y. Sato, M. Sekino, and A. Satoh, "Overcharge reaction of lithium-ion batteries," *Journal of Power Sources*, vol. 146, no. 1-2, pp. 97–100, Aug. 2005. [Online]. Available: http://linkinghub.elsevier.com/retrieve/pii/S0378775305005112

[65] Q. Yuan, F. Zhao, W. Wang, Y. Zhao, Z. Liang, and D. Yan, "Overcharge failure investigation of lithium-ion batteries," *Electrochimica Acta*, vol. 178, pp. 682–688, Oct. 2015. [Online]. Available: http://www.sciencedirect.com/science/article/pii/S0013468615302140

[66] Y. Zheng, K. Qian, D. Luo, Y. Li, Q. Lu, B. Li, Y.-B. He, X. Wang, J. Li, and F. Kang, "Influence of over-discharge on the lifetime and performance of LiFePO4/graphite batteries," *RSC Advances*, vol. 6, no. 36, pp. 30 474–30 483, Mar. 2016. [Online]. Available: http://pubs.rsc.org/en/content/articlelanding/2016/ra/c6ra01677d

[67] Y. Fernandes, A. Bry, and S. de Persis, "Identification and quantification of gases emitted during abuse tests by overcharge of a commercial Li-ion battery," *Journal of Power Sources*, vol. 389, pp. 106–119, Jun. 2018. [Online]. Available: https://linkinghub.elsevier.com/retrieve/pii/S0378775318302581

[68] C. Essl, A. W. Golubkov, E. Gasser, M. Nachtnebel, A. Zankel, E. Ewert, and A. Fuchs, "Comprehensive Hazard Analysis of Failing Automotive Lithium-Ion Batteries in Overtemperature Experiments," *Batteries*, vol. 6, no. 2, p. 30, Jun. 2020, number: 2 Publisher: Multidisciplinary Digital Publishing Institute. [Online]. Available: https://www.mdpi.com/2313-0105/6/2/30

[69] "NFPA 69: Standard on Explosion Prevention Systems." [Online]. Available: https://www.nfpa.org/codes-and-standards/all-codes-and-standards/list-of-codes-and-standards/detail?code=69

[70] R. A. Ogle, "Explosion hazard analysis for an enclosure partially filled with a flammable gas," *Process Safety Progress*, vol. 18, no. 3, pp. 170–177, 1999, _eprint: https://onlinelibrary.wiley.com/doi/pdf/10.1002/prs.680180310. [Online]. Available: http://aiche.onlinelibrary.wiley.com/doi/abs/10.1002/prs.680180310

[71] R. Zalosh, "Flammable Gas and Vapor Explosions," in *SFPE Handbook of Fire Protection Engineering*, M. J. Hurley, D. Gottuk, J. R. Hall, K. Harada, E. Kuligowski, M. Puchovsky, J. Torero, J. M. Watts, and C. Wieczorek, Eds. New York, NY: Springer New York, 2016, pp. 2738–2765. [Online]. Available: https://doi.org/10.1007/978-1-4939-2565-0_69

[72] Y.-D. Jo and K.-S. Park, "Minimum amount of flammable gas for explosion within a confined space," *Process Safety Progress*, vol. 23, no. 4, pp. 321–329, 2004, _eprint: https://aiche.onlinelibrary.wiley.com/doi/pdf/10.1002/prs.10042. [Online]. Available: https://aiche.onlinelibrary.wiley.com/doi/abs/10.1002/prs.10042

[73] H. Le Chatelier, "Estimation of firedamp by flammability limits," *Annals of Mines*, vol. 19, no. 8, pp. 388–395, 1891.

[74] J. G. Quintiere, "Fundamentals of Fire Phenomena," in *Fundamentals of Fire Phenomena*. John Wiley & Sons, 2006, pp. 77–115.

[75] M. Vidal, W. Wong, W. J. Rogers, and M. S. Mannan, "Evaluation of lower flammability limits of fuel–air–diluent mixtures using calculated adiabatic flame temperatures," *Journal of Hazardous Materials*, vol. 130, no. 1, pp. 21–27, Mar. 2006. [Online]. Available: http://www.sciencedirect.com/science/article/pii/S0304389405004218

[76] G. A. Melhem, "A detailed method for estimating mixture flammability limits using chemical equilibrium," *Process Safety Progress*, vol. 16, no. 4, pp. 203–218, 1997. [Online]. Available: http://onlinelibrary.wiley.com/doi/abs/10.1002/prs.680160403

[77] R. Bounaceur, P.-A. Glaude, B. Sirjean, R. Fournet, P. Montagne, M. Vierling, and M. Molière, "Prediction of Flammability Limits of Gas Mixtures Containing Inert Gases Under Variable Temperature and Pressure Conditions." American Society of Mechanical Engineers, Jun. 2017, pp. V04AT04A072–V04AT04A072. [Online]. Available: https://proceedings.asmedigitalcollection.asme.org/proceeding.aspx?articleid=2649966

[78] D. G. Goodwin, H. K. Moffat, and R. L. Speth, "Cantera: An Object-Oriented Software Toolkit For Chemical Kinetics, Thermodynamics, And Transport Processes. Version 2.3.0," Jan. 2017. [Online]. Available: cantera.org

[79] D. Clodic and T. Jabbour, "Method of test for burning velocity measurement of flammable gases and results," *HVAC&R Research*, vol. 17,

no. 1, pp. 51–75, Feb. 2011, publisher: Taylor & Francis _eprint: https://www.tandfonline.com/doi/pdf/10.1080/10789669.2011.543252. [Online]. Available: https://www.tandfonline.com/doi/abs/10.1080/10789669.2011.543252

[80] G. Smith, D. Golden, M. Frenklach, and N. Moriary, "GRI-Mech 3.0." [Online]. Available: http://combustion.berkeley.edu/gri-mech/version30/text30.html

[81] J. Johnplass, M. Henriksen, K. Vaagsaether, J. Lundberg, and D. Bjerketvedt, "Simulation of burning velocities in gases vented from thermal run-a-way lithium ion batteries," *Linköping University Electronic Press*, no. 138, pp. 157–161, Sep. 2017.

[82] J. Liu, X. Zhang, T. Wang, X. Hou, J. Zhang, and S. Zheng, "Numerical study of the chemical, thermal and diffusion effects of H2 and CO addition on the laminar flame speeds of methane–air mixture," *International Journal of Hydrogen Energy*, vol. 40, no. 26, pp. 8475–8483, Jul. 2015. [Online]. Available: http://www.sciencedirect.com/science/article/pii/S036031991501071X

[83] C. Liu, B. Yan, G. Chen, and X. S. Bai, "Structures and burning velocity of biomass derived gas flames," *International Journal of Hydrogen Energy*, vol. 35, no. 2, pp. 542–555, Jan. 2010. [Online]. Available: http://www.sciencedirect.com/science/article/pii/S0360319909017637

[84] S. Turns, *Introduction to Combustion: Concepts and Applications*. MCGRAW-HILL US HIGHER ED, 2011.

[85] K. Zhang and X. Jiang, "An investigation of fuel variability effect on bio-syngas combustion using uncertainty quantification," *Fuel*, vol. 220, pp.

283–295, May 2018. [Online]. Available: https://www.sciencedirect.com/science/article/pii/S0016236118301662

[86] "NFPA 68: Standard on Explosion Protection by Deflagration Venting." [Online]. Available: https://www.nfpa.org/codes-and-standards/all-codes-and-standards/list-of-codes-and-standards/detail?code=68

[87] "EN: 14994: 2007. Gas explosion venting protective systems - Google Scholar." [Online]. Available: https://scholar.google.com/scholar_lookup?title=14994%3A%202007.%20Gas%20explosion%20venting%20protective%20systems&author=EN%2C%20BS&publication_year=2007

[88] V. Molkov and M. Bragin, "Hydrogen–air deflagrations: Vent sizing correlation for low-strength equipment and buildings," *International Journal of Hydrogen Energy*, vol. 40, no. 2, pp. 1256–1266, Jan. 2015. [Online]. Available: https://www.sciencedirect.com/science/article/pii/S0360319914032017

[89] C. R. Bauwens, J. Chaffee, and S. B. Dorofeev, "Vented explosion overpressures from combustion of hydrogen and hydrocarbon mixtures," *International Journal of Hydrogen Energy*, vol. 36, no. 3, pp. 2329–2336, Feb. 2011. [Online]. Available: http://www.sciencedirect.com/science/article/pii/S0360319910006671

[90] J. Chao, C. R. Bauwens, and S. B. Dorofeev, "An analysis of peak overpressures in vented gaseous explosions," *Proceedings of the Combustion Institute*, vol. 33, no. 2, pp. 2367–2374, Jan. 2011. [Online]. Available: http://www.sciencedirect.com/science/article/pii/S1540748910002877

[91] A. Sinha, V. C. Madhav Rao, and J. X. Wen, "Modular phenomenological model for vented explosions and its validation with experimental and

computational results," *Journal of Loss Prevention in the Process Industries*, vol. 61, pp. 8–23, Sep. 2019. [Online]. Available: http://www.sciencedirect.com/science/article/pii/S0950423019302773

[92] ——, "Performance evaluation of empirical models for vented lean hydrogen explosions," *International Journal of Hydrogen Energy*, vol. 44, no. 17, pp. 8711–8726, Apr. 2019. [Online]. Available: http://www.sciencedirect.com/science/article/pii/S0360319918329689

[93] A. Sinha and J. X. Wen, "A simple model for calculating peak pressure in vented explosions of hydrogen and hydrocarbons," *International Journal of Hydrogen Energy*, vol. 44, no. 40, pp. 22 719–22 732, Aug. 2019. [Online]. Available: http://www.sciencedirect.com/science/article/pii/S0360319919308717

[94] S. R. Mulpuru and G. B. Wilkin, "A model for vented deflagration of hydrogen in a volume," Atomic Energy of Canada Ltd., Tech. Rep. AECL–6826, 1982. [Online]. Available: http://inis.iaea.org/Search/search.aspx?orig_q=RN:13705575

[95] O. R. Hansen and D. M. Johnson, "Improved far-field blast predictions from fast deflagrations, DDTs and detonations of vapour clouds using FLACS CFD," *Journal of Loss Prevention in the Process Industries*, vol. 35, pp. 293–306, May 2015. [Online]. Available: https://www.sciencedirect.com/science/article/pii/S0950423014001831

[96] J. K. Clutter, J. T. Mathis, and M. W. Stahl, "Modeling environmental effects in the simulation of explosion events," *International Journal of Impact*

Engineering, vol. 34, no. 5, pp. 973–989, May 2007. [Online]. Available: https://www.sciencedirect.com/science/article/pii/S0734743X06000595

[97] V. C. M. Rao and J. X. Wen, "Numerical Modelling of Vented Lean Hydrogen–Air Deflagrations using HyFOAM," *26th International Colloquium on the Dynamics of Explosions and Reactive Systems (ICDERS)*, p. 8, 2017.

[98] T. Skjold, H. Hisken, S. Lakshmipathy, G. Atanga, M. Carcassi, M. Schiavetti, J. R. Stewart, A. Newton, J. R. Hoyes, I. C. Tolias, A. G. Venetsanos, O. R. Hansen, J. Geng, A. Huser, S. Helland, R. Jambut, K. Ren, A. Kotchourko, T. Jordan, J. Daubech, G. Lecocq, A. G. Hanssen, C. Kumar, L. Krumenacker, S. Jallais, D. Miller, and C. R. Bauwens, "Blind-prediction: Estimating the consequences of vented hydrogen deflagrations for homogeneous mixtures in 20-foot ISO containers," *International Journal of Hydrogen Energy*, vol. 44, no. 17, pp. 8997–9008, Apr. 2019. [Online]. Available: https://www.sciencedirect.com/science/article/pii/S0360319918321013

[99] T. Skjold, H. Hisken, L. Bernard, L. Mauri, G. Atanga, S. Lakshmipathy, M. Lucas, M. Carcassi, M. Schiavetti, V. Chandra Madhav Rao, A. Sinha, J. X. Wen, I. C. Tolias, S. G. Giannissi, A. G. Venetsanos, J. R. Stewart, O. R. Hansen, C. Kumar, L. Krumenacker, F. Laviron, R. Jambut, and A. Huser, "Blind-prediction: Estimating the consequences of vented hydrogen deflagrations for inhomogeneous mixtures in 20-foot ISO containers," *Journal of Loss Prevention in the Process Industries*, vol. 61, pp. 220–236, Sep. 2019. [Online]. Available: https://www.sciencedirect.com/science/article/pii/S0950423019302517

[100] C. R. Bauwens, J. M. Bergthorson, S. B. Dorofeev, and F. Global, "Critical

Peclet Numbers for the Onset of Darrieus-Landau Instability in Atmospheric-Pressure Methane-Air Flames," *C. R.*, p. 6, 2015.

[101] C. R. L. Bauwens, J. M. Bergthorson, and S. B. Dorofeev, "Experimental investigation of spherical-flame acceleration in lean hydrogen-air mixtures," *International Journal of Hydrogen Energy*, vol. 42, no. 11, pp. 7691–7697, Mar. 2017. [Online]. Available: http://www.sciencedirect.com/science/article/pii/S036031991630965X

[102] C. R. Bauwens, J. M. Bergthorson, and S. B. Dorofeev, "Experimental study of spherical-flame acceleration mechanisms in large-scale propane–air flames," *Proceedings of the Combustion Institute*, vol. 35, no. 2, pp. 2059–2066, Jan. 2015. [Online]. Available: http://www.sciencedirect.com/science/article/pii/S1540748914002764

[103] O. J. Ugarte, V. Akkerman, and A. S. Rangwala, "A computational platform for gas explosion venting," *Process Safety and Environmental Protection*, vol. 99, pp. 167–174, Jan. 2016. [Online]. Available: https://linkinghub.elsevier.com/retrieve/pii/S0957582015001998

[104] H. Sezer, F. Kronz, V. Akkerman, and A. S. Rangwala, "Methane-induced explosions in vented enclosures," *Journal of Loss Prevention in the Process Industries*, vol. 48, pp. 199–206, Jul. 2017. [Online]. Available: http://www.sciencedirect.com/science/article/pii/S0950423017303601

[105] S. Ogunfuye, H. Sezer, F. Kodakoglu, H. F. Farahani, A. S. Rangwala, and V. Akkerman, "Dynamics of Explosions in Cylindrical Vented Enclosures: Validation of a Computational Model by Experiments," *Fire*, vol. 4, no. 1,

p. 9, Mar. 2021, number: 1 Publisher: Multidisciplinary Digital Publishing Institute. [Online]. Available: https://www.mdpi.com/2571-6255/4/1/9

[106] R. K. Kumar, H. TAMM, and W. C. HARRISON, "Combustion of Hydrogen at High Concentrations. Including the Effect of Obstacles," *Combustion Science and Technology*, vol. 35, pp. 175–186, 1983. [Online]. Available: http://www.tandfonline.com/doi/abs/10.1080/00102208308923709

[107] A. J. Harrison and J. A. Eyre, "External Explosions" as a Result of Explosion Venting," *Combustion Science and Technology*, vol. 52, no. 1-3, pp. 91–106, Mar. 1987. [Online]. Available: http://www.tandfonline.com/doi/abs/10.1080/00102208708952570

[108] C. R. Bauwens, J. Chaffee, and S. Dorofeev, "Effect of Ignition Location, Vent Size, and Obstacles on Vented Explosion Overpressures in Propane-Air Mixtures," *Combustion Science and Technology*, vol. 182, no. 11-12, pp. 1915–1932, Oct. 2010. [Online]. Available: http://www.tandfonline.com/doi/abs/10.1080/00102202.2010.497415

[109] T. Forcier and R. Zalosh, "External pressures generated by vented gas and dust explosions," *Journal of Loss Prevention in the Process Industries*, vol. 13, no. 3, pp. 411–417, May 2000. [Online]. Available: http://www.sciencedirect.com/science/article/pii/S0950423099000443

[110] R. K. Eckhoff, "Dust explosions in the process industries," 1991, publisher: Butterworth, Stoneham, MA (United States).

[111] "Chapter 17 - Explosion," in *Lees' Loss Prevention in the Process Industries (Fourth Edition)*, S. Mannan, Ed. Oxford: Butterworth-

Heinemann, Jan. 2012, pp. 1367–1678. [Online]. Available: https://www.sciencedirect.com/science/article/pii/B9780123971890000173

[112] J. M. Biggs and J. Biggs, *Introduction to structural dynamics*. New York: McGraw-Hill, 1964.

[113] U. D. of Defense, *UFC: Structures to Resist the Effects of Accidental Explosions*, Sep. 2014. [Online]. Available: https://www.wbdg.org/ffc/dod/unified-facilities-criteria-ufc/ufc-3-340-02

[114] PEC, "Methodology Manual for the Single-Degree-of-Freedom Design Spreadsheets (SBEDS)," US Army Corps of Engineers - Protective Design Center, Tech. Rep. PDC TR-06-01, Sep. 2008.

[115] N. Null, *Design of Blast-Resistant Buildings in Petrochemical Facilities*. American Society of Civil Engineers, Nov. 2010. [Online]. Available: https://ascelibrary.org/doi/10.1061/9780784410882

[116] PDC, "Single Degree of Freedom Structural Response Limits for Antiterrorism Design," US Army Corps of Engineers - Protective Design Center, Tech. Rep. PDC TR-06-08, Jan. 2008.

[117] C. Oswald and M. Bazan, "Comparison of SDOF Analysis Results to Test Data for Different Types of Blast Loaded Components," in *Structures Congress 2014*. Boston, Massachusetts, United States: American Society of Civil Engineers, Apr. 2014, pp. 117–130. [Online]. Available: http://ascelibrary.org/doi/10.1061/9780784413357.012

[118] PDC, "Comparison of Calculated Single-Degree-of-Freedom Response to Blast

Test Data," US Army Corps of Engineers - Protective Design Center, Tech. Rep. PDC TR-08-02, Sep. 2008.

[119] K. 11, "Train car explodes near downtown Houston," Apr. 2017. [Online]. Available: https://www.youtube.com/watch?v=eKXZLUpueaQ&ab_channel=KHOU11

[120] M. Smith, "Lithium Ion Battery Fire - Griffith University (Brisbane), 15th March 2020," Queensland Fire and Emergency Services, Tech. Rep., Jul. 2020.

[121] B. Ma, J. Liu, and R. Yu, "Study on the Flammability Limits of Lithium-Ion Battery Vent Gas under Different Initial Conditions," *ACS Omega*, vol. 5, no. 43, pp. 28 096–28 107, Nov. 2020. [Online]. Available: https://pubs.acs.org/doi/10.1021/acsomega.0c03713

[122] J. Herman and W. Usher, "SALib: An open-source Python library for Sensitivity Analysis," *The Journal of Open Source Software*, vol. 2, no. 9, p. 97, Jan. 2017. [Online]. Available: http://joss.theoj.org/papers/10.21105/joss.00097

[123] I. M. Sobol, "Global sensitivity indices for nonlinear mathematical models and their Monte Carlo estimates," *Mathematics and Computers in Simulation*, vol. 55, no. 1, pp. 271–280, Feb. 2001. [Online]. Available: https://www.sciencedirect.com/science/article/pii/S0378475400002706

[124] A. Saltelli, "Making best use of model evaluations to compute sensitivity indices," *Computer Physics Communications*, vol. 145, no. 2, pp. 280–297, May 2002. [Online]. Available: https://www.sciencedirect.com/science/article/pii/S0010465502002801

[125] G. Ruffo, "Hyundai Kona Electric Blast: High Voltage Battery Area Had The Most Damage," Jun. 2020. [Online]. Available: https://insideevs.com/news/430353/hyundai-kona-eletric-blast-battery-most-damage/

[126] "Standard Garage Sizes for 1, 2, 3, or 4 Cars (with Chart)," Oct. 2019. [Online]. Available: https://www.garagetooladvisor.com/design/garage-sizes/

[127] A. L. Jaffe, G. A. Riveros, and G. A. Kopp, "Wind Speed Estimates for Garage Door Failures in Tornadoes," *Frontiers in Built Environment*, vol. 5, 2019, publisher: Frontiers. [Online]. Available: https://www.frontiersin.org/articles/10.3389/fbuil.2019.00014/full

[128] D. Hill, "McMicken Battery Energy Storage System Event Technical and Recommendations," DNVGL, Tech. Rep. 10209302-HOU-R-01, Jul. 2020. [Online]. Available: http://www.firefighternation.com/wp-content/uploads/sites/10/2020/07/document.pdf